Time-scale dependent modeling and control of LVDC microgrids

Eduardo Rene Vasquez Mayen
Electrical engineer

Electrical engineering Ph.D. thesis

Thesis Jury:

Prof.	Hervé Jeanmart	UCLouvain	Chairman
Prof.	Emmanuel De Jaeger	UCLouvain	Supervisor
Prof.	Marc Bekemans	UCLouvain	
Prof.	Bruno Dehez	UCLouvain	
Dr.	Benoît Bidaine	CE+T Power	
Prof.	Jan Desmet	Universiteit Gent	

September, 2024
Louvain-la-Neuve, Belgium

Acknowledgements

I would like to thank Professor Emmanuel De Jaeger for trusting me with the work of this PhD. Professor De Jaeger possesses vast knowledge in power systems, from which I have learned immensely. Throughout these years, his door was always open to discuss and help me with the challenges I faced. I deeply appreciate his support and guidance.

I would also like to thank the members of my thesis jury: Bruno Dehez, Mark Bekemans, Hervé Jeanmart from UCLouvain, Benoît Bidaine from CE+T, and Jan Desmet from Universiteit Ghent, for their time and involvement in this work. The feedback I received from all of them has undoubtedly improved the quality of the manuscript and the research.

I want to recognize and thank project MIRaCCLE (Micro-réseau Industriel avec Raccordement en Courant Continu et Luminaires Extérieurs), supported by the Walloon Region, and the Energy Transition Fund—FPS Economy project "BEST" for their support of my PhD. I was able to participate in and contribute to both projects during my PhD. Thanks to them, I was able to discover and study new technologies that will play an important role in the future of power systems.

I would also like to acknowledge the other researchers from our power systems team who were always available to discuss and exchange ideas with me. I would particularly like to thank Guy Wanlongo and Quentin Delhaye. Guy aided me during my master's thesis and also during the first year of my PhD, helping me navigate the world of scientific publications and motivating me to publish my first works. Quentin was equally valuable during my PhD; he was always willing to discuss my work and offer ideas, reviews, or assistance with mathematical formulations.

I also extend my gratitude to Julien Allard, with whom I collaborated during his master's thesis. His work and the exchanges we had during that time were valuable supports to this research.

I am grateful for the administrative support of Nathalie Sergoigne, Catherine Bauwens, Astrid Leduc and Isabelle Hennau.

To my colleagues and professors in MEED, thank you! I appreciate you for welcoming me into this research group and sharing with me daily. I value our exchanges during coffee breaks, MEED seminars, birthday celebrations, badMEEDton, and many more. Without all of you, these four years would not have been the same.

Finally, I want to thank my family, who have supported and motivated me despite the distance. I also thank my friends for being there for me. This work would not have been possible without them.

Abstract

In the current evolving distribution grid, microgrids are emerging as valuable tools that can facilitate the integration of renewable energies. In recent years, DC microgrids have garnered interest due to several advantages. These advantages include fewer conversions, the absence of reactive power and frequency, and lower line losses. As a developing technology, there are still many aspects to be studied to facilitate their implementation. This thesis aims to contribute to a better understanding of DC microgrids.

The following work provides an overview of the current state of DC microgrids. Their advantages over AC microgrids are discussed and illustrated. The different topologies and DC bus configurations are described. Potential power quality issues are examined. The current challenges of the technology are explored. Finally, the current state of standardization and existing implementations are detailed.

This work presents three major contributions. First, an overview and comparison of different control methods for converters in DC microgrids are provided. Both first level controls and second level controls are detailed and simulated. The second contribution of this work concerns a power flow algorithm tailored for DC microgrids. This power flow method is adapted for bipolar DC microgrids and further developed as a sequential power flow. This sequential power flow allows the study of the behavior of a DC microgrid over extended periods. The sequential power flow is then used to compare the performance of unipolar and bipolar DC microgrids. The final contribution of this work concerns the modeling of High Frequency AC link three-port DC/DC/DC converters. The functioning of this type of converter is covered in detail. An averaged model and possible control schemes for this type of converter are proposed.

Contents

List of Figures

List of Tables

Acronyms

ACD Average Current and Average Droop Resistance Droop.

ACS Average Current Sharing.

ACV Average Current and Voltage.

ACVD Average Current and Average Voltage Droop.

AD Adaptive Droop.

AVR Average Voltage Restoration.

CSI Current Source Inverter.

DACS Digital Average Current Sharing.

DER Distributed Energy Resources.

DG Distributed Generator.

EMC Electromagnetic Compatibility.

EMI Electromagnetic Interferance.

EMS Energy Management System.

ESS Energy Storage System.

EV Electric Vehicles.

HDG High Droop Gain.

HFAC High Frequency AC.

HVDC High Voltage DC.

IEC International Electromechanical Commission.

LCOE Levelized Cost of Energy.

LV Low Voltage.

LVDC Low Voltage DC.

MGCC Microgrid Central Controller.

MPPT Maximum Power Point Tracking.

MV Medium voltage.

MVDC Medium Voltage DC.

NPC Neutral Point Clamped.

OPF Optimal Power Flow.

PI Proportional Integral.

PV Photovoltaics.

PWM Pulse Width Modulation.

SC Self-consumption.

SCI Self-consumption Index.

SoC State of Charge.

SS Self-sufficiency.

SSCB Solid State Circuit Breaker.

SSI Self-sufficiency Index.

TFEC Total Final Energy Consumption.

THD Total Harmonic Distortion.

VR Voltage Restoration.

VSC Voltage Source Converters.

VSI Voltage Source Inverter.

VUF Voltage Unbalance Factor.

List of Publications

List of publications developed during the Phd:

In this thesis

E. V. Mayen and E. De Jaeger, "Linearised bipolar power flow for droop-controlled dc microgrids," in *2021 International Conference on Engineering and Emerging Technologies (ICEET)*, 2021, pp. 1–6. DOI: 10.1109/ICEET53442.2021.9659746

E. V. Mayen and E. De Jaeger, "Industrial dc microgrid analysis through linear power flow," in *2022 IEEE International Conference on Environment and Electrical Engineering and 2022 IEEE Industrial and Commercial Power Systems Europe (EEEIC / I&CPS Europe)*, 2022, pp. 1–6. DOI: 10.1109/EEEIC/ICPSEurope54979.2022.9854709

J. Allard, E. V. Mayen, and E. De Jaeger, "Resonance model comparison for high-frequency ac link three-port converter," in *2023 IEEE International Conference on Environment and Electrical Engineering and 2023 IEEE Industrial and Commercial Power Systems Europe (EEEIC / I&CPS Europe)*, 2023, pp. 1–6. DOI: 10.1109/EEEIC/ICPSEurope57605.2023.10194661

E. Vasquez Mayen and E. De Jaeger, "Comparative study of unipolar and bipolar industrial dc microgrids through linear power flow," in *27th International Conference on Electricity Distribution (CIRED 2023)*, vol. 2023, 2023, pp. 194–198. DOI: 10.1049/icp.2023.0273

E. Vasquez Mayen and E. De Jaeger, “Average modeling of high frequency ac link three-port dc/dc/dc converters,” *Electricity*, vol. 5, no. 2, pp. 397–425, 2024, ISSN: 2673-4826. DOI: `https://doi.org/nbqb`. [Online]. Available: `https://www.mdpi.com/2673-4826/5/2/21`

Other works

E. V. Mayen, E. De Jaeger, G. W. Ndiwulu, *et al.*, “Voltage unbalance compensation for islanded microgrids with hybrid control approach,” in *2021 International Conference on Engineering and Emerging Technologies (ICEET)*, 2021, pp. 1–6. DOI: `10.1109/ICEET53442.2021.9659678`

G. Wanlongo Ndiwulu, E. Vasquez Mayen, and E. De Jaeger, “Effect of a large proton exchange membrane electrolyser on power system small-signal angular stability,” *Electricity*, vol. 4, no. 4, pp. 381–409, 2023, ISSN: 2673-4826. DOI: `10.3390/electricity4040021`. [Online]. Available: `https://www.mdpi.com/2673-4826/4/4/21`

In publication

E. V. Mayen, G. W. Ndiwulu, V. Kluyskens, *et al.*, “Non-linear control of pem electrolyzers in dc microgrids,” in *2024 IEEE International Conference on Environment and Electrical Engineering and 2021 IEEE Industrial and Commercial Power Systems Europe (EEEIC / I&CPS Europe)*, 2024, pp. 1–6

G. W. Ndiwulu, E. V. Mayen, and E. a. De Jaeger, “Dynamic interactions of a high-current thyristor-rectifier interfaced pem electrolyzer with the angular dynamics of synchronous machines,” in *2024 IEEE International Conference on Environment and Electrical Engineering and 2021 IEEE Industrial and Commercial Power Systems Europe (EEEIC / I&CPS Europe)*, 2024, pp. 1–6

Chapter 1

Introduction

The energy distribution system is the set of interconnections via distribution lines that connect the different energy production sources to the loads that require energy. It is thanks to this network that the different appliances in our homes can be used seamlessly. This very same distribution system also supplies the energy demand of shopping malls, hospitals, and factories.

In its beginnings, the distribution system evolved progressively as it expanded to fulfill the needs of a growing society. However, it is now at a point where new challenges have arisen. These new challenges require a significant adaptation of the existing system to ensure it can continue providing the necessary energy. The general context from which these challenges originate and why microgrids can act as a solution for them are given hereafter.

1.1 Environmental Background

In recent years, the importance of addressing global warming has been highlighted. A common understanding and awareness of this global issue led to the Paris Agreement in 2015, where it was pledged to limit global warming to below 2 degrees Celsius. With the same objective in mind, European leaders set the goal to achieve carbon neutrality by 2050. Other countries have also set similar net zero emission targets. The People's Republic of China aims to achieve net zero emissions by 2060, India has set 2070 as its target year, and Indonesia has also set 2060 as its target year [10]. The implementation of different policies and technological developments has boosted the adoption of renewable energies. Proof of this is the increase in investment in renewable energies. In 2015, 1 trillion USD was invested in renewable enregies, a number that has significantly increased; by 2022, the investment exceeded 1.4 trillion USD [10].

In order to reach these goals, the energy supply in Europe has been adapting and experiencing a significant shift. In terms of energy sources, this implies a shift from traditional fossil fuels towards renewable energies. As shown in Fig. 1.1, globally, fossil fuels remain the main source in terms of energy consumed by the end user, also referred to as the total final energy consumption (TFEC). Furthermore, between 2011 and 2021, the TFEC increased by 16% [11].

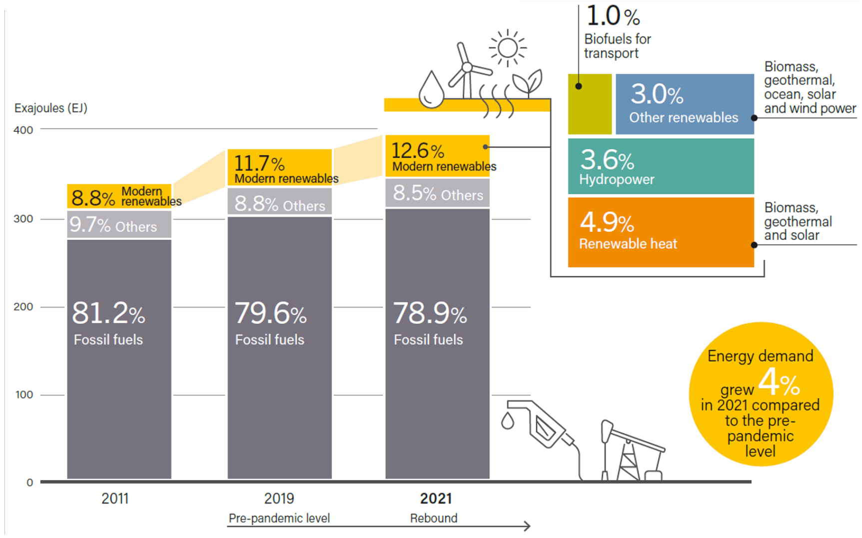

Figure 1.1: Total final energy consumption by source, 2011, 2019 and 2021 [11]

The challenge faced is not only increasing the share of renewable energies, but also dealing with the increasing electricity demand, which is expected to increase by 2-3% from 2021 to 2030 [12].

1.2 Renewable Energies

Renewable energies have been proposed as energy sources free of carbon emissions. Thus, they play an important role in the current energy transition, where lower carbon emissions are desired due to present environmental concerns. The main renewable energies on the rise are solar photovoltaic (PV) and wind energy. The growth of renewable energies during the last years has been significant. This growth has been motivated not only by the implemented policies and the general awareness of consumers but also by advancements in technologies, which have allowed a significant drop in the cost of renewable energies, as shown in Fig. 1.2. Fig. 1.2 shows the evolution of the levelized cost of energy (LCOE) for various renewable energies between 2010 and 2022. Offshore and onshore wind perceived a reduction in LCOE, and a more significant reduction is observed for PV and concentrating solar power.

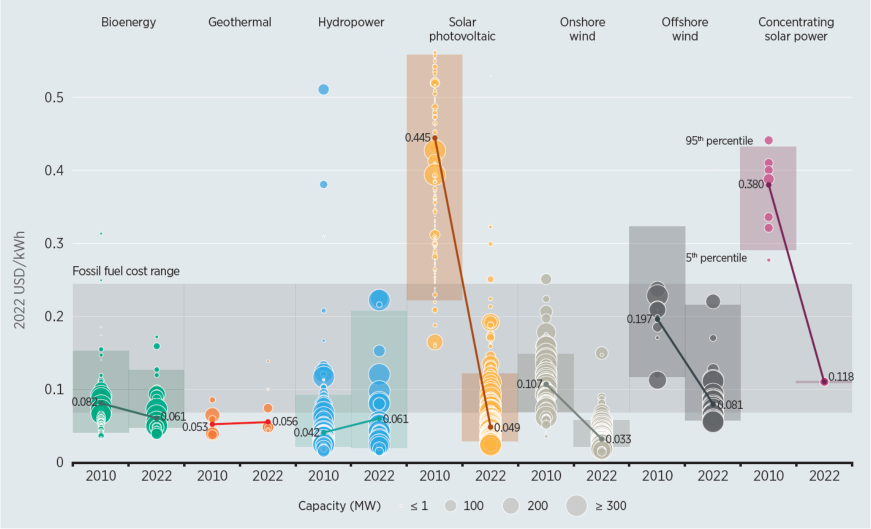

Figure 1.2: Global weighted average LCOE from newly commissioned, utility-scale renewable power generation technologies, 2010-2022 [13]

In 2021, renewable energies represented 12.7 % of total final energy consumption, and in 2022, they accounted for 30% of power generation. Furthermore, in 2022, the installed PV capacity grew by 243 GW, while the wind power capacity grew by 77 GW [12].

While the adoption of renewable energies is a positive development, their integration into the distribution network is not without challenges. One of the most notable factors is the variable nature of solar and wind energies. This variability makes it difficult to match the energy supply and demand, which can affect the stability of the network.

The mismatch in demand and supply reduces the efficiency of renewable energies as well. For example, in 2021, grid operators in the United Kingdom curtailed 7 terawatt-hours of wind energy, equivalent to 4% of the country's annual wind energy production. Similarly, in 2020, the California Independent System Operator curtailed 1.4 terawatt-hours of solar power, which accounted for 5% of the total production [12].

Energy storage systems (ESS) have been used to compensate for the unpredictable power profile of renewable energies. ESS allow storing surplus energy and using it when renewable energy production is low. As smart appliances and smart meters become more widespread, it is expected that consumers will adjust their consumption as an alternative way to match energy production and consumption.

Due to the adoption of renewable energies, other challenges are generated in the transmission system and the distribution system limits. The transmission system is mostly affected by large scale renewble energies generation plants, which are often located in remote areas. These renewable sources are situated far from existing transmission lines or where the transmission lines have limited capacity. In the case of the distribution system, the adoption of renewable energies at a local level generates new energy flows. These new flows require changes to the protection of the distribution system or an overall reinforcement of the infrastructure [14].

1.3 Other challenges

The evolution of different technologies also contributes to the need for renovating the current distribution grid. The utilization of renewable energies such as PVs in houses and commercial buildings has increased. This represents energy flows from places that were not previously expected. Furthermore, the amount of power consumed is increasing, partially due to new smart devices that shape the consumption curve. In part, due to their activity profile that can differ from normal consumption, and also due to the magnitude of their energy consumption. Among these new devices,some stand-out: electric vehicles (EVs), heat pumps, and PV panels. These two represent new types of loads with significant consumption. With the rise of interconnected devices, the use of smart energy management systems will become widespread. All of these factors contribute to an increased bidirectional power flow for which the grid was not initially designed.

1.4 Microgrids and their advantages

The current and expected increase in renewable energy generation has two impacts on the current distribution grid. First, the total amount of power flowing through the distribution grid will increase. According to [11], the lack of grid capacity contributes to holding back the shift towards renewable energies. Secondly, it represents a shift from centralized power production towards decentralized production. As a consequence, power will be generated and will have to flow through lines that were not initially designed with this in mind.

In this context, microgrids provide a valuable solution that can adapt to the changes faced in the network. Definitions of a microgrid can be:

"Microgrids are systems that have at least one distributed energy resource and associated loads and can form intentional islands in the electrical distribution systems. Within microgrids, loads and energy sources can be disconnected from and reconnected to the area or local electric power system with minimal disruption to the local loads." [15]

"Micro-grid is a small-scaled autonomous power grid system that consists of multiple energy generations from renewable and non-renewables resources, energy storage systems (ESS) and power electronic converters. Micro-grid can be operated either in standalone mode or connected to the utility grid" [16]

In layman's terms, a microgrid is a smaller version of the main distribution grid. This smaller grid can operate independently in islanded mode or be connected to the main AC grid. The main energy sources in microgrids are distributed generators (DG), which tend to be renewable energies that are installed locally. These renewable energies are also referred to as distributed energy resources (DER). Thus, the basic elements in a microgrid are the DG/DER, the ESS to compensate for power fluctuations, and the loads. Fig. 1.3 illustrates the basic structure of a microgrid.

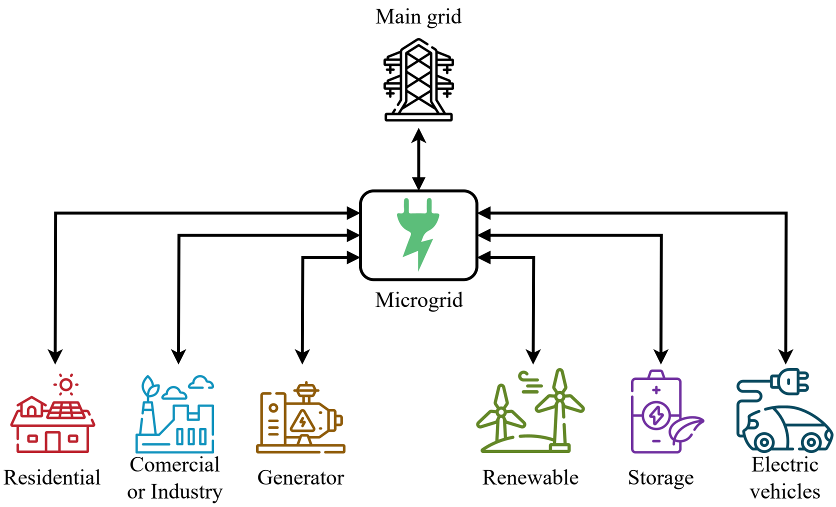

Figure 1.3: Representation of a typical microgrid [17]

The concept of microgrids has been evoked as early as 2002. The core idea is that it operates as a single system that provides power to a local area. From the point of view of the main grid, this system operates as a single dispatchable load which can adapt to the needs of the main distribution system. The power electronics used to connect all the elements in the microgrid provide the needed controllability and flexibility. Through this controllability, the microgrid enhances local reliability, reduces feeder losses, supports the local voltage, and can contribute to a better power quality by mitigating voltage dips for example [18]. Three defining properties of microgrids are [19]:

- Ease of integration of new resources
- Ease of scaling its size up or down
- Equitable role for each resource in determining the operation of the microgrid.

Microgrid are expected to be the main building block of the future smart grid. This is because microgrids allow the implementation of the expected smart grid features such as [20]:

- Energy efficiency, sustainability and RESs inputs

- Reliability, security, ESSs and DG units (renewable based)
- Sensing, measurements and advanced control methods
- Load usage awareness, real-time Energy Management System (EMS) and advanced load components (Electric vehicles, heaters, etc)
- Integrated information and communication infrastructures with full cyber-security

It is expected that microgrids will bring benefits to both users and the utility grid. As a single controllable unit, they can provide power or ancillary services to the main distribution system. For the users, microgrids can improve power quality, reduce the effects of voltage sags, and offer an uninterrupted power supply for critical loads (such as data centers or hospitals) [20]. They are also an effective and affordable tool for rural electrification [21]. However, one of their main value propositions, resiliency, is hard to quantify [22]. The benefits of microgrids can be summarized as [22]:

Price stability Microgrids offer protection from fluctuating electricity bills.

Economic Benefit Microgrids can achieve this by lowering peak load prices, engaging in demand response markets, and providing frequency management services.

Increased reliability and resilience Operating in the island mode can ensure a constant supply of electricity.

Renewable integration Microgrids facilitate the implementation and coordination of renewable energy sources.

Increase power quality Microgrids allow to have a better control over the grid power quality parameters.

Grid support Microgrids can reduce grid congestion and peak load demands. Additionally, they can provide energy, capacitive, and ancillary services.

1.5 Thesis Questions and Objectives

As highlighted before, microgrids are powerful tools that can play an important role in the current energy context. The main focus of this thesis is the study of DC microgrids. The study includes their advantages and challenges, their control, and how to model them. The questions researched in this thesis are:

- Why use DC over AC for a microgrid?
- Which DC bus configuration to use: unipolar or bipolar?
- What are the different type of control methods?
- How to simulate a DC microgrid in steady-state?
- How to model the different elements in a microgrid?
- How do the different control methods compare?

1.6 Contributions

The main contributions of this thesis can be summarized in three main points:

- The linear power flow approach for DC microgrids has been expanded by incorporating bipolar microgrid modeling and a sequential approach to simulate the microgrids over an extended period.
- An overview and comparison of first and second level control methods for DC microgrids has been performed
- An in-depth study of three-port converters has been proposed, including their state-space and average modeling

The linear power flow approach was initially proposed only for unipolar DC microgrids. The author further developed the model to include bipolar DC microgrids. Afterwards, the model was further developed by implementing a sequential approach, culminating in a comparison between unipolar and bipolar DC microgrids. The ability to simulate bipolar microgrids allows for the evaluation of a different DC bus topology. This modeling calculates the currents in the neutral conductor, which are a key source of losses in bipolar microgrids. The sequential powerflow approach facilitates the study of different DC microgrid topologies over an extended period of time. This allows for the analysis of the expected performance of the DC microgrids in terms of line losses, line currents, and voltage regulation. The sequential power flow and its results serve as valuable tools for sizing and performance analysis.

The general overview of the control methods presents several first level and second level controls. The overview provides a description and implementation of the control method, helping the reader implement each control method easily. The control methods are compared under four criteria, assisting the reader in identifying the pros and cons of each. This comparison is further elaborated on in Chapter 6, where the different control methods are implemented in a test DC microgrid. An analysis of the results is provided, along with recommendations for the use cases of the different control methods.

High Frequency AC (HFAC) link converters propose an interesting solution; however, their study in the literature is limited. This thesis summarizes the different characteristics of HFAC link converters, particularly three-port converters. The detailed study of HFAC converters will help the reader understand the operating principles of HFAC converters and the influence of parameters on the switching frequency. The proposed state-space model provides an alternative modeling approach for this type of converter, which the reader can use as a basis for their analysis. Additionally, it proposes an initial average model for both two-port and three-port converters. Such models can be particularly useful for including these converters in studies involving parallel three-port converters, such as the simulation of DC microgrids with multiple distributed three-port converters.

All the different modeling approaches presented in this thesis constitute a useful guide that can help in the modeling of DC microgrids.

1.7 Thesis Structure

The structure of the thesis is as follows:

In Chapter 2, the concept of DC microgrids is presented in detail. The interest in their implementation, advantages, and challenges is explored. The current state of standardization is briefly described. Chapter 3 describes the control of DC microgrids. This chapter explains the different control levels and how to coordinate different converters acting in parallel. Chapter 4 presents the steady-state analysis of DC microgrids. This analysis is performed through a power flow analysis designed for DC distribution and microgrids. Chapter 5 focuses on the modeling of the power electronics converters that intervene in a DC microgrid. The modeling includes DC/DC converters, AC/DC converters, and 3-port converters. Chapter 6 implements dynamic simulations of DC microgrids. These simulations are then used to compare the different control methods described in Chapter 3. Finally, Chapter 7 provides the conclusions and final remarks of this thesis.

A graphical guide for the reader is provided in Fig. 1.4. If the reader wants an introduction to the subject matter, they can start with Chapter 2. If the reader wants to know more about the control of converters, Chapter 3 provides the needed knowledge. The main outputs of the thesis are found in Chapters 4, 5, and 6. They are independent from each other. Readers interested in the proposed power flow model can refer to Chapter 4. The only prerequisite is a good understanding of droop control and DC microgrid voltage architectures. Readers interested in the average modeling of power electronics and the modeling of three-port converters can refer to Chapter 5. The only prerequisite for Chapter 5 is, once again, an understanding of droop control as it is utilized to control three-port converters. Readers interested in the comparison of the control methods can refer to Chapter 6. To fully understand the comparison performed in Chapter 6, reading Chapter 3 is necessary. This is because all the different control methods compared are detailed in Chapter 3.

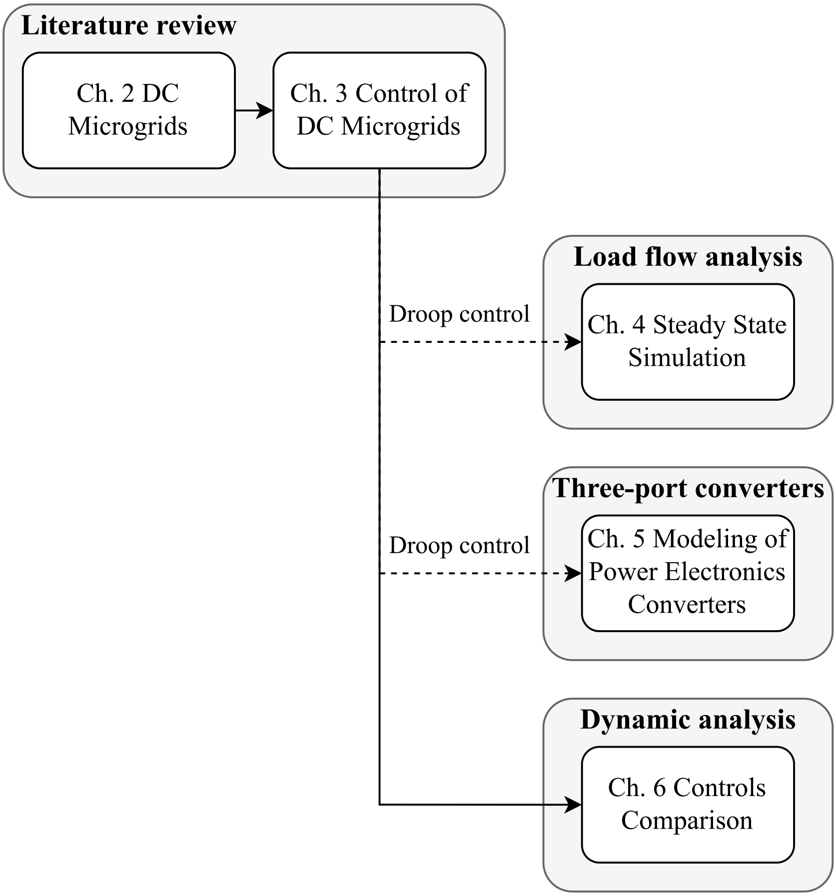

Figure 1.4: Outline of the thesis chapters

Chapter 2

DC Microgrids

Chapter contributions

- DC microgrids and their advantages are introduced
- The existing challenges and the current state of standardization are presented
- Existing DC microgrid projects are highlighted

Historically, DC Voltage has been in competition with AC Voltage. Initially, DC was used for residential and commercial customers, but its limited transmission range prevented its large-scale implementation. To cover greater distances, a higher voltage was required. In the 19th century, this was complicated for DC as it required multiple machines connected in series to change the voltage. In contrast, AC voltage could be changed via transformers that did not require complex mechanical devices. Thus, AC voltage found its main application in transmission. Eventually, AC voltage phased out DC voltage in distribution to consumers. However, interest in DC distribution never disappeared. Thanks to improvements in solid-state components and simplified converter stations, higher voltages were explored. Notable applications include the Sakuma interconnection in Japan in 1965, and the Itaipu Dam line between Brazil and Paraguay, used between 1984 and 1987 [23].

In recent years, distribution in DC has gained increased interest due to its characteristics and advantages. This has led to the construction of more High Voltage DC (HVDC) links for energy transfer such as the NEMO link which is a submarine link between the United Kingdom and Belgium. During its first two years of operation, it was used to transfer 12 TWh between the two countries [24]. Similar HVDC connections are being installed in different countries. In Belgium, further projects such as Tritonlink [25] and the Princess Elisabeth Island [26] are planned.

Similarly, DC microgrids have been gaining traction in the context of microgrids, leading to increased research in this area. This chapter examines the advantages of a DC distribution system compared to its AC counterpart. It begins with an overview of existing topologies, architectures, and grounding schemes. Additionally, it highlights various power quality issues specific to DC systems. Finally, the chapter concludes by discussing some of the main challenges and risks associated with the implementation of DC microgrids.

2.1 AC vs DC microgrids

The implementation of AC microgrids is more widespread than that of DC microgrids. Indeed, AC microgrids benefit from similarities with the main AC distribution grid. Consequently, many existing techniques in the main AC grid can be readily adapted for use in AC microgrids.

On the other hand, DC microgrids present different characteristics and therefore cannot rely on the same techniques as AC microgrids. Nevertheless, DC microgrids offer different advantages. These include [27]–[29]:

Absence of frequency Unlike its AC counterpart, there is no frequency in the distribution system. This presents an advantage as it simplifies the control scheme, resulting in reduced complexity. Instead of controlling two variables (voltage and frequency), only one variable (voltage) needs to be controlled. Additionally, the absence of frequency eliminates the need for synchronization when connecting elements.

Absence of reactive power Being a DC system, there is no reactive power circulating within the system. This means that there is no need to control the reactive power. Consequently, the full capacity of the cable to be utilized for active power transfer.

Fewer conversions Renewable energy sources such as Photovoltaic (PV) panels naturally output their power in DC. In traditional systems, the output of the PV panel would need to be converted into AC before injecting it into the distribution system. However, in a DC distribution system, this step is unnecessary. his feature is also beneficial for energy storage systems like batteries and supercapacitors, which primarily operate in DC. Furthermore, many loads such as lights, home appliances, and computers utilize DC voltage. Therefore, DC distribution can eliminate an extra conversion step for these loads. However, some DC-DC conversions are still needed for voltage level adjustments or control for example. Fewer conversions result in lower conversion losses, leading to a more efficient system. This concept is illustrated in Fig. 2.1.

Lower line losses Because there is no reactive power, the amount of current circulating is minimised, resulting in reduced line losses. Furthermore, DC distribution does not experience the skin effect, further decreasing line losses.

Reduced cost The reduced line losses, coupled with the increased line capacity, enable the use of lines with smaller cross-sections. Moreover, the need for fewer conversions may result in a reduced number of converters. These factors combined can lead to lower costs compared to its AC counterpart.

Fully controllable A DC distribution-based system relies on power electronics for its operation. These power electronics devices require precise control. As a result, a DC distribution system is inherently a fully controllable distribution system.

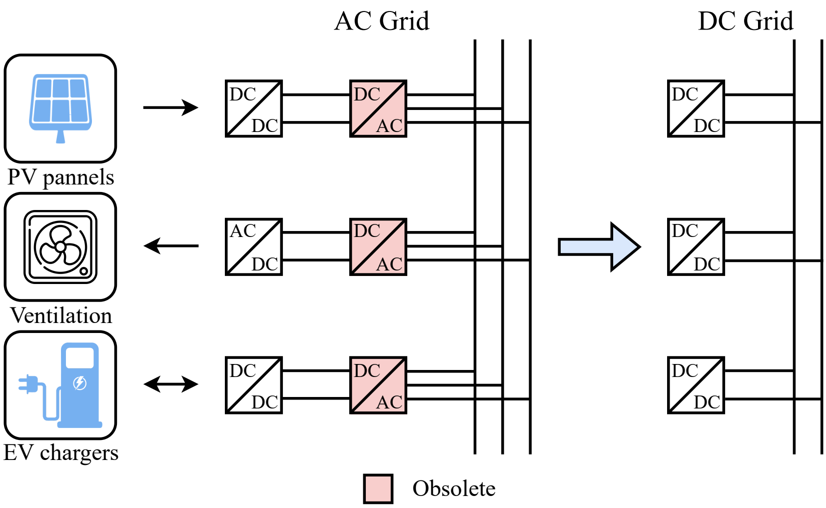

Figure 2.1: Obsolete converters in a DC network

As proposed in [30], [31], DC systems exhibit advantages in terms of power transfer capabilities. Let's compare four systems: single-phase AC, three-phase AC, unipolar DC, and bipolar DC. The AC systems have a phase voltage V_{RMS} and a current I_{RMS}. Considering a power factor pf, their power capacity can be described as follows:

$$P_{1\phi} = V_{RMS} I_{RMS}\, pf \tag{2.1}$$
$$P_{3\phi} = 3 V_{RMS} I_{RMS}\, pf \tag{2.2}$$

For DC systems, the voltage will be equal to the peak value of V_{RMS}. Assuming the same wires are used, this is not an issue as the insulation of AC systems is designed for the peak voltage. Regarding the current, it remains equal to the RMS value for thermal reasons. Therefore, the power capacities of unipolar and bipolar systems are as follows:

$$P_{\text{Unipolar}} = \sqrt{2} V_{RMS} I_{RMS} \tag{2.3}$$
$$P_{\text{Bipolar}} = 2\sqrt{2} V_{RMS} I_{RMS} \tag{2.4}$$

If a pf of 0.95 is considered, the following ratios can be found:

$$\frac{P_{\text{Unipolar}}}{P_{1\phi}} = \frac{\sqrt{2}}{pf} \tag{2.5}$$

$$\frac{P_{\text{Unipolar}}}{P_{3\phi}} = \frac{\sqrt{2}}{3pf} \tag{2.6}$$

$$\frac{P_{\text{Bipolar}}}{P_{3\phi}} = \frac{2\sqrt{2}}{3pf} \tag{2.7}$$

As proposed in [30], the power losses P_l in a three-phase AC network are given by (2.8). For a two-wire DC system and a three-wire DC system, one can refer to equations (2.9) and (2.10) respectively.

$$P_{l\,3\phi\text{AC}} = 3I_{AC-RMS}^2 R_{AC} \tag{2.8}$$

$$P_{l\,\text{UDC}} = I_{DC}^2 R_{DC} \tag{2.9}$$

$$P_{l\,\text{BDC}} = 2I_{DC}^2 R_{DC} \tag{2.10}$$

These results are similar to the comparison made in the Dutch standard NPR 9090 [32], as shown in Table 2.1. The table also highlights that a bipolar system and a unipolar system with twice its nominal voltage have the same power capacity. Further discussion on this standard is provided in a subsequent section.

Table 2.1: Comparison of low-voltage AC and DC configurations [32]

LVDC	**LVAC**	**Pmax for 16 A RMS**
Unipolar 350 V	230 V, 1 ph	5.6 kW DC / 3.7 kW AC
Unipolar 700 V	400 V, 3 ph	11.2 kW DC / 11.1 kW AC
Bipolar 350 V	400 V, 3 ph	11.2 kW DC / 11.1 kW AC
Bipolar 700 V	690 V, 3 ph	22.4 kW DC / 19.1 kW AC

For simplicity, let us assume that the line resistances are the same for both DC and AC distribution networks. Considering that all three systems have the same amount of line losses, the expressions in (2.11) and (2.12) are found. These equations lead to the estimations found in (2.13) and (2.14).

$$I_{UDC} = I_{AC-RMS}\sqrt{\frac{3R}{R}} \tag{2.11}$$

$$I_{BDC} = I_{AC-RMS}\sqrt{\frac{3R}{2R}} \tag{2.12}$$

$$I_{UDC} \cong 1.732 I_{AC-RMS} \tag{2.13}$$

$$I_{BDC} \cong 1.224 I_{AC-RMS} \tag{2.14}$$

This means that for the same losses, a unipolar DC system can increase its current by 73% with respect to a three phase AC system. Meanwhile, a bipolar DC system can increase it by 22%. While the result is interesting, it is important to remember that for the unipolar system having a same amount of losses does not imply the power transfered is the same as the three phase system.

In [30], the performance of an AC grid and a bipolar DC grid on Cigre's Low Voltage distribution benchmark network is compared. The same loads are used, but due to the voltage level decrease a difference in the active load power is obtained. The AC system provides 188.4 kW while the DC system provides 239.9 kW. The total losses amount to 11 kW in the AC grid and to 6.8 kW in the bipolar microgrid, resulting in a ratio of 0.67. This result closely aligns with the ratio of 2/3 mentioned in CIRED's report [31]. However, the methodology used to derive this ratio is not explained in the CIRED report.

In the same vein, studies in the literature propose an easy adaptation of the existing AC infrastructure for LVDC (Low voltage DC) distribution. As explained in [33], traditional AC transmission employs five conductors (three phases, one neutral, and the protective earth or grounding conductor). This configuration can be adapted for unipolar and bipolar DC distribution, as shown in Fig. 2.2. In this figure, L+ and L- represent the positive and negative conductors respectively. PE stands for protective earth, and M corresponds to the neutral conductor. In [34], cable configurations for four-conductor wires are also proposed. The cable configurations for bipolar systems with TN-s and TT grounding are shown in Fig. 2.3. Further details on these grounding schemes will be provided in the subsequent chapter.

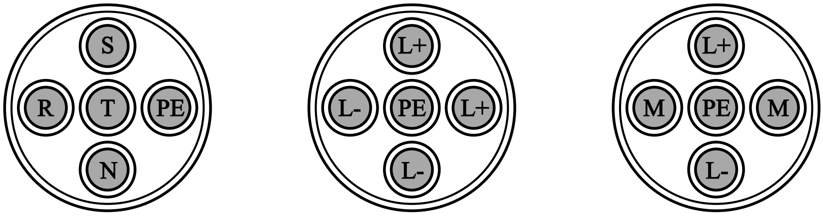

(a) LVAC cable (b) Unipolar LVDC cable (c) Bipolar LVDC cable

Figure 2.2: Configuration of five-conductor cables in DC systems [33]

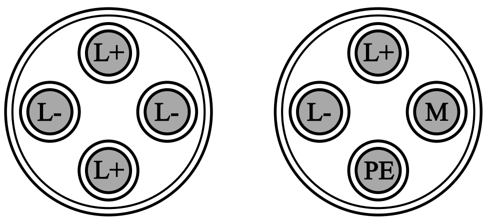

(a) TN-S grounding (b) TT grounding

Figure 2.3: Configuration of four-conductor cables in bipolar DC systems [34]

Considering the ease with which cables can be repurposed, the next step is to evaluate the performance of these lines under DC voltage. Research conducted in [34] assesses the ampacity of the same line under both AC and DC voltage. The ampacity is primarily limited by heat dissipation resulting from ohmic losses and dielectric losses in the insulation or screens. However, in medium voltage (MV) and LV AC systems, dielectric losses are typically neglected. These losses have an even smaller contribution for DC loads as they are proportional to the frequency and are thus neglected.

An ideal DC current increases the ampacity of cables compared to the AC case. However, DC current may contain ripple currents, which can generate eddy currents and circulating currents in both the screens and the conductors. Additionally, higher-frequency ripples can result in non-uniform current distribution within the conductors.

The main results of [34] show an increased ampacity in the lines under DC distribution. Total harmonic distortion (THD) is used to measure the ripple of the current. Even when considering a THD of 0.029 p.u in the current, the losses were lower than in the AC system. The lines were also tested in terms of thermal limits. For the same maximum temperature, the lines in DC showed an increase in ampacity close to 21%. Furthermore, no increased aging in the connections was detected. While the results are positive, two main factors need to be kept in mind. First, the allowed THD in the DC current is not known, as standards are still in development. Second, although the increased ampacity is beneficial, the primary source of increased transmission capability would be an increased voltage. The voltage levels to be used in DC distribution are discussed later in this chapter, as it is a key question in the standardization process.

The recent work in [35] has also suggested the possibility of developing DC distribution-designed transmission lines. This consideration arises from the recognition that key factors affecting electrical stress for DC distribution differ from those for AC. The proposed main key factors for DC cables include breakdown strength, space charge, electrolytic corrosion, polarity reversal, and surge superimposition.

2.2 Microgrid Topology

DC microgrids can be classified into three main topologies: radial, ring, and interconnected. Each topology has its own advantages and drawbacks. They are described here after [27]. Note that they are illustrated with a connection point to the main AC grid; however, they can also operate in islanded mode.

Radial Microgrids

A radial microgrid consists of a singular DC bus as depicted in Fig. 2.4. The primary advantage of this topology is its ease of implementation. However, this simplicity also means it to lacks flexibility under fault conditions. Indeed, a single fault has the potential to disrupt all the elements connected to this bus. To reduce this risk a bipolar distribution bus can be implemented.

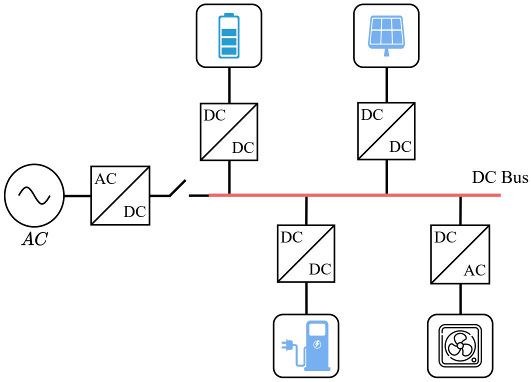

Figure 2.4: Radial topology DC microgrid

Ring Microgrids

In this topology, parallel paths are introduced to overcome the limitations of the radial topology. These parallel paths are interconnected via switches that enable the isolation of faulty sections within the microgrid. However, a fault occurring at the point of connection to the AC grid would still result in the isolation of the microgrid. This topology is shown in Fig. 2.5.

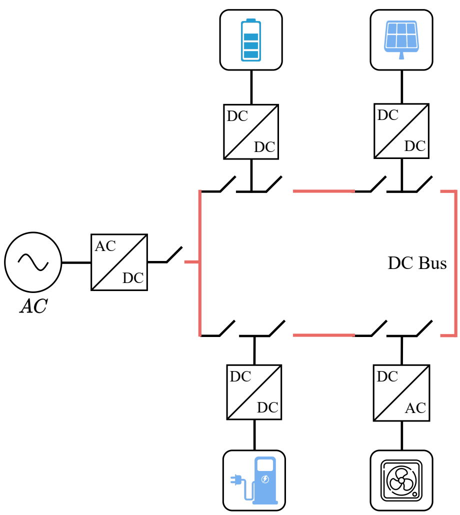

Figure 2.5: Ring topology DC microgrid

Interconnected Microgrids

In an interconnected microgrid, reliability is improved by providing multiple points of connection to the main AC grid. Interconnected microgrids can be classified as either mesh-type or zonal-type, as shown in Fig. 2.6 and Fig. 2.7 respectively. The main difference between these two types is that in zonal microgrids, parts of the microgrid are designated into zones. Within each zone, there are two redundant DC buses. This configuration can be visualized as a cascade of DC microgrids with a symmetrical structure. While this approach significantly improves reliability, it comes at the expense of a more complex design and operation.

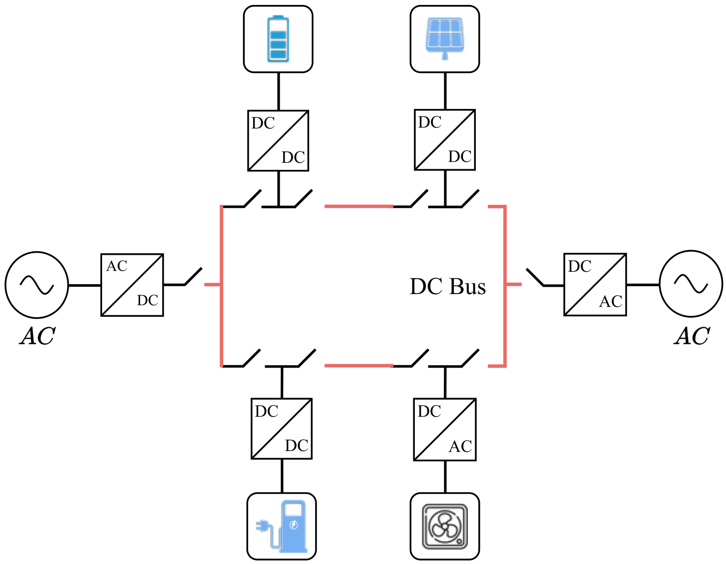

Figure 2.6: Mesh topology DC microgrid

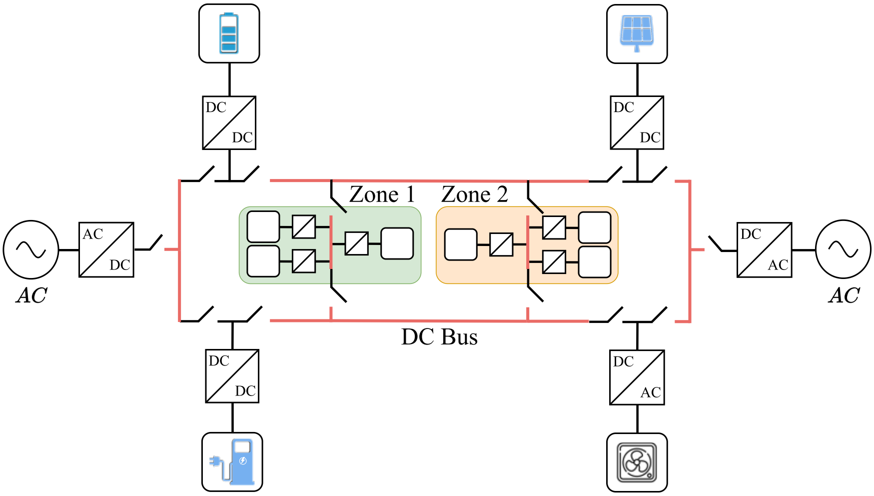

Figure 2.7: Zonal topology DC microgrid

2.3 DC bus configuration

When discussing DC distribution systems, there are two possible bus configurations: a two-wire system, referred to as a **Unipolar** distribution system, and a three-wire system, known as **Bipolar**. The third conductor in the bipolar system is the neutral conductor, positioned between the positive and negative poles. This additional conductor enables the bipolar architecture to access more voltage levels. Both possible architectures are illustrated in Fig. 2.8. In this section, the advantages and disadvantages of each architecture will be described.

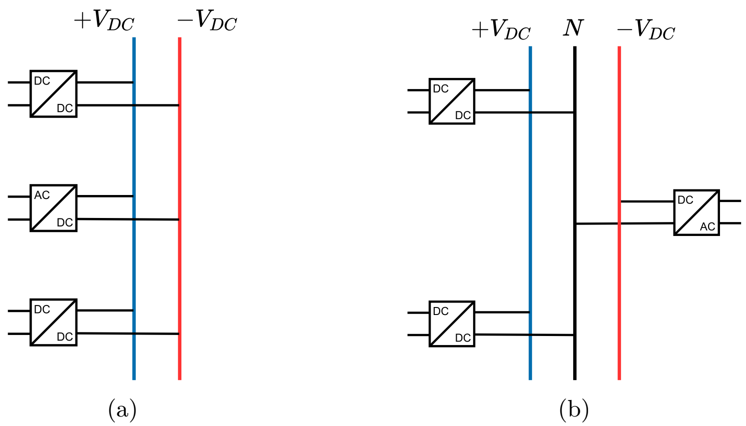

Figure 2.8: DC distribution bus configurations: (a) Unipolar (b) Bipolar

2.3.1 Unipolar system

In a unipolar system, the different elements are connected between the positive and negative pole, allowing access to only one voltage level. Therefore, this voltage level must be carefully chosen, as line losses, the number of required converters, and transmission capability all depend on it. The unipolar system offers simplicity in implementation and carries no risk of voltage imbalances. Due to its simplicity, control of the system is also less complex. However, one of its disadvantages is its limited flexibility compared to a bipolar system, as it provides only one voltage level. Additionally, the system lacks redundancy, and a single fault can result in system shutdown [27], [33].

2.3.2 Bipolar system

The addition of a neutral conductor to bipolar networks brings several advantages. One notable advantage is increased flexibility, as the system can implement different voltage levels. If the connection is made between $+V_{DC}$ and the neutral conductor, the voltage equals $+V_{DC}$. Alternatively, if the connection is between $+V_{DC}$ and $-V_{DC}$, the resulting voltage will be $2 \times V_{DC}$. Furthermore, this system also proposes increased reliability; in the event of a fault in one pole, the other pole can continue to operate. It also provides increased power capacity and reduces line losses.

However, bipolar networks come with a significant disadvantage: the risk of voltage unbalance. If the distribution of the loads or the injection by the generators is uneven, this will lead to a voltage unbalance between the poles. The voltage unbalance results in circulating current in the neutral conductor that must be managed. Controlling these voltage imbalances is one of the main challenges for bipolar systems [27], [33].

It is worth mentioning that the reduction in line losses compared to a unipolar system is applicable when the voltage of the unipolar system matches that of each pole in the bipolar system. That is, if $V_{DC\,\text{Unipolar}} = V$ and $+V_{DC} = -V_{DC} = V$, the current circulating in the unipolar system will be twice that of the bipolar system, as the current is split among the two poles in the bipolar system. If $V_{DC\,\text{Unipolar}} = 2V$, then the amount of current circulating will be the same, and thus the losses will be equal. A balanced bipolar network is equivalent to a unipolar system operating at twice the voltage of each pole. Nevertheless, it is important to remember that voltage unbalances and currents in the neutral can increase the losses of the bipolar system.

To establish the bipolar bus, specific configurations for the converters are required. These configurations vary from using single converters to cascaded Voltage Source Converters (VSC). Various methods for achieving the two voltage levels are illustrated in Fig. 2.9 [33].

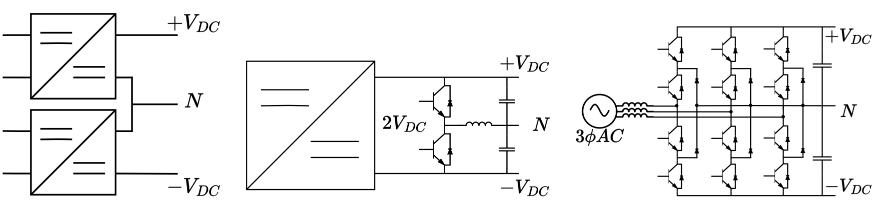

(a) Two cascaded VSCs

(b) VSC with a voltage balancer

(c) Three level neutral point clamped converter

Figure 2.9: Example of topologies to form a bipolar distribution network

2.4 Power quality in DC

DC systems also face power quality issues, which can originate from the DC microgrid itself or the AC grid when connected to it. Poor power quality can lead to equipment damage and poor operation, resulting in both technical and economic impacts [36]. The most common power quality issues for DC microgrids include [27], [36]:

- Voltage transients from the AC grid
- Voltage swells and dips
- Voltage supply interruptions
- Distortion/ripples due to resonances and power electronics converters
- Electromagnetic interference compatibility (EMC)
- Inrush currents
- DC bus faults
- Voltage unbalance in bipolar DC buses
- Circulating currents

These common power quality issues are classified based on their duration and the frequencies that they affect, as shown in Fig. 2.10. A similar classification was performed in [37]. This classification, shown in Fig. 2.11, categorizes the phenomena according to their duration-amplitude and frequency-amplitude.

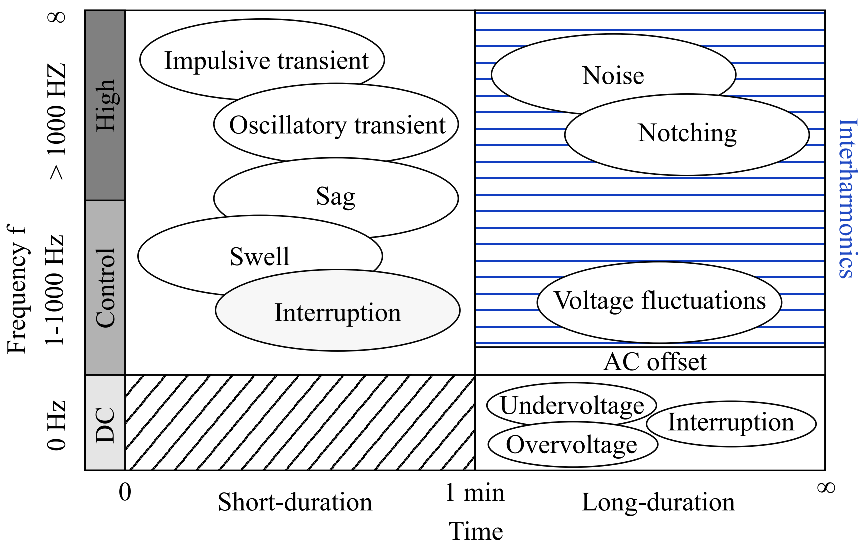

Figure 2.10: Time–frequency classification of DC power quality issues [38]

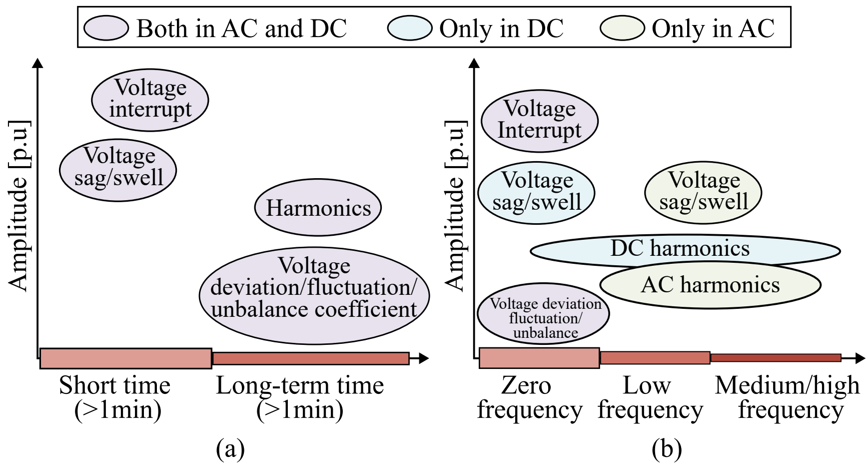

Figure 2.11: Characteristics of AC/DC power quality: (a) Multi time scale distribution characteristics and (b) Broadband distribution characteristics [37]

One phenomena of interest is harmonics and their equivalent in DC microgrids. In the literature, it is sometimes stated that DC microgrids do not have harmonics, others claim that interharmonics are present rather than harmonics. The work presented in [37] proposes a different definition for harmonics in DC. The difference between AC and DC total harmonic distortion is highlighted. AC harmonic distortion corresponds to the distortion that exists between the harmonic components and the ideal sinusoidal signal. Meanwhile, DC harmonic distortion refers to the distortion between harmonic components beyond the DC component. By definition, harmonics are integer multiples of the power frequency. Following this definition, harmonics do not exist in DC distribution as the power frequency is $0Hz$. Thus, in [39] DC ripple is proposed as a power quality indicator instead of harmonics.

This DC ripple can originate from switch-mode converters and their Pulse Width Modulation (PWM) control. They cause additional conduction losses and losses in the filter capacitors. More importantly, they can perturb measurement devices and communication signals [38]. This, in turn, can also affect the control signals for the converters. The DC ripple found in DC microgrids can have a negative impact on different elements [37]:

- DC ripple can lead to an increased peak-to-peak current flowing into the batteries. Above a certain threshold, it can reduce battery efficiency and lifespan.
- DC ripple can result in wasted converter capacity and impact the lifespan of power electronics components.
- DC ripple can affect the implementation of maximum power point tracking (MPPT).
- DC ripple can produce noise and vibrations in electric motors, thus affecting their efficiency and lifespan.

One source of problems can be the connection to the main AC distribution grid. The AC grid can affect the DC microgrid in three different ways. First, faults in the AC system can cause voltage fluctuations in the DC voltage. Another issue is that voltage unbalances in AC grid will cause a low-frequency harmonic through the DC converter. Finally, single-phase AC loads connected to the DC system will introduce second-order "harmonics". This is because the DC-AC converter will have an output power composed of a DC component and an AC component with an angular frequency of twice the load frequency. Assuming that the input power is equal to the output power, the input current of the AC-DC converter will also have an AC component with twice the frequency of the load [37].

Other problems related to voltage variations can originate from faults and load changes. Furthermore, there is no standard concerning the tolerance for voltage dips or swells. However, standards do exist for railway systems, aircraft, and telecommunication applications [36].

Voltage deviations represent another power quality issue. These deviations are due to various factors including wire diameter, power supply distance, and power flow distribution. They are primarily caused by voltage drops due to resistance and the current flowing through the distribution system. In DC systems, these deviations are solely related to conductor resistance. Allowing a higher voltage deviation can increase the power supply radius and range. However, this comes at the cost of increased complexity in converter design and control, as well as heightened requirements for equipment safety and insulation [37].

The increased use of DC/DC converters in DC microgrids can lead to two problems. First, the elevated switching frequency can cause electromagnetic interference (EMI). To address this issue, converters are used with EMI filters. However, these converters are connected to the DC grid, the EMI filters can induce inrush currents, which may result in voltage oscillations or sags. The second problem is linked to the capacitors in such converters. The capacitors, along with the impedance of the DC bus cable, can create resonance frequencies, potentially leading to the amplification of DC ripple.

One power quality problem specifically linked to bipolar DC microgrids is the issue of voltage unbalance. Voltage unbalance occurs due to unequal loading of the positive and negative poles, causing a voltage difference between poles that results in currents that do not cancel each other. This, in turn, causes a current to flow in the neutral conductor, leading to an increase in line losses, which is undesired. This problem also occurs in AC distribution systems. Similarly to AC systems, voltage unbalance can be measured via a Voltage Unbalance Factor (VUF), defined as [40]:

$$\begin{aligned} \%VUF_{DC} &= \frac{\text{Pole Voltage deviation}}{\text{Average Pole voltage}} * 100 \\ \%VUF_{DC} &= \frac{|V_{p,i} - V_{n,i}|}{(V_{p,i} - V_{n,i})/2} * 100 \end{aligned} \tag{2.15}$$

Where $V_{p,i}$ and $V_{n,i}$ are the positive and negative pole voltages respectively. One common way to counter this problem is the use of voltage balancers. Voltage balancers are essentially converters that achieve balancing by redistributing energy consumption or generation. The most basic topology is shown in Fig.2.12. This topology, derived from the buck/boost converters, regulates its inductor current to keep the neutral balanced, redistributing surplus current and minimizing neutral current [33].

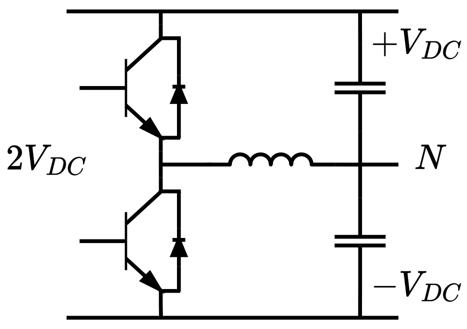

Figure 2.12: Buck/boost voltage balancer

Different architectures offer different advantages. Furthermore, the duty cycle of the voltage balancers can be adjusted by a controller to improve the performance of the voltage balancer. However, these are additional devices that increase the system cost. Another option is to reduce voltage unbalance by influencing the control of the converters on each voltage pole. For more information concerning the state of the art of voltage balancers, the reader may refer to the work performed in [41].

These power quality phenomena can be classified into transient and steady-state phenomena. The defining characteristic of transient events is that they involve a large amplitude change and a short-term disturbance. On the other hand, steady-state phenomena show small amplitude changes but occur over a longer time frame. Fig. 2.13 classifies the different power quality issues into either transient or steady-state phenomena. Furthermore, the different events that are the origin of these phenomena are shown on the right side. Notice that there is a coupling between different phenomena. Indeed, the existence of one might lead to the other. DC ripple on the DC network will directly result in changes in the DC voltage amplitude, which is a distortion of the voltage. In bipolar microgrids, allowing greater voltage deviations can lead to voltage unbalances.

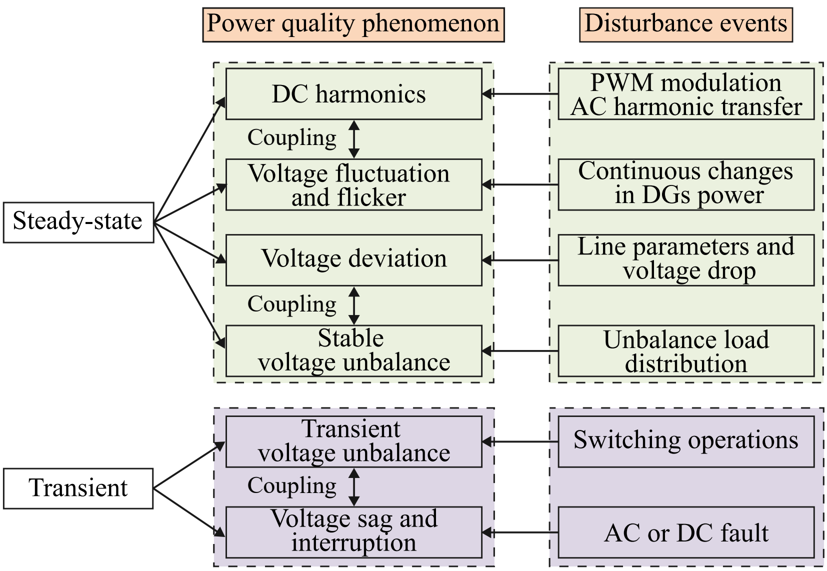

Figure 2.13: Correlation between power quality phenomena [37]

In [38], the applicability of existing power quality definitions in standards IEC 61000 and IEEE Std1159 to LVDC distribution is studied. IEC 61000 concerns the Electromagnetic compatibility while IEEE Std1159 is the recommended practice for monitoring electric power quality. The results from the analysis are summarized in Table 2.2. The first two columns indicate whether the power quality issue is applicable or not. The following two columns show whether the power quality issue has a definition and an indicator in the IEC 61000 standard. The last two columns describe the same but for the IEEE Std1159 standard.

Table 2.2: Applicability of power quality standards and definitions to $DC\mu G$ [38]

Power quality issue	**AC**	**DC**	**IEC 61000**		**IEEE Std1159**	
			Definition	Indicator	Definition	Indicator
Power frequency variations	■	□	□	□	□	□
Transients						
Impulsive/Surge	■	■	✓	✓	✓	✓
Oscillatory	■	■	×	×	✓	✓
Short-duration variations						
Sag/Dip	■	■	✓	✓	✓	✓
Swell	■	■	✓	✓	✓	✓
Interruption	■	■	✓	✓	✓	✓
Long-duration variations						
Undervoltage	■	■	×	×	✓	✓
Overvoltage	■	■	×	×	✓	✓
Interruption	■	■	✓	✓	✓	✓
Imbalance						
Voltage	■	■	Δ	Δ	Δ	Δ
Current	■	■	Δ	Δ	Δ	Δ
Waveform distortion						
AC offset	□	■	×	×	×	×
DC offset	■	□	□	□	□	□
Harmonics	■	□	□	□	□	□
Interharmonics	■	■	✓	✓	✓	✓
Noise	■	■	×	×	✓	✓
Notching	■	■	×	×	✓	✓
Voltage fluctuations	■	■	✓	Δ	✓	Δ
Legend	■ Issue applicable □ Issue not applicable ✓ Definition/indicator is available and applicable Δ Current definition/indicator requires reconsideration × no definition/indicator defined					

The recent work in [37] proposes different power quality indices. This proposition arises from the need to standardize the criteria and the definition of phenomena such as harmonics and ripples. The proposed index system is based on the AC system index, taking into account the characteristics of DC microgrids. The resulting index divides phenomena into DC voltage quality and DC harmonic distortion. The proposed index system is shown in Fig. 2.14, where it also shows which indices are applicable to unipolar and bipolar microgrids. Notably, the main difference between them is that the DC voltage quality problems related to voltage unbalance are not applicable in unipolar microgrids.

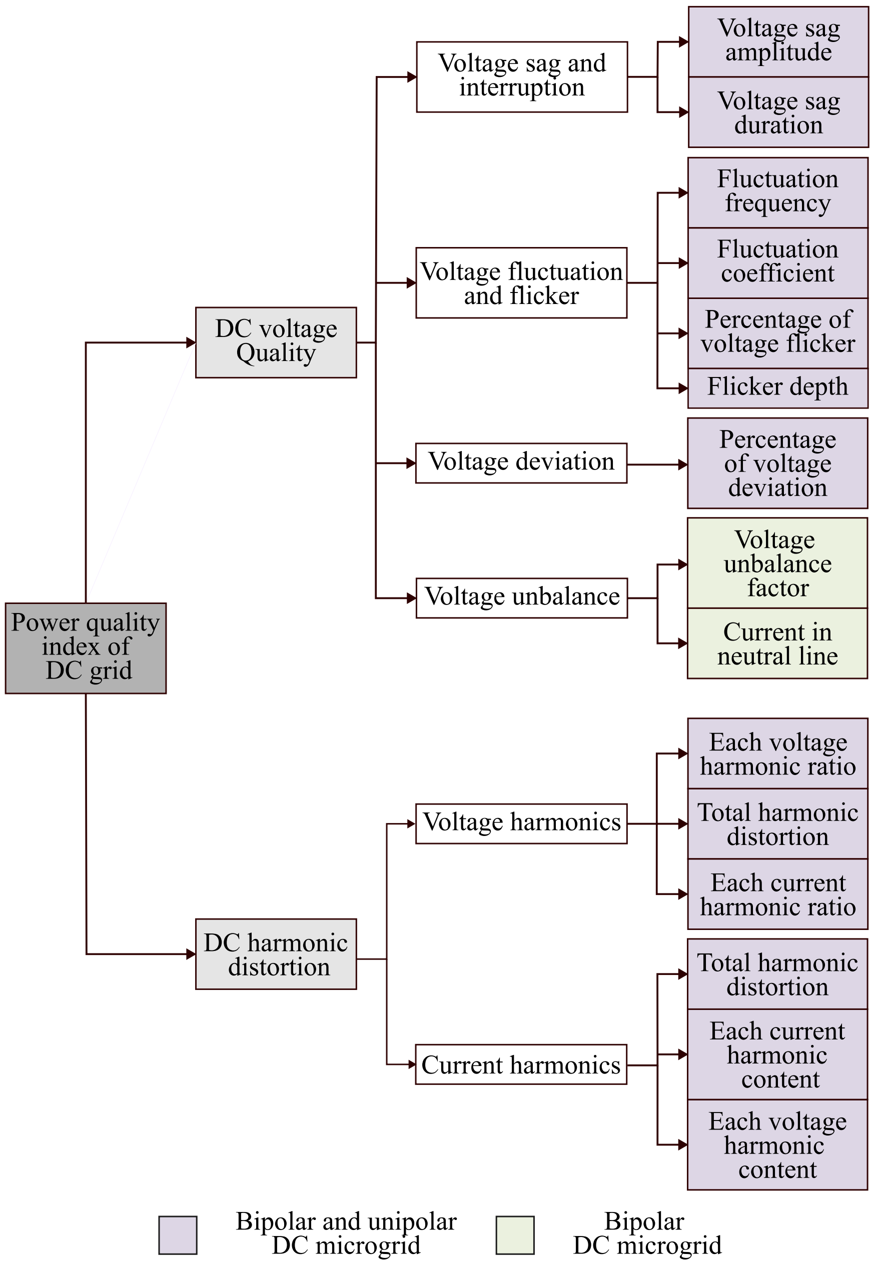

Figure 2.14: Index system of DC power quality [37]

2.5 Challenges/Risks in DC

Compared to AC distribution, DC distribution has a lower maturity level as a technology. While advances in this field have been steady, there are many challenges and risks associated with the technology that need to be overcome. This section aims to give the reader a non-exhaustive overview of the difficulties that can be found.

2.5.1 Protection

The protection of DC microgrids is one of the main challenges being faced. The primary challenges include the development of reliable and economically viable protection techniques. Such techniques and necessary devices have not yet been established, in part due to the lack of standards that slows down their development. Concretely, the major challenges for fault protection in DC microgrids can be considered [42]:

- Challenges due to system blackout and grounding
- Absence of natural zero crossing
- Arcing and fault clearing time
- Protection integration issues due to various modes of operation and the disruptive nature of renewable energy sources
- Difficulties in detecting and pinpointing fault location in case of lack of frequency and phase information
- Increased number of voltage source converters (VSCs) and circuit breakers
- Constraints linked to communication delays and cybersecurity

One key point mentioned in the previous list is the absence of zero crossing. The absence of zero crossing makes clearing DC faults harder and places more demands on protection devices. Without zero crossing, AC breakers cannot be used on DC grids unless the breaker is rated for higher voltages and currents. However, higher-rated devices come with increased prices, making this solution non-ideal. Hybrid breakers can also provide protection but are equally limited by their cost. Furthermore, converters can be easily damaged if they contribute to the fault for more than a few milliseconds. This requires a faster response time than that of AC protection mechanisms [43].

To protect the distribution system, different protection devices can be used. Among these, the simplest devices are fuses. While fuses are a low-cost solution, they need to be replaced after each operation. Another disadvantage is that they cannot distinguish between transient and permanent faults. Devices such as molded case circuit breakers and mechanical circuit breakers have slow response times and are therefore limiting for DC distribution, where the fault current can quickly reach 2 to 3 times the nominal load current [44].

One of the most promising protection devices is the solid-state circuit breaker (SSCB). SSCBs provide a faster response compared to other mechanical circuit breakers and can interrupt the flow without arcing, which is challenging for mechanical circuit breakers. SSCB reduce the short circuit current by applying a voltage that opposes the voltage across the SSCB. This is achieved through a voltage clamping mechanism, which allows them to absorb residual energy and drive the system current to zero. One type of these devices is the snubber circuit. Various types of snubbers exist, such as C-type, RC, and RCD. One major challenge is that SSCBs need to sustain short bursts of current that can be up to 5-10 times the nominal value. These surge currents cause an increase in conduction losses and can lead to overheating and damage of the semiconductors. To avoid this, bulky cooling systems may be needed [44], [45].

2.5.2 Faults in DC

During a fault, the VSC capacitor will discharge, leading to significantly high values for the peak current. Furthermore, the fault can force diodes into their conducting state. This can cause the fault current to flow towards elements where it cannot be interrupted. The faults have three stage behavior: capacitor discharge state, diode freewheeling state, and input source feeding state as shown in Fig. 2.15 [44]. Additionally, there are no zero-crossing currents in DC. This makes it difficult to interrupt the faults with traditional devices such as fuses and circuit breakers. Thus, proper grounding architecture, fault detection strategies, and equipment are needed.

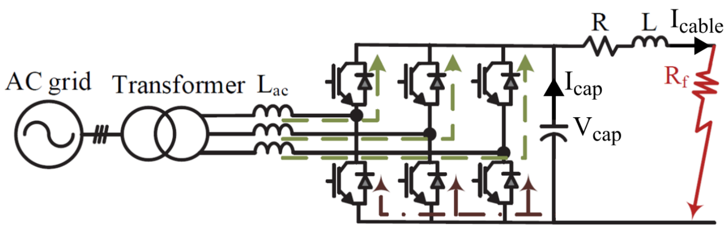

(a)

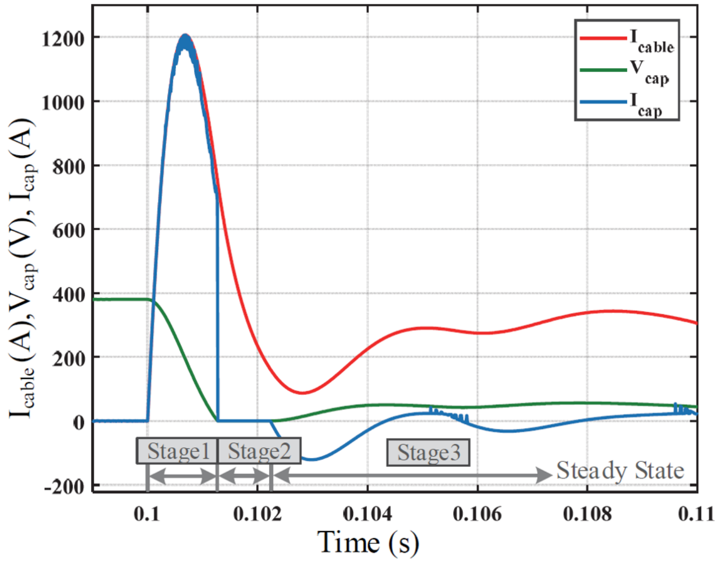

(b)

Figure 2.15: Fault three stage behavior: (a) Equivalent scheme of VSC under a short-circuit fault, (b) Cable current i_{cable}, DC-link capacitor voltage V_{cap}, and capacitor current I_{cap} during the short-circuit fault. Adapted from [44]

Several works have been performed to characterize the types of faults. [44], [46], [47], propose describing each stage circuit via equations. Consequently, the first stage shown in Fig. 2.16a can be described by the equations of a second-order RLC resonant circuit. Considering the initial condition for the current I_0, the system is described by (2.16).

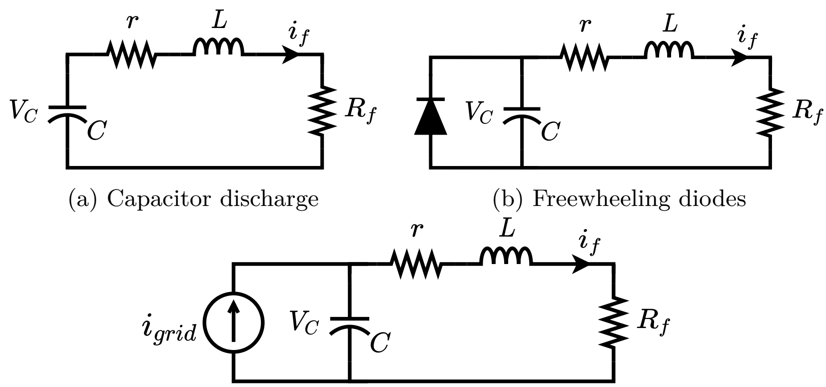

(a) Capacitor discharge

(b) Freewheeling diodes

(c) Grid-side current feeding

Figure 2.16: Equivalent circuit of converter during a short circuit

$$i_f(s) = \frac{V_C}{\omega_d * L} e^{-\alpha t} sin(\omega_d t) + I_0 e^{-\alpha t} \left[cos(\omega_d) - \frac{\alpha}{\omega_d} sin(\omega_d t) \right] \tag{2.16}$$

Where I_0 is the initial current, $\alpha = r/2L$, $\omega_d = \sqrt{\omega_0^2 - \alpha^2}$, and $\omega_0 = 1/\sqrt{LC}$. The response of the system will be different depending on whether it is an overdamped, critically damped, or underdamped system. Once the voltage of the capacitor reaches zero, the free-wheeling diode stage will start. This stage, in turn, can be described by the equation:

$$I = I_0' e^{R/L} t \tag{2.17}$$

With I_0' being the current value when entering the free-wheeling diode stage. It is important to remember that there are two types of faults: pole to pole and pole to ground. Equation (2.16) describes the case of a pole to pole fault. For a pole to ground fault, the fault resistance R_f needs to be taken into account. A pole to pole fault usually has the condition $R < 2\sqrt{LC}$, but for a pole to ground fault, the condition becomes $R_f + R < 2\sqrt{LC}$. A large enough fault resistance R_f such that $R_f + R > 2\sqrt{LC}$, will transform the response into a first-order damped process. This has the consequence that the voltage will not drop to zero, and therefore there will be no free-wheeling diode stage [47], [48]. Thus, the first stage is followed directly by the third stage. When comparing both types of faults, a key difference is that the over-current in ground faults is lower and not as serious as a pole to pole fault [48]. Indeed, pole to pole faults are considered easily detectable and more severe, although pole to ground faults are the most common ones [42], [49]. The characterization of faults is a subject of interest with many challenges that are out of scope in this thesis. Further research has focused on characterizing the impact of the number of converters and their distance to the fault [46], the influence of the converter topology on the fault characteristics [50], and the influence of unipolar and bipolar systems on faults [51]. For a more detailed discussion on the behavior of faults in DC, one can refer to the following thesis [52]. Notice that in this subsection only external cable faults have been discussed. However, internal faults can happen in converters due to internal component failure. The work shown in [53], provides an introduction to this type of faults and their classification.

2.5.3 Grounding in DC

The objective of the grounding architecture is to ease the detection of faults, minimize stray currents, and reduce the common-mode voltage. The grounding systems can be categorized into five different types: TT, TN-C, TN-S, TN-C-S, and IT. The first letter denotes if the system is connected to earth (T) or isolated (I). The second letter indicates if the exposed parts are connected to earth (T) or the earthed neutral (N). Fig. 2.17 illustrates TT and IT grounding. In TT, the earthing and the protective earth are grounded separately. For IT grounding, the earthing of the system is done via a high resistance or completely ungrounded while the protective earth is grounded.

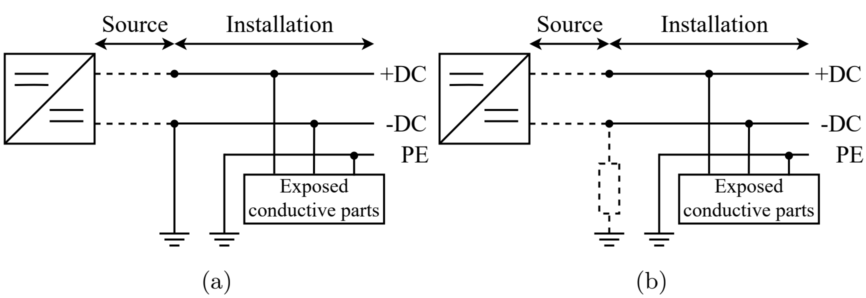

Figure 2.17: Types of grounding: (a) TT (b) IT [32], [44]

The different types of TN grounding schemes are shown in Fig. 2.18. It is shown that TN-S has a protective earth conductor, but it is grounded together with the negative pole. Meanwhile, in TN-C, the negative conducor and the protective earth are combined. Finally, TN-C-S is a combination of the other two methods. One part of the system is grounded as a TN-C method, and the other is grounded as a TN-S system.

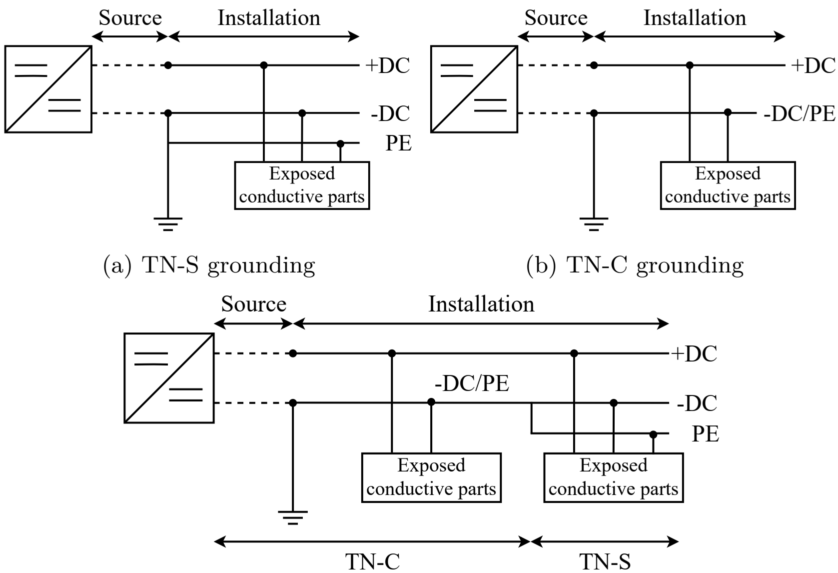

(a) TN-S grounding (b) TN-C grounding

(c) TN-C-S grounding

Figure 2.18: Types of TN grounding [32], [44]

Each grounding method has its advantages and disadvantages. The preferred use case for each depends on the application. In the case of LVDC distribution systems, corresponding standards are still in development. Most recently, a new standard to cover LVDC distribution has been developed in the Netherlands. The national guideline NPR 9090 [32] covers LVDC distribution ranging from $350V$ to $1400V$. This standard divides the voltage range into zones and recommends protection mechanisms for each zone as presented in Fig. 2.19 [33]. The NPR 9090 norm recommends using a TN-S grounding system for zones 1 to 3 and 4A. Zone 4B can be implemented with an IT grounding because it corresponds mainly to USB-C connections.

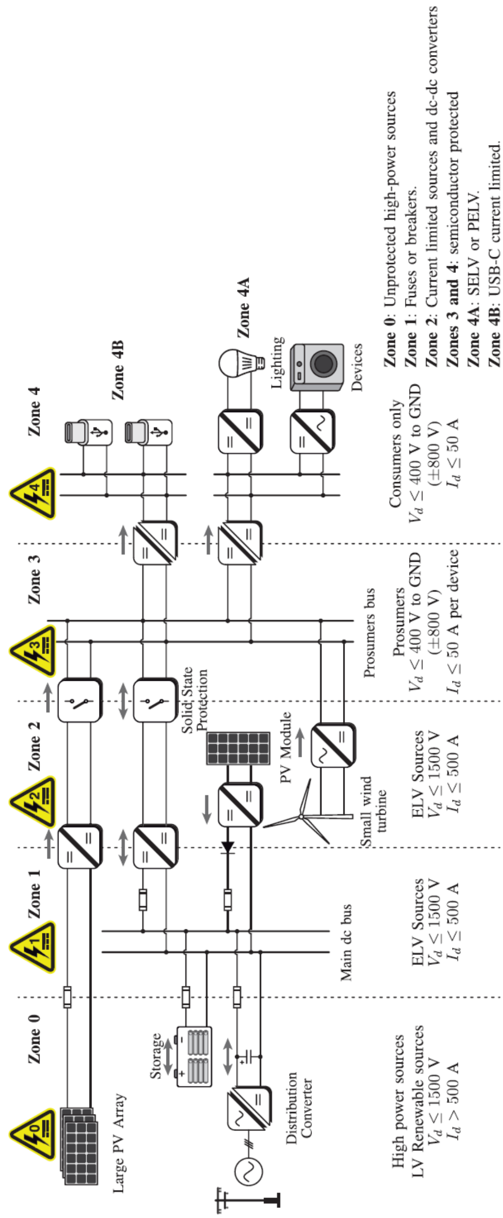

Figure 2.19: Safety zones or risks classification example according to NPR 9090[32], [33]

Furthermore, protection is needed against corrosion caused by ground leakage currents due to voltage drops in the neutral conductors. To avoid this, two systems are used: TN-SCD and TN-SCDD. These two systems, shown in Fig. 2.20, utilize anti-parallel diodes. TN-SCD grounds the main source directly, while the other sources are grounded through the capacitor diode array. TN-SCDD is used when there are multiple sources, and they are all grounded equally.

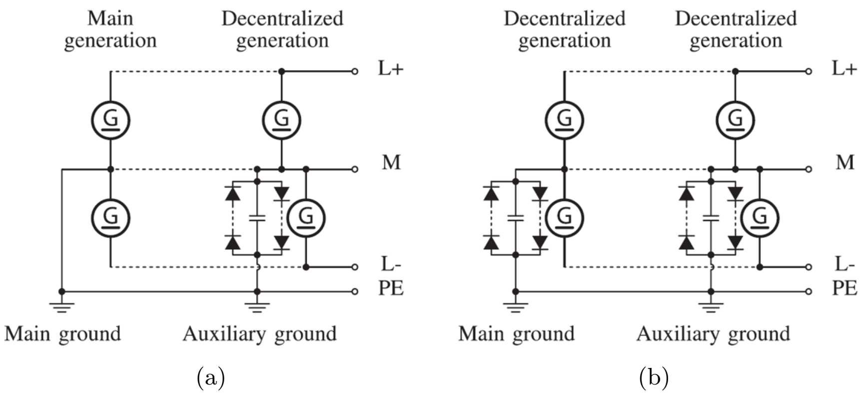

Figure 2.20: TN-S grounding for: (a) Systems with a main generation unit (b) Systems with multiple generation units [32], [33]

The absence of standards leads to another challenge, namely, the lack of hardware or specialized protection elements such as solid-state circuit breakers. Indeed, the demand for DC protection devices, while increasing, is lower than that for AC elements. Without a standard, manufacturers are more reluctant to produce DC protection devices for MVDC/LVDC distribution systems.

2.5.4 Converter stability

The stability of the converters in DC microgrids is also a challenge. This is due to the constant power load (CPL) behavior introduced by converters that are controlled to ensure that the power provided to the load remains constant. CPLs act as a negative impedance, which can destabilize the system [54].

The characteristic curve of a CPL is illustrated in Fig. 2.21. Because power is kept constant, if the load voltage V_{cpl} decreases, the load current i_{cpl} must increase. This causes the resistance seen from the source side of the converter to have a negative incremental value [55]. This negative resistance reduces the damping of the system and tends to destabilize it. The effects of CPL loads in DC distribution systems are [54]:

- Reduces the equivalent resistance of the system
- High inrush current as voltage build-up slowly from its initial value
- Reduced system damping and stability margins
- May lead to voltage collapse

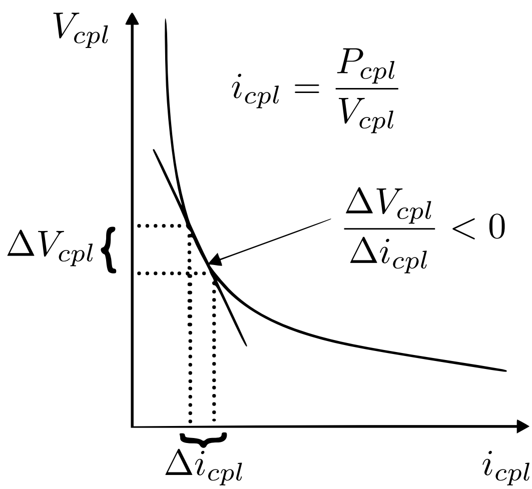

Figure 2.21: V-I characteristics of a typical CPL
[54]

To ensure that the systems remain stable, various stability criteria have been proposed in the literature. These criteria are used to study the stability of the systems and define forbidden regions that must be avoided. One example is the Middlebrook criterion, which considers the minor loop gain through the input and output impedance to define the limits of the forbidden zone [56]. The work presented in [57] provides an introduction to the different criteria.

There also exist stabilization techniques to maintain system stability. These can be classified as passive or active damping techniques. Passive damping techniques modify the hardware, while active damping techniques modify the control structures. An introduction to active damping techniques can be found in [54]. While these techniques exist, converter stability remains a complex issue, especially when considering systems with multiple converters.

2.5.5 Other challenges

Without going into detail, several other challenges exist. In the context of faults, fault identification itself is a problem. Several approaches exist for fault detection, including overcurrent protection, current derivative protection, directional overcurrent protection, distance protection, and differential protection. Fault detection mechanisms based on complex techniques involving signal processing, fuzzy logic, and machine learning have also been proposed [42], [44]. Communication delays in fault identification mechanisms can also pose a challenge. As explained before, the response time to a fault is critical to protect the system and the devices. As distribution systems become more interconnected and rely more on communication among devices and users, cybersecurity is steadily becoming a challenge that cannot be ignored.

2.6 Standardization

Standardization is a key element, especially for a developing technology such as this one. Standardization for DC distribution is relatively new and therefore lacking. While standards exist for ship power and airplanes, these have different constraints due to their enviroments. Therefore, these standards are not necessarily applicable to terrestial DC microgrids. The lack of standards presents a significant challenge for multiple sectors. In the academic world, lack of standards leads to a lack of reference values and also a lack of references with which to compare certain results. These problems increase when trying to develop pilot projects. Although these pilots themselves are supposed to aid in the development of standards, the lack of standards poses many roadblocks. This is especially true in terms of protection and operation of the system. The problem scales further as manufacturers of different elements, including the protection devices, struggle to develop a product if the guidelines and target values are missing. These three sectors are interlinked, and the problems of each one cascade to each other. Thus, there is a palpable need for standardization in DC distribution. This section aims to briefly show the different efforts being made in standardization.

As previously mentioned, NPR 9090 [32] is one recent national guideline that aims to standardize the requirements for DC distribution. One of the key points of this proposal is the choice of voltage levels. For LVDC distribution, the voltage levels of $350V$, $700V$, and $1400V$ are proposed. $350V$ is chosen due to its compatibility with $230V$ AC-designed equipment without modifications and eliminating front ends. Another important contribution is the definition of the safety zones as shown in the previous section and Fig. 2.19. Another standardization effort is proposed through IEC-TR-63282 [39]. One of the proposals of this work is DC voltage regions. These are referred to as voltage bands. Along with these voltage bands, four operation ranges and a series of states are defined. The definitions for the voltage bands, operation ranges, and voltage states are provided in Table 2.3, Table 2.4, and Table 2.5 respectively. These different parameters result in the voltage map shown in Fig. 2.22.

Table 2.3: Voltage bands in DC systems [39]

Band	**Description**
U_1 and B_1	Undervoltage disconnecting voltage and blackout band
U_2 and B_2	Minimum voltage for continuous operation with full functionality and Critical band
U_3 and B_3	Maximum continuous operating voltage and Nominal band
U_4 and B_4	Maximum temporary operating voltage and switching, commutation, and protection devices operation band
U_5 and B_5	Overvoltage disconnecting voltage and overvoltage protection devices non-operating band
U_6 and B_6	Maximum voltage that equipment overvoltage protection devices clamp and overvoltage protection devices operation band
B_7	Prohibited band

Table 2.4: DC voltage operation ranges [39]

Range	**Description**
R_1	Transient state limited to a short time
R_2	System fault range where disconnection of the faulty element is required
R_3	Voltage control where system balance issues are addressed
R_4	Continuous operating range

Table 2.5: DC voltage operation states[39]

State	**Description**
A_1	Blackout state
A_2	Emergency state where action must be taken to reduce stress on the system
A_3	Normal state
A_4	Abnormal state
A_5	Overvoltage state without clamping
A_6	Overvoltage state with clamping
A_7	Prohibited state

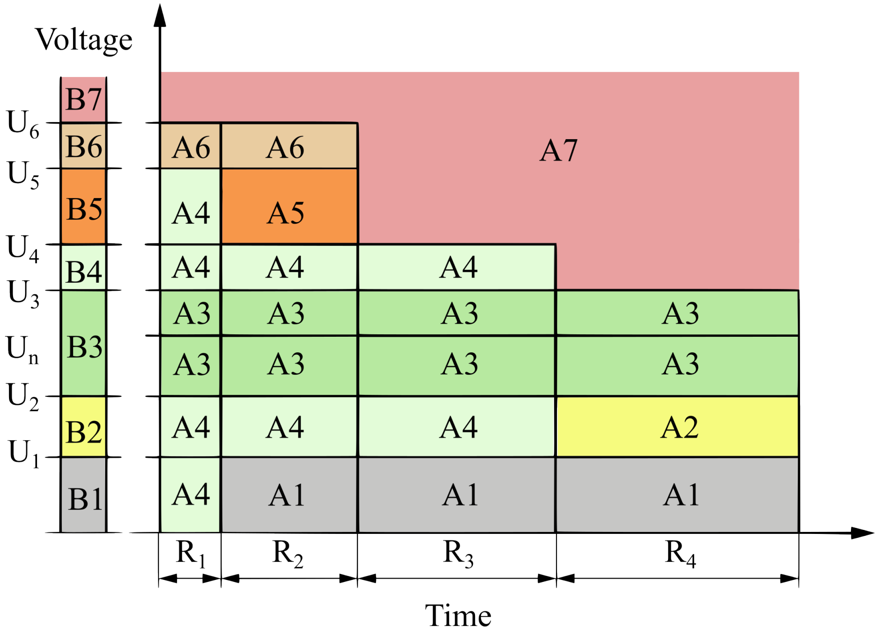

Figure 2.22: DC Voltage areas for safe interoperability [39]

Another effort towards standardization is the working group report from CIRED. The work performed in [31] covers different aspects of DC distribution ranging from LVDC up to HVDC. The report covers different implementations of DC distribution and also highlights the challenges. An important result of this work is an overview of the different standards and works dealing with standardization. Table 2.6 shows the found standards for LVDC ($\leq 1500V$) distribution. Table 2.6 demonstrates that there are many efforts being done to work towards standardization and at the same time provides references that can be used to develop unified international standards.

Table 2.6: Overview of relevant standards for DC systems [31]

Application	**Design**	**Protection criteria**	**Safety**	**Power quality**	**Earth and bonding**	**Switchgear and circuit breaker**
General	IEEE 946-2020 IEC 60038 IEC 60364-1	BS EN 60947-2	IEC 62477-1	IEC TR 63282	IEC 50162	IEC 60947-1 IEC 60947-2 IEC 60947-3
Microgrids	IEEE P2030.10					
Public networks	IEEE P2030.10.1 IEEE P2030.10.2	BS EN 60947-3	IEEE P2984 IEC 61439-2 IEC 61557	IEC TR 63282 IEC 61000-2-2	ESQCR	IEC 61439-1
Power converter	IEC TS 62578 IEC 60146-1-1 IEC 60146-2 IEC 62909-1 IEC 62909-2		IEC 62477-1	IEC 61204-3		
Residential	IEEE P2030.10.2 IEEE P2847			IEC 61000-4-17 IEC 61000-4-29		IEC 61008-1
Telecom/ICT	ITU T L.1201 ITU T L.1204			ITU T L.1200		
Data center			IEC 62040-1			
LED lighting			IEC 60598-1 IEC 61347-1			
Solar PV		IEC 60269-6	IEC 61643-32			
Ship power	IEC 60092-201	IEC 60092-202 IEC 60092-507				

The first signs of convergence in standardization are emerging; however, there is still a significant amount of work to be done. Concretely, common definitions for several aspects are needed. These definitions include standard nominal voltage values and their operating ranges. Definitions for the power quality phenomena that exist in DC are also needed. Furthermore, a standardized way of measuring these phenomena is required. Equally, a common ground for safety and protection is needed. This includes a consensus on the grounding scheme for DC systems and protection devices suited for DC microgrids.

2.7 Existing implementations

Despite the previously mentioned challenges, there are several implementations of microgrids around the world (other than for naval and aerial applications). There are existing applications in data centers, research labs, and commercial buildings. There are also examples of DC microgrids for public distribution and a few for industrial DC microgrids.

One example is a LVDC distribution network implemented by the Korea Electric Power Corporation (KEPCO). In this project, an existing AC connection was replaced by an LVDC line in a rural area of Gwangju. The line has been in operation since October 2016 and shows a stable operation with a fluctuation of 5% [58]. Another project from KEPCO is a distribution line for the island of Seogeochado, which uses a $\pm 750V$ system. This project included the installation of renewable energies, ESS, and EV charging stations [31].

In Finland, the energy company Suur-Savon Sähkö Oy and the Lappeenranta University of Technology (LUT) constructed a research site for LVDC. This LVDC distribution microgrid is shown in Fig.2.23. The site also utilized $\pm 750V$ and was also used by the distribution system operator [59], [60].

In [31], more implementation instances of DC microgrids are detailed, such as the LV-Engine project in the United Kingdom, a DC industry project in Germany, and a hybrid AC-DC microgrid in China. One interesting project detailed is the N470 Project in the Netherlands. It is a commercial project where a road and its systems were renovated. This renovation involved the implementation of a DC microgrid, shown in Fig. 2.24, that spans 4.7 km. It is also the first dutch project developed taking into account the previously mentioned guideline NPR 9090.

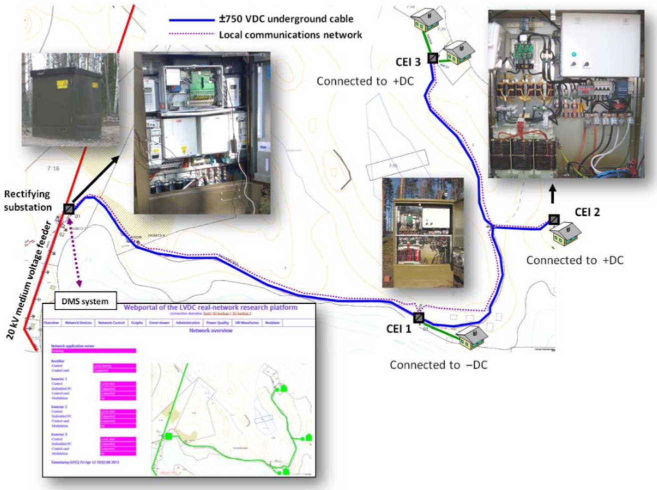

Figure 2.23: LVDC distribution network of the research site in Finland [60]

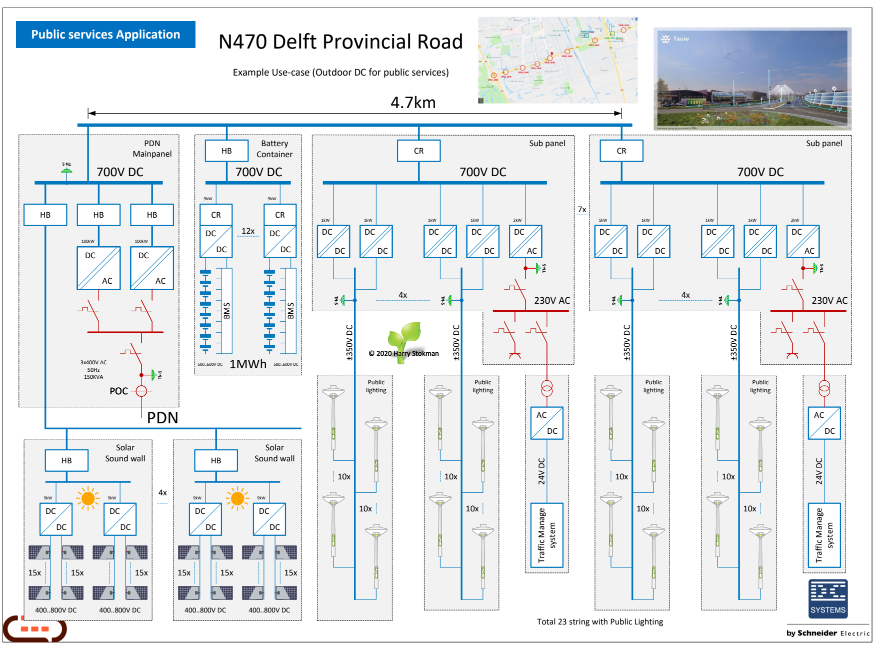

Figure 2.24: Single-line diagram of the N40 site system [61]

Another recent implementation is an LVDC microgrid that supplies HD Hyundai Group's Global R&D center in Pangyo, Seoul. The DC loads consist of LED lighting, electric heat pumps, EV chargers, and a DC laboratory. The main distribution is performed through a 380V network. The implementation was a joint effort from KEPCO KEPRI and KERI. The system began commercial operation at the end of 2022 [62].

A DC microgrid industrial project can be found in Belgium. Project MIRACCLE (Micro-réseau Industriel avec Raccordement en Courant Continu et Luminaires Extérieurs) aims to interconnect different industrial consumers in a DC network. The connected consumers will share energy produced from PV panels and exchange with the main grid through a single point of connection [63].

Equally, [64] provides a list of other microgrid projects around the world. These projects and their scope are listed in Table 2.7. Finally, the following link provides interactive microgrid map. This map, shown in Fig. 2.25, shows DC microgrid projects from around the world and classifies them according to the type of application. References for most of the projects are also provided [65].

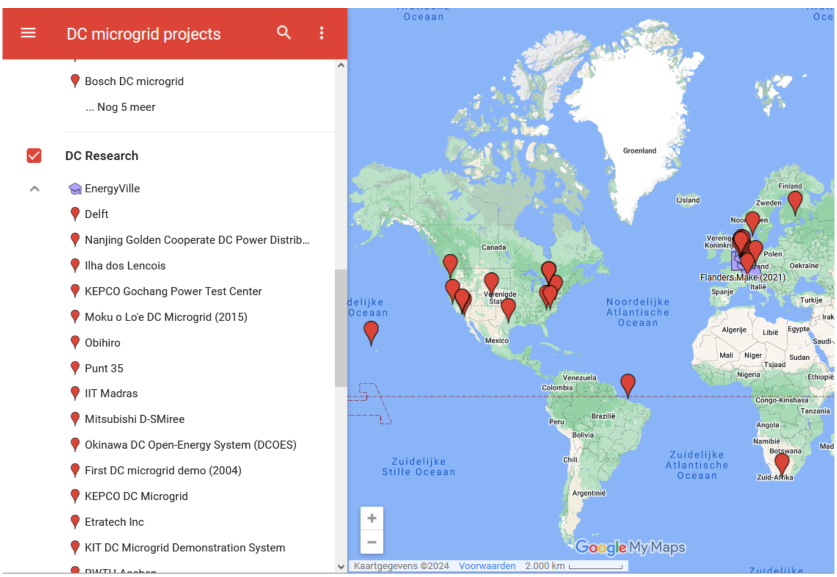

Figure 2.25: Interactive map overview of LVDC grid projects worldwide [65]

Table 2.7: Overview of Microgrid Projects [64]

Microgrid Project	**Scope of Project**
ABN Amro Bank's Circle Pavilion in Amsterdam	Very efficient sustainable circular building in Amsterdam. The Office has 3000 sq.m of meeting rooms with a 350V DC microgrid support.
Public Lighting by Citytec (Nieuw Reijerwaard Business Park)	Europe's largest DC lighting system boasts reduced resource consumption, enhanced reliability, and efficiency. It operates on a 350V DC supply and is integrated into a smart microgrid with advanced control and protection systems.
Demo DC Grid Hengelo	DC users are linked to a smart microgrid directly connected to solar panels. A 700V DC project in the Netherlands focusing on renewable energy, including EV charging, public lighting, and peak shaving batteries.
Energy Neutral Homes in Stroomversnelling	A national project involving six housing corporations aims to convert approximately 110,000 houses into zero-energy homes, known as "Nul-op-de-Meter" or "Zero-on-the-energy-meter" homes.
DC Flexhouse	To develop a strategy for replacing conventional AC-based homes with DC technology. An industry-institute collaborative project with ABB and Hague university of applied sciences.
DC and sustainability in the greenhouse	A DC version of the current ballast for the greenhouse market aims to reduce energy wastage during AC-DC conversion. It features a highly efficient centralized control-based conversion of AC to DC, instead of local conversion, to maximize energy savings.
Washington DC university DC microgrid	Gallaudet University, Scale Microgrid Solutions, and Urban Ingenuity collaborate on a solar plus storage microgrid to power the university and surrounding homes via a community solar plan. The microgrid includes 2.5 MW of solar panels on various campus rooftops and parking garages, a 1.2 MW/2.5 MWh lithium-ion battery, and a 4.5 MW combined cooling, heat, and power (CCHP) system.

Microgrid Project	**Scope of Project**
McKinleyville wastewater treatment plant	Expected to be completed in 2022, this project involves a 580 kW solar array paired with 500 kW of energy storage backup, intended to power the wastewater treatment plant.
Montgomery County's electric bus depot microgrid	Aiming for net-zero emissions by 2035, the Brookville Smart Energy Bus Depot features a 5.6 MW microgrid with approximately 2 MW of battery storage.
Los Angeles transportation electrification	7.5 MW EV charging stations coupled with solar and storage.
Florida's neighborhood microgrid project	Incorporating 37 homes in the Medley at Hillsborough development, the project examines the microgrid's resilience during disruptions in the upstream AC network. It aims to assess the integration of diverse renewable sources and mitigate peak loads.
UK microgrid project on residential electrification	A private microgrid project involving 162 houses, slated for completion by 2025, emphasizes the implementation of an energy-as-a-service concept. It prioritizes decarbonization, striving for zero carbon-ready, all-electric homes without gas connections.
Ameresco, microgrid project, California	Designed to transform the 165,000-acre training center into a net-zero energy facility by 2022, the microgrid, developed by Ameresco, integrates 3.75 MW of PV and 5 MWh of storage to meet training needs. It operates autonomously, incorporating diverse controls and interconnection for both new and existing generation and energy storage.
New Jersey's town center project	Implementing 10.5 MW of new or existing PV generation and 2.9 MW of new or existing battery storage, along with a minimum of 30 new or existing charging stations, the project targets an annual reduction of over 24,000 tons of carbon dioxide emissions.

2.8 Evaluation and future perspectives

This chapter has reviewed in detail the applications and potential benefits of DC distribution. With this the information in mind, one question may arise: should the existing AC system be replaced with a more efficient DC system?

In the author's opinion, the objective of DC deployment is not to replace the existing AC system. Instead, DC distribution and microgrids should be seen as complementary elements to the current infrastructure, allowing both to coexist. DC should be applied in contexts where it is beneficial and needed. Therefore, the main interests of DC are others: alleviating congestion, increasing the hosting capacity of renewable energies, serving as a distribution backbone, and facilitating the implementation of energy storage systems. While there are gains in terms of converter losses by avoiding DC/AC conversions, the main efficiency gain will come from access to a higher voltage level. However, the aforementioned interests are much stronger motivators than the mere efficiency gain.

The logical follow-up question is: If there are so many benefits and interest, why is the implementation of DC microgrids not common? The last two sections summarize the main reasons. Challenges in standardization and fabrication of protection elements are key obstacles. Once these barriers are tackled, the implementation of DC microgrids will likely spread throughout distribution systems. The CIRED report "DC Distribution Networks - WG 2019-1" has listed the key elements that will enable a breakthrough in the implementation of DC distribution and DC microgrids [31]:

- Techno-economic planning tools need to be developed
- Clear use cases demonstrating exploitation strategies and business models for products and services need to be formulated
- International standards and regulations have to be defined
- The long-term impact of DC integration into MV and LV public networks needs to be studied
- Operational safety and experience must be gained from pilot projects to ensure a reliable and trustworthy future supply system

Chapter 3

Control of DC Microgrids

Chapter contributions

- Two control classifications are presented
- A review of first level controllers is presented. Their implementation, advantages, and disadvantages are discussed
- A review of second level controllers is presented. Their implementation, advantages, and disadvantages are discussed

As mentioned in the previous chapter, one advantage of microgrids is that all the devices are controllable as they are interfaced by power electronics converters. Indeed, the converters used by the different elements need to receive specific control signals. This gives rise to certain questions. What control signal do we need to give? How is this signal generated?

From the perspective of the converter, it needs to receive Pulse Width Modulation (PWM) signals that dictate the control of the switches. However, how is this PWM signal generated? The general control structure of a converter is shown in Fig. 3.1. The energy source or load is connected to the microgrid via a converter. The control loop is responsible for generating the control signals for the converter. This is achieved by first implementing a control method that provides a voltage or current reference according to the objectives of the control method. Subsequently, this reference is fed into what is known as the inner control loop. The inner control loop compares the reference value against the measured value. The difference between these two values is then inputted into a Proportional Integral (PI) controller, which adjusts its output to reach the reference value. The output of the PI controller can range from being the duty cycle to be used by the converter, to generating the reference signal values that are then used to generate the PWM command.

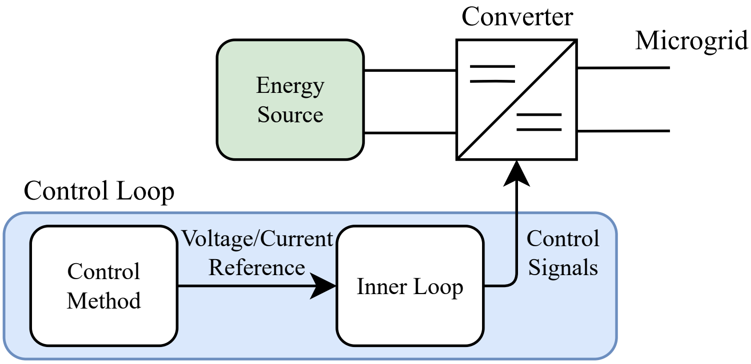

Figure 3.1: Converter control architecture

There is an abundance of different types of controllers with different roles, objectives, advantages, and disadvantages. All these controllers can fall into different categories. In this section, two of the main ways to classify the controllers are presented. These are: based on their communication and based on their response time. These two classifications are used for both AC and DC microgrid controllers.

3.1 Control schemes classification based on their communication

The different types of controllers exchange information to varying extents. Thus, it is possible to classify them according to their type of communication and exchange of information. According to these criteria, the controllers can fall into three different categories: Centralized, Decentralized, and Distributed. These three different types of controllers are shown in Fig. 3.2.

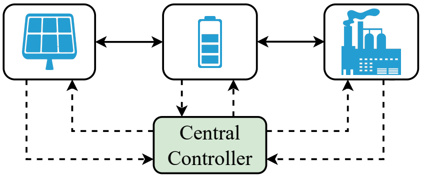

(a) Centralized control

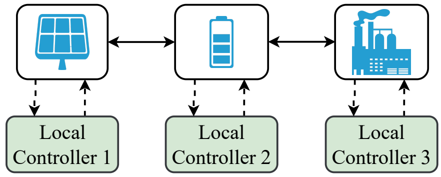

(b) Decentralized control

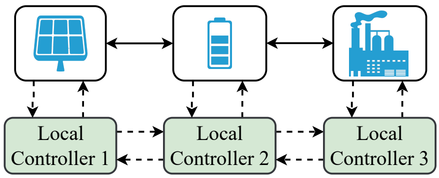

(c) Distributed control

Figure 3.2: Control schemes classification based on their communication[66]

In centralized types of controllers, the system is managed by the microgrid central controller (MGCC). The MGCC receives information from the different elements in the microgrid and issues commands to all the different converters based on the information it has. This exchange of data requires a robust communication system between the different elements and the MGCC. Thus, the system is dependent on effective communication with the MGCC. While from a coordination point of view, this controller is easy to implement, one of its main drawbacks is that the system has a single point of failure. Indeed, if the MGCC is unable to operate properly, the entire network will be disturbed.

The opposite of the centralized controller would be the decentralized controller. In this type of controller, the different units of the microgrid each have their own control that acts based on local measurements. This characteristic offers certain advantages. Since there is no need to exchange information with other controllers, the communication requirements can be reduced. The system no longer has a single point of failure as each unit is independent. Additionally, it is easier to add new units to the network, meaning there is easier scalability. However, this type of control still has a drawback: due to the lack of communication among converters, coordination among them is difficult.

The final classification is distributed control. The architecture of this control is highly similar to that of the decentralized controllers. Each converter has its own controller that acts based on local measurements. The differentiating factor is that in this case, the controllers communicate with each other, usually via a low-bandwidth network. Thanks to the information exchange among the converters, the system can improve its performance in terms of load sharing and voltage. Should there be a problem with the communication network, the system would simply become a decentralized controller.

3.2 Control schemes classification based on their response time

Another possible classification for the different control methods is based on their response time. This method of classification is called hierarchical control. Hierarchical control consists of multiple levels, as shown in Fig. 3.3. Each level of hierarchical control operates on a different time scale and control bandwidth, with distinct roles and objectives. One important characteristic is that each level supervises the lower levels. Because of this interaction among levels, the control is managed so that commands from the upper levels have a minimal impact on the stability and performance of the lower levels [67]. Hierarchical control is divided into four different levels:

Inner control loop (Level 0) This is the lowest level in the architecture. It concerns the inner voltage and current control loops that ensure the regulation of the output voltage and current of a converter.

Primary control (Level 1) Ensures that the local voltage and current are close to the nominal values or stability requirements. It also ensures the distribution of the loads among the different units, also referred to as power/load sharing.

Secondary control (Level 2) Focuses on the compensation of steady-state voltage deviations from the nominal values of the network. It can also control the connection and disconnection of the microgrid to the main grid.

Tertiary control (Level 3) It regulates the power exchange between the microgrid and the main grid. In both islanded and connected DC microgrids, it can be used to optimize operating costs, balance energy storage, or reduce losses.Additionally, it can be used to achieve further financial goals or other objectives, such as minimizing CO2 emissions.

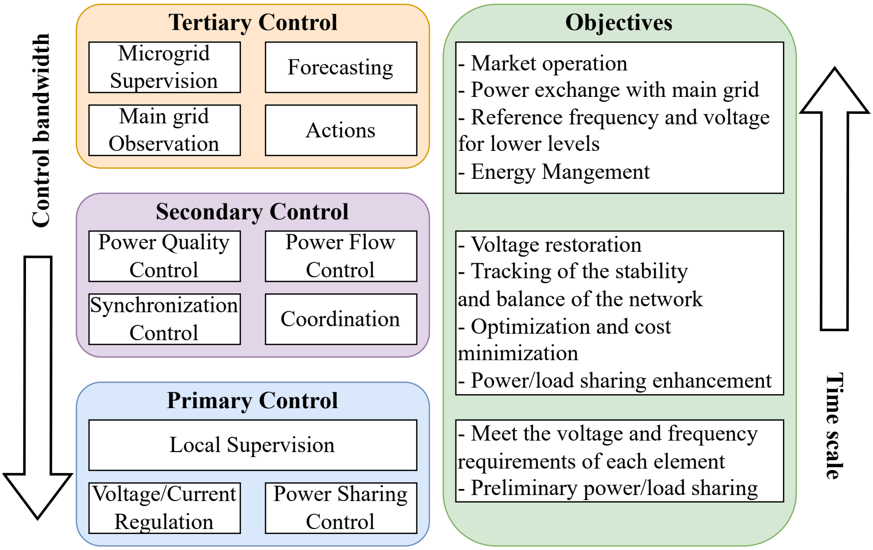

Figure 3.3: Hierarchical control architecture and objectives [68]–[70]

In the context of this thesis, the controls up to the secondary layer are considered. Due to the time scale and complexity of tertiary control, it is considered out of scope for this work. Indeed, tertiary control usually involves complex optimization problems that merits its own study.

3.3 First level control

The first level control methods that ensure proper voltage/current regulation and basic load sharing are discussed in this section. A general overview of the existing primary control methods is given in Fig. 3.4.

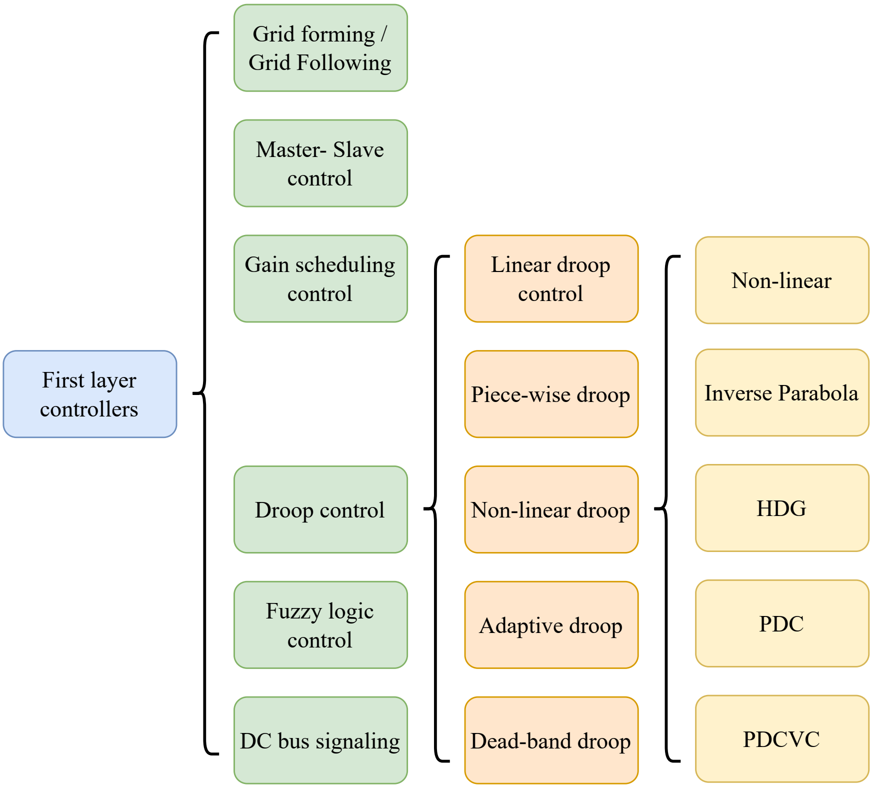

Figure 3.4: General overview of first layer controllers [68], [71]

Table 3.1 provides an overview of the first-level controls that will be analyzed in the following section. The controllers are compared in terms of their ability to share a load, regulate the DC microgrid voltage, reliability, and the need for communication for their implementation. Reliability reffers to the ability of the control scheme to continue normal operation if one or multiple converters are disconnected or lost.

Table 3.1: Comparison of first level control methods

Control	**Load sharing**	**Voltage regulation**	**Reliability**	**Communication required**
Droop	✓	✓	✓	✗
Non-linear droop	✓	✓	✓	✗
Piecewise droop	✓	✓	✓	✗
Master-slave	✓	✓	✗	✓
Grid forming and grid following	✗	✓	✗	✗

3.3.1 Droop control

Droop control is one of the most implemented control schemes due to its modularity and ease of implementation. It is a method widely used in AC microgrids as well. The droop control consists of implementing a so-called "virtual resistance", which is referred to as the droop parameter. Droop control consist in reducing or increasing the reference output voltage of the converter proportionally to the output current. The droop control is implemented as:

$$V_{DC} = V_{DC}^{*} - R_d I_o \tag{3.1}$$

The measured output current I_o is multiplied by the virtual resistance (droop parameter R_d). The resulting voltage is then subtracted from the reference or nominal voltage V_{DC}^{*}. This control process is shown in Fig. 3.5.

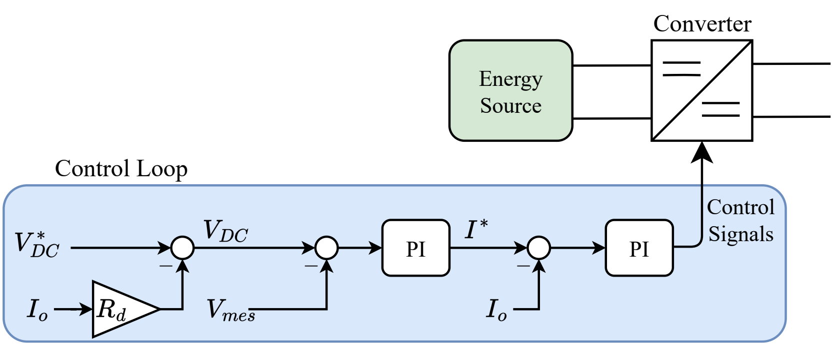

Figure 3.5: Droop control implementation

By appropriately choosing the value of R_d for each converter, the load distribution among them can be ensured. The droop parameter R_d defines the slope of the V-I curve of the different converters. The droop parameter can be calculated as shown in (3.2). It is obtained by dividing the maximum allowed voltage deviation by the maximum output current of the converter. A graphical representation of the droop control is shown in Fig. 3.6. The converter with the steepest slope will have a low output current. In contrast, the converter with the shallowest slope will have a higher output current for a smaller voltage deviation.

$$R_d = \frac{\Delta V}{Io_{max}} \tag{3.2}$$

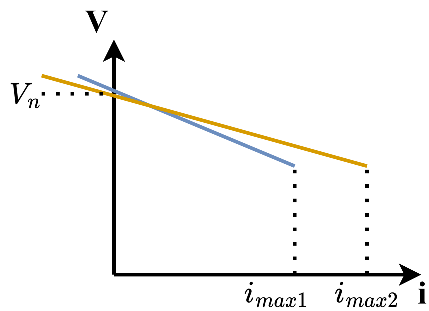

Figure 3.6: Droop control load sharing

The droop control can be implemented as Current-Voltage, Power-Voltage, Voltage-Current, or Voltage-Power control. In the I-V and P-V controls, the voltage is measured, and the current/power injection is regulated based on the voltage. In the V-I/V-P control schemes, the current/power is measured, and the voltage is adjusted accordingly [68].

If the V-I/P scheme is used, it is equivalent to controlling the converter in voltage mode. The reference voltage is calculated as it was shown in (3.1). The current control mode corresponds to the I/P-V control scheme. In these cases, the reference current is given by:

$$I_o = \frac{V_{DC}^{*} - V_{DC}}{R_d} \tag{3.3}$$

One final disadvantage of droop control is that there is an inherent tradeoff between voltage regulation and power sharing. This tradeoff is illustrated in Fig. 3.7. If a small droop parameter (the allowed voltage deviation is small) is used, the voltage regulation will be good. However, the load sharing will be affected as the shallow slope leads to greater differences in power injection. On the other hand, with a large droop parameter (a bigger voltage deviation is allowed), the load sharing is more accurate, but the voltage will suffer from larger deviations [28], [68].

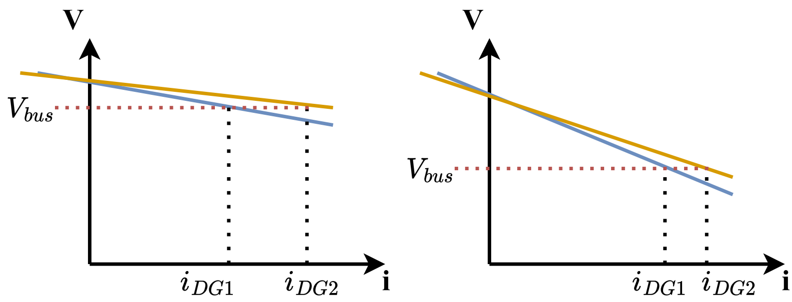

Figure 3.7: Droop control tradeoff

While this inherent tradeoff exists, there are two factors that can affect the load sharing accuracy: voltage sensing error and different line resistances [72], [73]. Errors in the measured voltage will result in different operating points of the V-I droop curve. On the other hand, the impact of resistance can be analyzed as follows. To analyze the impact of line resistances on the load sharing, the circuit shown in Fig. 3.8 is considered.

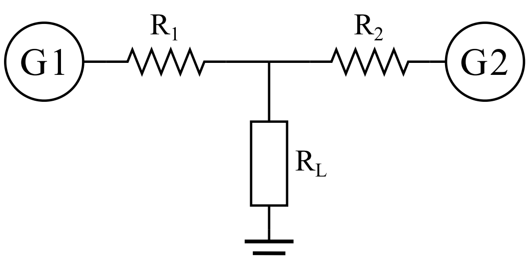

Figure 3.8: Two sources feeding a load

Here, two sources feed a single load. Each source is connected to the load via a line with resistance R_1 and R_2. Ideally, both sources will provide the same amount of current and split the load equally. By applying Kirchhoff's laws to the circuit shown, the following expressions for the currents can be obtained [74]:

$$I_1 = \frac{R_L(V_1 - V_2) + V_1 R_2}{R_L R_1 + R_L R_2 + R_1 R_2} \tag{3.4}$$

$$I_2 = \frac{R_L(V_2 - V_1) + V_2 R_1}{R_L R_1 + R_L R_2 + R_1 R_2} \tag{3.5}$$

Where I_x corresponds to the current given by each source, R_1 and R_2 are the line resistances, and R_L is the load resistance. The difference in load sharing is then calculated as:

$$\Delta I = I_1 - I_2 = \frac{2(V_1 - V_2)}{R_1 + R_2 + \frac{R_1 R_2}{R_L}} + \frac{V_1 R_2 - V_2 R_1}{R_L R_1 + R_L R_2 + R_1 R_2} \tag{3.6}$$

In (3.6), it is seen that one part of the load sharing difference is directly linked to the voltage sensing error, while the second part is more directly related to the difference in line resistance. The load sharing difference can be expressed through the current-sharing error eI:

$$eI = \left| \frac{\Delta I}{I_1 + I_2} \right| \times 100 \tag{3.7}$$

If a droop control is added to the sources, the circuit becomes as shown in Fig. 3.9. The line resistance is the sum of the actual line resistance and the droop resistance. This total resistance can be expressed as $R_{T1} = R_{d1} + R_1$. Considering the droop resistances R_{d1} and R_{d2}, equations (3.4) and (3.5) become:

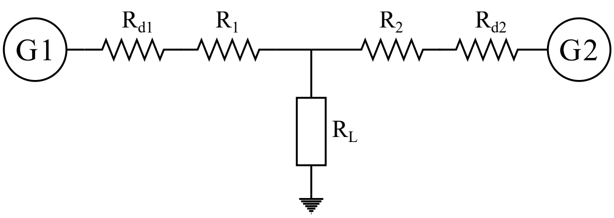

Figure 3.9: Two sources feeding a load with droop control

$$I_1 = \frac{R_L(V_1 - V_2) + V_1 R_{T2}}{R_L R_{T1} + R_L R_{T2} + R_{T1} R_{T2}} \tag{3.8}$$

$$I_2 = \frac{R_L(V_2 - V_1) + V_2 R_{T1}}{R_L R_{T1} + R_L R_{T2} + R_{T1} R_{T2}} \tag{3.9}$$

The difference in current is calculated once again, neglecting the voltage sensing error, in (3.10). In this equation it can be seen that by adding even a small droop resistance, the load sharing error will be reduced. This is thus the interest and advantage of this controller.

$$\Delta I = I_1 - I_2 = \frac{V_1 R_{T2} - V_2 R_{T1}}{R_L R_{T1} + R_L R_{T2} + R_{T1} R_{T2}} \tag{3.10}$$

This point is further illustrated in Fig. 3.10. The previous circuit with two sources is considered. The length of line 2, L_2 (R_2), is fixed at 500m. On the other hand, the length of line 1 L_1 (R_1) is changed from zero up to 5 km. The line considered has a resistance of 0.194 Ω/km. The current sharing error is calculated at different points with and without droop control. Two cases are considered for the droop control: one that allows a 2% voltage deviation and another that allows a 5% voltage deviation at the output of the converter. The difference between these two is that the equivalent resistance provided by each control is different. The bigger the voltage deviation allowed, the higher the resistance provided by the droop control.

When L_1 has a length of 0 meters, it is equivalent to having the load connected directly to the source. In this situation, it can be seen that the current sharing error is equal to 100%. This means that the entire load is provided by the source $G1$. However, if droop control is implemented, it can be seen that the amount of current sharing error is reduced. As the 5% droop provides a greater resistance, it reduces the current sharing error more than the 2% version. As the length of L_1 increases, it approaches the length of L_2, and thus the amount of current sharing error is reduced. At 500m, the line lengths are the same, and thus the error is reduced to zero. After this point, the length of L_1 continues to increase beyond the length of L_2. Consequently, the error progressively increases. Even though the error increases, the amount of current sharing error is always less when using droop control. Thus, the interest of implementing droop control is highlighted.

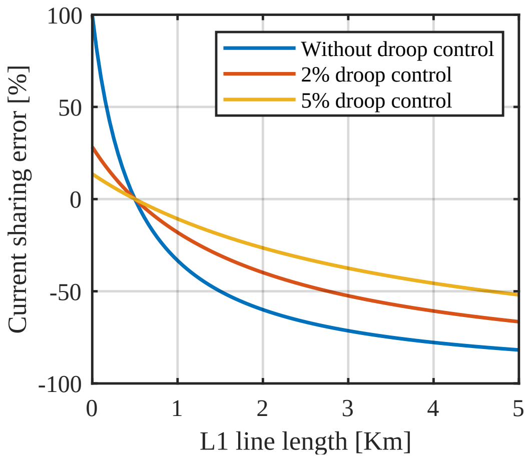

Figure 3.10: Current sharing error as a function of the length of line L_1

Knowing that line resistance can significantly affect load sharing accuracy, is it possible to account for it in the design of a DC microgrid?

It might be desirable to choose the droop resistance in order to limit the current sharing error. While it is possible to develop the mathematical equations as previously shown, for multiple nodes and case scenarios, this is not a practical approach. A better-suited tool is to use a power flow program to systematically test different case scenarios. The developed linear DC power flow (explored in the next chapter) is used to test how to limit the current sharing error. As shown in Fig. 3.11, there are five different positions where loads might be connected. Through the power flow program, the load position that causes the most current sharing error can be identified.

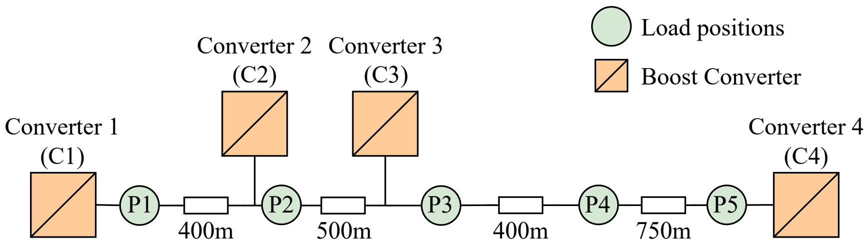

Figure 3.11: Possible positions for loads on test microgrid

In order to define the current sharing error for multiple converters, a metric had to be established. The current sharing error ϵic_n for a converter n is defined as the deviation of its output current with respect to the average current provided by all the converters, as shown in (3.11). Using this metric, the worst-case scenario was identified. Using loads of 40 kW, it was found that multiple loads force droop controlled converters to provide more current, thus reducing the current sharing error. The highest amount of current sharing error was found when a single load was present.

$$\epsilon ic_n = (1 - \frac{ic_n}{ic_{avg}}) \times 100 \tag{3.11}$$

The power flow program calculated the current supplied by each converter when a single 40 kW load was at the different positions shown in Fig. 3.11. The converter currents obtained in each case are shown in Fig. 3.12. Notice that when the load is connected next to a converter, the adjacent converter provides more current even though it is droop controlled. Fig. 3.13 shows the current sharing error for each converter. As expected, the converter that provides the most current in each case has the highest current sharing error, as it deviates the most from the average current.

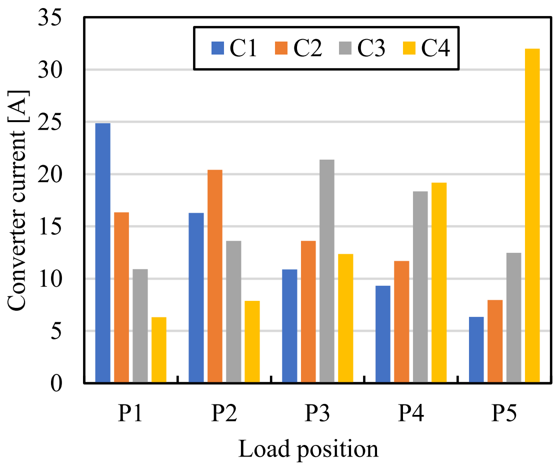

Figure 3.12: Output current of each converter according to the position of the load

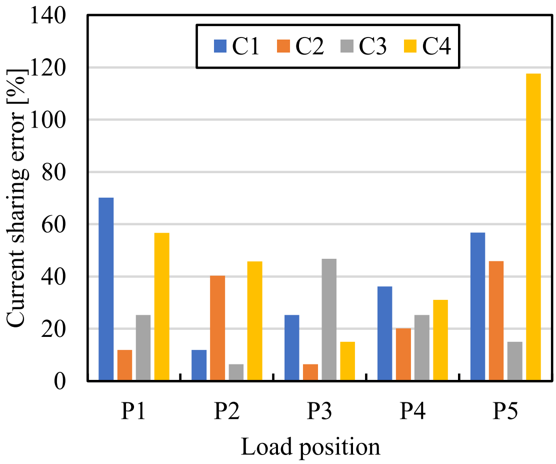

Figure 3.13: Current sharing errror for each converter in function of the load position

Among the different load positions, it is observed that P5 is the worst case in terms of current sharing. Indeed, the significant line distance and thus line resistance that separates C4 and the load from the rest of the grid significantly impacts the load sharing. The other converters supply less current, and thus C4 provides more than expected. To limit the current sharing error in the worst-case scenario, the power flow program is used to test several droop resistances with the load at position P5. Allowing a larger voltage deviation improves the load sharing as the resulting droop resistance is higher. Fig. 3.14 shows the obtained current sharing error for converter C4 when all the converters operate with different droop resistances. The initial case is a droop control allowing a 5% voltage deviation. The allowed voltage deviation is increased up to a 24% voltage deviation. It is shown that this approach successfully reduces the current sharing error. However, the current sharing value remains high. Furthermore, in most cases, a 25% voltage deviation might not be acceptable. Thus, it is of interest to explore other alternatives to improve the load sharing.

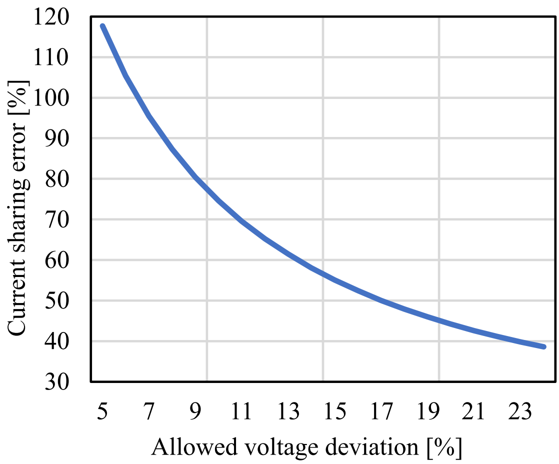

Figure 3.14: Resulting current sharing error according to the allowed voltage deviation

The main inconvenience of droop control is that the line resistances can affect the load sharing. A higher droop resistance can reduce the effect of line resistances, but can lead to significant voltage deviations. To further improve the benefits of droop control, more complex implementations of it have been developed. In [75], an adaptive droop control is proposed. In this implementation, the droop parameter value changes as a function of the state of charge of the batteries to which the converter is coupled. In [72], a non-linear droop slope is proposed. By considering a non-linear characteristic, better voltage regulation and load sharing can be achieved. Non-linear droop controls are described hereafter.

3.3.2 Non-linear droop control

To overcome this tradeoff and improve the performance of linear droop control, non-linear droop controls were proposed. While the starting and endpoint of the linear droop curve are kept the same, the path that connects the two of them is modified. The implementation of the control remains the same as linear droop control, as shown in Fig. 3.15, but how the offset added to the reference voltage is generated is changed.

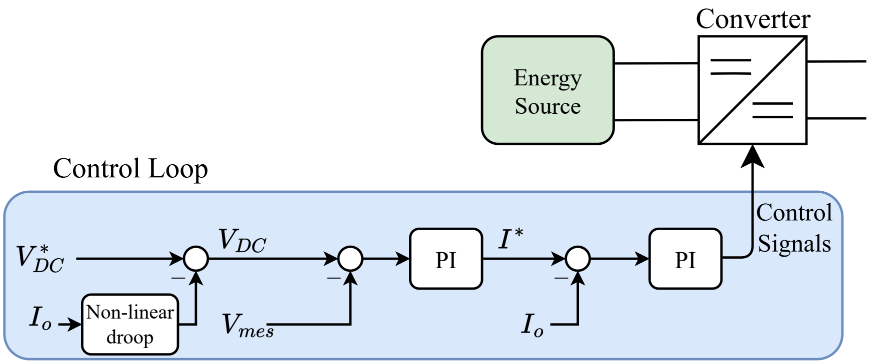

Figure 3.15: Nonlinear droop control implementation

In [72], [73], various non-linear droop controls are proposed. The general expression is given by (3.12). Here, the shape of the curve depends on two additional parameters m and n, which can have non-integer values. Examples of the possible curves, as shown in Fig. 3.16, are parabola ($m = 1$, $n = 2$), inverse parabola ($m = 2$, $n = 1$), and ellipse ($m = 2$, $n = 2$). A simpler expression can be obtained when $m = 1$ as shown in (3.13).

$$V_{p.u} = 1 - \Delta V_{p.u}\left(1 - \sqrt[m]{1 - (i_{p.u})^n}\right) \tag{3.12}$$

$$V_{p.u} = 1 - \Delta V_{p.u}(i_{p.u})^n \tag{3.13}$$

In the case of (3.13), the droop resistance can be described by (3.14). It is seen that the full-load droop resistance is n times higher than linear droop[72]. Finally, if m and n are set equal to 1, the expression becomes the equation for linear droop control.

$$R_{d\,p.u} = n\Delta V_{p.u}(i_{p.u})^{n-1} \tag{3.14}$$

In [74], a High Droop Gain (HDG) control was proposed. Here, two V-I curves are considered, and the curve with the highest droop resistance is selected. This method ensures having a high resistance value under light load conditions and a higher resistance under heavy load. This results in better voltage and load sharing performance. In this case, the two considered droop curves are the linear and parabola droop.

Fig. 3.16 shows the voltage curve for each of the previously described methods. Similarly, Fig. 3.17 illustrates the droop resistance provided by each control method, which can be obtained by taking the derivative of the voltage equations. It is important to note that HDG control changes its slope at an output current of 0.5 p.u. To better understand HDG control, one can look at the droop resistances shown in Fig. 3.17. HDG follows either the linear droop or the parabola droop voltage curve, as seen in Fig. 3.16. It follows the curve that provides the highest resistance. Thus, it can be seen that before an output current of 0.5 p.u, the linear droop provides the highest resistance. At 0.5 p.u, the parabola control resistance is higher, and thus, the voltage curve of the HDG control starts following that of parabola droop.

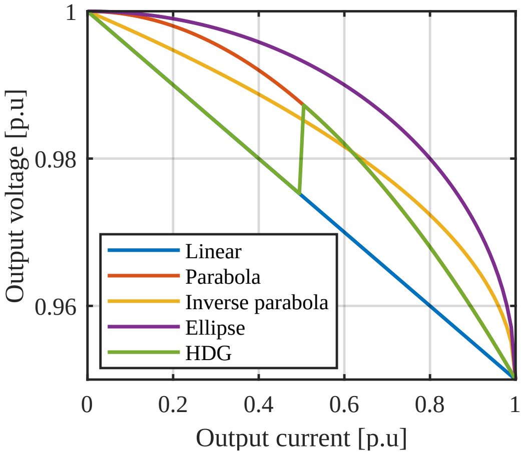

Figure 3.16: Linear and non-linear droop control voltage curves

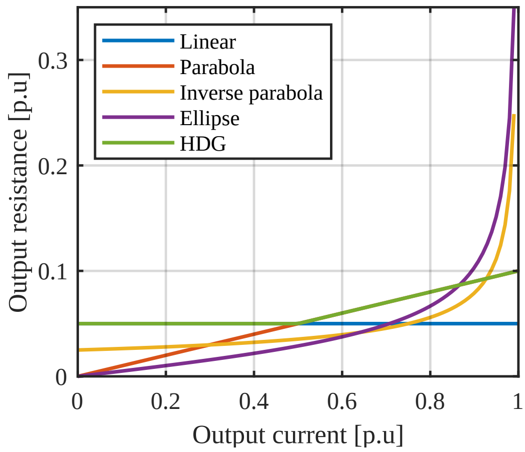

Figure 3.17: Linear and non-linear droop control output droop resistance

3.3.3 Piecewise droop control

Piecewise droop control is a control strategy that falls between linear control and the non-linear control. It consists of dividing the droop slope into different segments. Each segment is designed so that a low droop value is applied with light loads and high droop values are applied with heavy loads [76]. This control methods seeks to mitigate the tradeoff between voltage regulation and load sharing. Thus, better voltage regulation is provided under light load conditions, while improved load sharing is achieved under heavy load conditions [77]. Implementations of this type of controller can also be found in [78], [79]. Examples of piecewise droop curves are illustrated in Fig. 3.18.

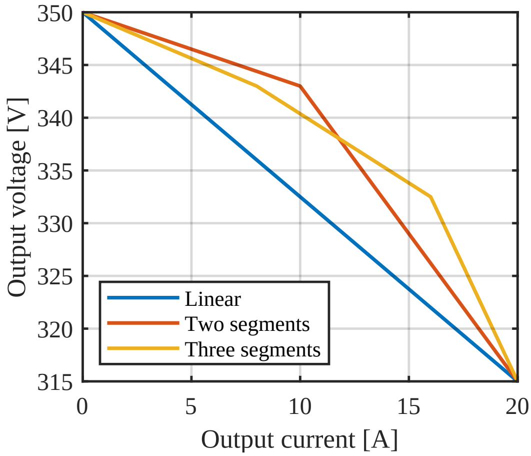

Figure 3.18: Examples of piecewise linear droop curves

Based on the works of [76]–[79], the author proposes the following implementation of this control. For a three-segment droop, it is desired for each segment to have a droop resistance R_{d1}, R_{d2}, and R_{d3}. The droop parameter is calculated as shown in (3.15). ΔV_i is the desired voltage deviation for each segment, and I_{seg_i} is the maximum output current for each segment.

$$R_{di} = \frac{\Delta V_i}{I_{seg_i}} \tag{3.15}$$

During the first section of the curve, the droop curve is imposed by the classic droop equation as shown in (3.16), as long as $I_o \leq I_{seg1}$. Once I_o surpasses the current of the first segment, the droop equation becomes as shown in (3.17), as long as $I_{seg1} \leq I_o \leq I_{seg2}$.

$$V_{DC} = V_{DC}^{*} - R_{d1}\, I_o \tag{3.16}$$

$$V_{DC} = V_{DC}^{*} - R_{d1}\, I_o - (R_{d2} - R_{d1})(I_o - I_{seg1}) \tag{3.17}$$

The rightmost term consists of the difference of droop resistances. This difference is equivalent to adding the resistances necessary so that the total droop resistance equals R_{d2}. The difference between I_o and I_{seg1} ensures that this additional term contributes only after surpassing the current of the first segment. The same logic applies to the last segment, as shown in (3.18), which is valid for $I_o \geq I_{seg2}$.

$$V_{DC} = V_{DC}^* - R_{d1}\, I_o - (R_{d2} - R_{d1})(I_o - I_{seg1}) - (R_{d3} - R_{d2})(I_o - I_{seg1} - I_{seg2}) \quad (3.18)$$

The implementation of the controller remains similar to the implementation of the nonlinear controller shown in Fig. 3.15. The only change is the equation that is implemented to generate the offset added to the reference voltage. This equation can be implemented as shown in Fig. 3.19. Here, ΔR_d represents the difference between the droops described in the previously mentioned equations. Additionally, instead of using a switch, saturations that implement a zero lower bound were implemented in order to avoid oscillations due to switching between cases.

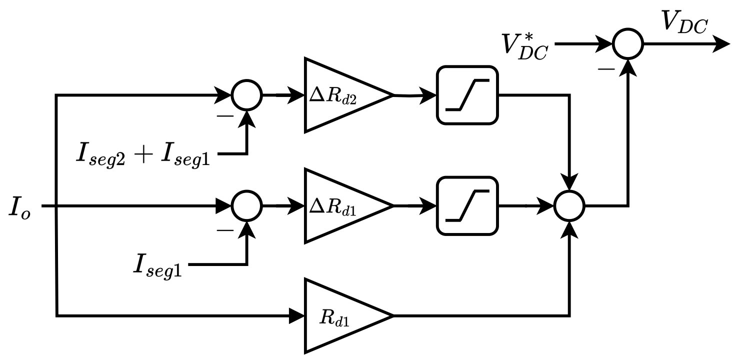

Figure 3.19: Implementation of piecewise segment equations

While the advantage of this method is being able to select the desired slopes for different points, this method still has some disadvantages. Mainly, different converters can find themselves at different parts of the slope and thus have different droop resistances. Furthermore, if switching is used to change the slope, this can lead to fluctuations and instabilities around the switching point. This can be alleviated via the introduction of hysteresis [72].

3.3.4 Master-slave control

In Master-slave control, there is a single unit that acts as the master. The master provides the reference current for the rest of the converters. The master acts as a Voltage source inverter (VSI), and the slaves act as Current source inverters (CSI). An implementation of this controller is shown in Fig. 3.20. This method requires communication between the different converters. It is indeed a centralized type of controller and thus has a single point of failure. If the master fails, the rest of the converters are not given a command.

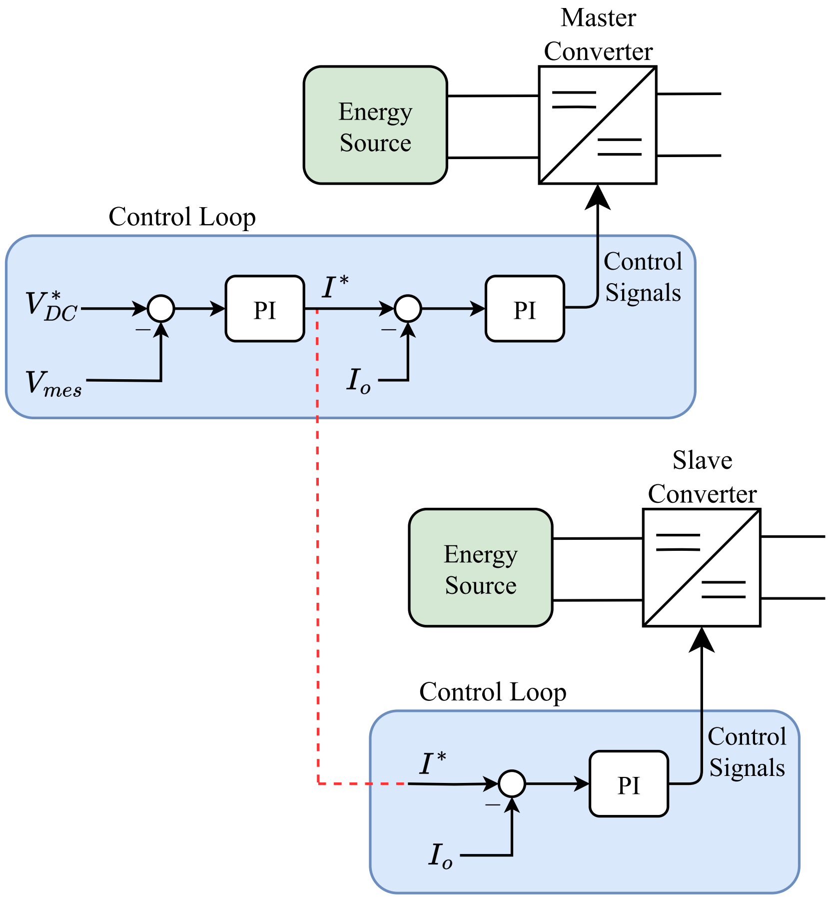

Figure 3.20: Master-Slave control implementation

Depending on the role of the master, the control can be categorized as [28], [80]:

- Dedicated: The master is fixed.
- Rotary: The master is arbitrarily chosen.
- High-crest current: The converter with the highest current is chosen as the master.

3.3.5 Grid Forming and Grid Following control

Another method of controlling the converters in a DC microgrid is by considering them either as Grid Forming or Grid Following units. The Grid Forming units act as voltage sources that have the role of imposing the line voltage. They inject or absorb power to maintain the voltage at the nominal value. Grid Following converters focus only on injecting the reference current they are given. This reference current is arbitrary and is not provided by a central controller. Fig. 3.21 shows the control implementation of a Grid Forming converter and Fig. 3.22 shows the implementation of a Grid Following converter.

This type of control is the simplest one as it does not require communication among the converters or the definition of external parameters. However, it requires that the Grid Forming converter has enough power capacity to sustain the microgrid voltage. Additionally, the lack of coordination among the converters can lead to non-optimal operation.

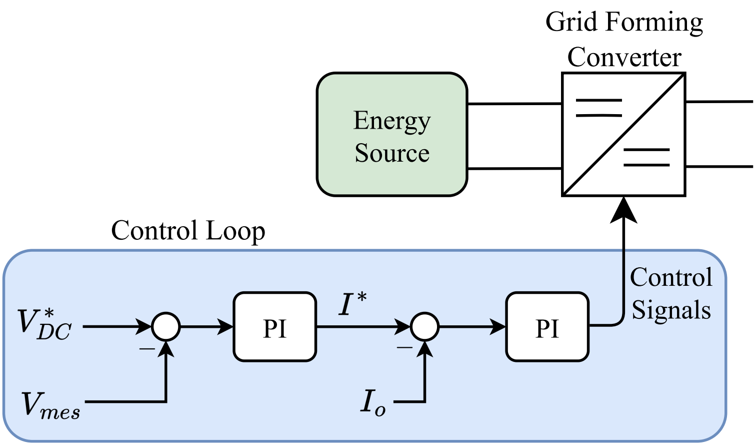

Figure 3.21: Grid Forming converter control implementation

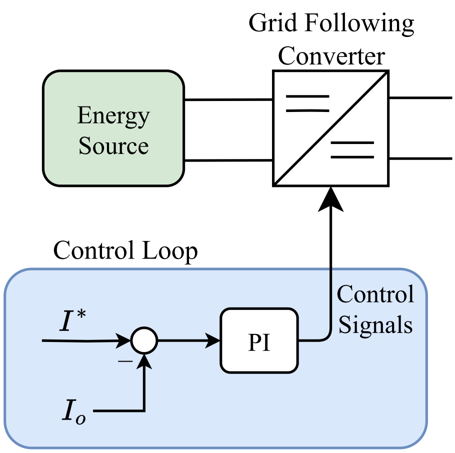

Figure 3.22: Grid Following converter control implementation

3.4 Second level control

The second level controls have a larger time scale than the primary control. The main objective of adding these control loops to the primary level is to improve power quality and load sharing. A general overview of the controllers found by the author is given in Fig. 3.23.

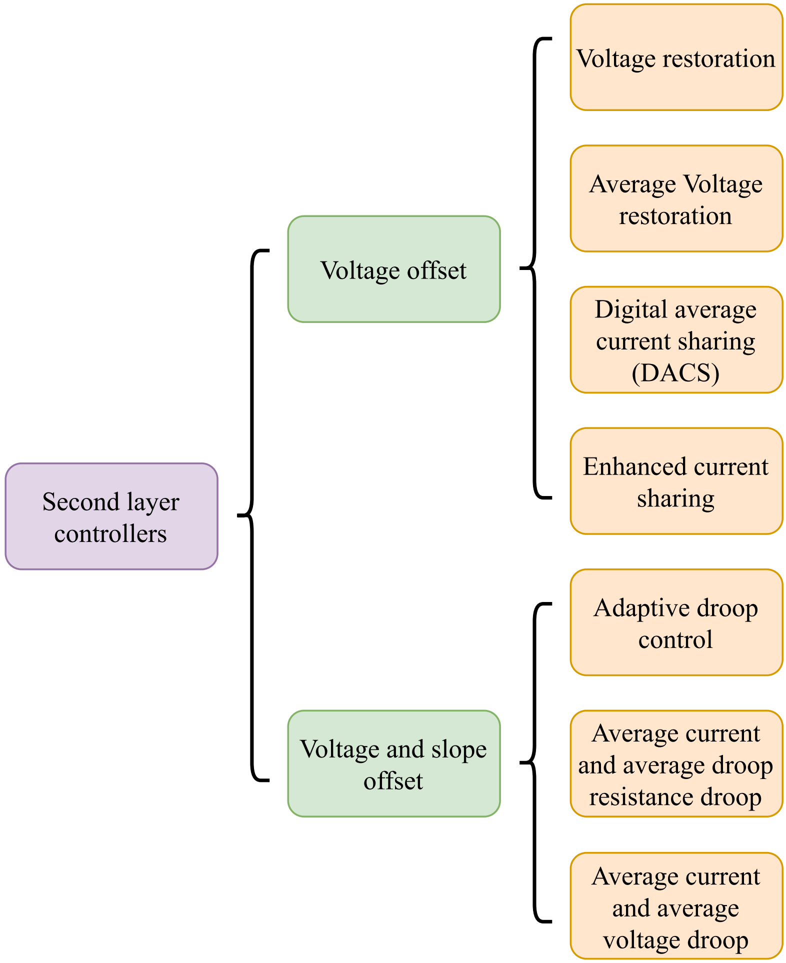

Figure 3.23: General overview of second layer controllers

The different controllers will be developed in this section. The methods are highly similar, and thus to distinguish them more easily, the proposed benefits of each control method have been summarized in Table 3.2. Furthermore, Table 3.3 compares them. In table 3.3, it is highlighted if the controller improves only the voltage regulation or the load sharing aswell. Additionally, how this improvement is achieved is also compared. As shown in Fig. 3.23, the second level control can add a voltage offset or an offset to both the voltage and the droop resistance. As an additional point, it is noteworthy that some of the controllers presented lack designated names within their respective papers. Consequently, the author exercised discretion in assigning titles to these controllers based on the actions implemented by each.

Table 3.2: Proposed benefits of secondary control methods

Second level control	**Benefit**
Voltage restoration [67]	Solves the problem of voltage deviation due to droop control. The voltage at a single point is improved. It can be used to connect the microgrid to a stiff source.
Average voltage restoration	Instead of improving the voltage for a single point, the overall voltage deviations in the DC microgrid are reduced.
DACS [81]	Helps obtain a voltage closer to nominal value while reducing the noise that could be found in the non digital version.
Average current and voltage control[82]	It improves both voltage regulation and uses the average current to improve load sharing.
Adaptive droop control[83], [84]	It uses an impedance correction term to adjust the droop term and provide proportional load sharing. Equally, the average voltage is used to improve the voltage regulation.
Average current and droop control [85]	Provides an enhanced dynamic performance under fast-changing loads through the added droop resistance control loop
Average current and voltage droop control [86], [87]	Droop resistance can be changed based on deviations from the output current or changes in the average DC bus voltage.

Table 3.3: Comparison of secondary control methods

Second level control	Improved load sharing	Improved voltage regulation	Voltage offset	Slope offset
Voltage restoration [67]	✗	✓	✓	✗
Average voltage restoration	✗	✓	✓	✗
DACS [81]	✗	✓	✓	✗
Average current and voltage control[82]	✓	✓	✓	✗
Adaptive droop control[83], [84]	✓	✓	✓	✓
Average current and average "'droop resistance" droop control [85]	✓	✓	✓	✓
Average current and average voltage droop control [86], [87]	✓	✓	✓	✓

3.4.1 Voltage restoration

Voltage restoration control is a centralized control method that uses low-bandwidth communication to send information to the converters. As previously discussed, the use of droop control can lead to steady-state voltage deviations from the nominal value. To compensate for this deviation, an upward voltage shift is performed by the second level controller. The voltage level at a specific or pilot node is compared to the reference value. The resulting error is then fed to a PI controller. The resulting compensation signal δV_o is then added to the reference voltage [67]:

$$V_{DC} = V_{DC}^{*} - R_d I_o + \delta V_o \tag{3.19}$$

The advantage of this method is that it can be easily implemented via a single PI controller and a single voltage measurement. However, the voltage shift will approach the voltage to its nominal value at the measuring point. The rest of the grid can perceive an improvement, but not to the same extent. Thus, it can be recommended to use the voltage measurement of a key point such as the Point of common coupling. Another possibility is to use an averaged voltage to generate δV. An implementation of this second level control is shown in Fig. 3.24.

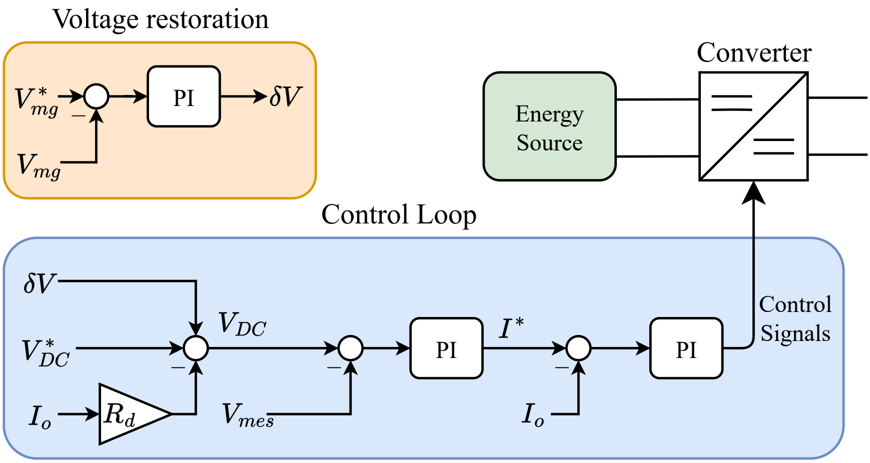

Figure 3.24: Voltage restoration control implementation

3.4.2 Average voltage restoration

While this control method is not directly referred to in a text, it is partially used in the remaining second level controllers. The main disadvantage of voltage restoration control is having to improve the voltage at a single point. To improve the voltage uniformly, it is proposed to use the average voltage in the microgrid $\overline{V_{mg}}$ instead of the voltage at a single node. The converters all send the grid voltage measured locally. Then, a controller calculates the average and utilizes it to generate the voltage compensation signal δV_o. The implementation of this controller is shown in Fig. 3.25. The main drawback of this method is its higher communication requirement. Furthermore, although the voltage is improved on average, this does not prevent voltages from deviating above or below the reference value.

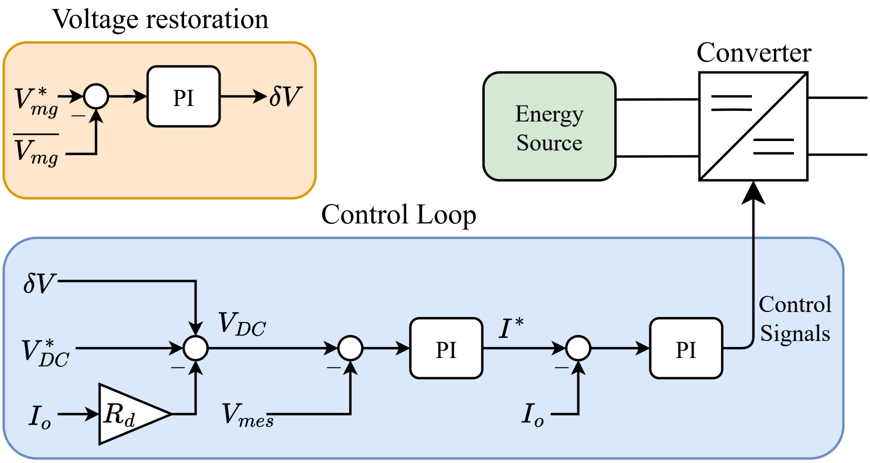

Figure 3.25: Average voltage restoration control implementation

3.4.3 Digital average current sharing

This method is based on Average Current Sharing (ACS) control. In ACS, a resistance is used to turn the output current into a voltage signal for each converter. However, this is a physical implementation that can be sensitive to noise [81], [88]. To address this inconvenience, the Digital Average Current Sharing (DACS) control was proposed. Instead of measuring the voltage through a physical line, the current of all the converters is digitally averaged. Using this average current, the controller adds an offset to the droop control of all the converters. This results in a shift that aligns the reference voltage of the converters towards the nominal value while keeping the load sharing. This offset can be described as:

$$V_{DC} = V^*_{DC} - R_d I_o + \Delta V \tag{3.20}$$

The voltage shift is defined by ΔV. It is obtained by first collecting and averaging the different output currents of the converters as in (3.21). Then, ΔV for a converter j can be calculated as shown in (3.22).

$$i_{avg} = \frac{\sum_{m=1}^{n} i_m}{n} \tag{3.21}$$

$$\Delta V_j = k_j i_{avg} i_j^{rated} \tag{3.22}$$

In (3.22), k_j represents the shift gain. When selecting the value of k_j, the following is considered: ΔV should be close to the maximum deviation caused by the droop control. This is to ensure that the shift compensates accordingly. To maintain load sharing, the product of the shift gain and the rated current of each converter should be consistent across all converters. Additionally, for stable operation, the shift gain should be smaller than the droop gain. Fig. 3.26 shows the described implementation of the second layer control.

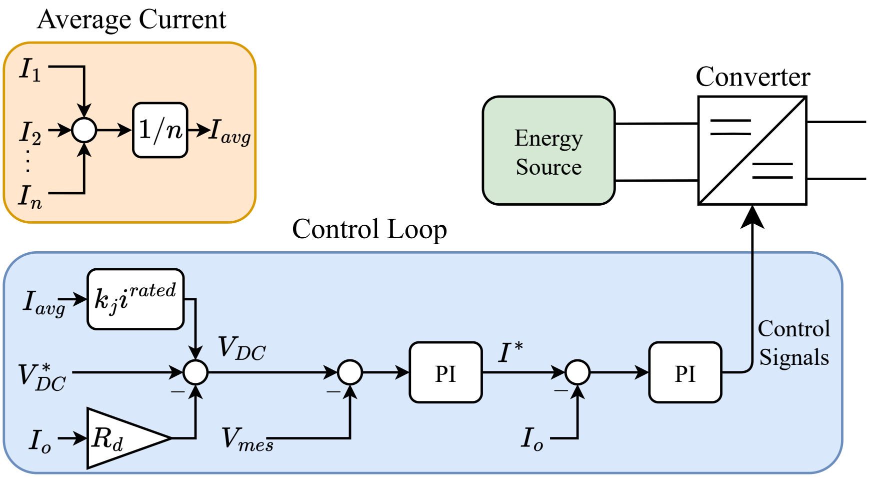

Figure 3.26: DACS control implementation

3.4.4 Average current and average voltage control

This second level controller has been proposed in [82]. It seeks to overcome the voltage and current sharing degradation that usually affect droop control. Thus, current sharing and voltage regulation are both improved via this method. Like in previous controllers, the voltage of the microgrid is measured, and a voltage offset δV is generated based on the microgrid voltage deviation. Here, a second offset is generated by comparing the converter current to the average current of all the converters. The resulting offset δi improves the load sharing. The equation describing this controller is shown in (3.23). Note that the output currents used by the second level controller can be divided by a factor k to impose current sharing proportions if needed. The implementation of this controller is shown in Fig. 3.27.

$$V_{DC} = V_{DC}^{*} - R_d I_o + \delta V + \delta i \tag{3.23}$$

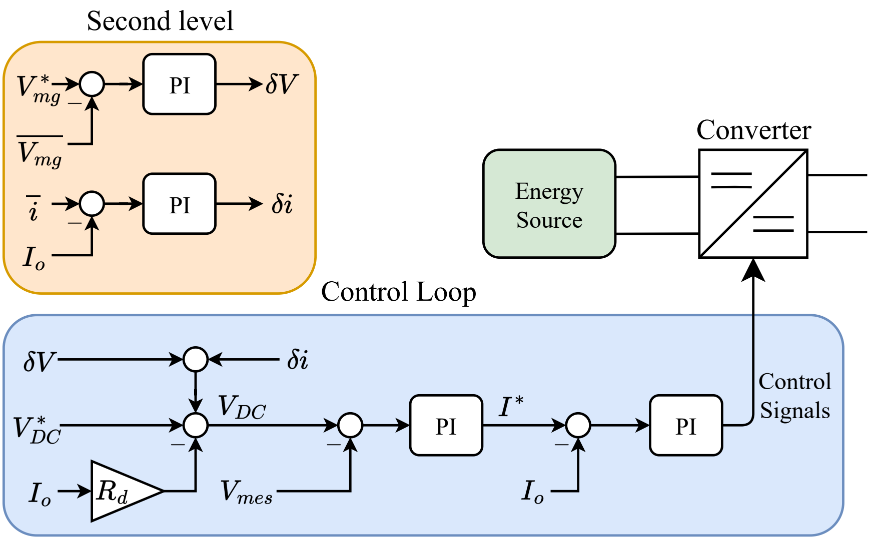

Figure 3.27: Average current and average voltage control implementation

3.4.5 Adaptive droop control

The second layer adaptive droop control is the first controller that proposes modifying the droop resistance. In [83], [84], the local converter current is compared to the average converter current. Here, the current utilized is the current in per unit, which is proportional to the nominal current of each converter. Unlike the previous controller, the offset generated by the current controller δr is subtracted from the droop resistance as shown in (3.24). The generated offset is subtracted from the droop resistance so that if the output current is below the average, a smaller droop resistance will cause the converter to provide more current. In the opposite case, if the current provided is above the average, a greater droop resistance will cause the converter to output less current. The resulting modifications to the virtual impedance ensure proportional load sharing. As in previous control methods, the voltage offset δV improves the voltage regulation in the DC microgrid. The implementation of this controller is shown in Fig. 3.28.

$$V_{DC} = V_{DC}^{*} - (R_d - \delta r)I_o + \delta V \quad (3.24)$$

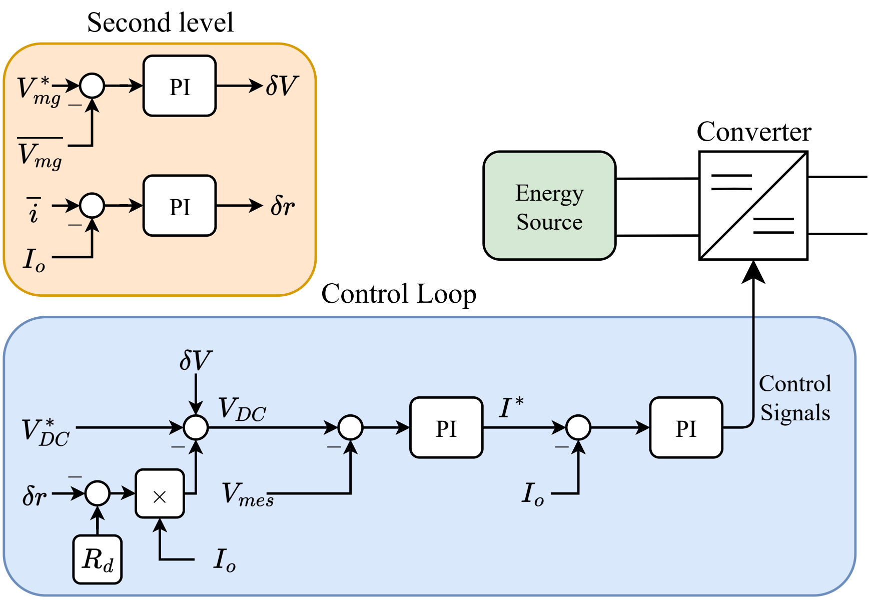

Figure 3.28: Adaptive droop control implementation

3.4.6 Average current and average "droop resistance" droop control

Proposed in [85], this controller also modifies the droop slope to improve load sharing. As in the previous controller, two offsets are implemented: a voltage offset δV and a droop offset δr. The key difference in this controller is that the droop offset δr is the result of two controller outputs. One controller regulates output current based on the averaged current, and the other controller regulates based on the droop resistance and the average droop resistance. This choice is justified by the fact that if only the average current is used, multiple combinations of droop resistances can be achieved, wich can significantly differ from the initial value. To avoid this, the additional controller based on the average droop resistance is implemented. This additional controller adds an additional constraint that limits the droop values. The proposed controller is described by (3.25), and δr is described by (3.26) where G_{pir} and G_{pic} are the PI controllers for the droop resistance and average current respectively. The implementation of this controller is depicted in Fig. 3.29.

$$V_{DC} = V_{DC}^{*} - (R_d - \delta r)I_o + \delta V \tag{3.25}$$

$$\delta r = G_{pir}(R_d - \bar{R}_d) - G_{pic}(\bar{i} - I_{mes}) \tag{3.26}$$

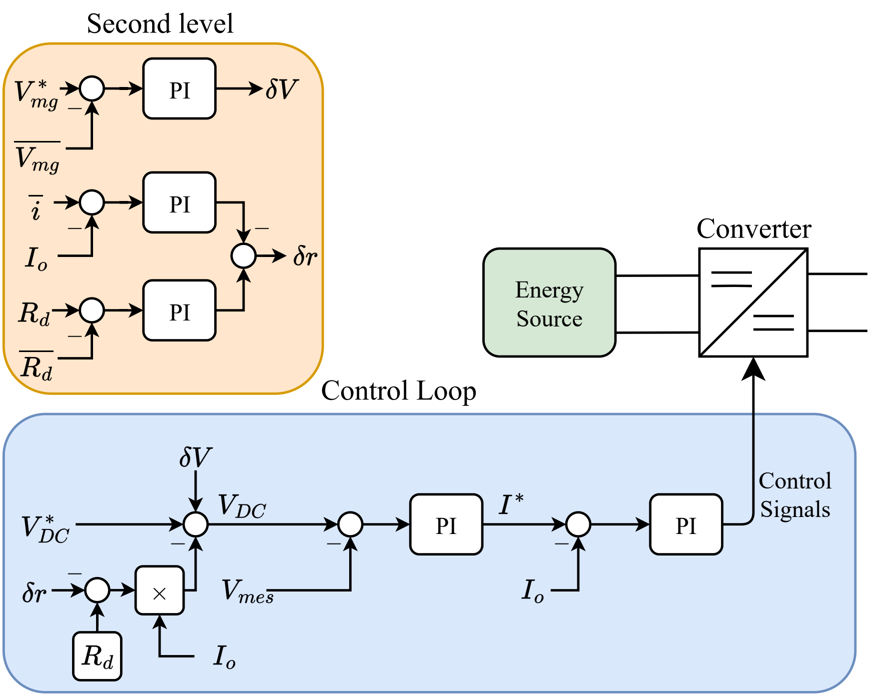

Figure 3.29: Average current and average “droop resistance” droop control implementation

3.4.7 Average current and average voltage droop control

The final controller has been proposed in [86], [87]. In this controller, two offset terms are generated δV and δr. While δV is generated as in the previous controllers, δr is generated through an average current controller and the voltage offset δV. Thus, δr is obtained through the following equation:

$$\delta r = -\delta V/V^* - G_{pic}(\bar{i} - I_{mes}) \tag{3.27}$$

Where δV is divided by the nominal voltage V^* so that both terms are in per unit and thus comparable in magnitude. The proposed advantage of the method is that the voltage offset δV has a twofold function: first, it acts as a voltage shift that improves the voltage regulation. Second, it modifies the droop resistance depending on the voltage deviation. The contribution of δV to the droop parameter can be analyzed as follows: if the voltage is below average, δV will be positive. Thus, the final droop will be equal to $R_d - (\delta V)$. This results in a smaller droop resistance that will cause the voltage to deviate less. The opposite will happen in the case the voltage is above the average. The implementation of this controller is shown in Fig. 3.30.

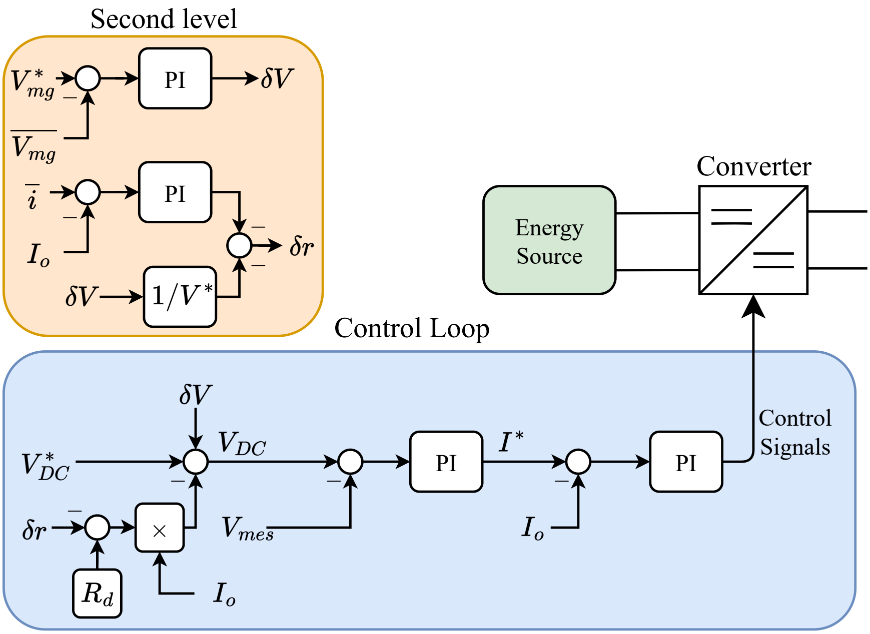

Figure 3.30: Average current and average voltage droop control implementation

3.5 Conclusion

In this chapter, an overview of the different control methods has been provided. Following the presented classification, both primary and secondary level controllers have been discussed. For the first level controllers, a non-exhaustive list of existing controllers was presented, and out of these, five were selected and detailed. Special attention was given to droop control and related controllers, namely non-linear droop and piecewise droop. This is due to the popularity of droop control which leads to its recurring utilization, attributed to its benefits and ease of implementation.

Second level controllers were also detailed. As demonstrated, these controllers are built on top of droop control and aim to address its shortcomings, such as voltage deviations and precise load sharing. The different controllers will be implemented and compared in Chapter 6, where the different advantages and disadvantages will be highlighted.

In the author's opinion, one key takeaway from this chapter is the influence of line resistance and droop resistance. Indeed, in DC distribution, line resistance plays a critical role and significantly impacts load sharing. As demonstrated in the chapter, the presence of droop control reduces the current sharing error. The value of the droop resistance significantly affects the accuracy of load sharing. The different controllers are created to compensate for these issues. Piecewise and nonlinear control seek to provide a varying droop resistance to improve voltage regulation at low currents and load sharing at high currents. Second level controllers similarly aim to improve voltage regulation at all points and enhance current sharing.

Chapter 4

Steady State Simulation

Chapter contributions

- A power flow suited for DC microgrids is presented
- The introduced power flow is developed into a power flow suitable for bipolar DC microgrids and into a sequential power flow
- The study of a DC microgrid's performance via sequential power flow is developed
- A comparison of the performance of unipolar and bipolar DC microgrids is proposed using the developed tool

The steady-state analysis of power systems refers to the determination of electrical quantities under certain conditions or states. To perform these studies, a tool called power flow, also referred to as a load flow, is used. A power flow is an important tool as it gives an overall view of the system. It offers insights into the steady-state voltages, power injections, and line flows of the system. This perspective can be valuable for understanding the operation and control of the system. Additionally, it provides an indication of the magnitudes of electrical quantities. This information can be utilized for sizing components and optimizing the system[89], [90].This is a well-studied and widely used tool for AC distribution systems. Various existing methods include Gauss-Siedel, Newton Raphson, and distribution power flow. However, DC distribution grids have characteristics that prevent the direct application of these existing methods. Additionally, when considering DC microgrids operating in islanded mode, traditional methods face further challenges. The main differences that impact existing methodologies are [90], [91]:

Absence of slack bus In a traditional system, there is typically a designated slack bus where the voltage is fixed. It is assumed that one bus acts as a voltage regulator while others control power injection. When considering an islanded DC microgrid, there is no slack bus as it might be impractical to consider a DC source with limited power, such as renewable source, as a stiff voltage source that can compensate for power indiscriminately when it has a limited capacity.

Impact of droop control Droop control is frequently used in DC microgrids. To ensure proper load sharing, the source should not behave as a stiff voltage source. The power injections are not fixed and will vary with bus voltages. Therefore, bus injections can not be specified beforehand.

In the context of DC microgrids, power flow analysis provides additional crucial information. Considering the nature of droop control, both load sharing and local voltage regulation might not be accurate. However, both load sharing and voltage regulation are crucial elements for DC microgrids. Thus, based on the analysis of power flow results, the droop parameter or the control strategy for the microgrid might need to be adapted [91].

This chapter describes the implementation of a power flow adapted to DC microgrids. This power flow can be applied to both unipolar and bipolar DC microgrids. Afterwards, a methodology for simulating the performance of a DC microgrid over a given time frame is detailed. This methodology is based on the sequential use of the power flow described. Examples for each of the described points are given. The chapter concludes with a comparison of the performance between a unipolar DC microgrid and a bipolar DC microgrid.

4.1 Linearized Unipolar Power Flow

The proposed power flow method used is a linearized power flow. This method allows the modeling of nodes that can simultaneously contain droop-controlled dispatchable generators, non-dispatchable generators, and different types of loads in the power flow. The modeled loads can be constant power, constant current, constant impedance, or a mix of the previously mentioned types. Additionally, it avoids the usage of iterative techniques like the Newton-Raphson method or the trust region method. Since it relies on solving linear equations, it does not require the computation of the Jacobian matrix, thus providing a faster technique. The power flow can be solved in a single iteration unless power limits are imposed on the dispatchable generators. This power flow approach allows studying a microgrid operating in grid-connected mode, islanded mode, or connected to a stiff grid [90].

To solve the power flow problem, an equation for the current injection at each node is needed. To develop this equation the DC network shown in Fig. 4.1 can be considered. In Fig. 4.1 a DC network with N_B system buses is considered. g_{ij} represents the conductance of the line between nodes i and j.

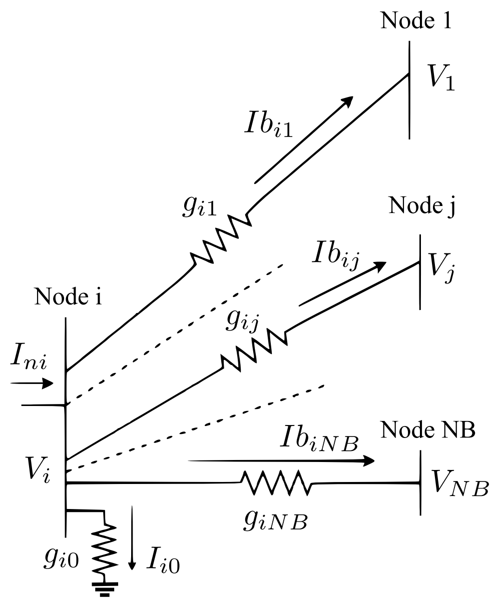

Figure 4.1: DC network used to derived the power flow equation [90].

Equation (4.1) represents the current injection at a node i in a system of N_B system buses per pole. The left-hand side expresses the relationship between the node current I^+_{ni} and node voltages V^+ expressed through the conductance matrix G^+. The superscript $^+$ is used to identify the variables concerning the positive pole. In the following section it will be used along with the superscript $^-$ to describe bipolar DC bus systems. The right-hand side of the equation is composed of five elements. The first element corresponds to the current injection due to the droop-controlled generator, where V_0 is the no load reference voltage and R^+_{di} is the droop parameter. The second one is the current injection linked to the non-dispatchable generators, and the last components are the current drawn by the constant power load, constant current load, and constant impedance load, respectively. For simplicity, only constant power loads will be considered as shown in (4.2).

$$I^+_{ni} = \sum_{\substack{j=1 \\ j\neq i}}^{N_B} G^+_{ij}V^+_j + G^+_{ii}V^+_i = \frac{V_{0i} - V^+_i}{R^+_{di}} + \frac{P^+_{ndgi}}{V^+_i} - \frac{P^+_{Pi}}{V^+_i} - \frac{P^+_{Pi}}{V_{0i}} - \frac{P^+_{Pi}V^+_i}{V_{0i}} \quad (4.1)$$

$$I^+_{ni} = \sum_{\substack{j=1 \\ j\neq i}}^{N_B} G^+_{ij}V^+_j + G^+_{ii}V^+_i = \frac{V_{0i} - V^+_i}{R^+_{di}} + \frac{P^+_{ndgi}}{V^+_i} - \frac{P^+_{Pi}}{V^+_i} \quad (4.2)$$

Equation (4.2) is not linear due to the V^+_i terms found at the denominator of the elements corresponding to the non-dispatchable generator and the constant power load. To linearize the system, the node voltages are expressed in per unit. When expressed in per unit, the node voltage can be described in terms of the voltage deviation ΔV^+_i.

$$V^+_i = 1 - \Delta V^+_i \quad (4.3)$$

In [90], by defining a function $\phi(\Delta V^+_i)$, and by developing the Taylor series around zero, it is found that the higher order terms can be neglected. The Taylor series expansion is given by (4.4). Thus, it is possible to define (4.3) as (4.5). Considering that in power systems, voltage deviations are typically around 5% or 10%, it can be deduced that the higher-order terms will have minimal impact. For example, with a 10% voltage deviation ΔV^+_i will be equal to 0.10. The second term of the Taylor series $(\Delta V^+_i)^2$ would have a value of 0.01. The higher-order terms would become even smaller.

$$\frac{1}{1-\Delta V_i} = \sum_{k=0}^{\infty} (\Delta V_i^+)^k = 1 + \Delta V_i^+ + (\Delta V_i^+)^2 + ... \tag{4.4}$$

$$\frac{1}{1-\Delta V_i} = \frac{1}{V_i} = 1 + \Delta V_i = 2 - V_i \tag{4.5}$$

By using (4.6) to calculate the error, Fig. 4.2 can be obtained. It can be seen that for a high voltage deviation of 0.15 per unit , the voltage error corresponds to 2.25%. Therefore, neglecting the higher-order terms of the Taylor series only introduces a relatively small inaccuracy in the calculation.

$$\xi(V_i^+) = 100(1 - (2 - V_i^+)V_i^+) \tag{4.6}$$

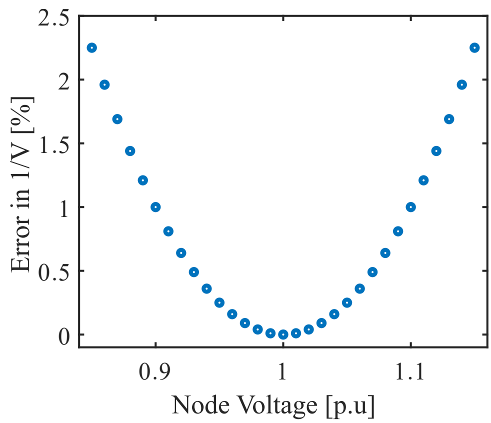

Figure 4.2: Percentage of error in calculation for different voltages

By using (4.5), the right side of (4.2) can be expressed as the following linear equation:

$$I_{ni}^+ = \frac{V_{0i} - V_i^+}{R_{di}^+} + (P_{ndgi}^+ - P_{Pi}^+)(2 - V_i^+) \tag{4.7}$$

Thus, the system can be expressed as a set of linear equations, as shown in (4.8). To solve the power flow, the equations can be set as a system of the form $Ax = B$, where x is the vector of unknown voltages.

$$\sum_{\substack{j=1\\j\neq i}}^{N_B} G_{ij}^{+}V_j^{+} + (G_{ii}^{+} + \frac{1}{R_{di}^{+}} - P_{Pi}^{+} + P_{ndgi}^{+})V_i^{+} = \frac{V_{0i}}{R_{di}^{+}} - 2(P_{Pi}^{+} - P_{ndgi}^{+}) \quad (4.8)$$

To demonstrate the linear loadflow, the following example is developed. Two sources feed a single load of 27 kW as shown in Fig. 4.3. These sources correspond to a droop-controlled battery and a PV system acting as a non-dispatchable generator. The type of load considered is a constant power load. The nominal voltage used is 700 V and the line resistances have a value of 0.0224 Ω.

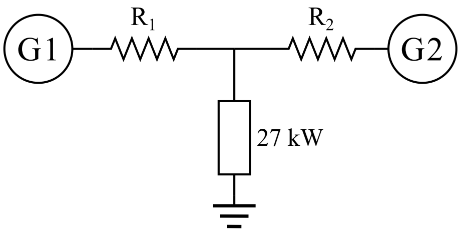

Figure 4.3: 3 node test grid for linear power flow

Using the same droop parameter and line resistance on both sides, the result shown in Fig. 4.4 is obtained. In this figure V is the voltage in p.u of the node. PV and Bat correspond to the power injected by the PV and the battery respectively at each node. During the first test, only the batteries provide power. The two droop controlled batteries provide the same amount of power and have the same voltage which is not equal to the nominal value as imposed by the droop control. Fig. 4.5 shows the same result when one line is longer and thus has a higher resistance value. The load is provided the correct amount of power, but it is not distributed equally among the two converters eventhough the same droop parameter is used. Indeed, as mentioned in in Chapter 3, the line resistances influence the accuracy of the load sharing. Note that if (3.8) is used to calculate the current given by each source, it will provide a different result. This is because (3.8) and (eq:I2d) are valid for constant impedance loads.

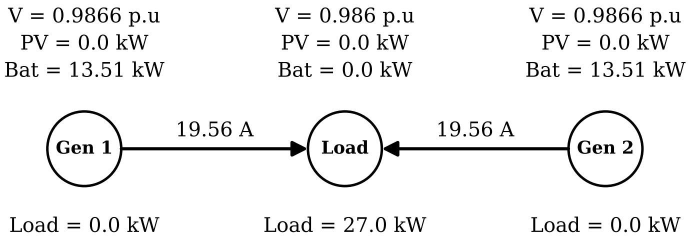

Figure 4.4: 3 node linear power flow under identical parameters

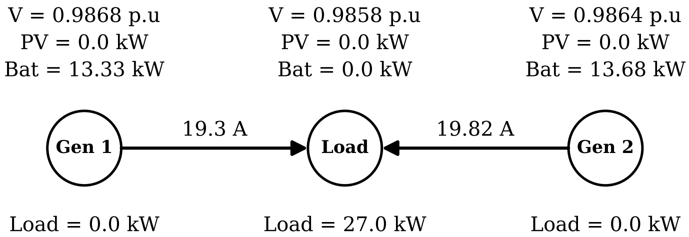

Figure 4.5: 3 node linear power flow with different line resistances

Finally, an example with power injection comming from PV pannels is shown in Fig. 4.6. Here, 10 kW are provided directly by the PV pannels. The remaining power is the provided throught the droop controlled batteries. Notice that the node Gen 1 is closer to nominal voltage. This can be attributed to the fact that a part of the power comming from this node is not regulated via the droop control and thus does not further deviate the voltage.

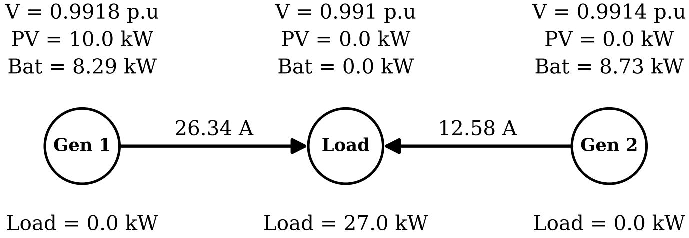

Figure 4.6: 3 node linear power flow with PV injection

4.2 Linearized Bipolar Power Flow

The previously described power flow applies to a 2-wire system. For a bipolar DC distribution system, the formulation of the problem has to take more factors into account. Two elements have to be added to the model: the negative pole and the neutral pole. The positive and negative poles are independent of each other and thus can be modeled individually. However, the voltage at the neutral pole depends on the voltages of both the positive and negative poles.

To model these two elements, it is important to take into account the current convention. It is considered that in the negative pole nodes, the loads draw current from the neutral, and the current returns to the neutral via the generators. The sign convention for the negative nodes is compared to that of the positive nodes in Fig. 4.7 [92], [93].

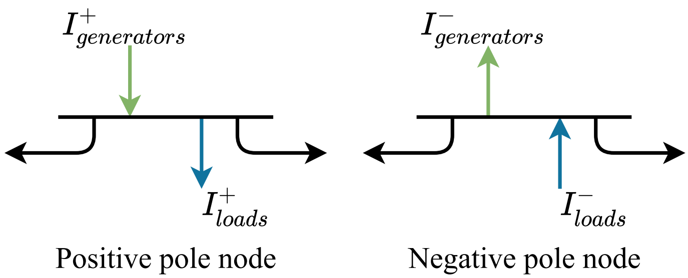

Figure 4.7: Current convention at positive and negative nodes

For the neutral pole, it is considered that the drooped controlled generators and the non-dispatchable generators in the positive pole draw current from the neutral. The loads on the positive pole inject current into the neutral. The opposite is true for the negative pole, the generators inject current into the neutral, and the loads draw from it. The previously described current convention is illustrated in Fig. 4.8.

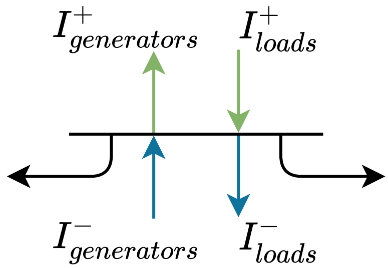

Figure 4.8: Current convention at neutral nodes

4.2.1 Negative Pole Model

The negative pole is essentially the same as the positive pole except for the sign convention. Therefore, the sign for the droop-controlled source, the non-dispatchable generator, and the load are changed accordingly. These modifications are applied in (4.9) through (4.11).

$$I^-_{ni} = \sum_{\substack{j=1 \\ j\neq i}}^{N_B} G^-_{ij}V^-_j + G^-_{ii}V^-_i = \frac{-V_{0i} - V^-_i}{R^-_{di}} - \frac{P^-_{ndgi}}{V^-_i} + \frac{P^-_{Pi}}{V^-_i} \tag{4.9}$$

$$I_{ni} = \frac{-V_{0i} - V^-_i}{R^-_{di}} + (P^-_{Pi} - P^-_{ndgi})(2 + V^-_i) \tag{4.10}$$

$$\sum_{\substack{j=1 \\ j\neq i}}^{N_B} G^-_{ij}V^-_j + (G^-_{ii} + \frac{1}{R^-_{di}} - P^-_{Pi} + P^-_{ndgi})V^-_i = \frac{-V_{0i}}{R^-_{di}} + 2(P^-_{Pi} - P^-_{ndgi}) \tag{4.11}$$

4.2.2 Neutral Pole Model

To apply the same process for solving the power flow, an equation for the current at the neutral node similar to the one shown in (4.2) is needed. Considering the current convention, it is possible to determine that the current at a neutral node can be described as follows:

$$I_{Neutral} = (I^{+}_{loads} + I^{-}_{generators}) - (I^{+}_{generators} + I^{-}_{loads}) \tag{4.12}$$

To fully express the current of the neutral node, an equation in the shape of (4.2) and (4.9) is formulated. However, unlike the positive and negative pole nodes, the neutral nodes do not have any generators or loads themselves. Therefore the resulting equation would be:

$$I^{n}_{ni} = \sum_{\substack{j=1 \\ j\neq i}}^{N_B} G^{n}_{ij} V^{n}_{j} + G^{n}_{ii} V^{n}_{i} = I_{Neutral} \tag{4.13}$$

Thus, substituting the right hand side of (4.13) with (4.7) and (4.10) and rearranging one can obtain (4.14). When substituting (4.7) and (4.10) it is important to adjust the signs of the generators and loads according to the neutral node convention described before in (4.12).

$$\begin{aligned} &\sum_{\substack{j=1 \\ j\neq i}}^{N_B} G^{n}_{ij} V^{n}_{j} + G^{n}_{ii} V^{n}_{i} - (\frac{1}{R^{+}_{di}} - P^{+}_{Pi} + P^{+}_{ndgi}) V^{+}_{i} - (\frac{1}{Rd^{-}_{i}} - P^{-}_{Pi} + P^{-}_{ndgi}) V^{-}_{i} \\ &= -(\frac{V^{+}_{0i}}{R^{+}_{di}} - 2(P^{+}_{Pi} - P^{+}_{ndgi})) + (\frac{V^{-}_{0i}}{R^{-}_{di}} - 2(P^{-}_{Pi} - P^{-}_{ndgi})) \end{aligned} \tag{4.14}$$

One final consideration that has to be added to the system is the grounding point. A single neutral node has to be assigned as the grounding point. Therefore, one neutral node has to be modeled according to (4.15) instead of (4.14). In other words, implementing (4.15) ensures that the sum of the voltages across the positive, neutral, and negative pole for a single node are equal to zero.

$$V^{+}_{i} + V^{-}_{i} - V^{n}_{i} = 0 \tag{4.15}$$

Thus, by using equations (4.8), (4.11), (4.14), and (4.15), a system of linear equations in matrix form **Ax=B** can be constructed. This system can be easily solved to find the voltages and currents of the entire bipolar grid.

4.2.3 Bipolar power flow demonstration

To demonstrate the developed linear model, two different examples are provided. The first one will illustrate how the currents in the neutral cancel in a balanced grid and how the currents in the neutral appear when there is an unbalance in a DC microgrid that has the same configuration in the positive and negative pole. The second example models a DC microgrid that has different elements in the positive and negative pole. These tests are done in a microgrid that contains 4 nodes in each pole and has a reference voltage of 750 V. The nodes are grouped in 4 sets named from A to D. Each set contains a corresponding positive, negative, and neutral node. The conductor parameters shown in Table 4.1 are used. Thus, class 5 plain copper conductors are considered. The values for the resistance of the conductor are those found in the stantard IEC60228 [94]. The line lengths and resistances of the DC microgrid are given in 4.2.

Table 4.1: Resistance of class 5 & 6 plain copper conductors conductors[94]

Cross-section [mm²]	**Maximum Resistance [Ω/km]**
70	0.272
150	0.129
185	0.106
300	0.0641
500	0.0384

Table 4.2: Used line parameters with a 185 mm² conductor

Line	**Length [m]**	**Resistance [Ω]**
A to B	250	0.0265
B to C	200	0.0212
C to D	300	0.0318

The microgrid configuration for the first example is illustrated in Fig. 4.9. The microgrid has two equal droop-controlled generators on each pole that feed three loads each. These loads have an equal power demand as shown in the parameters in Table 4.3.

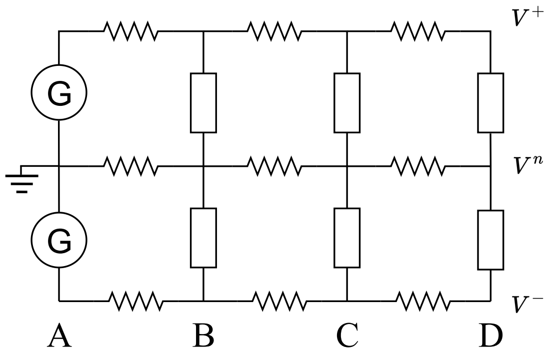

Figure 4.9: DC microgrid used in the unbalance example

Table 4.3: Unbalance test microgrid parameters

DG Droop Parameters		
No Load reference voltage	750	[V]
R_{dA}^{+}	0.2296	[Ω]
R_{dA}^{-}	0.2296	[Ω]
Load Parameters		
Base load	10	[kW]

In the first example, two cases are considered: a load ratio of 1:1 between the positive and negative poles, and a load ratio of 1.2:1. When the loads on the positive and negative poles are in a 1:1 ratio, each load has a demand of 10 kW. In the 1.2:1 ratio case, the loads on the positive pole are 12 kW each, while those on the negative pole are 10 kW each. The results in terms of voltages and currents are shown in Table 4.4 and Table 4.5, respectively. With a 1:1 ratio, the voltages on both poles are equal, indicating a balanced system. Due to the symmetry of the microgrid, the currents are the same in each pole. These currents, having the same magnitude, cancel each other out, resulting in no current flowing through the neutral pole. In the case of a 1.2:1 ratio, the imbalance caused by the differing load ratios is reflected in the voltage of the neutral pole. Since the poles are independent of each other, the results for the negative pole remain the same as before. However, the positive pole's results change due to the load variation, leading to currents of different magnitudes. This imbalance causes current to flow through the neutral conductor.

Table 4.4: Node voltages with different load ratios

	1:1 load ratio			1.2:1 load ratio		
Node	$V^+[p.u]$	$V^n[p.u]$	$V^-[p.u]$	$V^+[p.u]$	$V^n[p.u]$	$V^-[p.u]$
A	0.9876	0	-0.9876	0.9850	0.0025	-0.9876
B	0.9861	0	-0.9861	0.9833	0.0028	-0.9861
C	0.9854	0	-0.9854	0.9824	0.0030	-0.9854
D	0.9848	0	-0.9848	0.9817	0.0031	-0.9848

Table 4.5: Line currents with different load ratios

	1:1 load ratio			1.2:1 load ratio		
Line	$I^+[A]$	$I^n[A]$	$I^-[A]$	$I^+[A]$	$I^n[A]$	$I^-[A]$
A to B	40.58	0	-40.58	48.84	-8.26	-40.58
B to C	13.52	0	-13.52	32.57	-5.51	-27.06
C to D	0.9	0	-0.9	16.29	-2.76	-13.54

The microgrid used for the second example is shown in Fig. 4.10. The positive pole has two PVs which are the non-dispatchable generators, one droop-controlled generator, and a load. On the negative pole, there are two droop-controlled generators and two loads. The parameters used for this power flow are shown in Table 4.6. In the case of the droop-controlled generators on the negative pole, DG_A^- has a smaller droop coefficient and is thus expected to provide more power than the other DG on the negative pole DG_D^-. The line parameters remain as shown in Table 4.2.

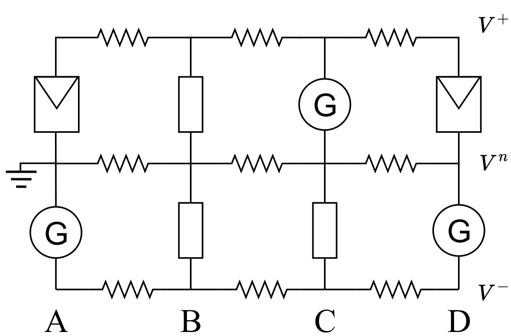

Figure 4.10: DC microgrid with multiple sources for unbalance demonstration

Table 4.6: Multiple sources test microgrid parameters

DG Droop Parameters		
No Load reference voltage	750	[V]
R_{dA}^{-}	1.12	[Ω]
R_{dC}^{+}	5.64	[Ω]
R_{dD}^{-}	4.63	[Ω]
PV Parameters		
P_{ndgA}^{+}	24	[kW]
P_{ndgD}^{+}	18	[kW]
Load Parameters		
P_{PB}^{+}	72.5	[kW]
P_{PB}^{-}	32.5	[kW]
P_{PC}^{-}	54	[kW]

The previously described system is then solved using the linearised power flow, and the voltages and currents of the nodes are found. The obtained voltages and currents are shown in Table 4.7 and Table 4.8. As the results show, there is degree of unbalance in the microgrid. This result is evidenced by the high currents in the neutral pole.

Table 4.7: Obtained microgrid node Voltages with multiple sources

Set	$\boldsymbol{V^{+}[p.u]}$	$\boldsymbol{V^{n}[p.u]}$	$\boldsymbol{V^{-}[p.u]}$
A	0.9840	-0.0053	-0.9787
B	0.9829	-0.0066	-0.9763
C	0.9848	-0.0092	-0.9756
D	0.9858	-0.0082	-0.9776

Table 4.8: Obtained microgrid line currents with multiple sources

Line	$\boldsymbol{I_{n}^{+}[A]}$	$\boldsymbol{I_{n}^{n}[A]}$	$\boldsymbol{I_{n}^{-}[A]}$
A to B	32.51	36.93	-69.44
B to C	-65.81	90.89	-25.08
C to D	-24.34	-24.34	48.68

The power injected by each droop-controlled source is shown in Table 4.9. On the negative pole, it is shown that DG_A^- injects more power than DG_D^- as was specified by the droop parameters. On the positive pole, DG_C^+ provides less power than what the load is demanding as the remaining part is complemented by the PV panels P_{ndgA}^+ and P_{ndgD}^+.

Table 4.9: Obtained DG power injection

DG	**Power Injection**
DG_A^-	50.97 [kW]
DG_C^+	30.63 [kW]
DG_D^-	35.7 [kW]

The system shown here is simplified for demonstration purposes. In a more complex system, each node could have loads of different types, a droop-controlled generator, and a non-dispatchable generator. The proposed linearized power flow method is able to solve these types of systems. Furthermore, it is possible to impose power limits on the dispatchable generators if the power flow is allowed to iterate. Due to the complexity of bipolar microgrids, it is thus of interest to develop tools, such as the one shown, that allow the study of the steady-state of the system.

4.3 Sequential Simulation

With the previously described linear power flow models, it is possible to take a step further and use them to simulate the evolution of a DC system. In other words, by sequentially applying the power flow, it is possible to simulate the general behavior of a DC microgrid over long periods of time, assuming a sequence of steady-state conditions with a specified time step. For a more realistic simulation, certain information is required. First, consumption data for the loads to be connected are needed, with quarterly hour samples commonly used for this purpose. This data allows for the reproduction of the consumption profile and peak power demand. If PV systems are part of the network, appropriate irradiance data is also needed. Similarly, if other renewable sources, such as wind turbines, are included, wind speed data would be needed. Additionally, parameters for the batteries, such as rated battery capacity, output power or discharge rate, and the resistance of the distribution lines, should be included to complete the simulation.

To simulate the DC microgrid, an algorithm workflow similar to the one presented in [95] is adopted. The used algorithm workflow is presented in Fig. 4.11. As a first step, the variables defining the microgrid such as the line resistances, droop resistances, and battery parameters, are defined. The PV production data and consumption profiles are also loaded. Once the initialization stage is done, the first PV production and load demand data are selected. Afterward, a function checks the state of charge (SoC) of the batteries. Based on the SoC, and the maximum output power, the power limit P_{lim} of each battery is obtained. The maximum output power of the battery is the highest value P_{lim} can be given. However, sometimes a smaller value based on the SoC can be used for P_{lim}. If there are any limits imposed on the maximum and minimum percentage of SoC, they will also be taken into account for the calculation of P_{lim}. The power limit, the consumption, and PV production data are fed into the linear power flow algorithm.

The limitation of P_{lim} based on the SoC comes from the fact that the sequential power flow considers time steps of 15 minutes. Thus, there should be enough charge in the battery to provide the calculated power for 15 minutes. For example, consider a 100 kWh battery at 25% SoC that can only discharge up to 20% of its SoC. This means that it only has 5 kWh available. For a 15 minute time step, the available power of this battery is 20 KW, as providing 20 kW for 15 minutes will cause it to reach its 20% SoC limitation.

Once the linear power flow is calculated, the power given by the batteries is calculated. Indeed, the result of the power flow is the total power in each node. However, the power from the PVs and the load demand at each node are already known. Therefore, by adding these three quantities the power absorbed or supplied by the battery can be known. The power given or absorbed by the battery is then used to update the battery's SoC. This process is repeated until the final set of values is reached. Additionally, the charge and discharge losses of the battery can be considered in the calculation of P_{lim} and the update of the SoC. For example, if a 2% loss is considered while discharging, P_{lim} could be multiplied by a factor of 0.98. Afterwards, when updating the SoC, a factor of 1.02 can be considered. This would effectively make the battery provide less power due to the losses and update the SoC considering them.

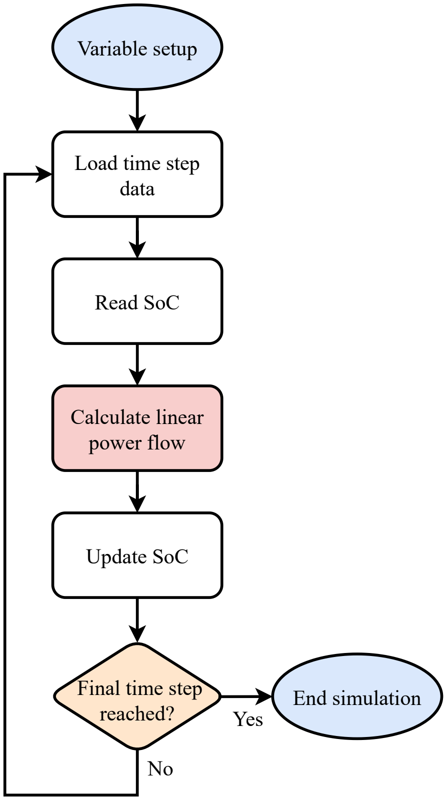

Figure 4.11: DC Microgrid algorithm workflow

The calculation of the linear power flow shown in the previous graph takes into account several details. In the DC microgrid, one node can take the role of the point of connection to the main AC grid. The AC grid is modeled as a droop-controlled source. If the microgrid is self-sufficient, this node will not participate in power injection. This is imposed by setting its droop resistance R_d equal to infinity. If power is to be imported or exported via the main AC grid, this node will act as a grid-forming node. It means that it will impose the nominal voltage at that node and regulate any excess or lack of power. This is achieved by setting its droop resistance to a significantly small value.

Note that if an islanded DC microgrid is simulated, there will be no AC grid node. It is indeed possible to simulate such a case with the proposed tool. If there is no AC node and the sources in the islanded DC microgrid cannot provide enough power, three options are available. First, it could be accepted that not enough power is available and continue with a significant deviation in voltage from the nominal value. A second option is to stop the simulation if the resulting grid voltage is too low. A final option could be to implement a load shedding system and disconnect non-essential loads.

The algorithm workflow for the calculation of the linear power flow is illustrated in Fig. 4.12. The first step is the implementation of the linear power flow, as described in the previous sections. The results obtained by solving the $Ax = B$ system of equations are then used to calculate the power at each node. Utilizing the known load demand and PV production, the power corresponding to the battery is calculated. This value is then compared to the power limit P_{lim}. If it is within the limits, the linear power flow algorithm returns the found values. Otherwise, the batteries that exceed their power limit are set as non-dispatchable generators. This is achieved by fixing their droop parameter equal to infinity and setting the non-dispatchable power P_{ndgi} equal to the sum of the power coming from the PVs and the battery P_{lim}. The parameters are then updated, and the linear power flow is allowed to iterate.

If all the batteries are acting as non-dispatchable units, the node corresponding to the point of connection to the grid is set as a grid-forming node. The batteries will provide or store power according to their power limit P_{lim}, and the main grid node will compensate for any remaining power unbalance. Thus, in the final iteration, no battery should surpass its power limit P_{lim}, and the linear power flow will return the found values.

While adding power limits requires the system to iterate, it will not significantly slow down the computation. For each time step, a system of N_B nodes will iterate a maximum of N_B times. This is because the main grid node becomes activated when all the batteries are set as non-dispatchable units.

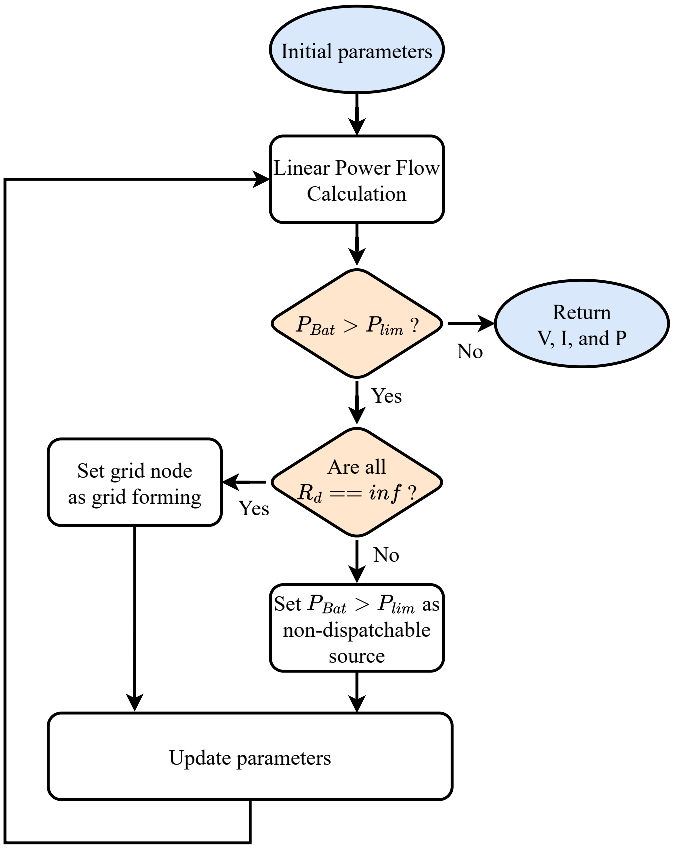

Figure 4.12: DC linear power flow workflow with constraints

As mentioned, the batteries are functioning as droop-controlled sources. The droop parameter for each battery is calculated using its rated power and discharge rate. The discharge rate measures the battery's capacity to supply power relative to its rated capacity. For example, if an 80 kWh battery can only output 40 kW at a time, it has a discharge rate of 0.5. With these parameters, the droop parameter can be calculated by determining the battery's maximum output current as shown in (3.2).

When updating the SoC, the duration of the time step has to be taken into account. This is because the power charged or discharged has to be integrated to obtain its value in kilowatt-hours (kWh). Subsequently, the obtained power in kWh is then used to update the SoC percentage before advancing to the next time step. Note that P_{lim} takes the time step into account when imposing the battery limit. Thus, the SoC limits are respected during each time step.

4.3.1 Sequential Simulation Case Study

To showcase the proposed methodology, the DC microgrid, comprising 5 nodes, shown in Fig. 4.13 is simulated. The rightmost node connects to the main AC grid, while the other 4 nodes represent various industrial consumers. Each industrial consumer includes a load, PV production, and a droop-controlled battery. For simplicity, only constant power loads are considered. Energy within the microgrid is shared, meaning excess power from PVs is used to supply other loads or charge batteries. If all loads are adequately powered and batteries fully charged, surplus power is directed to the main AC grid.

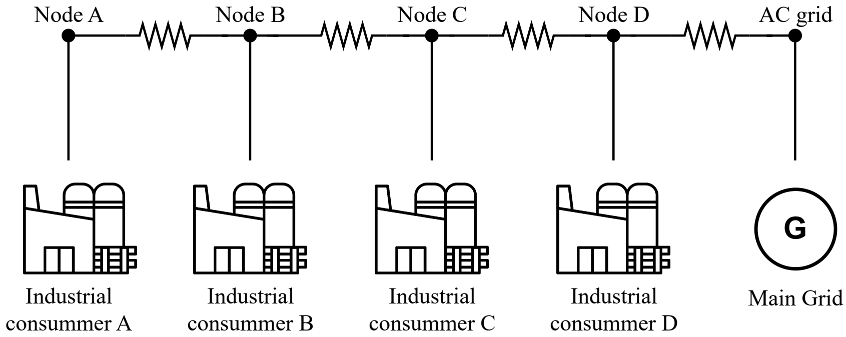

Figure 4.13: Industrial DC microgrid test grid layout

The simulation is carried out using consumption profiles derived from metering data sampled every 15 minutes, spanning a duration of 10 months. Additionally, historical irradiance data corresponding to the Western European region is also incorporated. An example of the consumption profile for consumers over the course of one week is shown in Fig. 4.14.

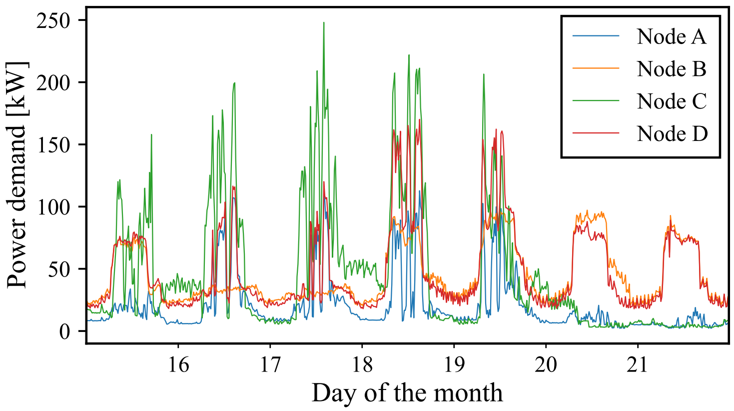

Figure 4.14: Typical consumption profile for a week in June

The battery capacity, E-rate, droop parameter, and the PVs capacity are detailed in Table 4.10. E-rate refers to the discharge capacity in terms of power. An E-rate of 1 means that the battery can fully discharge in one hour. As a consequence, the E-rate, along with the battery capacity, defines the maximum output current of the converter, which in turn defines the droop control slope. Additionally, Table 4.11 presents the individual demand, import, and export of energy values for each consumer in the absence of the DC microgrid. These values, derived from consumption data, serve as the baseline for assessing the benefits of the DC microgrid in terms of reducing energy imports. The line lengths and resistances of the microgrid are given in Table 4.12.

Table 4.10: Consumers Battery and PV Parameters

Consumer	**Battery [kWh]**	**E-rate**	$R_d[\Omega]$	P_{PV} [kWp]
A	100	1.5	-0.0933	100.5
B	200	0.5	-0.1400	150.75
C	130	1	-0.3769	100.5
D	200	0.8	-0.3063	184.25

Table 4.11: Energy Balance of Consumers Over 10 Months Without a DC Microgrid

Consumer	Demand [MWh]	Import [MWh]	Export [MWh]
A	144.92	73.33	23.81
B	300.91	171.41	13.62
C	352.41	275.95	18.95
D	328.37	174.76	21.29
Total	1126.61	695.45	77.66

Table 4.12: DC microgrid line parameters with a 300 mm^2 conductor

Line	Length [m]	Resistance [Ω]
A to B	500	0.0321
B to C	250	0.0160
C to D	440	0.0282
D to Grid	680	0.0436

4.3.2 Nominal Voltage Analysis

First, the proposed approach is used to study potential nominal voltage values for the DC microgrid and their impact on total energy imports from the main AC grid and line losses. This reduction in total energy imports occurs because consumers in the microgrid share surplus energy among themselves. The reduction is determined by comparing the total energy imported from the main AC grid to the DC microgrid with the total import in the absence of the DC microgrid, as provided in Table 4.11. To achieve this, the industrial microgrid is simulated with different voltage levels. Each simulation covers a 10-month period. The obtained results are shown in Fig. 4.15. At a nominal voltage of 500 V, total line losses approximate 40 MWh. With respect to the total load demand of 1126.61 MWh, these line losses represent 3.55%. As the voltage level increases, total line losses begin to decrease. Higher voltage level allows transporting energy more efficiently, consequently reducing total energy imports. It is noteworthy that higher voltages lead to the most significant reductions in imported energy. Conversely, the energy import reduction at 500 V is negative. This is because the reduction is calculated with respect to the total energy import from Table 4.11, which does not consider line losses. In essence, the potential reduction in energy imports achievable by the microgrid is negated by the high line losses in this scenario.

While higher voltage levels have a better performance in terms of line losses and energy import reduction, the incremental gain between each voltage level begins to diminish. Moreover, higher voltage levels can have an impact on the sizing of the components, the efficiency of power electronics, and the protection devices. Indeed, higher voltage levels will require converters rated for different higher voltage levels. Equally, the protection devices will have to be rated for the new higher voltage level. Another element of consideration is the voltage to ground which can be important in the protection scheme.

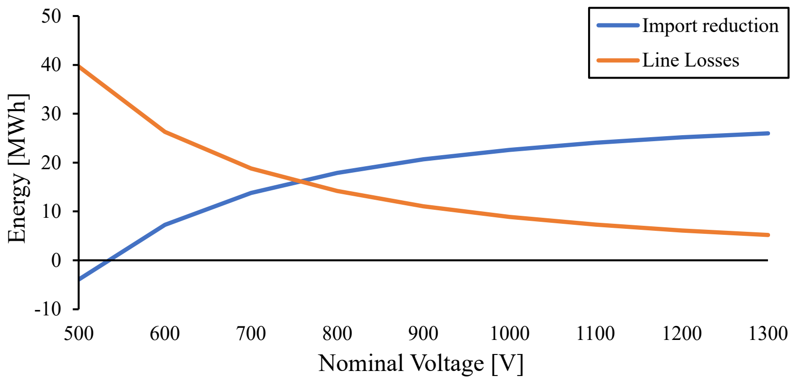

Figure 4.15: Energy import reduction and line losses based on nominal voltage level

4.3.3 1 kV DC Microgrid Analysis

In this case study, a nominal voltage of 1kV is used for the DC microgrid, resulting in the outcomes presented in Table 4.13. This Table shows a reduction in energy import of 22.62 MWh. The demand and production of the industrial consumers remain the same. However, without the DC microgrid, the surplus energy was injected into the main AC grid. With the DC microgrid, the surplus power generated within the microgrid is shared among its members rather than being imported from the AC grid. This energy sharing results in a reduction of 3.25% of the total energy that would otherwise be imported. This 3.25% energy import reduction is due solely to the introduced DC microgrid. The simulation also allows for the analysis of voltage deviations at each time step. Fig. 4.16 shows a box plot for the voltage value at each node, expressed in per unit. This and the following box plots show the first and third quartile values as the edges of the box, the median as a horizontal line inside the box, whiskers that indicate the 1.5 interquartile range (IQR), and the outliers. The IQR is defined as the difference of the third quartile and the first quartile. It is shown that the voltages stay close to the nominal value. Node A experiences the most significant voltage deviation. This deviation is likely due to its relatively long distance from the main AC grid node. In a DC grid, voltage differences between nodes are necessary for power transfer. In this particular example, when all the power is supplied by the grid, the power transfer occurs unidirectionally from right to left. This results in a chaining effect of voltage differences, leading to a lower voltage level at the leftmost node.

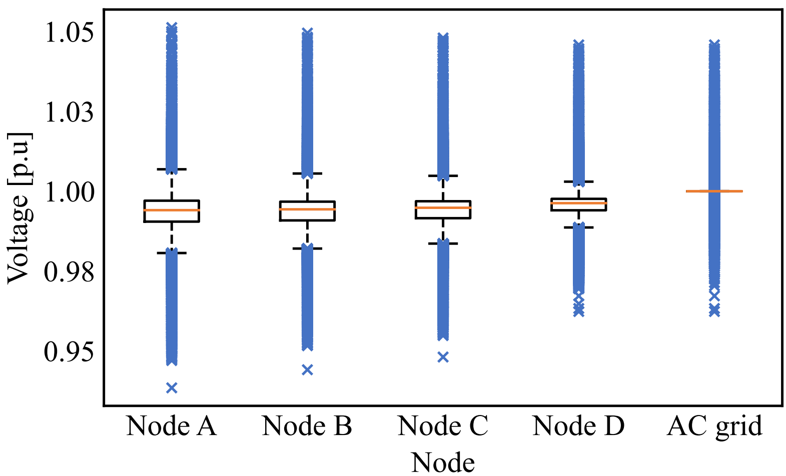

Figure 4.16: DC microgrid node voltage box plot: median, first and third quartile, 1.5 interquartile range, and outliers

Table 4.13: DC microgrid Simulation Energy Analysis

Import [MWh]	**Import reduction [MWh]**	**Export [MWh]**
672.83	22.62	46.29

Through the linear power flow performed at each time step,the expected line currents can be determined. Thus, this analysis allows recording of the current values, as shown in Fig. 4.17. In Fig. 4.17 it is shown that the maximum currents have a significantly higher amplitude compared to their mean values. The line connecting the AC main grid to consumer D registers highest maximum value, which is expected given that all energy imports or exports must traverse this line. Thus, it can be seen that as the lines extend further from the main AC grid node, their maximum currents decrease. With these results, it can be decided if the obtained currents are acceptable or if they exceed the conductor's current carrying capacity, in which case a higher conductor cross-section is needed. Equally, the expected line losses can be calculated with the obtained data.

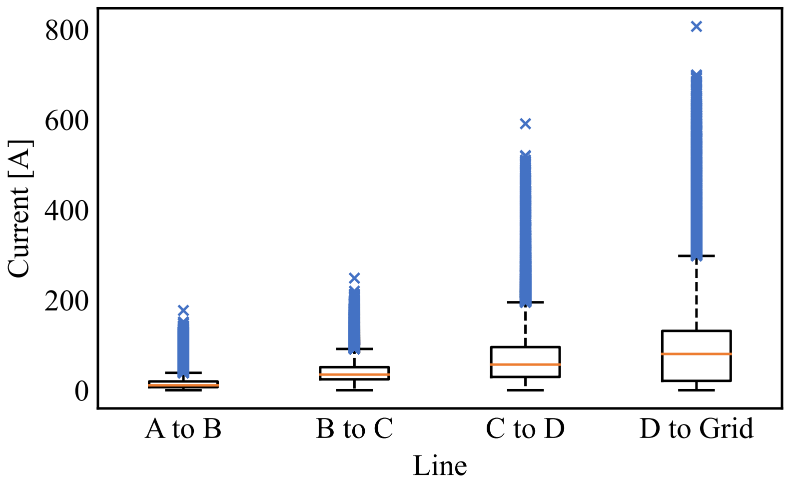

Figure 4.17: DC microgrid line current box plot: median, first and third quartile, 1.5 interquartile range, and outliers

4.3.4 SCI and SSI

Based on the logged data for each time step, two important metrics can be calculated: the self-consumption index (SCI) and the self-sufficiency index (SSI). Different definitions for these indices have been developed in the literature. A simple definition is provided in [96] for self-consumption (SC) and self-sufficiency (SS):

$$SC = \frac{\text{Locally generated and consumed energy}}{\text{Local energy generation}} \tag{4.16}$$

$$SS = \frac{\text{Locally generated and consumed energy}}{\text{Total energy consumption}} \tag{4.17}$$

Similarly, the work in [97] proposes a self-sufficiency rate (SSR) and self-consumption rate (SCR) defined as:

$$SSR = 1 - \frac{\int_{t_1}^{t_0} \text{Power load - Power PV}\, dt}{\int_{t_1}^{t_0} \text{Power load}\, dt} \tag{4.18}$$

$$SCR = 1 - \frac{\int_{t_1}^{t_0} \text{Power load - Power PV}\, dt}{\int_{t_1}^{t_0} \text{Power PV}\, dt} \tag{4.19}$$

In [98], the SC and SS are defined by the overlap in PV generation P_{pv} and the load P_{load}. Furthermore, the power stored in batteries $P_{storage}$ is taken into account. Thus, the following definitions are provided:

$$SC = \frac{\int_{t_1}^{t_0} \min(P_{load}, P_{pv} + P_{storage})\, dt}{\int_{t_1}^{t_0} P_{pv}\, dt} \tag{4.20}$$

$$SS = \frac{\int_{t_1}^{t_0} \min(P_{load}, P_{pv} + P_{storage})\, dt}{\int_{t_1}^{t_0} P_{load}\, dt} \tag{4.21}$$

The definition in this thesis is the one provided in [99]. According to [99], the SCI is a measurement of the PV energy that is either directly consumed or stored in the ESS. Meanwhile, the SSI corresponds to the energy consumption that is instantly supplied either by the PVs or the ESS. These indexes are calculated for the entire DC microgrid, thus the total load, PV, and battery power need to be considered. The calculation of the SCI and SSI is performed as shown in (4.22) and (4.23) respectively.

$$SCI = \frac{\sum_t^T \min(P_{pv,tot}(t), P_{load,tot}(t) + P_{charge,tot}(t))}{\sum_t^T P_{pv,tot}(t)} \tag{4.22}$$

$$SSI = \frac{\sum_t^T \min(P_{load,tot}(t), P_{pv,tot}(t) + P_{discharge,tot}(t))}{\sum_t^T P_{load,tot}} \tag{4.23}$$

In Fig. 4.18, the obtained SCI and SSI are shown as the base case, with values of 90.78% and 41% respectively. A high SCI of 90.78% means that about 90 % of the PV energy produced is directly used by the microgrid and 10% is injected into the main grid. This high SCI could indicate efficient utilization of the PVs or undersized PVs. Conversely, the SSI shows that the microgrid needs to rely on imported energy for more than half of its consumption. Using the proposed methodology, three additional case scenarios and their impact on the SCI and SSI are examined. These scenarios are: doubling the battery energy storage capacity, doubling the PVs kWp potential with the same irradiance and angle, and doubling both the battery storage capacity and kWp potential of each consumer respectively. The energy imported and exported for each case are shown in Fig. 4.19.

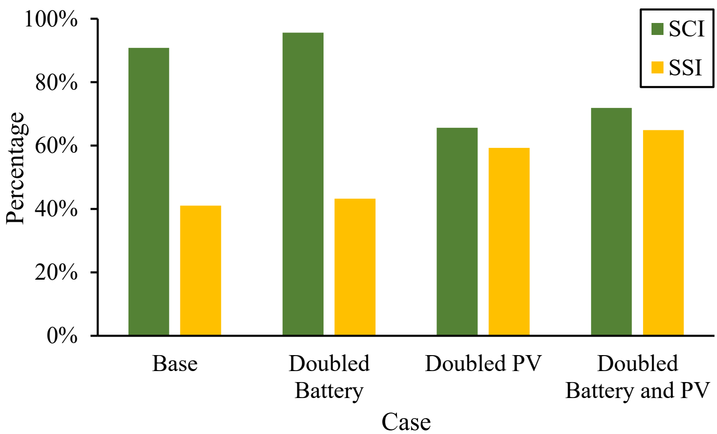

Figure 4.18: Indexes comparison across different case scenarios

As shown in the results, increasing the ESS capacity has a minimal impact as most of the PV energy was already being used. While the increase in storage allows for more energy to be stored, it's insufficient to significantly affect the SSI. The increased PV potential case has a more significant influence on the SCI and SSI as shown in Fig. 4.18. The SSI is increased, but the SCI is greatly reduced. This is due to the lack of sufficient ESS to store all the energy being produced by the PVs. This can be seen in Fig. 4.19 as the exported energy in this case increases significantly. The final scenario involves doubling both the PVs' potential and ESS capacity. As Fig. 4.19 shows, the increased storage capacity leads to a reduction in the amount of energy exported. This is because the increased battery capacity allows it to store more energy during the PV pannels' peak production. Thus, the PV panels inject less energy into the main AC grid. The energy is instead stored and used by the DC microgrid thus further reducing the total energy import from the main grid.

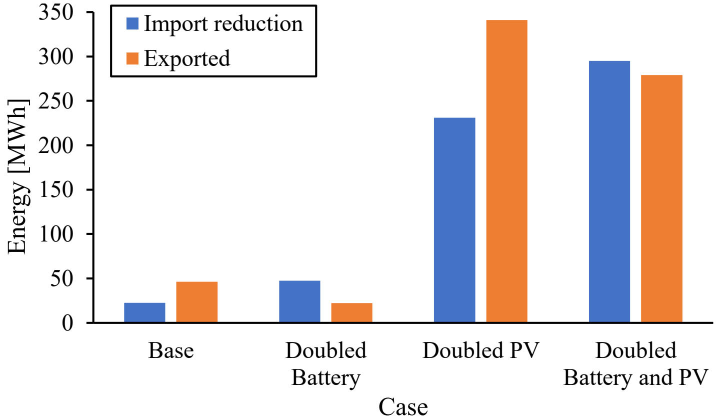

Figure 4.19: Energy import reduction and exported energy in each case scenario

4.3.5 Influence of consumption profiles

An essential factor that impacts all of the previous results is the compatibility of the consumption profiles. The consumption profiles have a significant impact on several aspects of the microgrid's behavior. A change in the consumption pattern can easily affect the amount of energy shared and the currents experienced in the lines. To illustrate this concept, the proposed methodology is applied to the DC microgrid, but the consumption profile of Node C is shifted by different time increments. For example, in Fig. 4.20, the consumption of Node C is shifted two hours forward. The impact that these shifts have on the results is outlined below.

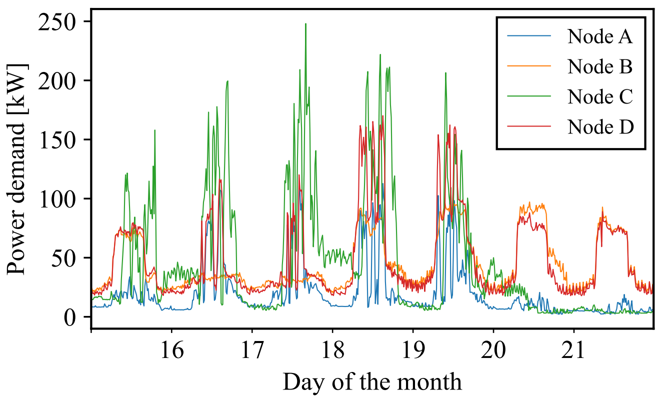

Figure 4.20: Typical consumption profile with Node C shifted two hours forward

Fig. 4.21 presents the variation in the total line losses as the consumption profile of Node C is shifted. The results indicate that a one hour shift in either direction will result in a reduction of the line losses. This effectiveness stems from the fact that by shifting the consumption, the peak demand of Node C no longer aligns with the peak demand of other nodes. Thus, the amount of current that will flow in the lines is reduced. In this case study, shifting the consumption forward is more effective in reducing the number of losses. This can be explained by looking at the profiles shown in Fig. 4.22. Node C has a peak in demand that occurs in the morning. By shifting its consumption foward by two hours, as shown in Fig. 4.22, this peak demand occurs when PV panels are producing more energy and other loads demand less power. This results in a lower amount of current circulating in the microgrids, thus reducing the losses. A 10% line losses reduction is achieved with a 4 hour shift. This 10% corresponds to a reduction of 0.9 MWh.

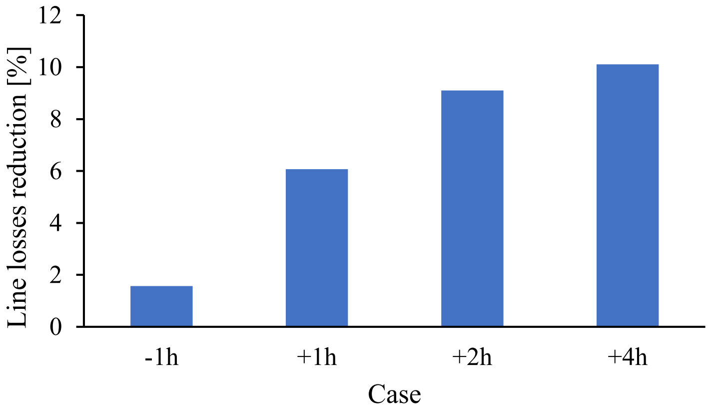

Figure 4.21: Total line losses reduction with shifted consumption profile for Node C

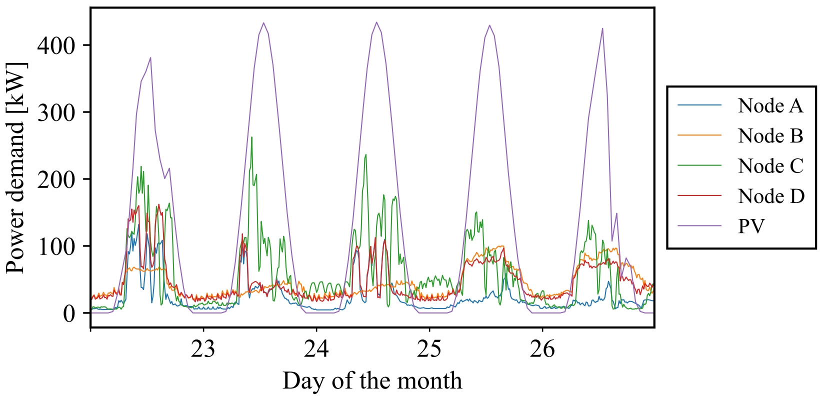

Figure 4.22: Consumption profile of Node C shifted two hours foward compared to PV profile

As previously mentioned, the peak demand of Node C does not align itself with that of the other consumers in these scenarios, as illustrated in Fig. 4.23. A one hour foward shift in the consumption profile results in a reduction of peak power demand by 7.56 % (61 KW) compared to the base case. This lower peak demand potentially simplifies microgrid operation by making it easier for the microgrid to meet its own demand. A 4 hour shift causes a reduction of 12.11 % which corresponds to a reduction of 37.73 kW. Additionally, it may allow for sizing the converter connecting to the main

AC grid with a lower power rating, offering potential economic benefits.

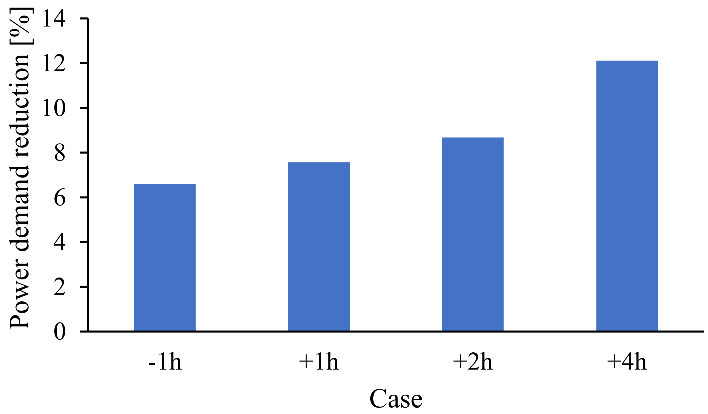

Figure 4.23: Peak power demand reduction with shifted consumption profile for Node C

4.3.6 Multiple points of connection

As previously discussed, nodes close to the point of connection to the AC main grid experience higher currents due to all the imported energy having to transit from right to left. In this section, the possibility of adding a second point of connection to the main grid on the left side is explored, as shown in Fig. 4.24.

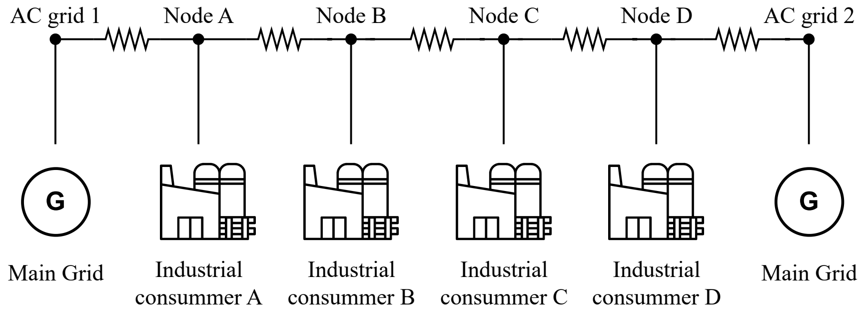

Figure 4.24: Industrial DC microgrid test grid layout with two points of connection to the main AC grid

The DC microgrid is once again simulated but with two points of connection to the main AC grid. Through these two points of connection, energy can be imported from both ends, leading to improved voltage regulation as shown in Fig. 4.25. The voltage deviations of Nodes A, B, and C are less significant compared to the base case depicted in Fig. 4.16. With the option to exchange energy through either AC grid node, not all the energy needs to pass through node D, resulting in reduced currents in the lines and smaller voltage differences between each node. Fig. 4.26 shows a box plot of the currents in each line with two points of connection to the main grid. Compared to the base case, where all imported energy passes through a single point of connection, the current flowing through the point of connection to the main grid is now split between the two AC grid nodes. Notably, the maximum current experienced by the line connecting Node C to Node D is significantly reduced, whereas Line B to C experiences a smaller reduction, and Line A to B shows a slight increase.

The more evenly distributed line currents also lead to lower total line losses. Indeed, the line losses, in this case, are reduced from 8.90 MWh to 4.01 MWh. Another advantage of this layout is the increased reliability for connecting to the main AC grid since two points of connection are available. However, it's important to consider that a second point of connection to the grid incurs an additional cost. Therefore, there is a tradeoff that needs to be considered.

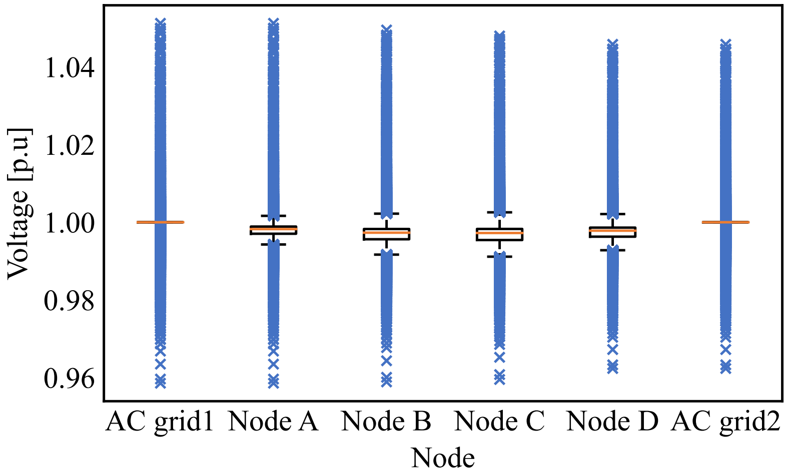

Figure 4.25: DC microgrid with two points of connection to the main grid node voltage box plot: median, first and third quartile, 1.5 interquartile range, and outliers

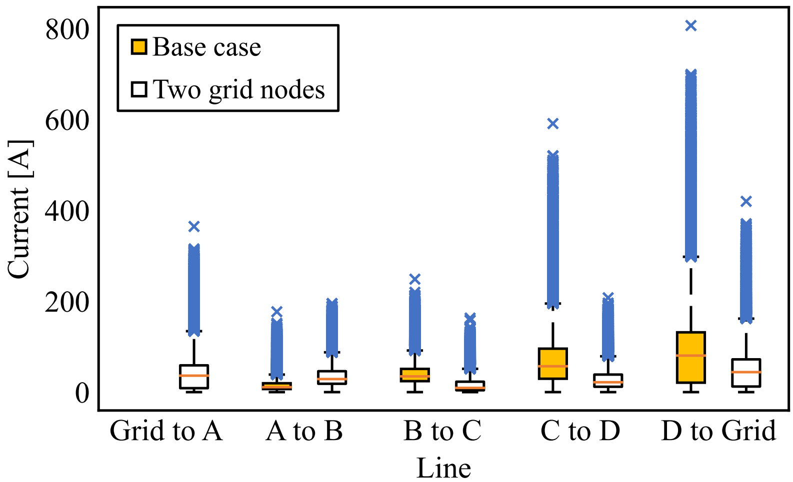

Figure 4.26: DC microgrid with two points of connection to the main grid line current box plot comparison: median, first and third quartile, 1.5 interquartile range, and outliers

4.4 Comparison of Unipolar and Bipolar DC Microgrid Performance

With the developed tool, one last analysis is performed. This is a comparison of the performance between a unipolar microgrid and a bipolar microgrid. The sequential linearized power flow is used to calculate the performance of each system. The comparison is performed in terms of the experienced voltage deviations, median and maximum currents, and the line losses. Two other possibilities are evaluated: a bipolar system with a reduced line cross-section and a unipolar system with an increased voltage. The DC microgrid used for the comparison is shown in Fig. 4.27. It is a radial network with a single point of connection to the main AC grid at its end. The microgrid consists of 8 different industrial prosumers each having his own load, PV production, and a droop-controlled battery.

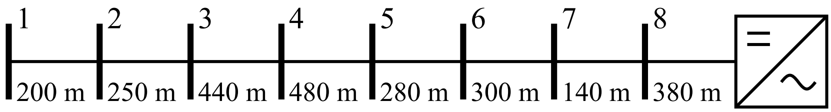

Figure 4.27: DC microgrid layout for performance comparison

The consumption profiles consist of metering data sampled every 15 minutes over a period of 12 months. Historical irradiance data corresponding to the Western European region is used for PV production. An example of the consumption over one week is shown in Fig. 4.28.

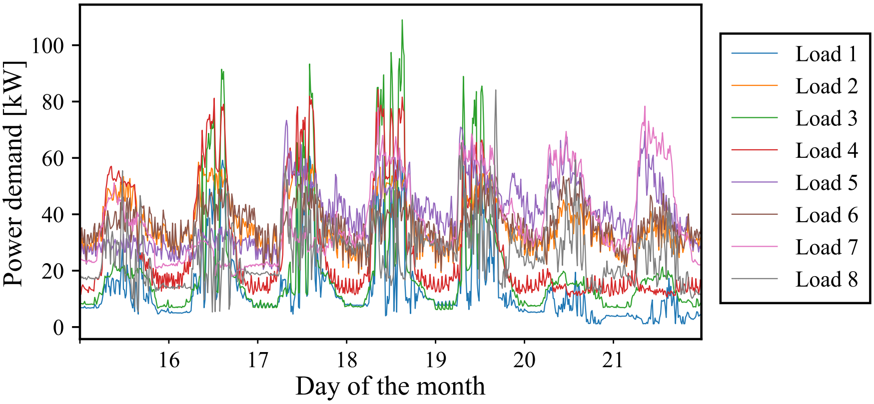

Figure 4.28: Typical consumption profile for a week in June

The yearly consumption and PV production for each prosumer are given in Table 4.14. To make a valid comparison between the two DC bus configurations, the 8 prosumers are divided into two groups of four for the bipolar system. Furthermore, the groups were selected to ensure similar consumption and PV production on both poles. The reasoning is as follows. First, having groups of similar sizes allows power sharing between the prosumers, as would be found in a unipolar system. This is also why similar PV production is used as a criterion. Second, ensuring similar consumption minimizes the amount of voltage unbalance between the poles. These constraints help create a bipolar system that is comparable to the unipolar configuration in its functioning and exchanges. Thus, in the bipolar microgrid, the positive pole has a yearly load of 1207.68 MWh and PV production of 699.57 MWh. The negative pole has 923.90 MWh and 623.35 MWh for the load and PV production, respectively. Despite the similar yearly demand on both poles, voltage unbalance may still occur due to variations in consumption at each time step.

Table 4.14: Prosumer parameters and pole distribution in the bipolar DC microgrid

Prosumer	**Yearly Demand [MWh]**	**Yearly PV Production [MWh]**	**Battery Capacity [kWh]**	**E-rate**	**Bipolar Pole Position**
1	120.80	115.18	340	0.5	-
2	314.99	152.45	450	0.5	+
3	178.85	194.80	575	1	+
4	238.53	186.33	550	0.8	-
5	362.37	210.04	620	0.5	+
6	317.10	152.45	450	1.2	-
7	351.47	142.29	420	1.5	+
8	247.46	169.39	500	1	-
Total	2131.58	1322.92	3905		

The distribution lines initially used have a cross-section of 500 mm^2. The length and resistance of each line between prosumer are given in Table 4.15.

Table 4.15: Distribution Line Parameters with a 500 mm^2 conductor

Line	**Length [m]**	**Resistance [Ω]**
1 to 2	200	0.0077
2 to 3	250	0.0096
3 to 4	440	0.0169
4 to 5	480	0.0184
5 to 6	280	0.0108
6 to 7	300	0.0115
7 to 8	140	0.0054
8 to Grid	380	0.0146

4.4.1 700 V with a 500 mm^2 cross-section

Fig. 4.29 shows box plots of the voltages found in the unipolar system and each pole of the bipolar system throughout the simulated year, using nominal voltages of 700 V and ±700 V, respectively. From the median and the first and third quartiles, it can be observed that the voltage remains close to the nominal value. Both bipolar poles show a tighter spread and a closer 1.5 IQR range. For the sake of clarity, the outliers have been omitted in the following box plots.

These results are obtained by implementing the described sequential power flow in Python. The simulation of the year involves performing 35036 time steps. With an intel core i5-10300H procesor and 32 GB of ram, it takes 9 minutes with 27 seconds to simulate the unipolar microgrid. The bipolar microgird takes 19 minutes to simulate. The increase in time is due to it having to consider an additional pole. The negative pole is independent of the positive pole.If the power limit of a battery is reached on the negative pole, it can cause the system to iterate even if there is no conflict on the positive pole.

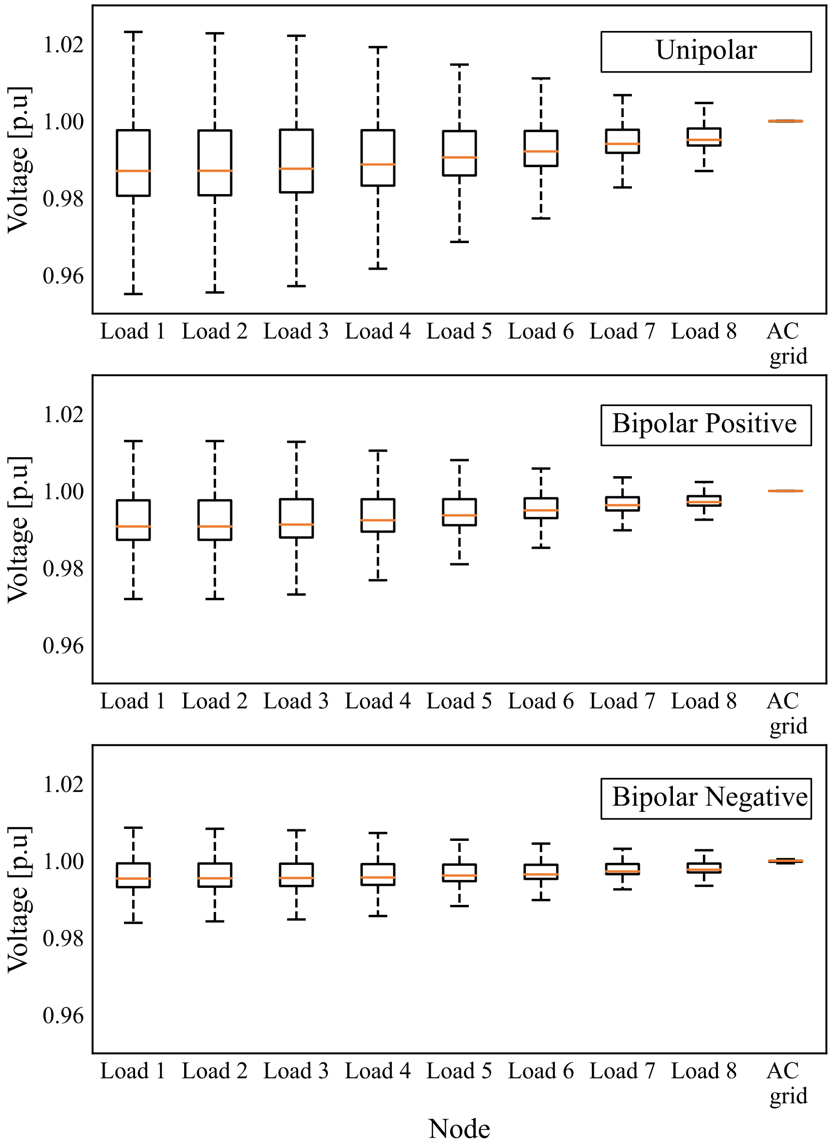

Figure 4.29: Unipolar and bipolar DC microgrid node voltage box plot comparison: median, first and third quartile, and 1.5 interquartile range

Fig. 4.30 shows the highest experienced voltage deviations, i.e., the highest outliers. The unipolar system generally experiences the highest voltage deviations, reaching a minimum of 0.9295 V p.u at its lowest point. Meanwhile, the positive and negative poles show a better voltage quality, with lower experienced deviations. The positive pole registered a minimum of 0.9441 V p.u, and the negative pole a minimum of 0.9397 V p.u.

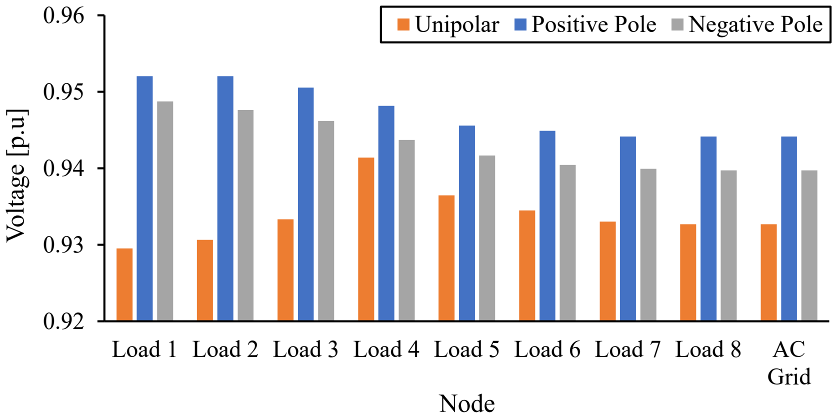

Figure 4.30: Highest Experienced Voltage Deviations

The difference in the voltage deviations can be attributed to the experienced currents in each system. Fig. 4.31 and Fig. 4.32 show the median currents in the lines and the highest current experienced, respectively. The unipolar system experiences significantly higher median and maximum currents. This can be explained by the fact that, when all the energy is imported from the main AC, in the unipolar system, all the imported energy from the main AC grid is channeled through the rightmost part of the grid. Here, this current must supply the demand of 8 prosumers. In contrast, in the bipolar system, this demand is divided between the two poles. The high current in the unipolar system leads to higher voltage drops in the lines, and the need for a more significant difference in voltage between the nodes to transfer the power. This results in higher voltage deviations. It is also noticed that the median and maximum currents show a descending pattern from right to left. This pattern is also due to the chosen topology: When moving to the left side, the amount of current that will flow corresponds to the demand of fewer prosumers at each step.

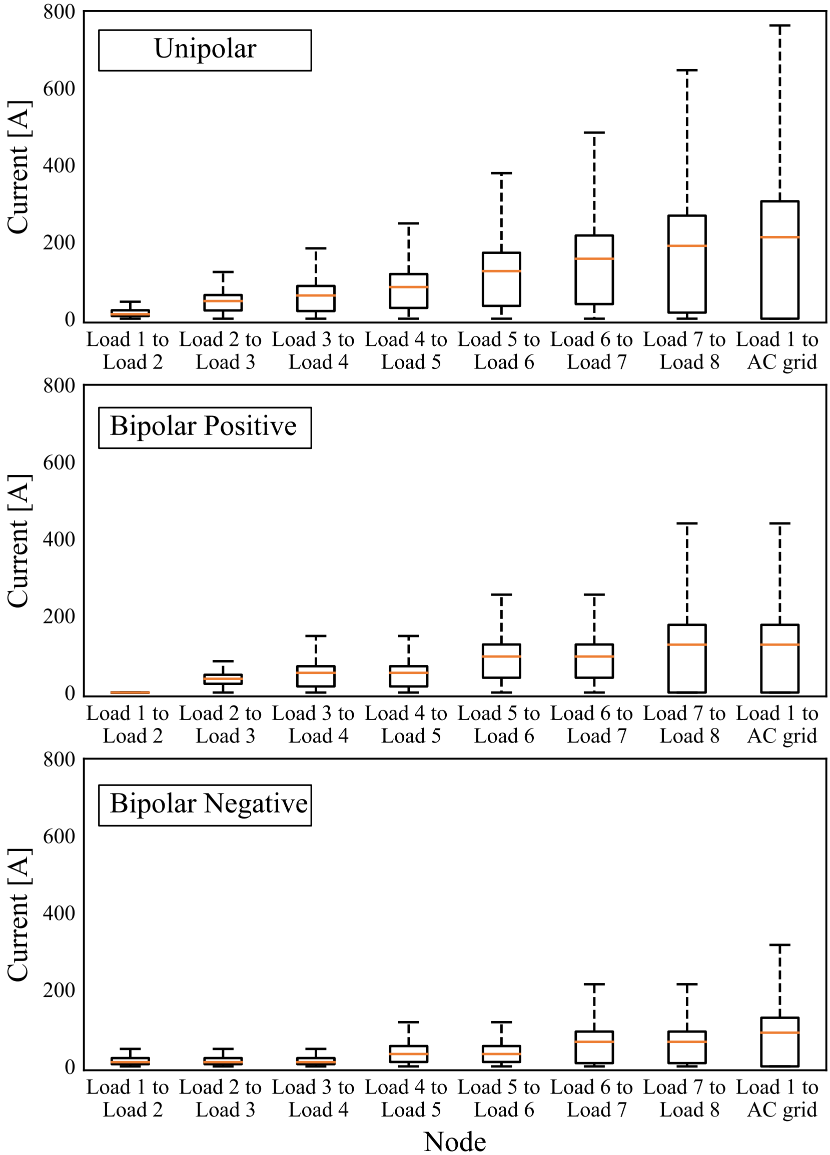

Figure 4.31: Unipolar and bipolar DC microgrid line current box plot comparison: median, first and third quartile, and 1.5 interquartile range

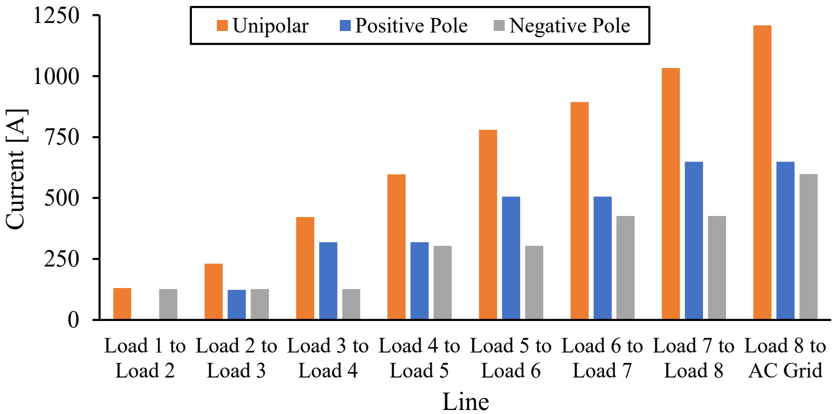

Figure 4.32: Registered max currents

The line losses experienced in each case are shown in Fig. 4.33. The bipolar system exhibits close to 7.5 MWh fewer losses than the unipolar system. Furthermore, 2.4 MWh of the losses occur in the neutral conductor due to the voltage unbalance. If the system were always balanced, it would result in a system with almost half the amount of losses compared to its unipolar counterpart.

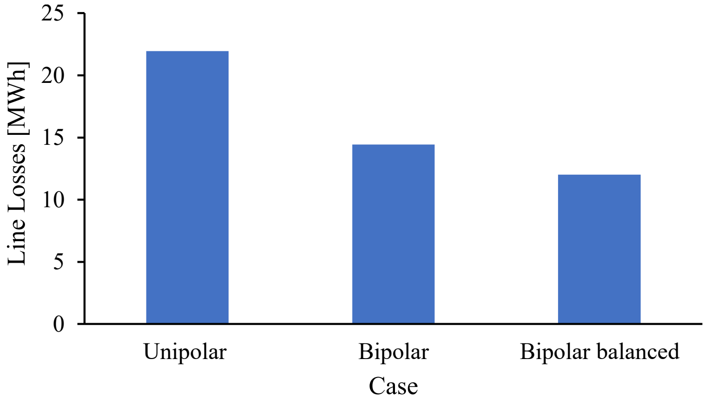

Figure 4.33: Annual line losses in each system

4.4.2 Bipolar system with a reduced 300 mm^2 cross-section

As the currents experienced by the bipolar system are lower, it is possible to reduce the cross-sections of the lines. While this decision offers an economic advantage, it will also increase the losses in the system. To show the viability of using a lower cross-section, the bipolar microgrid is simulated again using a line cross-section of 300 mm^2, resulting in an increase in line resistance of almost 67% (0.0384 Ω/km to 0.0641 Ω/km). Fig. 4.34 shows the box plot for the voltage in this case. With the smaller cross-section, the spread of the quartiles and the 1.5 IQR range has increased. The resulting box plot for the positive pole is similar to that of the unipolar system. The negative pole retains better voltage regulation, but it is worse compared to its 500 mm^2 counterpart.

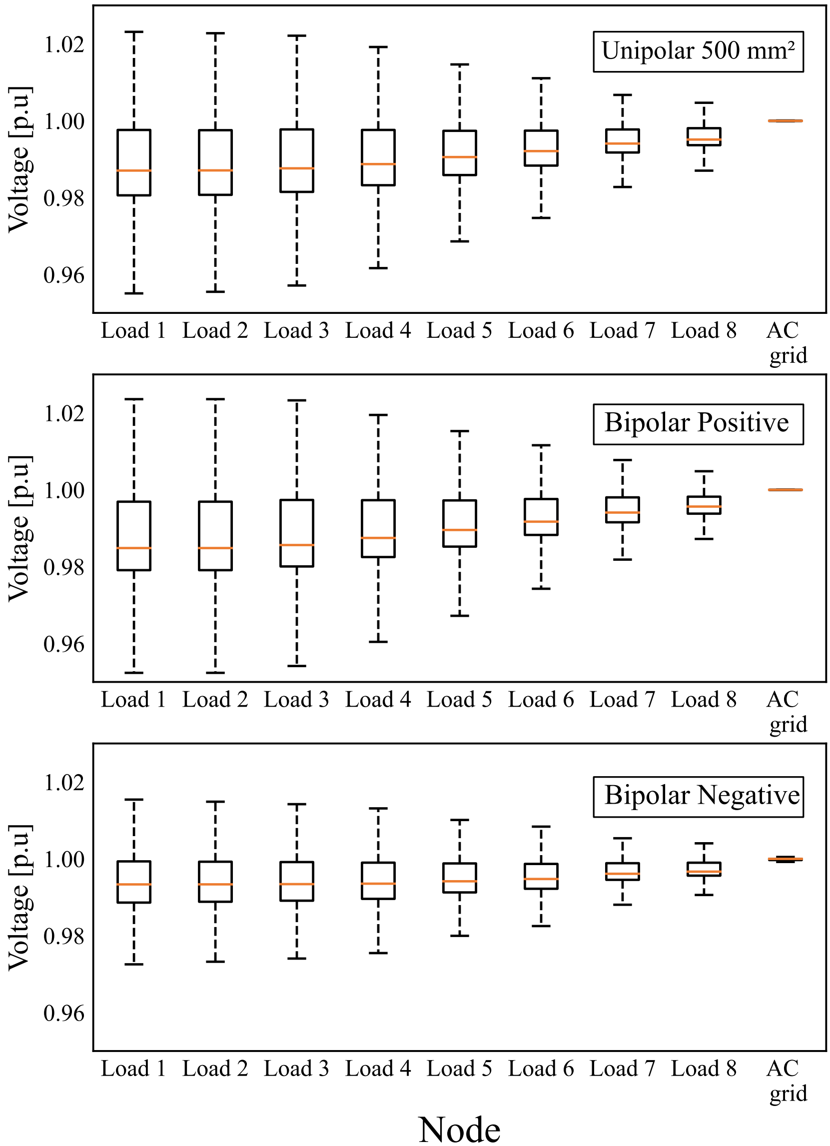

Figure 4.34: Unipolar and 300 mm² cross-section bipolar DC microgrid node voltage box plot comparison: median, first and third quartile, and 1.5 interquartile range

Fig. 4.35 shows the changes in the highest voltage deviations registered. The voltage in the positive and negative poles has been degraded for most of the nodes. However, the highest voltage deviations reached are on par with the unipolar microgrid with a 500 mm^2 cross-section. The resulting line losses are also shown in Fig. 4.36. The bipolar system with a lower cross-section shows slightly higher losses compared to the unipolar system. However, if the system was balanced and the losses in the neutral are removed, the bipolar system would still have fewer losses even with the reduction in the cross-section.

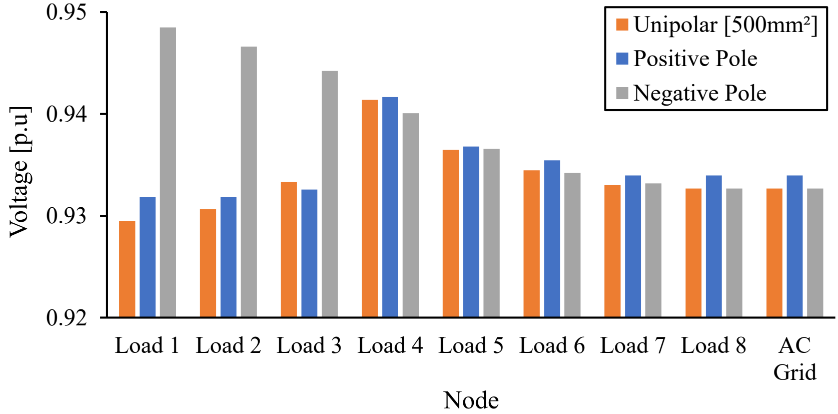

Figure 4.35: Highest voltage deviations in a bipolar system with a 300 mm^2 cross-section

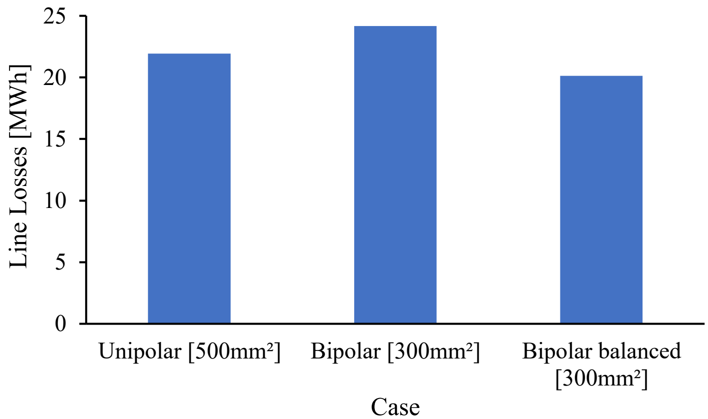

Figure 4.36: Annual line losses in a bipolar system with a 300 mm^2 cross-section

4.4.3 Increased voltage unipolar system

Three additional cases for the unipolar system are considered, featuring nominal voltages of 1.4 kV, 1 kV, and 850 V. The highest voltage deviations for these cases are shown in Fig. 4.37. The resulting box plots are shown in Fig. 4.38. The 1.4 kV system shows a better voltage than the bipolar system. Meanwhile, for 1 kV and 850 V cases, the voltages are comparable to those of the positive pole and negative pole in the bipolar system.

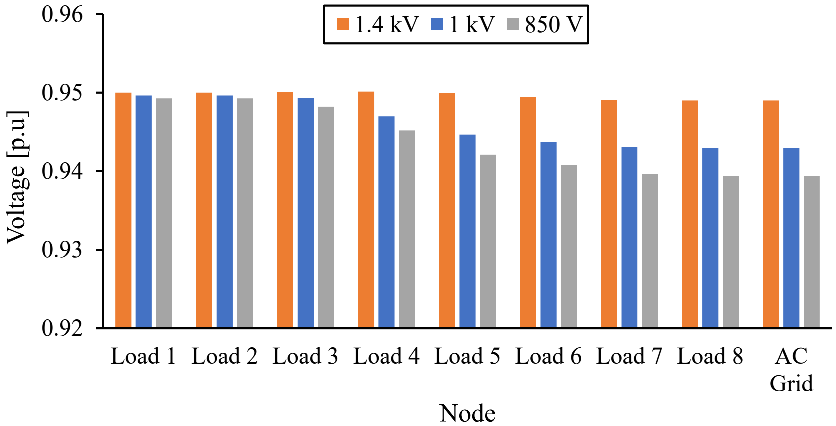

Figure 4.37: Highest voltage deviations in unipolar systems with an increased nominal voltage

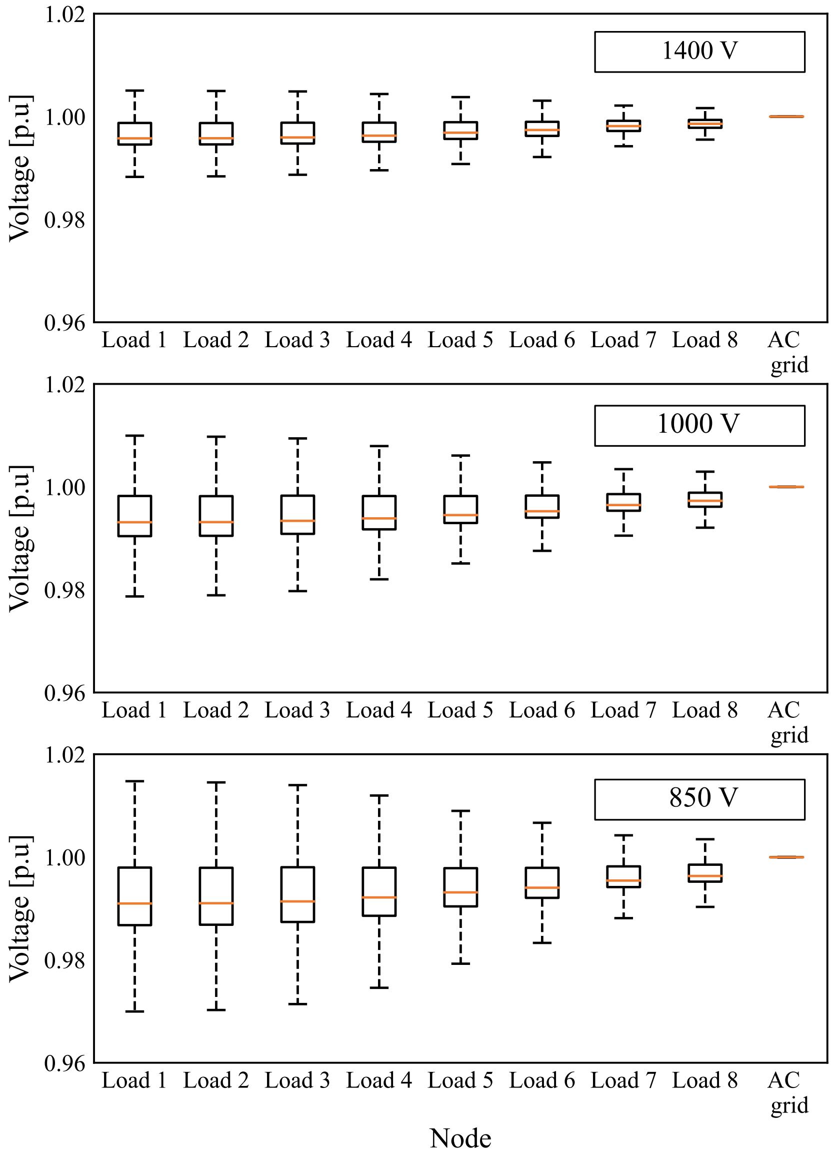

Figure 4.38: Unipolar with an increased nominal voltage node voltage box plot comparison: median, first and third quartile, and 1.5 interquartile range

The max currents experienced and the currents box plot in these microgrids are shown in Fig. 4.39 and Fig. 4.41. The 1.4 kV system exhibits values close to those found on the bipolar system. However, the bipolar system experiences these amplitudes on both poles. Meanwhile, the 1 kV and 850 V microgrids show improvements compared to the 700 V unipolar microgrid. Nevertheless, the registered max currents are higher than those of the bipolar system. The line losses of these unipolar systems are shown in Fig. 4.40. For the 1.4 kV system, the experienced line losses are significantly reduced. At 1 kV, the losses are slightly lower than what the balanced bipolar system would have. Finally, the 850 V microgrid has losses that are on par with the unbalanced bipolar microgrid.

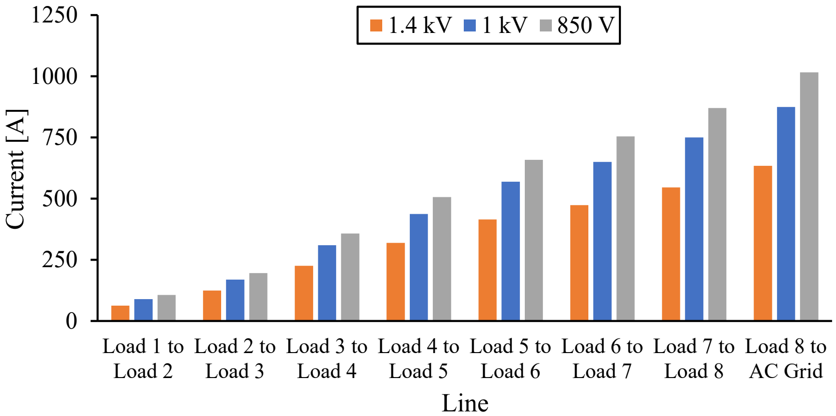

Figure 4.39: Maximum currents in unipolar systems with increased nominal voltage

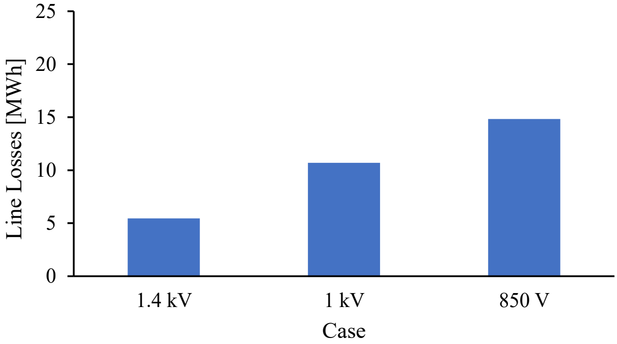

Figure 4.40: Annual line losses in unipolar systems with an increased nominal voltage

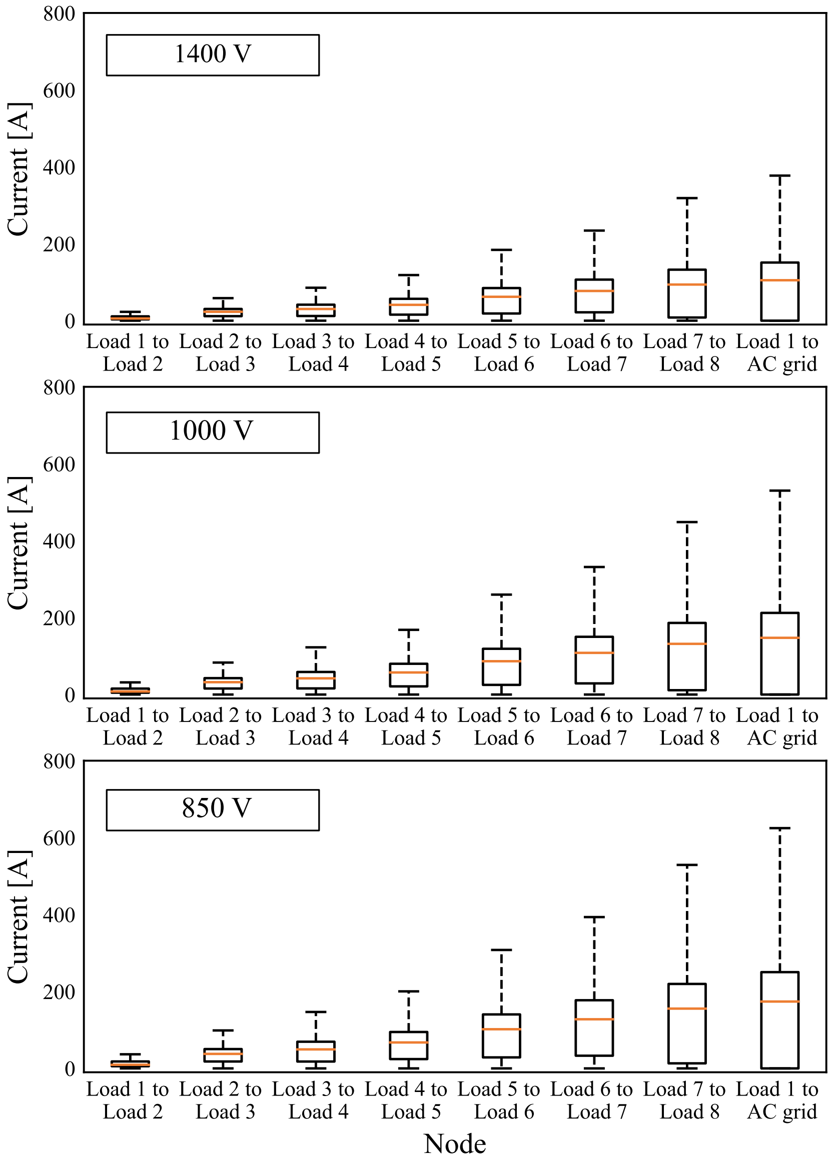

Figure 4.41: Unipolar with an increased nominal voltage line current box plot comparison: median, first and third quartile, and 1.5 interquartile range

4.4.4 Results analysis

The results indicate that the bipolar network experienced voltage unbalances, leading to losses in the neutral cable, which accounted for 16.7% of the total losses. The voltage unbalance could be exacerbated by an uneven distribution of prosumers among the poles or incompatible consumption patterns. Therefore, the importance of balancing the voltage between the two poles is emphasized. Despite the unbalance, the bipolar system exhibited fewer losses and better voltage regulation than the unipolar system. Additionally, using a lower cross-section in the bipolar system resulted in performance similar to that of the unipolar system.

The results also showed that a unipolar system with twice the voltage can perform better in terms of currents and losses. Unipolar systems with nominal voltages of 1 kV and 850 V show similar results in terms of voltage regulation and exhibit comparable losses when compared to a ±700 V balanced bipolar grid and a ±700 V unbalanced bipolar grid, respectively. As discussed in Chapter 2, the choice of voltage level is still a subject of research. Moreover, there are additional factors to consider. The converters used would need to be rated for higher voltages. The costs and conversion losses of these converters can differ significantly from the base case. Another element to consider is the voltage to the ground, which would be lower in the bipolar system than in the higher voltage unipolar configurations. Finally, using a bipolar network implies dividing the prosumers into groups. Depending on their production, storage, and consumption, this could result in a lower percentage of energy sharing and more energy being sent to the main AC grid. The choice between the two voltage architectures is both a technical and economic decision. It can be constrained by external factors such as limits imposed on the currents or required voltage levels.

4.5 Conclusion

In this chapter, the importance of power flow studies has been highlighted. As explained, DC microgrids require different methods for these studies compared to traditional AC grids. A method based on linearization has been shown. This method has then been adapted for bipolar microgrids. With the available power flow methods, a sequential algorithm was developed to allow the simulation of the microgrids across a period of time. Through sequential simulation, results that can aid in the sizing of the microgrid can be obtained. Furthermore, it is possible to estimate the amount of energy that will be consumed locally. Finally, a comparison between unipolar and bipolar microgrids was presented. This comparison highlighted the advantages of each topology and situations where one might be a more attractive solution than the other.

Research related to this domain is still actively developing. Other methods to calculate the power flow in DC systems have been proposed and continue to be iterated upon. Another closely related area of interest is the implementation of optimal power flows (OPF). In OPF studies, optimizations are performed to find the best parameters or configurations while utilizing power flow calculations. This type of optimization calculations could be used to study the influence of a level 3 controller that can coordinate the different load profiles/demands to optimize a financial parameter for example.

In the author's opinion, the work shown in this chapter has potential for expansion. For example, topology changes during simulation have not been considered in the previous examples. These types of changes could correspond to faults or temporary maintenance. If a system is simulated during an extended period, these type of events could take place. The proposed tool can be modified during simulation to implement such events. One possible area of interest is the development of an OPF program built upon the developed linear power flow method. The linear nature of the tool could prove beneficial when integrating it with an optimization program. Another viable route of research would be to analyze the impact of different types of loads. The ongoing energy transition is expected to introduce new types of loads such as EVs, electric trucks, heat pumps, and electrolyzers. These loads will be integrated into DC microgrids, necessitating an assessment of their impact. Therefore, representing these loads as either constant power, current, impedance loads or a combination of them poses an interesting question. Additionally, understanding the consumption profiles of these loads over extended periods of time will be necessary to analyze their impact. One final area of investigation could involve modeling different control methods. In the proposed tool, only droop control is considered and no second level controllers are implemented. However, there exists a variety of first level controllers. It would be interesting to model their current injection to assess how different controllers perform over time. This approach could also extend to second level controllers or the inclusion of an EMS.

Chapter 5

Modeling of Power Electronic Converters

Chapter contributions

- Average models for DC/DC and AC/DC converters are presented
- A state-machine model for three-port converters is proposed
- An analysis of the switching frequency of three-port converters is developed
- An averaged model for three-port DC/DC/DC converters is developed
- Different control schemes for three-port DC/DC/DC converters are proposed and demonstrated

Chapter 3 focused on the development of control systems that give the appropriate commands to the different converters. To fully realize the dynamic model of the microgrid, the converters receiving these commands have to be modeled. The models can be implemented with different levels of details. Because the inner structure of the converters is well known, it is indeed possible to realize a switched model. This model type is implemented by connecting the individual components (resistances, inductors, capacitance) along with the corresponding switches. While this type of model provides high fidelity, it also carries a heavy computational burden. In DC microgrids, nearly every energy source and load are interfaced by a converter. Simultaneously simulating numerous converters using switched models becomes impractical due to computational constraints. Therefore, there is interest in developing simpler models that maintain converter characteristics while reducing computational load. This chapter focuses on developing different averaged models of power electronics converters for microgrid simulation. First, DC/DC converters are presented followed by a similar implementation for AC/DC converters. The final part of the chapter presents a detailed study of three-port converters. Various aspects are explored, ranging from their commutation process to average modeling.

5.1 DC/DC converters

The majority of converters in a DC microgrid consist of DC/DC converters. Indeed, most consumer loads are DC appliances. Furthermore, PV installations and battery energy storage also output their energy natively in DC. Thus, in a DC microgrid system, it is expected to have several DC/DC converters. These converters and their characteristics need to be modeled. There are various approaches to modeling converters, as shown in the flowchart in Fig. 5.1. In this figure, two main paths are shown: state-based modeling (shown in grey) and average modeling (shown in blue). Both approaches can lead to three end results (shown in orange): state-space and line transfer functions, duty cycle to output transfer functions, and canonical circuit models.

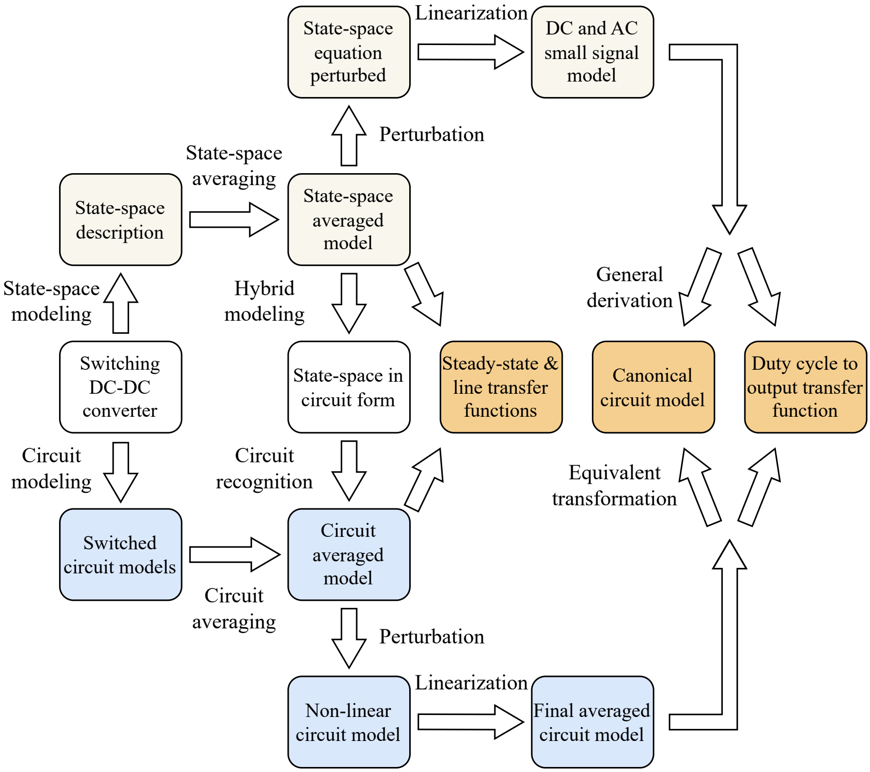

Figure 5.1: Flowchart of averaging approaches in modelling switching DC/DC converters [100]

In this work, the average model of converters utilizes the average circuit model, which can be derived from circuit averaging or from the state-space model. This average model is derived considering the principle of the DC transformer. It is a circuit realization of the state-space model that allows representing the relationships between the voltages and currents of the converter [100], [101]. The concept of the DC transformer was proposed in [100] as: "a useful circuit realization of the basic averaged model." In [100], it is developed that this circuit representation is equivalent to that of an ideal transformer. Thus, ideal DC and AC transformers were proposed. The DC transformer operates as an ideal transformer with a conversion ratio.

The DC transformer can be derived as follows [101]. The output voltage V_{out} of a DC/DC converter can be expressed as shown in (5.1), where the output voltage depends on the input voltage V_{in} and the converter conversion ratio $M(d)$, which is a function of the duty cycle d. Considering that the input power is equal to the output power, the input current i_{in} can be defined as shown in (5.2) through $M(d)$ and the output current i_{out}.

$$V_{out} = M(d)V_{in} \tag{5.1}$$
$$i_{in} = M(d)i_{out} \tag{5.2}$$

From the previous equations, it can be seen that the input current and the output voltage can be modeled as independent sources, and these equations coincide with those of an ideal transformer. This results in the implementation of a DC transformer as shown in Fig. 5.2. The input side of the transformer is represented by a current source, while the output side is represented by voltage sources. The voltage source imposes the output voltage based on the control duty cycle d and the corresponding function $M(d)$. The current source on the primary side acts as a load to represent the current that must be drawn from the energy source connected to the primary side. The current that needs to be drawn can be determined by measuring the output current and utilizing the known converter relationships.

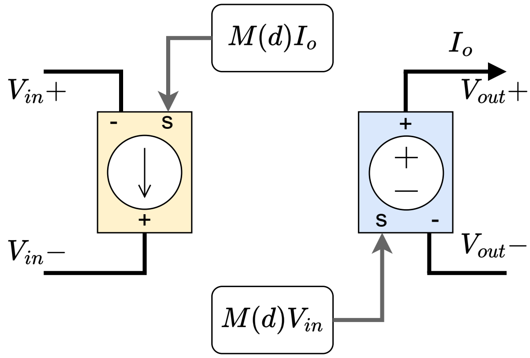

Figure 5.2: DC transformer equivalent circuit

Due to the simulation's time scale focus and the scope of this work, intricate elements associated with switching are not needed. Therefore, the objective of the averaged model is to represent the energy transfer from one side to the other while respecting/reacting to the control signal provided to the converter and maintaining the impedance of the converter.

The three fundamental DC/DC converters are the Buck converter, Boost converter, and Buck-Boost converter, each fulfilling a different function. The Buck and Boost converters respectively allow stepping down or stepping up the voltage. In contrast, the Buck-Boost converter allows performing both the step-up and step-down operations. These converters can be assimilated to an ideal DC transformer with a turn ratio of $1 : M(d)$, where $M(d)$ is a function of the duty cycle d. The definition of $M(d)$ is well known for these converters and is provided in Table 5.1.

Table 5.1: DC/DC converters transfer ratio

Converter	Buck	Boost	Buck-Boost
M(d)	d	$\frac{1}{1-d}$	$\frac{-d}{1-d}$

The work in [100] derived the DC transformer average model for buck converter, boost converter, and buck-boost converters, as shown in Fig. 5.3, Fig. 5.4, and Fig. 5.5, respectively. Fig. 5.3 illustrates the implementation of a buck converter via a switched model and the previously described DC transformer model. In Fig. 5.3a, the traditional switch model is shown where the duty cycle modulates via PWM the switching. In contrast, Fig. 5.3b shows the implementation of the buck converter using the DC transformer. The DC transformer is represented with the transformer symbol shown in Fig. 5.3b. This symbol represents one side being modeled with a current source while the other is via a voltage source as illustrated previously. Notice that in the DC transformer model, when the duty cycle equals 1, the circuit corresponds to the switched model with the switch closed, while if the duty cycle equals zero, the circuit corresponds to the switched model with the switch open.

Notice that in the boost converter and buck-boost converter representation, the complementary duty cycle $d' = 1 - d$ is used. It is also possible to move the impedances from one side of the transformer to the other; however, changes in impedance due to the duty cycle need to be accounted for. For example, lets consider that in a buck converter with $M(d) = d$ the load resistance R is to be move to the primary side. The equivalent load resistance on the primary side R' is calculated as $R' = R/d^2$. This can be useful if the duty cycle is fixed, but in dynamic simulations where the duty cycle constantly changes, it is of less interest.

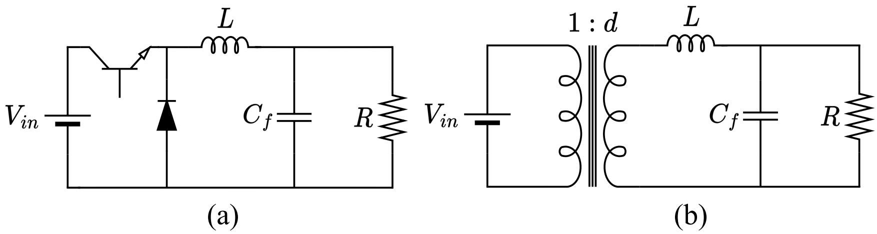

Figure 5.3: Buck converter models: (a) Switched model (b) DC transformer model [100]

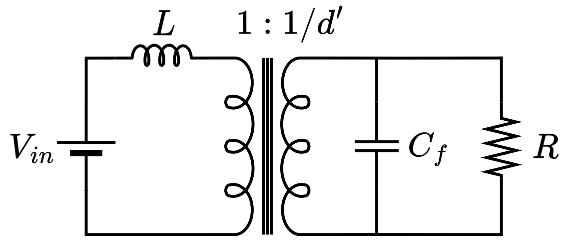

Figure 5.4: Boost converter DC transformer model [100]

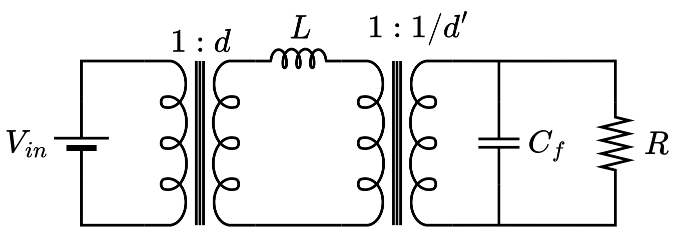

Figure 5.5: Buck-Boost converter DC transformer model [100]

5.1.1 Switched model vs average model simulation

To further illustrate the concept of the average model using the DC transformer, the performance of both models is demonstrated. This will be achieved by implementing both models in Matlab/Simulink. The example for the switched buck converter provided in simulink is used. This example can be accessed by typing “power_BuckConverter” in the command window. The simulated circuit is shown in Fig. 5.6. Here, an input voltage of 200 V is applied along with a duty cycle of 0.5, resulting in an output voltage of 100 V. The average model with the DC transformer is shown in Fig. 5.7. It's noteworthy that the main distinction is that the switching element has been replaced by the DC transformer.

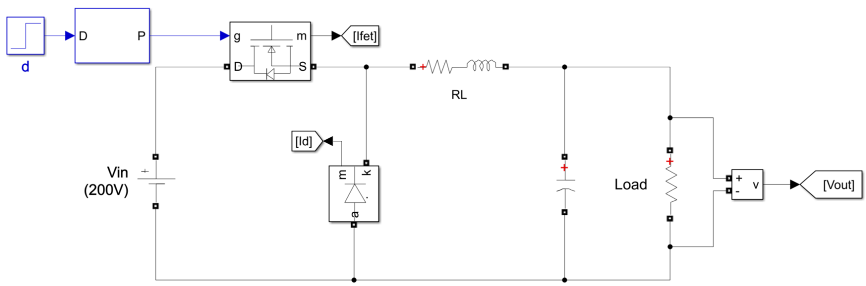

Figure 5.6: Compared buck converter switched model

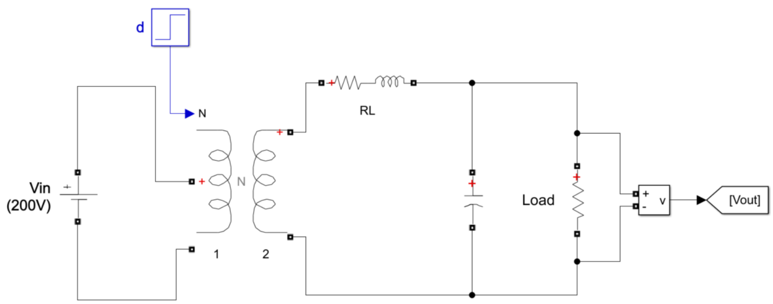

Figure 5.7: Compared buck converter average model

Both models are simulated, and the obtained result is shown in Fig. 5.8. Fig. 5.8a shows the waveform of the output voltage, reaching the expected 100 V. It is seen that the average model presents the same dynamics as the switched model. Fig. 5.8b zooms on the steady-state, showing the difference between the two models. It can be observed that due to the switching nature, there's a ripple in the output voltage in the switched model. In contrast, the average model produces only the DC value. Fig. 5.9 shows the response of both models to a step in the duty cycle from 0.5 to 0.75. As before, the average model follows the response correctly, providing the same result. The shown figures highlight the advantage of this type of average model: maintaining converter dynamics without incorporating switching dynamics, resulting in a less computationally demanding simulation.

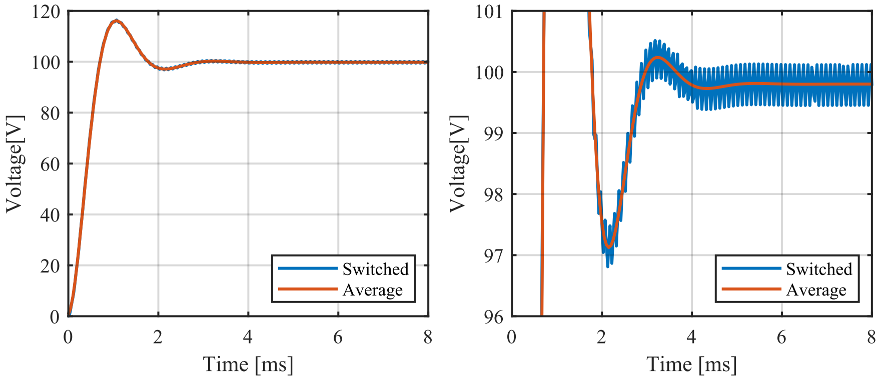

(a) (b)

Figure 5.8: Comparison switched model and average model with constant duty cycle: (a) Output voltage waveform (b) Zoom on steady-state value

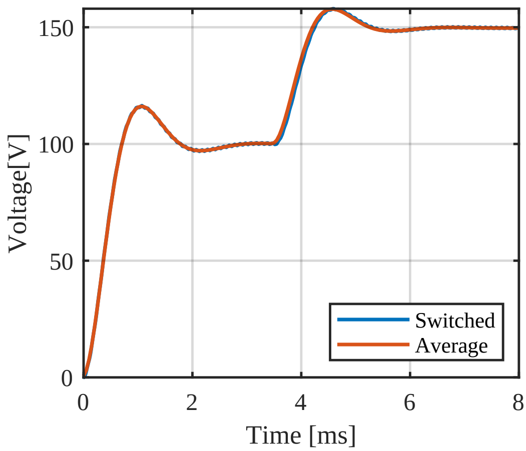

Figure 5.9: Comparison switched model and average model: step in duty cycle

Notice that although the voltage conversion could be implemented directly using only the DC transformer, it is crucial to include the different elements such as output filters. Indeed, these elements provide the impedance of the converter and thus characterize its behavior. Fig. 5.10 compares the response of the switched, average, and the DC transformer without impedances to a step in load demand. Notice that the DC transformer without impedance does not have the same initial response. Furthermore, when the load is increased at $t = 3.5$ ms, it is seen that the switched and average models experience a voltage dip. In contrast, the DC transformer alone does not exhibit this response.

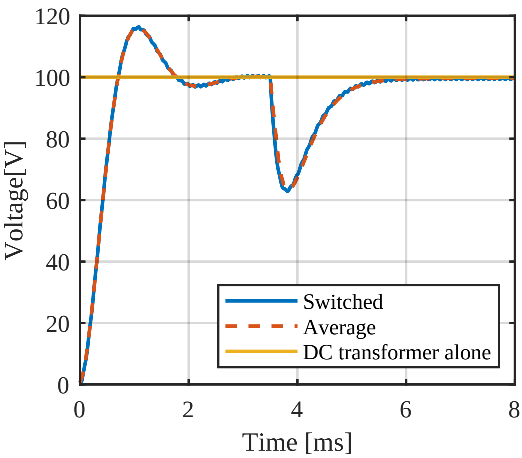

Figure 5.10: Switched model, average model, and DC transformer without impedance response to a step in load demand

5.2 DC/AC converters

Although distribution occurs in DC, AC to DC converters might still be needed. They can be required for certain loads and certainly for power exchange between the main AC grid and the DC microgrid. The same logic used for the DC/DC converters is applied here. One side of the converter is represented using voltage sources, while the other side is represented using current sources. The DC part is implemented via the current sources, while the AC network is connected to voltage sources. When dealing with an AC system utilizing a three-phase system, multiple voltage sources are used to input the correct behavior into the AC part. Three different converters are modeled: single-phase inverters, three-phase inverters, and Neutral Point Clamped (NPC) inverters. The duty cycle will be used to generate the corresponding PWM signals. Depending on the pulse given, the voltage source will assume a value is either negative, positive, or zero. The square signal generated by the voltage source is then smoothed via an LC filter, resulting in the required sine wave.

Let us first develop as an example the model for a half-bridge single phase inverter as shown in Fig. 5.11. Two current sources act as the current drawn from the DC source. Two sources are used as each one drains from either the upper or lower capacitor. On the right side, a single source is used as only one is needed in a single-phase inverter. The reference signals given to the sources are generated via the control shown in Fig. 5.12. The duty cycle is used to obtain the pulse given to the switch. The value of the positive voltage with the pulse and the negative voltage with the complementary pulse are added to generate the AC part voltage reference. The $V_{DC}\pm$ value is multiplied by the current in the inductor. This is the power given to the AC part. The calculated power can then be divided by the voltage to obtain the current in the DC part.

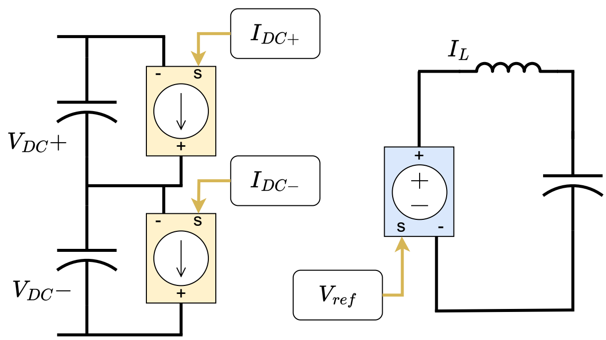

Figure 5.11: Average half-bridge single-phase inverter

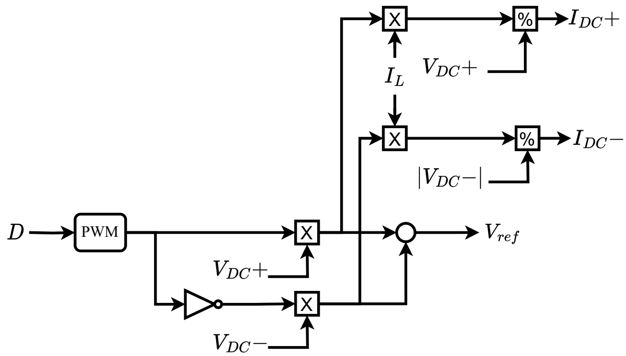

Figure 5.12: Average half-bridge-single phase inverter control signals

In the case of a three-phase inverter, the DC part can be implemented as shown before or with a single current source, depending on what is considered to be connected to the DC part. For the AC part, rather than using one voltage source for each phase, a simplification can be made. Instead of modeling the different switches, two voltage sources can be used to generate the output voltage. The three-phase inverter considered is shown in Fig. 5.13.

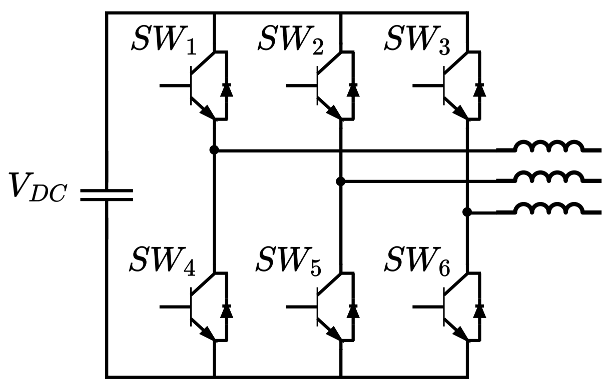

Figure 5.13: Three-phase inverter structure

There are six switches however the switches in the same branch are complementary. Thus, whenever SW_1 is close SW_4 must be open. To model this converter only switches SW_1, SW_2, and SW_3 need to be considered. The switching pattern of the inverter and the resulting line-to-line voltage are shown in Table 5.2. Notice that there is an overlap in certain combinations. This leads to the conclusion that by implementing two voltage sources representing the line-to-line voltages, the proper line-to-neutral voltages can be obtained. In this case, it is considered that V_{AB} and V_{BC} are the ones implemented. Thus, the AC side of thesimplified converter can be implemented as shown in Fig. 5.14. The DC side of the converter can be implemented using DC current sources, as previously shown, based on the power provided by the AC side.

Table 5.2: Three-phase inverter voltage pattern

Switching pattern			**Line to neutral voltage**			**Line to line voltage**		
SW1	SW2	SW3	V_{AN}	V_{BN}	V_{CN}	V_{AB}	V_{BC}	V_{CA}
0	0	0	0	0	0	0	0	0
1	0	0	2/3 V_{DC}	-1/3V_{DC}	-1/3V_{DC}	V_{DC}	0	$-V_{DC}$
1	1	0	1/3V_{DC}	1/3V_{DC}	1/3V_{DC}	0	V_{DC}	$-V_{DC}$
0	1	0	-1/3V_{DC}	2/3 V_{DC}	2/3 V_{DC}	$-V_{DC}$	V_{DC}	0
0	1	1	-2/3 V_{DC}	1/3V_{DC}	1/3V_{DC}	$-V_{DC}$	0	V_{DC}
0	0	1	-1/3V_{DC}	-1/3V_{DC}	-1/3V_{DC}	0	$-V_{DC}$	V_{DC}
1	0	1	1/3V_{DC}	-2/3 V_{DC}	-2/3 V_{DC}	V_{DC}	$-V_{DC}$	0
1	1	1	0	0	0	0	0	0

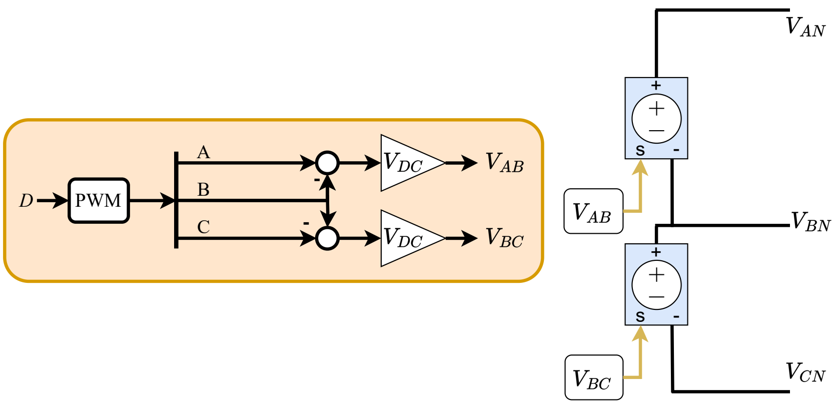

Figure 5.14: Average three-phase inverter AC side representation

The final model developed is the average model for an NPC inverter, as shown in Fig. 5.15. One difference between this converter and a full bridge inverter is the number of control pulses required due to the number of switches. Indeed, an NPC inverter requires 12 pulses for its operation. For the average model, the control of the pulses must be streamlined to determine what value to assign to the two voltage sources representing the AC side of the converter.

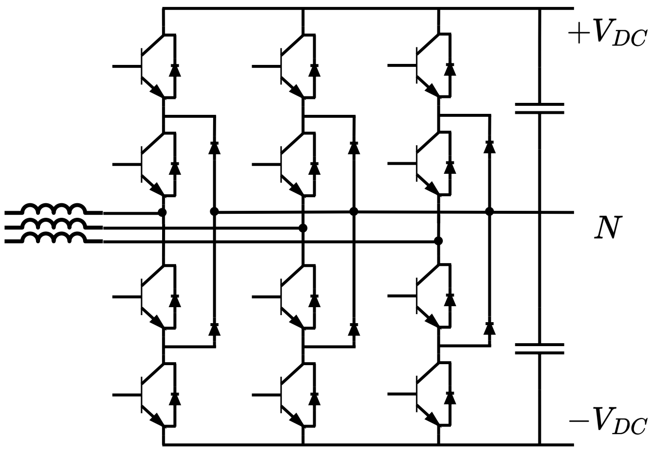

Figure 5.15: NPC inverter structure

To simplify the control, the four switches of each leg are considered. The switches grouped in Fig. 5.16 provide different outputs based on their combinations. The possible combinations are shown in Table. 5.3 and can output three possible voltage values: $+DC/2$, $-DC/2$, and 0. By analyzing the table, it can be seen that the output voltage can be determined with only two of the signals. If the pulses of SW_1 and SW_4 are considered, the result can be determined by the following subtraction: $SW_1 - SW_4$. Whenever SW_1 has a pulse, the output will be positive. Equally, if SW_4 has a pulse, the output will be negative. If both are activated, the output will be zero volts.

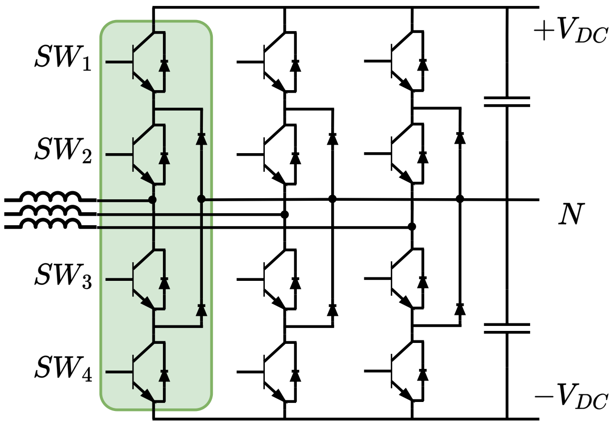

Figure 5.16: NPC inverter leg switches

Table 5.3: Switching behaviour of a NPC converter leg

SW_1	SW_2	SW_3	SW_4	Output voltage
On	On	Off	Off	$V_{DC}/2$
Off	On	On	Off	0
Off	Off	On	On	$-V_{DC}/2$

Therefore, the control for the voltage sources can be achieved by first determining the voltage of each leg with the previously mentioned method. Then, the identified voltages for each leg can be added as shown in Fig. 5.17. Through these operations, the reference voltage for each voltage source can be obtained. Note that instead of using the reference $V_{DC}/2$, the measured voltage of the capacitor can also be used. To generate the reference for the current source, the power supplied on the AC side is calculated; this power is then divided by two and further divided by the DC voltage to obtain the reference current. It is divided by two as the positive and negative DC voltages have their own current source. The resulting average model is shown in Fig. 5.18.

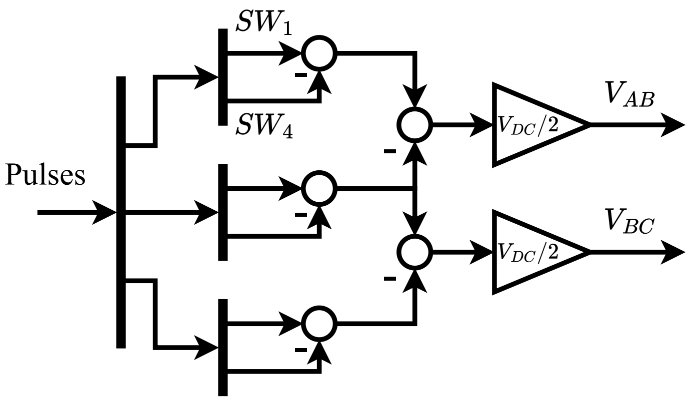

Figure 5.17: Average NPC inverter voltage sources control

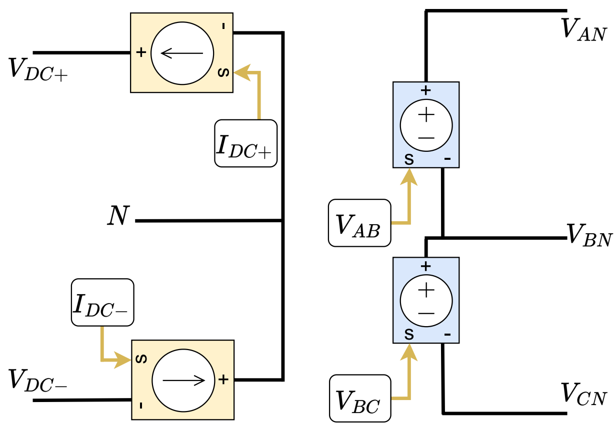

Figure 5.18: Average NPC inverter

5.3 HFAC link converter

In this section, converters that use High Frequency AC (HFAC) links are introduced. Among these converters, three-port converters provide the advantage of reducing the number of converters needed to connect different elements such as batteries, PVs, and loads. The three-port converter analyzed is a soft-switched HFAC link converter. This converter can be seen as an extension of a buck-boost converter where a capacitor is placed in parallel with the link inductor. The LC circuit creates resonating transients that allow for Zero voltage Switching (ZVS). This type of converter can be classified as a Quasi-square wave (QSW) converter [102]. The use of an HFAC link provides several advantages [103], [104]:

- It allows to change the link voltage for each converter port
- It provides electrical isolation between the converter ports
- It has an inherent bi-directional power flow capability
- It provides a reduction in the size and weight of heat dissipating components

The parallel HFAC link architecture was initially introduced as a universal power converter in [105]. The authors of [106] proposed a soft-switching AC link converter for medium and high-power applications, overcoming previous drawbacks such as an inability to supply output current at low voltages and a large dead time. This work was further explored in [107], showing the proposed converter as an AC/AC or AC/DC buck-boost converter for medium voltage applications. In [108], [109], the capabilities of the HFAC link converter as a PV inverter were demonstrated, highlighting its negligible converter losses due to the ZVS and the compactness of its high-frequency link inductor. The work in [110] connects several PV strings with different voltage levels via the use of this converter. In [111], the capabilities of the ZVS HFAC link inverter as a multiport system were demonstrated. The application of this converter for AC microgrid is explored in [112], where it is proposed that the application of the converter can be expanded to more than three ports. This three-port converter architecture has also been proposed as a technical solution for efficient delivery of energy to electric vehicle charging terminals in [113]. The work in [113] illustrated the converter's versatility, highlighting its capability to operate as an AC/DC/DC converter or as a DC/DC/DC converter.

The following section details the operation of this type of converter. A two-port converter is presented initially to allow the reader to better understand the converter architecture. The operational principles for both two-port and three-port converters are detailed. A representation of the HFAC link behavior via a state machine is proposed. Once the behavior of the converter is explained, an analysis of the switching frequency and its computation is presented. Afterwards, the state-space models for two-port and three-port converters are developed. From these state-space models, the average model is developed and validated. For the three-port DC/DC/DC converters, two cases are studied: a converter with two sources and one load, and a converter with one source and two loads. Finally, different control methods for the developed average models are proposed. These control methods consider the different elements that can be connected to the three-port converters: PVs with maximum power point tracking (MPPT), batteries, loads, and droop control ports for DC microgrid connection. At the end of this section, a test DC microgrid is implemented to demonstrate the different control methods and the capabilities of three-port converters.

5.3.1 Operation principle of HFAC link converters

The operational principle of the converter is detailed hereafter. This is done using a two-port converter to ease the understanding of the converter. The schematic of the studied two-port HFAC link converter is shown in Fig. 5.19. The converter has two DC ports and the HFAC link composed of an inductor and a capacitor. Notice that the switches connecting the ports to the HFAC link are bidirectional switches which can be implemented through IGBTs. Thus, through the proper switching technique, both DC ports have bidirectional power flow. The case where a source is connected to DC Port 1 and feeds a load connected to DC Port 2 is considered.

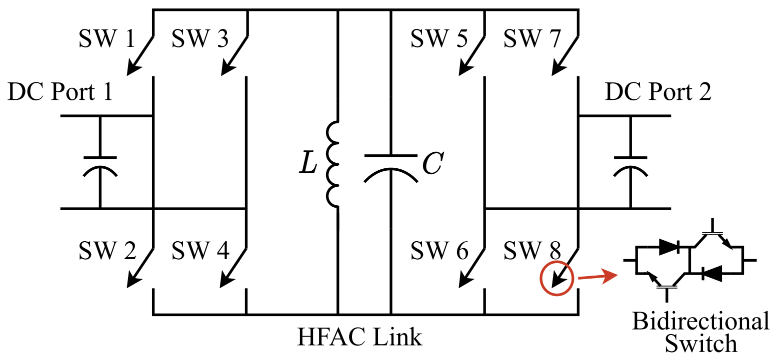

Figure 5.19: Schematic of a two-port DC/DC HFAC link converter

Mode 1: Link Charge During this first mode, illustrated in Fig. 5.20, the source connected to Port 1 charges the AC link. This connection is made via switches $SW1$ and $SW4$. The switches of the port supposed to charge the link during Mode 1 start conducting once the link voltage reaches the highest input voltage. This is to ensure that the switching occurs at zero voltage. The inductance L is then charged until the current reaches its reference value. Based on the high frequency of the link, it is considered that the voltage at the input port remains constant during this mode. From the inductance constitutive equation, it is possible to calculate the link current i_L as shown in (5.3).

$$i_L = \frac{1}{L}\int_0^t V_{DCPort1}\,dt = \frac{V_{DCPort1}(t)}{L} + i_L(0) \tag{5.3}$$

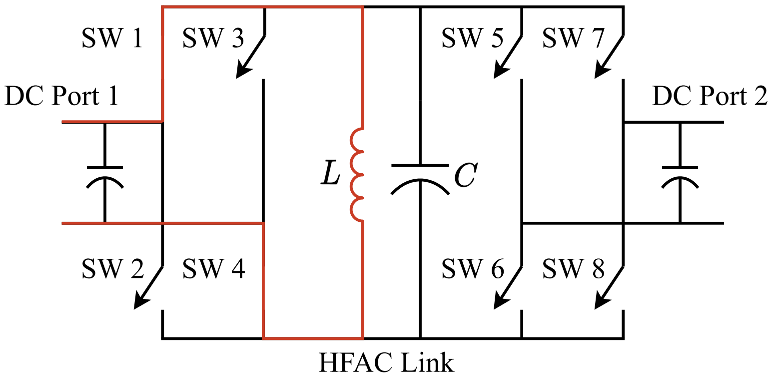

Figure 5.20: Two-port DC/DC converter circuit diagram during Modes 1 [114]

Mode 2 and 4: Partial resonance Between each charge or discharge mode, there is a resonance mode, as shown in Fig. 5.21. The objective of this mode is to change the link voltage to that of the next port. During this time, the switches do not conduct. The HFAC link will resonate, causing the voltage to change. The resonance will end when the zero-voltage condition is satisfied. This HFAC link, which is an LC parallel circuit, can be described by the following equations:

$$i_C = -i_L = C\frac{dV_C}{dt} \tag{5.4}$$

$$V_L = L\frac{di_L}{dt} \tag{5.5}$$

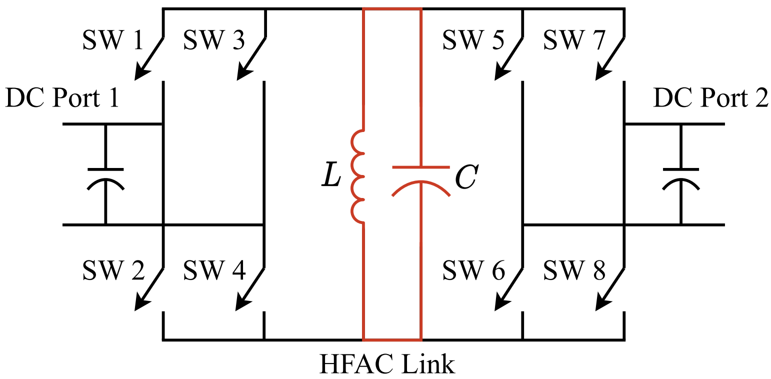

Figure 5.21: Two-port DC/DC converter circuit diagram during Modes 2 and 4 [114]

Mode 3: Link Discharge The energy stored in the link is discharged towards Port 2 via switches $SW5$ and $SW8$. The HFAC link does not fully discharge, and there is a certain amount of energy left in it. This energy is needed for the link to swing back to a predetermined voltage V_{max} that has a value slightly higher than the maximum input and output voltage [115]. This is done to guarante that if the voltage value at the end of the cycle is lower than the next voltage level there will always be enough energy in the link to swing to the next voltage value. A safety margin is for the highest voltage is considered thus resulting in V_{max}. This mode is shown in Fig. 5.22.

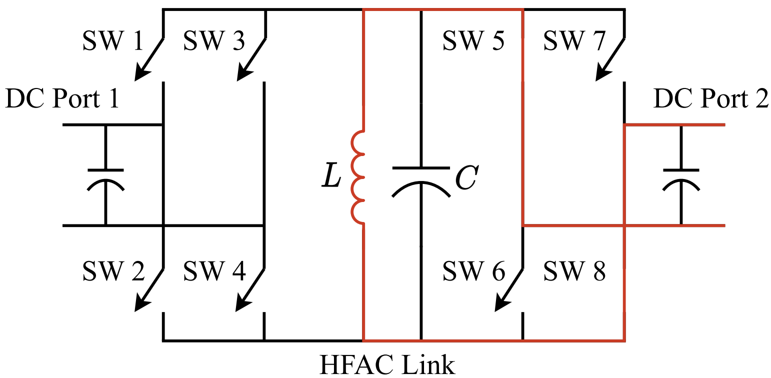

Figure 5.22: Two-port DC/DC converter circuit diagram during Mode 3 [114]

Mode 3 is followed by Mode 4. In other words, another resonance mode where the voltage will swing back to the predetermined highest voltage. This resonance is then followed by a set of modes having the same behavior as modes 1 through 4, except that the link charges and discharges with opposite polarity. Therefore, in this case, the complementary switches on the legs would be used.

The converter operating principle is summarized in Fig. 5.23. First, the HFAC link is connected to the input port. The inductance of the link is charged with a voltage $V_{DCPort1}$. Due to a constant voltage being applied to the inductance, the current increases linearly. Once it has been charged to the desired level, the HFAC link is disconnected, and resonance occurs due to the parallel LC circuit. Through this resonance, the voltage level is changed. Once the voltage level of the output port $V_{DCPort2}$ is reached, the HFAC link is connected with opposite polarity, and the inductance then discharges to the load. Since a constant output voltage is applied, the current is also discharged linearly. Once discharged, another resonance that goes through a maximum voltage level V_{max} occurs. This resonance changes the voltage back to the input voltage level. This is done with opposite polarity to transfer energy more efficiently. Notice that for a whole period T, two charge and discharge cycles are performed. Thus for one whole period there are two power transfer cycles. Note that in Fig. 5.23, a specific duration for the period is not given. This is because the duration of the period varies with the power transferred. The more the HFAC link is charged, the longer the charge and discharge will take, and consequently, the total period will be longer.

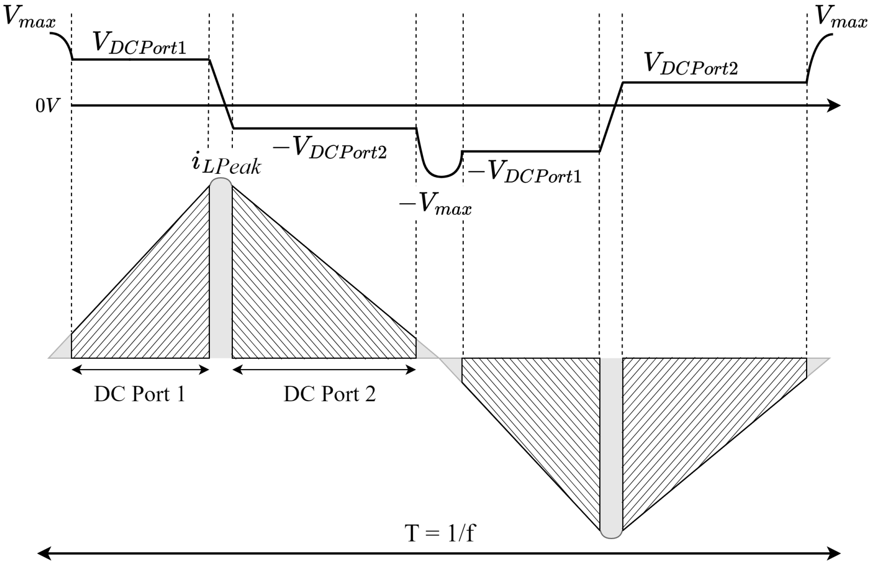

Figure 5.23: Two-port DC/DC converter HFAC link voltage and current waveform

This operation principle can be extended to three-port converters. The main difference will be that there will be either two charge cycles or two discharge cycles. This extra charge or discharge cycle implies an additional resonance period to swing to the third port voltage. The operation principle is illustrated in Fig. 5.24. Here, Port 1 and Port 2 with voltage V_1 and V_2 feed a load connected to Port 3 with voltage V_3. As shown the behavior is the same as the two-port converter but with an additional resonance and charge period. Notice that there is a specific order in which the ports are connected. The connection is performed from highest voltage to lowest when charging the link and from lowest to highest when discharging. This is done to reduce the duration of the resonance periods. The highest voltage will be closest to V_{max}. Furthermore, when discharging, it is more efficient to start from the lowest voltage as it is the closest one. Finishing the discharge at the highest voltage allows a short resonance to V_{max} and the highest charge voltage when considering the inverse polarity.

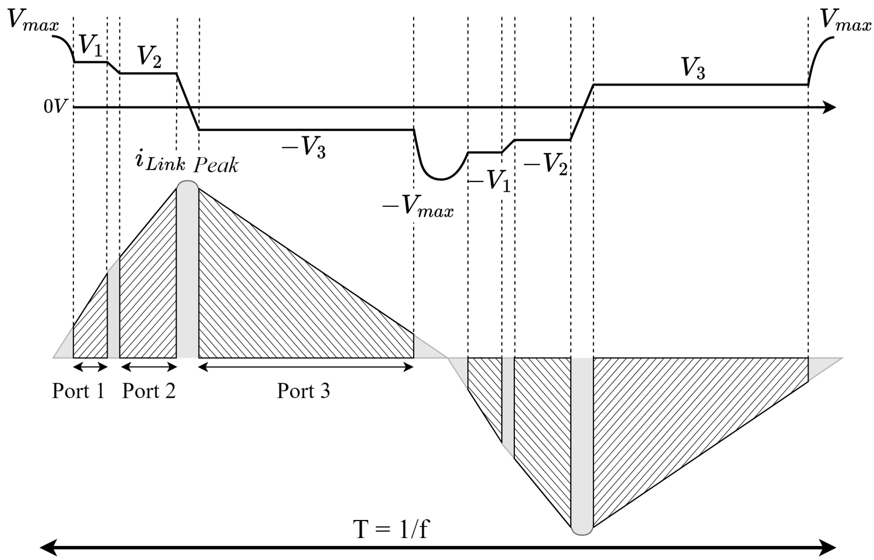

Figure 5.24: Three-port DC/DC/DC converter HFAC link voltage and current waveform

5.3.2 HFAC Link modeling and analysis

As previously mentioned, the HFAC link consists of an inductance and a capacitor in parallel. To better understand the behavior of the HFAC link, it is studied and simulated hereafter. As previously mentioned, during Mode 3 the inductor current does not reach zero when discharging. Indeed, there is always enough energy left (I_{end}) in the HFAC link to resonate to the next voltage. Particularly, in the final resonance at the end of each power cycle, a voltage V_{max} is always reached. During the charge period, the HFAC link has a starting current I_{start}, and during the discharge period, it has a final current I_{end}. Considering a two-port converter with an input voltage V_{in} and output voltage V_{out}, I_{start} and I_{end} can be defined as shown in (5.6) and (5.7), respectively [111], [115].

$$
\begin{aligned}
I_{\text{start}} &= \sqrt{(I_{\text{end}}^2 + \left(\frac{V_{C_f}}{L\omega_0}\right)^2 - \left(\frac{V_{in}}{L\omega_0}\right)^2)} \\
&= \sqrt{\frac{C}{L}(V_{\max}^2 - V_{in}^2)}
\end{aligned} \tag{5.6}
$$

$$
I_{\text{end}} = \sqrt{\frac{C}{L}(V_{\max}^2 - V_{out}^2)} \tag{5.7}
$$

The operation of the HFAC link for a two-port converter is illustrated in Fig. 5.25. By plotting the link voltage V_{Link} on the x-axis and the link current I_{Link} on the y-axis, a visual representation of the commutation cycle is obtained. The commutation cycle starts in the top right quadrant at I_{start}, where an initial positive link voltage is observed. Once the connection to Port 1 is performed, the link is charged (green arrow), resulting in the increase in the link current shown. Once the link has been charged to the desired value, resonance (yellow arrow) occurs, leading to a change in the link voltage and a horizontal shift towards the top left quadrant. This quadrant corresponds to a discharge mode, where the link is connected to Port 2 with reversed polarity, leading to the discharge (red arrow) of the link and a decrease in inductor current, as shown in the figure. Another resonance (purple arrow) takes place to start again the power cycle with reverse polarity. After resonance, the charge and discharge process starts once again, initiating from the bottom left quadrant and ending in the bottom right quadrant.

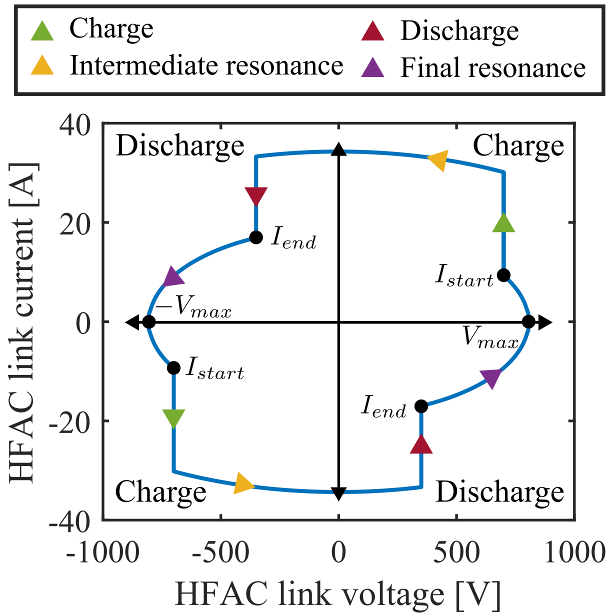

Figure 5.25: XY representation of HFAC Link behaviour

Utilizing the same XY representation, Fig. 5.26 compares the behaviour of the HFAC link to the converter from which it is derived. Fig. 5.26 compares the buck-boost converter inductor to the behaviour of the HFAC link. When comparing both converters, the differences in HFAC link converters are highlighted. First, HFAC link converters utilize a resonance period to change the voltage of the HFAC link. Secondly, HFAC link converters have horizontal symmetry due to their second power cycle using opposite polarity. Finally, the inductor of the Buck-boost converter is discharged complete at the end of each period.

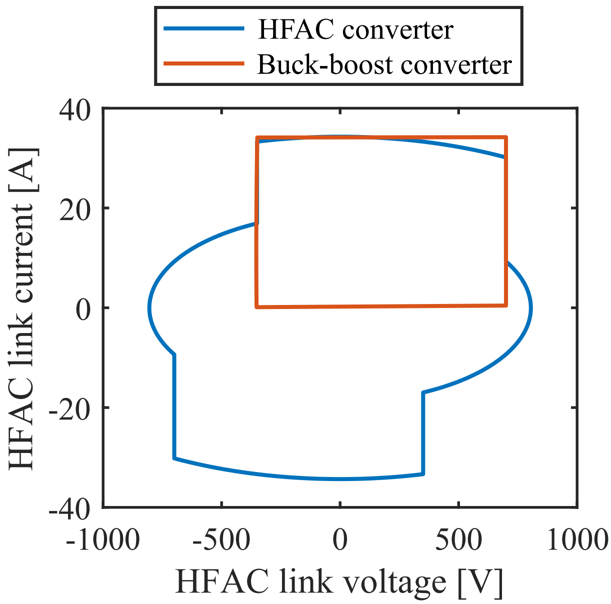

Figure 5.26: Comparison of HFAC link to Buck-boost converter

Notice that the resonance in HFAC link converters is not flat and has a small curve to it. This is due to the resonance, where both the capacitor voltage and the inductor current evolve sinusoidally. Each resonance is basically an oval or circle whose radius depends on the available energy. The difference in the radius due to the available energy is appreciated in the difference between the final and intermediate resonances in Fig. 5.27. Fig. 5.27 shows in gray the evolution of the current and voltage if the resonance is not interrupted. Two paths are shown: an inner circle representing the path that can be followed with the current I_{end}, and an outer circle representing the path that can be taken when the link is charged. It is also shown that between the highest port voltage and V_{max} a safety margin of 15% is considered.

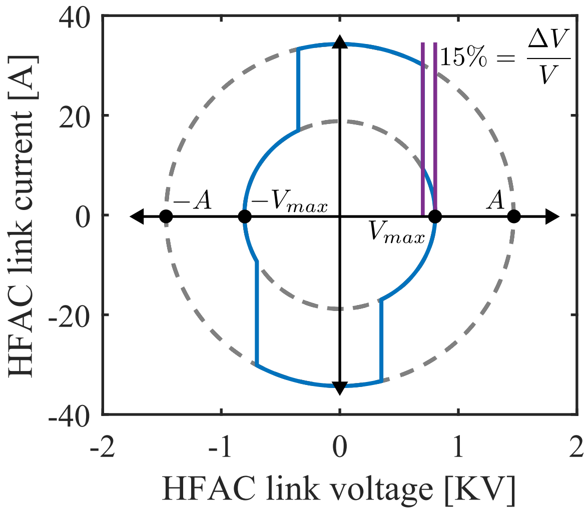

Figure 5.27: XY representation of HFAC Link voltage range

This behavior can be described by the equations of simple harmonic motion [116]. Using such equations, the resonance is modeled as:

$$V_{\text{Link}} = A\cos(\omega_0 t) \tag{5.8}$$

$$I_{\text{Link}} = \frac{A}{Z_0}\sin(\omega_0 t) \tag{5.9}$$

The definitions for ω_0, Z_0, and A are given in (5.10), (5.11), and (5.12) respectively. ω_0 is the resonance angular frequency, and Z_0 is the characteristic impedance. In (5.10) and (5.11), L is the HFAC link inductance and C is the HFAC link capacitor. A is the maximum voltage value, which can be calculated through the maximum energy that can be stored either on the capacitor E_{Cmax} or the inductor E_{Lmax}, and taking the smallest between the two as the limiting factor. Finally, ω_0 is the resonance angular frequency.

$$\omega_0 = \frac{1}{\sqrt{LC}} \tag{5.10}$$

$$Z_0 = \sqrt{\frac{L}{C}} \tag{5.11}$$

$$A = \sqrt{\frac{2(min(E_{Cmax}, E_{Lmax}))}{C}} \tag{5.12}$$

Having the values of V_{max} and the HFAC link capacitor C, the energy that needs to remain on the link can be calculated. Furthermore, with the simple harmonic motion equations, the voltage range of the HFAC link can be determined. Fig. 5.28 shows the voltage range for an HFAC link. In this example, the HFAC lin capacitor C has a value of $1.48\mu F$. The highest port voltage is arbitrarily set to 750 V and thus $V_{max} = 1.15 * 750 = 862.5$ V. Indeed, it is considered that a reasonable value for the safety margin V_{max} is 15% more than the maximum voltage. This value is proposed because a higher V_{max} would cause a longer final resonance, which is undesirable as no power is transferred during this time [115].

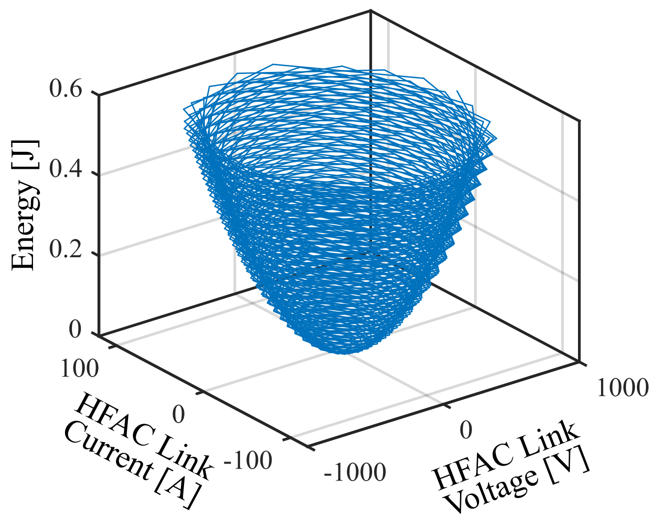

Figure 5.28: HFAC link max voltage range example

The energy in a capacitor can be defined as $E_c = 0.5\, C\, V^2$. If the desired voltage V_{max} is considered, the energy in the capacitor can be calculated as $E_c = 0.5\, C\, V_{max} = 0.5538$ joules. The energy left in the HFAC link is determined by the voltage V_{max} to be reached. If more energy is left in the HFAC link, a higher voltage range can be achieved; however, the voltage limits of the converter need to be taken into account.

The calculation of the current that needs to be left on the HFAC link depends on the different port voltage values. However, it also depends on the sizing of the components. First, to size the link inductance L two values need to be defined: the peak current in the inductance I_{Lpeak} and the desired frequency f at maximum power. As described in [112], the analysis can be based on half a cycle, as shown in Fig. 5.29, where n sources and m loads are considered.

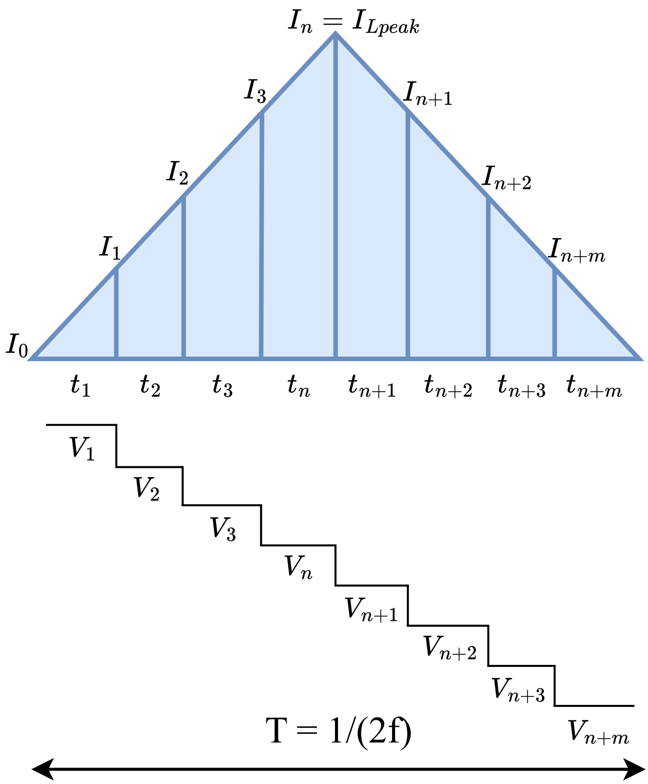

Figure 5.29: HFAC link half cycle current and voltages [112]

Based on the previous figure, the voltage of the inductor can be described by (5.13). Taking into account the trapezoidal shape, the average current is found as shown in (5.14). Thus, the exchanged power can be described by (5.15) and (5.16).

$$V_{i+1} = L\frac{I_{i+1} - I_i}{t_{i+1}} \tag{5.13}$$

$$I_{i+1,avg} = t_{i+1}(I_{i+1} + I_i)f \tag{5.14}$$

$$P_{i+1} = V_{i+1}I_{i+1,avg} \tag{5.15}$$

$$\sum_{i=0}^{i} P_{i+1} = \sum_{i=0}^{i} V_{i+1}I_{i+1,avg} = Lf\sum_{i=0}^{i}(I_{i+1}^2 - I_i^2) = Lf(I_{i+1}^2 - I_0^2) \tag{5.16}$$

Considering $I_0 = 0$, it is possible to relate the input power P_{in} and the peak current of the link as shown in (5.17). By manipulating (5.17), the expression for the peak current is found as shown in (5.18).

$$\sum_{i=0}^{n-1} P_{i+1} = LfI_{L,peak}^2 = P_{in} = -\sum_{i=n}^{n+m-1} P_{i+1} \tag{5.17}$$

$$I_{L,peak} = 2 * \sqrt{P_{in}} \sum_{i=0}^{n+m-1} \frac{\sqrt{\sum_{i=0}^{i} P_{i+1}} - \sqrt{\sum_{i=0}^{i} P_i}}{V_{i+1}} \tag{5.18}$$

Once $I_{L,peak}$ is known, the HFAC link inductance L can be sized. The input power to the inductor P_{in} can be calculated as $P_{in} = E/T$. Knowing that $T = 1/2f$, one can find $P_{in} = 2f\frac{1}{2}LI_{L,peak}^2$. Thus, the value of L can calculated as shown in (5.19).

$$L = \frac{P_{in}}{fI_{Lpeak}^2} \tag{5.19}$$

The remaining element to be sized is the HFAC link capacitor C. The HFAC link capacitor is chosen to have resonance periods smaller than the charge and discharge periods. This is because during these times, there is no power transfer, and thus it is undesired for it to take longer [115]. It is desired to keep the resonance period lower than 5% of the power cycle when at full power. This constraint is considered because there is no power transfer during the resonance period, so it is desirable to keep them as short as possible. [109], [111], [115]. Taking these constraints into consideration, the capacitor is sized so that:

$$\omega_0 = \frac{1}{\sqrt{LC}} >> 2\pi f \tag{5.20}$$

State Machine representation

From the previous descriptions, all the elements needed to simulate the behavior of the HFAC link are available. From (5.3), it is known that the current will increase or decrease linearly according to the voltage. Thus, the charge and discharge can be calculated using (5.3). In addition to the charge and discharge, the resonance needs to be simulated. From the previous description, it is now known that the resonance can be described using simple harmonic motion, and thus, it can be described using (5.8). The HFAC link is implemented for a two-port converter using the mentioned equations through the state machine shown below:

```
switch (state)

case 1, %Charge
    if (cycle*Il < I1)
        Il = Il + (u/L)*deltat;
        L1 = abs(Il);
    else
        state = 2;
        Ec = 0.5*C*(u^2);
        El = 0.5*L*(Il^2);
        A = sqrt(2*(Ec+El)/C);
        tinit = cycle*(1/wo)*acos(u/A);
    end

case 2, %Resonance
    if(cycle*u > -V2)
        tinit = tinit+deltat;
        Il = A*sin(wo*tinit)/Zo;
        u = A*cos(wo*tinit);
    else
        state = 3;
    end

case 3,  % Discharge
    if (cycle*Il > Ie)
```

```
            Il = Il + (u/L)*deltat;
            L2 = abs(Il);
        else
            state = 4;
            tinit = cycle*(1/wo)*acos(u/Vmax);
        end

    case 4, %Final resonance
        if (cycle*Il > -Is)
            tinit = tinit+deltat;
            Il = Vmax*sin(wo*tinit)/Zo;
            u = Vmax*cos(wo*tinit);
        else
            state = 1;
            cycle = -cycle;
        end
end
```

Case 1 describes the charge process. While the reference current I_1 is not achieved, the link charges linearly through the measured voltage u. The rate at which the link charges takes into account the simulation time step via the variable *deltat*. Once the reference is achieved, the total energy in the HFAC link is calculated, and the attainable maximum voltage A is determined. The current position on the resonance curve is also registered. Once this is done, the state machine moves to case 2, which uses the simple harmonic motion equations to describe the resonance. Once the next port voltage is attained, the state machine moves to Case 3, which describes the discharge process. The link is discharged until the end current is reached. At this point, the final resonance is performed in Case 4, and the process is repeated with opposite polarity. Through this process, the HFAC link voltage and current can be obtained as shown in Fig. 5.30.

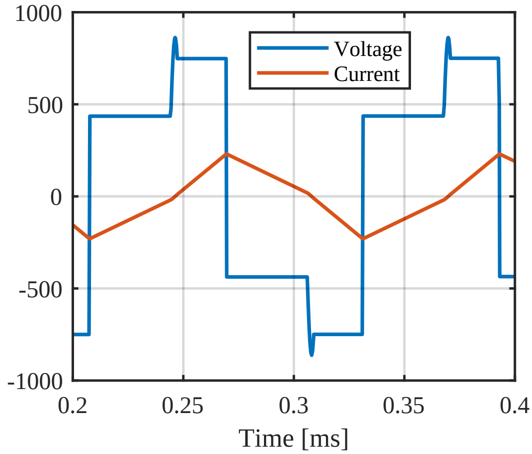

Figure 5.30: HFAC link state machine implementation

The state machine previously described can be extended to three-port converters. To achieve this, more cases need to be added to take into account the additional charge or discharge periods and the additional resonance period. Fig. 5.31 demonstrates such an implementation. Fig. 5.31a illustrates the XY representation where the charge and discharge quadrants can be identified. Notice that the illustrated case corresponds to two sources feeding one load. This can be appreciated when looking at the top right quadrant where the link is charged at two different voltage levels. Fig. 5.31b shows the evolution in time of the HFAC link voltage and current. The two charge periods can be equally appreciated.

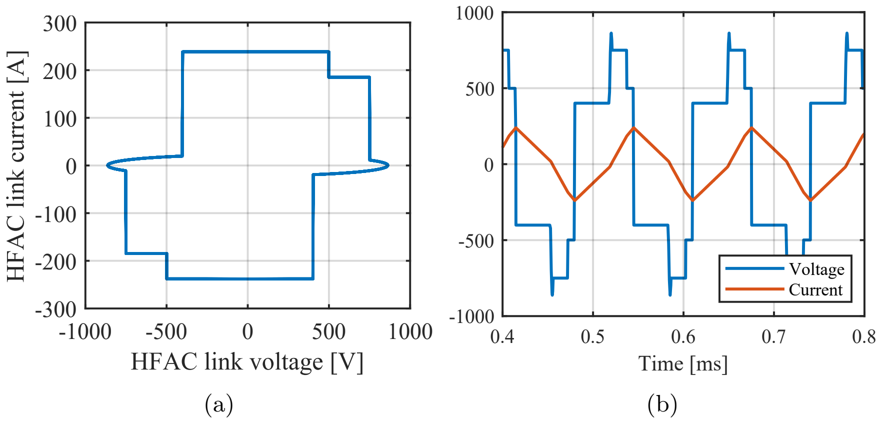

Figure 5.31: HFAC link with three-ports state machine implementation: (a) XY representation (b) Time domain representation

Another possible output of this state machine implementation is the output or input current of each port, as in Fig. 5.32. In Fig. 5.32, the current contributed by each port can be clearly seen. If the resonance periods are significant enough, they would also be easily observable as black spaces in between the currents.

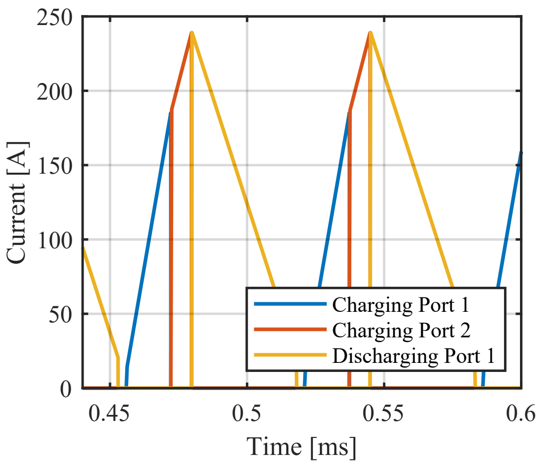

Figure 5.32: Three-port converter port current with state machine simulation

It is possible to develop control signals for the proposed machine based on the desired power for each port. Two methods are proposed hereafter, one based on link current and another based on link energy. The current control seeks to generate the reference link current for the first connected port I_1 and for the second connected port I_2. Note that in three-port converters, one port will always act as the balancing port, providing or absorbing power as needed. The peak current can be calculated as shown in (C1 5.2). The expected link frequency can then be obtained, and with it, the period t for each port is calculated as shown in (C1 5.4). With the periods obtained, the reference currents can be calculated as per the last equations. V_{sort} is a variable that corresponds to the voltage of each port sorted in decreasing order. As explained before, the connection of the ports is done from highest voltage to lowest to optimize the HFAC link resonance periods.

Algorithm 1: Three-port converter state machine current control

---

$$P_{balance} = -(P_{source} - P_{load}) \tag{C1 5.1}$$

$$I_{L,peak} = 2 * \sqrt{P_{in}} \sum_{i=0}^{n+m-1} \frac{\sqrt{\sum_{i=0}^{i} P_{i+1}} - \sqrt{\sum_{i=0}^{i} P_i}}{V_{i+1}} \tag{C1 5.2}$$

$$f = \frac{P_{in}}{LI_{Lpeak}^2} \tag{C1 5.3}$$

$$t_{i+1} = \frac{L}{f} \frac{\sqrt{\sum_{i=0}^{i} P_{i+1}} - \sqrt{\sum_{i=0}^{i} P_i}}{V_{i+1}}, \ i = 0, 1, 2, ..., n-1 \tag{C1 5.4}$$

$$I_1 = \frac{V_{sort_1} t_1}{L} \tag{C1 5.5}$$

$$I_2 = \frac{V_{sort_2} t_2}{L} \tag{C1 5.6}$$

A similar control can be implemented based on the HFAC link energy. The objective of this control is to generate the energy E_1 and E_2 that the HFAC link must reach before disconnecting from the first and second port. In this method, the energy that always remains on the HFAC link E_{base} is calculated, and it is taken into account to calculate the reference energy levels. This was not the case for the previously proposed current control, where I_{start} and I_{end} were neglected. Under certain conditions, this simplification has a negligible effect. The following subsection delves into this simplification and the details concerning the calculation of the commutation periods.

Algorithm 2: Three-port converter state machine energy control

$$E_{base} = 0.5LI_{end}^2 + 0.5CV_{end} \tag{C2 5.1}$$

$$I_{L,peak} = 2 * \sqrt{P_{in}} \sum_{i=0}^{n+m-1} \frac{\sqrt{\sum_{i=0}^{i} P_{i+1}} - \sqrt{\sum_{i=0}^{i} P_i}}{V_{i+1}} \tag{C2 5.2}$$

$$f = \frac{P_{in}}{LI_{Lpeak}^2} \tag{C2 5.3}$$

$$t_{i+1} = \frac{L}{f} \frac{\sqrt{\sum_{i=0}^{i} P_{i+1}} - \sqrt{\sum_{i=0}^{i} P_i}}{V_{i+1}}, \ i = 0, 1, 2, ..., n-1 \tag{C2 5.4}$$

$$T = t_1 + t_2 + t_3 \tag{C2 5.5}$$

$$E_1 = P_{sort1}T + E_{base} \tag{C2 5.6}$$

$$E_2 = E_1 + P_{sort2}T + E_{base} \tag{C2 5.7}$$

5.3.3 HFAC Link frequency calculation

In the literature, resonance periods are often neglected to simplify the computation of the link frequency and port periods. However, under certain conditions, these simplifications are no longer valid. An incorrect estimation of the frequency can lead to incorrect periods for each source/load, thus resulting in errors in the average power transferred among the ports of the converters. Therefore, validating which simplifications can be used and under which conditions is important.

This frequency is influenced by the power rating of the converter, the link charge and discharge times, and the duration of the resonance modes. As shown before, several resonance modes occur throughout a period of the converter. In some cases, these resonance periods can be significantly smaller than the total converter period. Thus, these resonance periods can be neglected in the calculations to reduce complexity. Here, three different methods for the calculation of the link frequency and the resonance time are presented. These methods are compared, and their impact on the calculation of the link frequency will be studied. The objective is to assess in which regimes the resonance periods have a significant impact on the HFAC link frequency. The three proposed methods are:

- *Neglected resonance*: The general analysis of the converter does not consider the resonance periods [112]. This method has in part already been presented as part of the converter's general analysis.
- *Reduced order*: Only the resonating periods during the power cycle are considered. This means the resonance between the end of one power cycle and the start of the next one is neglected. The computation is done using a reduced order calculation [105].
- *High order*: This method considers all the resonating periods during the power cycle. This method gives the closest results to the actual operating values [115].

Neglected resonance

While this method has been introduced in the general analysis, it is summarized here in a concise manner. In this method, it is assumed that once connected, the voltage of the port does not vary. The equation of the inductor for each mode i is:

$$V_{i+1} = L\frac{I_{i+1} - I_i}{t_{i+1}} \tag{5.21}$$

Where t_i is the duration of the mode. Taking into account the trapezoidal waveform of the link current, the average current transferred through the converter can be calculated as:

$$I_{i+1,avg} = t_{i+1}(I_{i+1} + I_i)f \tag{5.22}$$

Where f is the HFAC link frequency. Considering n sources and m loads and that there are two power cycles per period, the following relationship is obtained:

$$\sum_{i=0}^{n+m-1} t_{i+1} = \frac{1}{2f} \tag{5.23}$$

Using the voltage and average current expressions, and considering that the initial current is equal to zero, it is possible to relate the power exchanged and the peak current of the link as was shown in (5.17). By using (5.21) and (5.17), the expression for the peak current in the link can be found as demonstrated in (5.18) with $P_0 = 0$ [112]. Finally, by using (5.17), the frequency of the link for a power cycle based on the power and inductance can be found. The resulting equation is shown in (5.24).

$$f = \frac{P_{in}}{LI_{L,peak}^2} \tag{5.24}$$

Once the frequency is found, and with the help of the previous equations, it is possible to calculate the duration of each mode using the following equation:

$$t_{i+1} = \frac{L}{f} \frac{\sqrt{\sum_{i=0}^{i} P_{i+1}} - \sqrt{\sum_{i=0}^{i} P_i}}{V_{i+1}}, \; i = 0, 1, 2, ..., n-1 \tag{5.25}$$

Reduced order

As previously mentioned, the HFAC link behaves as an LC oscillator whose behavior can be described by (5.4) and (5.5). The *Reduced order* method relies on the assumption that the link current will not vary during the resonance mode, and only the voltage will change. With these assumptions, the resonance time can be calculated as:

$$V_{Link}(t_2) - V_{Link}(t_1) = -\frac{I_1 t_{res}}{C} \tag{5.26}$$

$$t_{res} = C \frac{V_{Link}(t_2) - V_{Link}(t_1)}{I_1} \tag{5.27}$$

I_1 corresponds to the link current before the resonance mode at time t_1. $V_{Link}(t_1)$ is the link voltage at the beginning of the resonance mode, and $V_{Link}(t_2)$ is the link voltage at the end of the resonance mode. Through an iterative process, the resonance period calculated using (5.27) is added to the duration of the other conduction modes to obtain the frequency of the link. The duration of the modes is recomputed using this new frequency, and the process is stopped when the change between iterations is small ($\sim 1Hz$).

High order

For an accurate result, none of the previous assumptions are taken into account. This means that both the voltage and the current are considered to vary during the resonance modes. At the end of the discharge mode, the current I_{end} that must remain on the HFAC link is considered. Equally, the current present in the HFAC link at the start of the charge phase I_{start} is taken into account. I_{start} and I_{end} can be calculated as shown in (5.6) and (5.7), respectively. In the case of a three-port converter, V_{in} is the first port to charge the HFAC link. That is, the charging port with the highest voltage. In contrast, V_{out} is the voltage of the last port to which the link is discharged, which should be the discharging port with the highest voltage. In this case, the duration of the resonance is given by (5.28)[115].

$$t_{r1} = \frac{1}{\omega_0}\left(\pi + \tan^{-1}\left(\frac{I_{start}L\omega_0}{V_{first}}\right) - \pi + \tan^{-1}\left(\frac{I_{end}L\omega_0}{V_{last}}\right)\right) \tag{5.28}$$

While this method provides an accurate solution, it has a higher numerical complexity since the function is non-linear. This non-linearity can increase the computation time and the complexity of the models as a system of 10 equations needs to be solved.

To test the accuracy of the different methods, the calculation of the link frequency for the different methods is performed in MATLAB and compared. The case presented in Fig. 5.33 is studied. PVs are connected to Port 1 and feed a load connected to Port 3, while a battery is connected to Port 2. The power injected by the PVs and the consumption of the load change at each step. The power injected by the PVs changes from $1kW$ to $30kW$, while the load increases from 0.9 kW to 15 kW. The battery charges with the exceeding power injected by the PVs. In Fig. 5.33, it is shown that there are three resonance periods per power cycle. As depicted in 5.33, the complete cycle of the converter is described as:

$$\frac{1}{2f} = t_{Port1} + t_{res1} + t_{Port3} + t_{res2} + t_{Port2} + t_{res3} \tag{5.29}$$

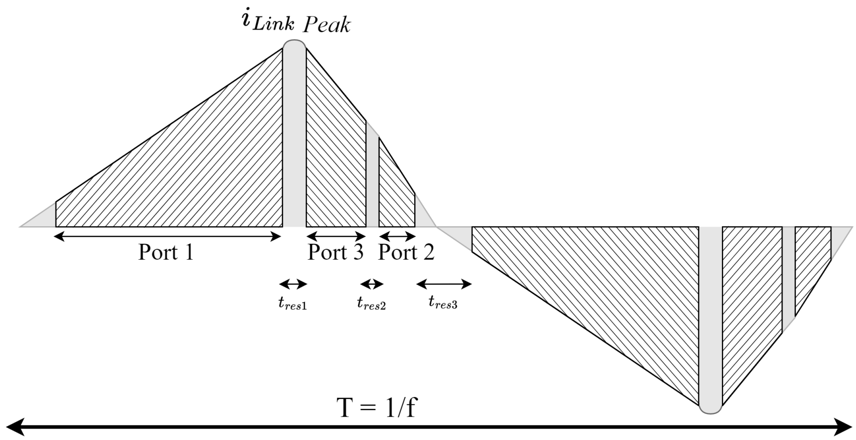

Figure 5.33: Link current waveform for Port 1 feeding Port 2 and Port 3

In (5.29), t_{res1} is the resonance period between Port 1 and Port 3. t_{res2} is the resonance period between Port 3 and Port 2. t_{res3} is the resonance occurring before the voltage swing to the voltage of Port 1. In the *High order* method, all of these resonance periods are considered. Meanwhile, the last resonance period t_{res3} is neglected in the *Reduced order* approach. The parameters used for the calculations are given in Table 5.4.

Table 5.4: Converter Parameters

Parameter	**Value**	**Parameter**	**Value**
Port 1 Voltage [V]	300	Link inductance [μH]	140
Port 2 Voltage [V]	400	Link capacitance [nF]	200
Port 3 Voltage [V]	200	Maximum power [kW]	30

The obtained results are shown in Fig. 5.34. As the power injected by the PVs increases, the link frequency decreases. The three curves follow the same profile except at low power. At low power levels, the method neglecting the resonance deviates significantly from the other two methods. Indeed, when the power transferred is low, the duration of resonance is comparable to or even longer than the transfer time [109]. Therefore, neglecting the resonance results in a frequency deviation from the more elaborate methods. In contrast, the *Reduced order* method shows a slight underestimation of the link frequency at low power levels.

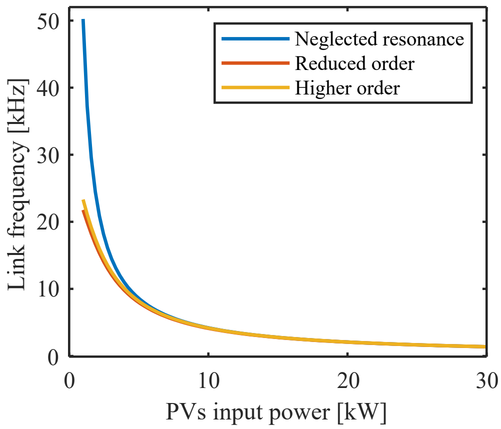

Figure 5.34: Link frequency calculated by each method at different power levels

To further illustrate this deviation in frequency, the waveform of the HFAC link current is drawn. Fig. 5.35a shows the waveform when the power injected by the PVs is 2.17 kW and the load demands 1.47 kW. The *Higher order* model has an additional starting point that corresponds to I_{start}, which is the leftover current on the link. The current in the *Reduced order* method stays constant during the resonance periods as it is one of the simplifications made. The waveform of the *Neglected resonance* method reflects the difference in the calculated frequency. At this power level, the resonance times are significant, and thus neglecting them leads to a different result. This is because the current fed to the link is low. Hence, the duration of the port connection is short. In contrast, the duration of the resonance remains relatively constant. Fig. 5.35b shows the HFAC link waveform when the PVs provide 8.03 kW and the load demands 4.31 kW. At this point, the duration of the resonances is small enough compared to the connection time of each port. Thus, it is seen that the three different models follow a similar waveform.

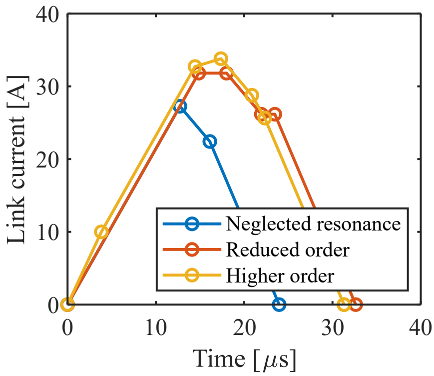

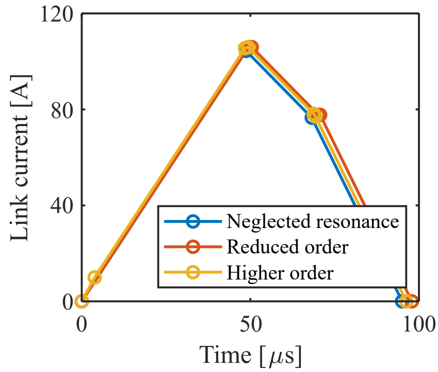

Figure 5.35: HFAC link current waveform with: (a) 2.17kW input power (b) 8.03kW input power

As shown in Fig. 5.34, the *Reduced order* method at lower power levels is more accurate than the method neglecting the resonance periods. The percentage of error of the *Neglected resonance* and *Reduced order* methods can be calculated by considering the most rigorous *High order* method as the reference. However, the degree of error in each method also depends on the voltage difference between each port. The error is calculated for each method for two voltages in Port 1: 300 V and 600 V. Fig. 5.36 shows the error percentage for the most simple method which is *Neglected resonance*. As seen previously, the amount of error at low power levels is non-negligible. The error starts at 115% with 300 V and 250% for 600 V. The error then decreases toward a negligible value.

The error obtained with the *Reduced order* method is shown in Fig. 5.37. It is seen that the error starts close to 5% when the voltage of Port 1 is 300 V. When the voltage is 600 V, the error increases towards 15%. However, this increased error is significantly less than with the *Neglected resonance* method. The increased error due to the voltage change can be explained by noticing that the voltage at the end of the cycle (V_{Port2} = 400 V) is lower than the input voltage (V_{Port1} = 600 V). When this is the case, the link no longer discharges to zero. The current left in the link is used to increase the link voltage back to the input voltage.

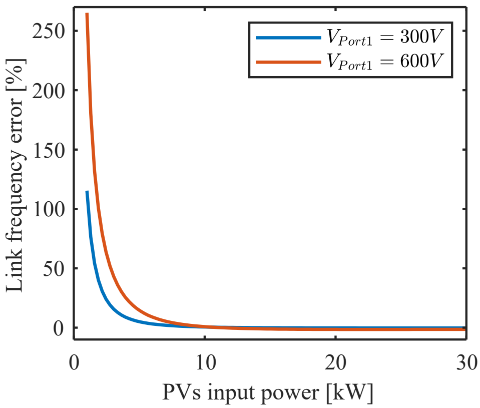

Figure 5.36: Link frequency calculation error with *Neglected resonance* method

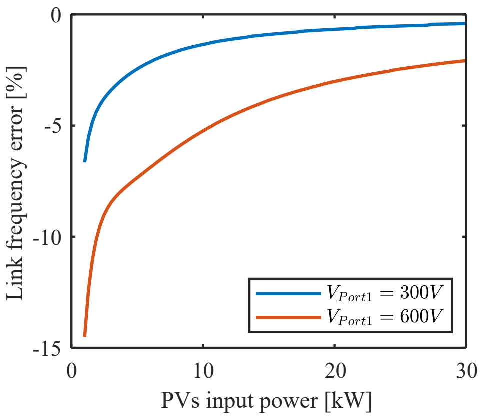

Figure 5.37: Link frequency calculation error with *Reduced order* method

In Fig. 5.38 the duration of each resonance period with respect to the total period is shown. This result is obtained using the higher order method, as the presence of a third resonance period suggests. During normal power operation, the duration of the final resonance period is more significant than the duration of the resonance periods between the charge and discharge of the link. This last resonance corresponds to the resonance that creates the voltage swing at the end of each power cycle. This result indicates that $t_{res,1}$ and $t_{res,2}$ can be neglected. Meanwhile, the last resonance $t_{res,3}$ could be kept to improve the accuracy of the result.

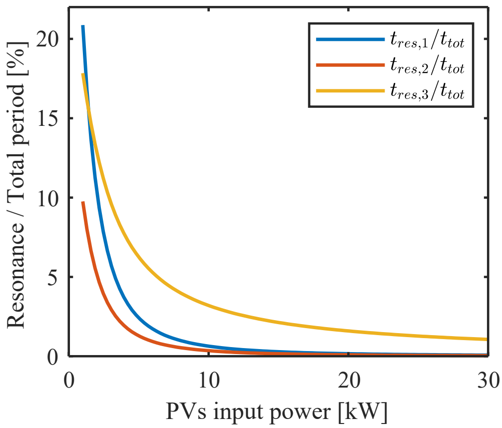

Figure 5.38: Duration of the resonance periods with respect to the total period

5.4 Modeling of HFAC link conveters

In the previous section, it was demonstrated that at medium to high power transfer, neglecting the resonance periods is a valid simplification with a low amount of error. In this section, an averaged model is proposed based on this simplification. The proposed averaged model is based on a state-space model that considers the resonance periods and the HFAC link capacitance can be neglected.

The main limitation of this model is that it will provide the correct steady-state values only when using the duty cycles calculated with the *Neglected resonance* and *Reduced order* methods. This limitation arises from the fact that, like the *Neglected resonance* and *Reduced order* methods, the state-space model does not consider the start and end currents, I_{start} and I_{end} respectively. If these two current points are considered, they change the inductor current peak value and the charge and discharge times. Thus, utilizing the duty cycles calculated with the *High order* method will not provide the correct results.

From the state-space model, an average circuit model is proposed. This model also has the same limitation. As the circuit is implemented through the DC transformer, a constant voltage is applied at the output of the DC transformer. This applied voltage does not take into account I_{start} and

I_{end}, and thus only the average values of the state variables are considered.

One final limitation of the models presented hereafter is that at low power levels, the damping is reduced, and thus the oscillatory behavior is accentuated.

5.4.1 Modeling of two-port HFAC link converters

State-space model

The simplified averaged model is developed using the state-space equations of the circuit shown in Fig. 5.39. In this state-space model, two major simplifications are considered. First, the resonance periods are not considered. The reason for this is that no energy transfer is performed during these periods; thus, for an averaged model, their impact is negligible. Additionally, the work in [114] showed that under normal operation, these resonance periods have a negligible duration with respect to the total period. Furthermore, to consider them, extra duty cycles are required. This, in turn, makes the control of the average model more complex. The second simplification is that the capacitance of the HFAC link is neglected. The reason for this is that the capacitance only participates in the resonance periods but does not participate in the storage or transfer of energy itself. Thus, it can be neglected without affecting the general results of the averaged model. However, the HFAC link capacitor is still illustrated in Fig. 5.39 to help identify the HFAC link.

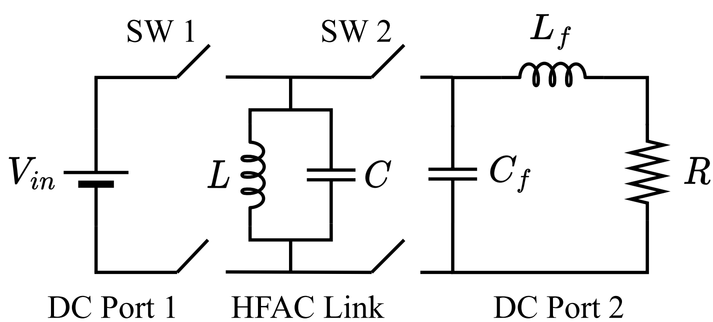

Figure 5.39: Two-port DC/DC converter simplified circuit diagram

With the previous simplifications applied, the state variables considered are the link inductance current I_L, the output filter capacitance voltage V_{C_f}, and the output filter inductance current I_{L_f}. The voltage V_{in} is considered as the only input. When the switch $SW1$ is closed and $SW2$ is open, the system is defined by the equations shown in (5.30). The inductance is charged by the input voltage, while the output capacitance discharges towards the load R. The second state is when $SW2$ is closed and $SW1$ is open, and thus the inductance discharges itself toward the load. This final state is described by the equations shown in (5.31).

$$\begin{cases} L\frac{dI_L}{dt} = V_{in} \\ L_f\frac{dI_{L_f}}{dt} = -I_{L_f}R + V_{C_f} \\ C_f\frac{dV_{C_f}}{dt} = -I_{L_f} \end{cases} \tag{5.30}$$

$$\begin{cases} L\frac{dI_L}{dt} = V_{C_f} \\ L_f\frac{dI_{L_f}}{dt} = -I_{L_f}R + V_{C_f} \\ C_f\frac{dV_{C_f}}{dt} = -I_L - I_{L_f} \end{cases} \tag{5.31}$$

With the previous equations in hand, the state-space model can be defined through a state matrix A, input matrix B, and the state vector x. The duration of the periods where $SW1$ or $SW2$ is closed (and the complementary switch is open) is represented by the duty cycles d_1 and d_2, respectively. Thus, the state-space model can be formulated as:

$$\dot{\bar{\boldsymbol{x}}} = \boldsymbol{A}\bar{\boldsymbol{x}} + \boldsymbol{B}\bar{\boldsymbol{u}} \tag{5.32}$$

Where :

$$\begin{aligned}
&A = d_1A_1 + d_2A_2 \\
&B = d_1B_1 + d_2B_2 \\
&A_1 = \begin{bmatrix} 0 & 0 & 0 \\ 0 & \frac{-R}{L_f} & \frac{1}{L_f} \\ 0 & -\frac{1}{C_f} & 0 \end{bmatrix}, A_2 = \begin{bmatrix} 0 & 0 & \frac{1}{L} \\ 0 & \frac{-R}{L_f} & \frac{1}{L_f} \\ -\frac{1}{C_f} & -\frac{1}{C_f} & 0 \end{bmatrix} \\
&B_1 = \begin{bmatrix} \frac{1}{L} \\ 0 \\ 0 \end{bmatrix}, B_2 = \begin{bmatrix} 0 \\ 0 \\ 0 \end{bmatrix}, \bar{x} = \begin{bmatrix} I_L \\ I_{L_f} \\ V_{C_f} \end{bmatrix}
\end{aligned}$$

From the state-space system, the definition for the steady-state values of the state variables is found as:

$$\begin{cases} I_L = \frac{V_{in}\, d_1}{R\, d_2^2} \\ I_{L_f} = -\frac{-V_{in}\, d_1}{R\, d_2} \\ V_{C_f} = \frac{-V_{in}\, d_1}{d_2} \end{cases} \tag{5.33}$$

Furthermore, using the state-transition matrix $\Phi = (sI - A)^{-1}$, the following transfer functions can be obtained through $H(s) = C\Phi B + D$:

$$\begin{aligned} \frac{I_L}{V_{in}} &= \frac{C_f L_f d_1 s^2 + (C_f R d_1^2 + C_f R d_1 d_2)s + (d_1^3 + d_1 d_2^2 + 2d_1^2 d_2)}{C_f L L_f s^3 + C_f L R s^2 + (2L d_1 d_2 + L_f d_2^2 + L d_1^2 + L d_2^2)s + R d_2^2} \\ \frac{I_{L_f}}{V_{in}} &= \frac{-d_1 d_2}{C_f L L_f s^3 + C_f L R s^2 + (2L d_1 d_2 + L_f d_2^2 + L d_1^2 + L d_2^2)s + R d_2^2} \\ \frac{V_{C_f}}{V_{in}} &= \frac{-d_1 d_2 (R + L_f s)}{C_f L L_f s^3 + C_f L R s^2 + (2L d_1 d_2 + L_f d_2^2 + L d_1^2 + L d_2^2)s + R d_2^2} \end{aligned} \tag{5.34}$$

Average model and Validation

To validate the model found, the output of the state-space model will be compared to the steady-state values calculated through the equations of the detailed model. Namely, it will be verified that with the same inputs, the state-space model outputs the correct average inductor current I_L, output current I_{L_f}, and output voltage V_{C_f}. From the procedure shown in [115], the inductance L can be sized based on the maximum power and a chosen link frequency. For this example, a converter with the parameters summarized in Table 5.5 is considered.

Table 5.5: Two-port DC/DC converter parameters

Parameter	**Value**	**Parameter**	**Value**
P_{max} [kW]	20	Link inductance [mH]	0.156
Link frequency [kHz]	5	Filter inductance [μH]	6.2
V_{in} [V]	750	Filter capacitance [μF]	120
V_{C_f} [V]	375		

To test the model, first, a load of 12 kW is tested. Based on the power and the port voltages, I_{Lpeak} is calculated as shown in (5.35) [109], [112]. Using the relationship between voltage and current in an inductor, the charge t_1 and discharge t_2 periods are found. Once the charge and discharge periods are found, the period can be calculated as shown in (5.38). Once the total period is known, the duty cycle for each port can be calculated using (5.39). To calculate the average current, the integral of the current waveform is taken. As it was shown in Fig. 5.23, the currents have a triangular waveform. Thus, the integral of the waveforms can be calculated as the areas of the triangles. The average input current and output current are the areas of their corresponding triangles over a period T. The average current of the link inductance L can also be calculated using the whole waveform using (5.40). Equally, once t_2 is known, the output current can be calculated as shown in (5.41).

$$I_{Lpeak} = 2\sqrt{P}\left(\frac{\sqrt{P}}{V_{in}} + \frac{\sqrt{P}}{V_{C_f}}\right) \tag{5.35}$$

$$t_1 = \frac{I_{Lpeak} * L}{V_{in}} \tag{5.36}$$

$$t_2 = \frac{I_{Lpeak} * L}{V_{C_f}} \tag{5.37}$$

$$T = t_1 + t_2 \tag{5.38}$$

$$d_1 = \frac{t_1}{T};\ d_2 = \frac{t_2}{T} \tag{5.39}$$

$$I_{Lavg} = \frac{1}{2T}\left(t_1\, I_{Lpeak} + t_2\, I_{Lpeak}\right) \tag{5.40}$$

$$I_2 = \frac{V_{sort_2} t_2}{L} \tag{5.41}$$

The values from Table 5.5 are used with the previously described equations to compute the inductor current I_L, output current I_{L_f}, and output capacitor voltage V_{C_f}. These same parameters are used in the state-space model described in (5.32), considering a duty cycle of $d_1 = 0.3333$ and $d_2 = 0.6667$, calculated using (5.39). The system of equations is then solved for x, yielding the steady-state values for the state variables. Table 5.6 compares the values obtained using the developed equations with those from the state-space model. Concretely I_L is obtained via (5.40) and I_{L_f} with (5.41). The results show that both methods provide identical values, therefore validating the state-space model. The given output voltage corresponds to the desired output. Furthermore, the output current I_f corresponds to the desired output power of 12 kW. The average current I_L also provides the expected result when compared against (5.40). The step response of the voltage V_{C_f} to the input V_{in} is shown to give the correct steady-state value in the step response of Fig. 5.40.

Table 5.6: Two-port DC/DC converter state-space model output values comparison.

Parameter	**Analytical equations**	**State-space model**
I_L [A]	48	48
I_{L_f} [A]	-32	-32
V_{C_f} [V]	-375	-375

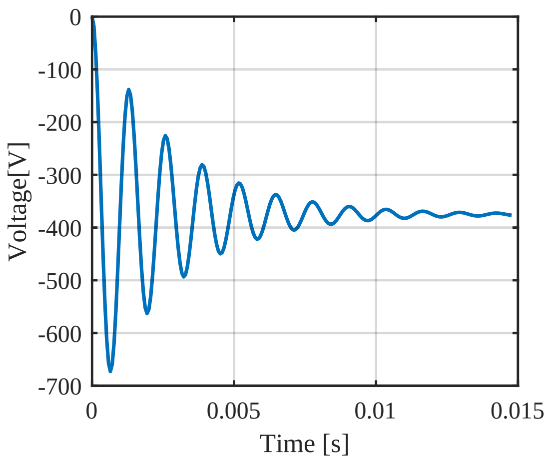

Figure 5.40: Two-port DC/DC converter state-space output voltage V_{C_f} step response to input V_{in}

The eigen values of the system can be obtained through the state-space model. These are shown in Table 5.7. These values indicate that there is two clearly dominant eigenvalues. The third value which has a minimal impact is linked mostly to the value of the output filter inductance L_f and load resistance R.

Table 5.7: Two-port DC/DC converter parameters eigenvalues

Real part	**imaginary part**
-3.5569E2	4.8566E3
-3.5569E2	-4.8566E3
-1.8894E6	0

The impact that each parameter has on the response of the system's output voltage V_{C_f} is shown in Fig. 5.41 through a pole-zero plot. For readability the eigenvalue corresponding to the left most value (-1.8894E6) is not shown. The parameters modified are L, R, C_f, and L_f. In this case the system's output voltage V_{C_f} has three poles. The two dominant are shown for readability. The original position of the pole is shown in blue while the displaced pole due to the change in parameter is shown in orange. The inductance and capacitance values were increased by steps of 50 μH and 50 μF, respectively. The resistance parameter was increased in steps of 5 Ω. It can be observed that the inductance L only affects the frequency of the oscillations in the system. Meanwhile, the load resistance R only influences the damping. The filter capacitance C_f affects both the damping and the frequency. Finally, the output filter inductance L_f has a reduced impact as the poles do not move significantly. Furthermore, all of the poles are located in the left-hand plane, indicating that the system is stable.

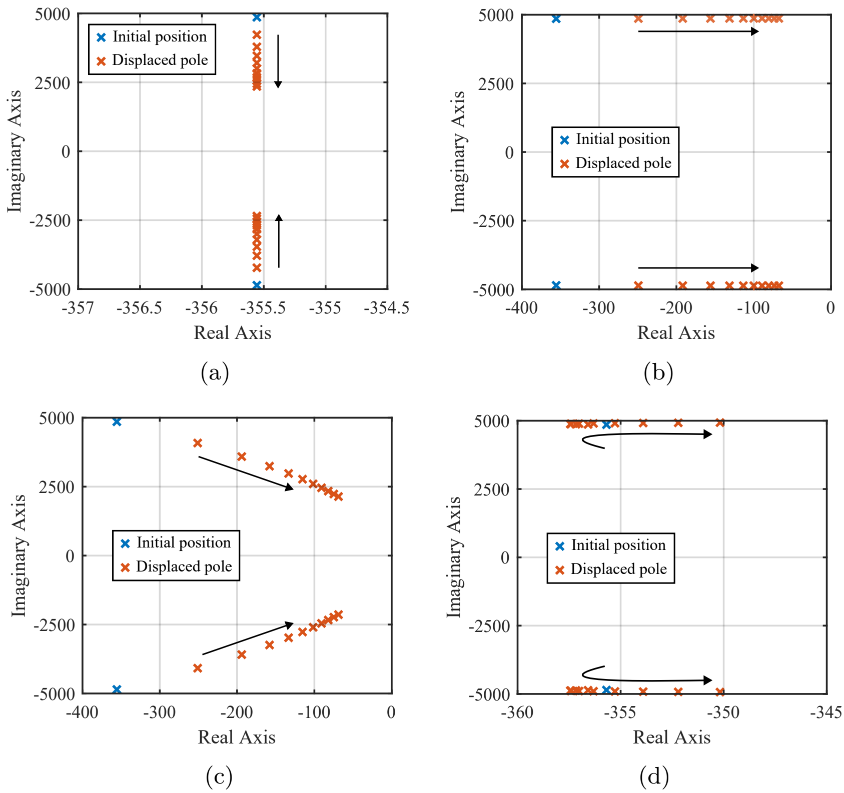

Figure 5.41: Influence of components parameters on two-port DC/DC converter state-space output voltage V_{C_f} response: (a) L (b) R (c) C_f (d) L_f

These results show the key parameters determine the behavior of the model: the HFAC link inductance, filter capacitor, and the load resistance. The inductance is a fixed parameter designed based on the maximum power of the HFAC link converter. The inductance L significantly affects the frequency response and the oscillatory behavior of the circuit. The filter capacitor C_f affects mainly the damping, but also the frequency of the response. On the other hand, the load resistance R varies depending on the load power. The pole-zero analysis shows that if the resistance is increased, the damping of the circuit is reduced. That is, under low power conditions, the circuit will oscillate more. This is why the proposed model is better suited for medium and high power transmission.

The primary aim of the developed model is to provide an averaged model that can be effectively utilized in dynamic simulations without imposing a significant computational burden. To this end, the concept of a DC transformer is used. The average model using the DC transformer is a circuit realization of the state-space model that allows representing the relationships between the voltages and currents of the converter [100], [101]. The DC transformer operates as an ideal transformer with a conversion ratio that is a function of the duty cycle. The main advantage of this method is that the correct voltage and current values are obtained, the converter still be controled via the duty cycles, while neglecting the switching. Because the switching behavior does not need to be modeled, the computational burden is significantly reduced. The implementation of the DC transformer is performed through the use of the Variable-ratio transformer block [117] in MATLAB/Simulink.

The two-port converter is implemented as shown in Fig. 5.42 with the parameters of Table 5.5. Thus, the average converter is controlled using the previous duty cycles d_1 and d_2. The proposed configuration allows controlling the system via the duty cycles while being able to measure the current of the link inductance placed between the two Variable-ratio transformers. Notice that when $d_1 = 1$ and thus $d_2 = 0$, the circuit corresponds to the simplified circuit of Fig. 5.39 with $SW1$ closed and $SW2$ open. Meanwhile, when $d_1 = 0$ and $d_2 = 1$, the circuit corresponds to the simplified circuit with $SW1$ open and $SW2$ closed. The output filter and the load are connected with inverted polarity, but the system can provide the same results with a positive sign if connected with normal polarity.

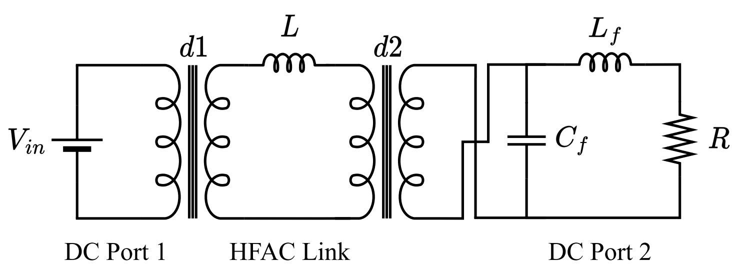

Figure 5.42: Two-port DC/DC average converter implementation

Three different signals are shown as results. First, the output voltage is shown in Fig. 5.43a, where it is seen that after the initial response, the system reaches the desired output voltage value of $-375V$. Furthermore, it is seen that the initial response exhibits a consistent alignment with the step response that was shown in Fig. 5.40. Afterwards, in Fig. 5.43b and Fig. 5.43c the resulting currents in the link and the output port are shown respectively. The link current I_L is shown to converge to the expected value of $48A$ as described previously. Equally, the output current has a final value of $-32A$ which results in the desired power transfer of 12 kW.

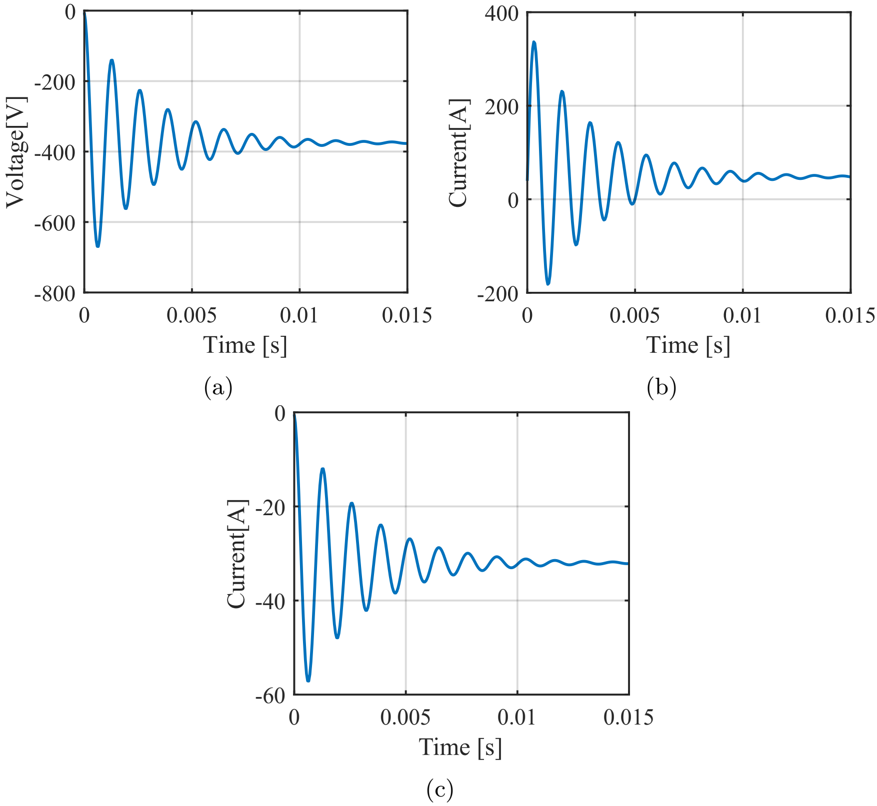

Figure 5.43: Two-port DC/DC converter average model output: (a) Output voltage V_{C_f} (b) Link current I_L (c) Output inductance current I_{L_f}

To further validate the model, the response of the output voltage to a drop in input voltage is investigated. The response is compared to that of the transfer function. The system is stable with an output voltage of $-375V$ when at time $t = 0.5s$, a 5% voltage drop occurs on the input voltage. The response of the dynamic model and the transfer function are compared in Fig. 5.44. The result shows that the systems have the same response and stabilize to the same output voltage of $-356.25V$. Thus, it is shown that the proposed model captures the dynamics of the converter.

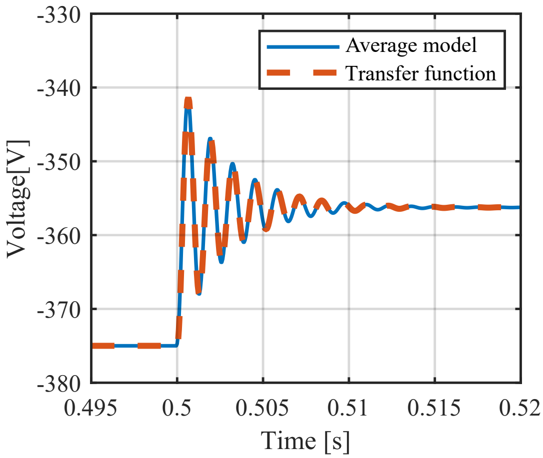

Figure 5.44: Two-port DC/DC converter output voltage response to a 5% input voltage drop

As a final validation step, the proposed average model is compared against the switched model of the converter. A two-port HFAC link converter has been implemented in Matlab/Simulink as shown in Fig. 5.45. This switched model is not controlled via the duty cycle. Instead, the switching is performed based on a reference peak HFAC link current I_{Lpeak} and the measured HFAC link voltage and current. Fig. 5.46 shows the control for four of the bidirectional switches. The Up signal controld the switches utilized for charging the HFAC link when the HFAC link voltage is positive. The Down signal controls the switches that discharge the HFAC link when the link voltage is negative. Via the logic gates and the S-R flip flops two conditions are checked: the sign of the HFAC link voltage and if the link current has attained the reference. When charging, the reference current corresponds to the link peak current. When discharging, the reference current is the current that must remain in the link at the end of the discharge. The remaining bidirectional switches are controlled simiarly through another pair of S-R flip flops with the conditions adjusted for the scond power sycle.

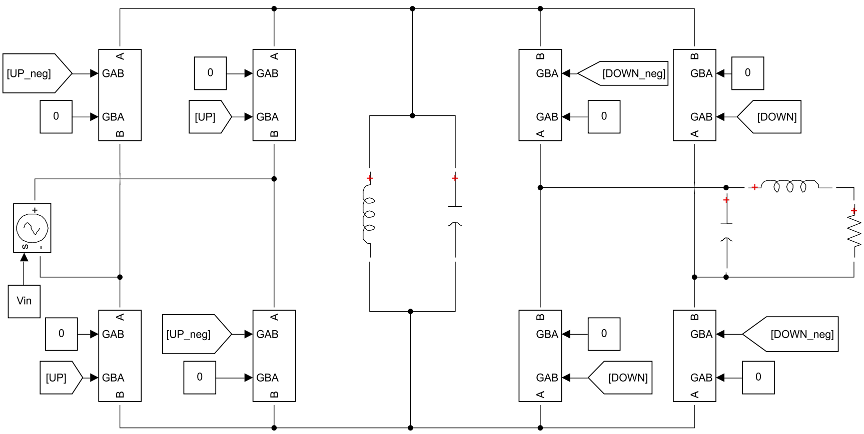

Figure 5.45: Two-port DC/DC converter switch model Simulink implementation

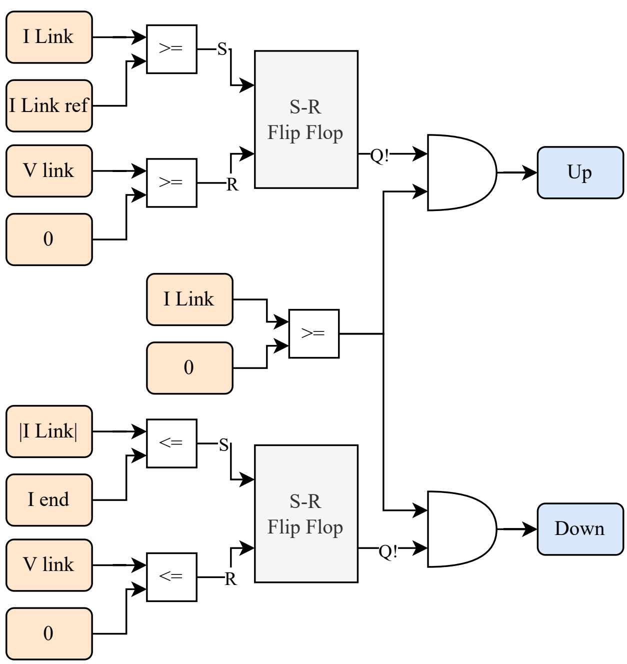

Figure 5.46: Two-port DC/DC converter switch model Simulink control

Using the same parameters as before, both models are given the corresponding references to provide an output voltage V_{C_f} of 375 V. At $t = 25$ ms, the reference is changed so that the output voltage becomes 350 V. Specifically, the switched model first has a reference $I_{Lpeak} = 96$ A, which then becomes $I_{Lpeak} = 87.6089$ A. The averaged model has a reference $d_1 = 0.3333$, which then changes to $d_1 = 0.3182$. The obtained results for the output voltage and HFAC link current are shown in Fig. 5.47a and 5.47b, respectively. The results show that the average model follows the switch model response. A small difference can be observed in the steady-state value, which can be attributed to the average model being ideal. For example, the diode resistance and forward voltage are not considered. It is observed that the transient dynamic of the average model oscillates before reaching its steady-state value. This is due to the step caused by the change in reference. If a control is implemented that changes the reference gradually, the oscillatory response will be attenuated. This is shown in Fig. 5.48, where instead of a step, a ramp signal is used to gradually increase the reference value.

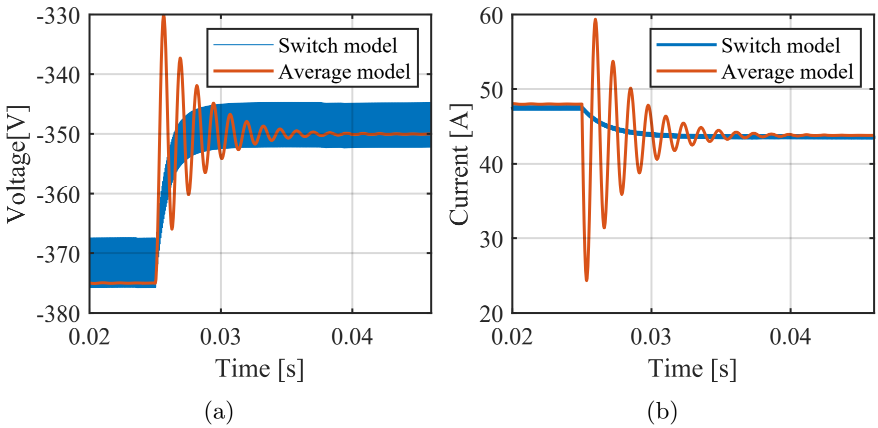

Figure 5.47: Switch and average two-port DC/DC converter response comparison: (a) Output voltage (b) HFAC link current

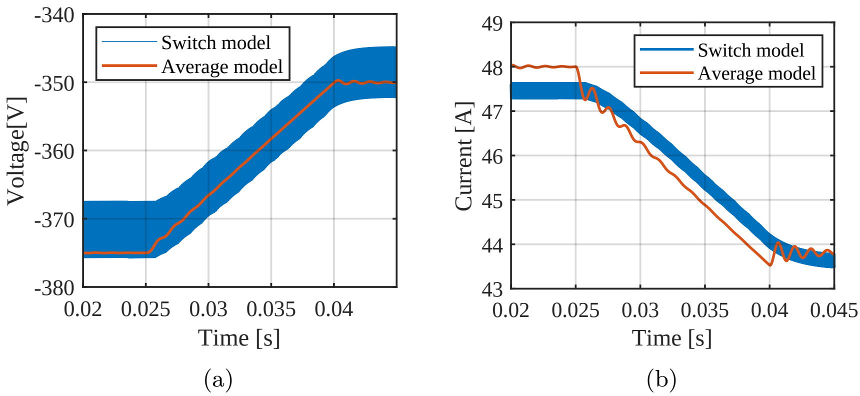

Figure 5.48: Switch and average two-port DC/DC converter ramp response comparison: (a) Output voltage (b) HFAC link current

5.4.2 Modeling of three-port converters: Two sources one load

State-space model

The methodology used in the previous section is applied to the three-port converter. The three-port converter considered has the topology shown in Fig. 5.49. The two sources are represented by V_1 and V_2. As in the previous section, the general operation of the converter is explained via the voltage and current waveforms shown in Fig. 5.50. First, the port with the highest voltage V_1 will charge the link inductance. After a resonance period, the second port will charge the last part of the inductance with a voltage V_2. Once the inductance is charged, the link will resonate to the third port voltage V_{C_f} and discharge the inductance. The process is then repeated with reversed polarity.

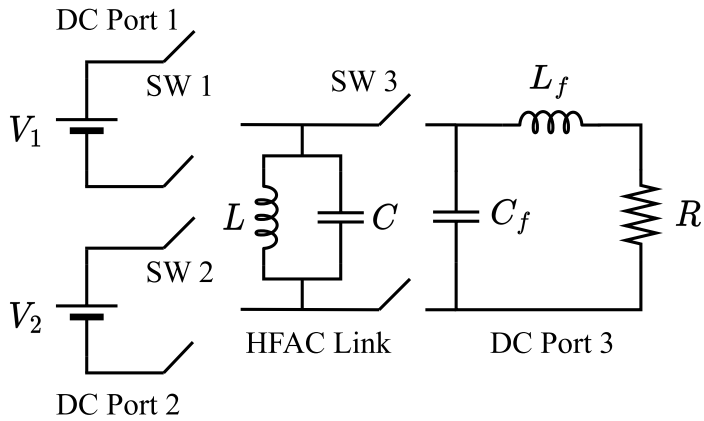

Figure 5.49: Three-port DC/DC/DC converter circuit diagram: two sources, one load

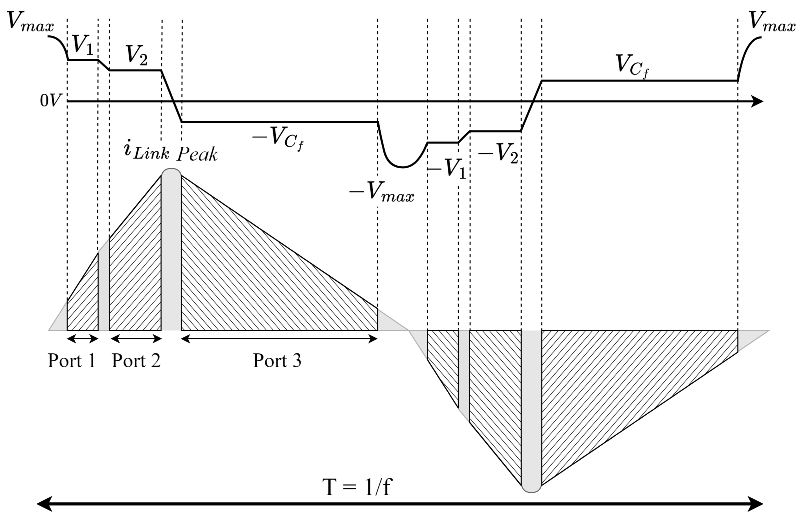

Figure 5.50: Three-port DC/DC/DC converter two sources one load HFAC link voltage and current waveform

The first step is to define the equations for each different state: when only $SW1$ is connected, when only $SW2$ is connected, and when only $SW3$

is connected. The state variables remain the same as in the two-port case. However, there is an additional input and an additional switch case, and thus, a third duty cycle d_3. The state equations for the connection of $SW1$, $SW2$, and $SW3$ are given in equations (5.42), (5.43), and (5.44), respectively.

$$\begin{cases} L\frac{dI_L}{dt} = V_1 \\ L_f\frac{dI_{L_f}}{dt} = -I_{L_f}R + V_{C_f} \\ C_f\frac{dV_{C_f}}{dt} = -I_{L_f} \end{cases} \tag{5.42}$$

$$\begin{cases} L\frac{dI_L}{dt} = V_2 \\ L_f\frac{dI_{L_f}}{dt} = -I_{L_f}R + V_{C_f} \\ C_f\frac{dV_{C_f}}{dt} = -I_{L_f} \end{cases} \tag{5.43}$$

$$\begin{cases} L\frac{dI_L}{dt} = V_{C_f} \\ L_f\frac{dI_{L_f}}{dt} = -I_{L_f}R + V_{C_f} \\ C_f\frac{dV_{C_f}}{dt} = -I_L - I_{L_f} \end{cases} \tag{5.44}$$

With the equations in hand, it is possible to set up the state-space model using (5.32) with :

$$A = d_1A_1 + d_2A_2 + d_3A_3$$
$$B = d_1B_1 + d_2B_2 + d_3B_3$$
$$A_1 = A_2 = \begin{bmatrix} 0 & 0 & 0 \\ 0 & \frac{-R}{L_f} & \frac{1}{L_f} \\ 0 & -\frac{1}{C_f} & 0 \end{bmatrix}$$
$$A_3 = \begin{bmatrix} 0 & 0 & \frac{1}{L} \\ 0 & \frac{-R}{L_f} & \frac{1}{L_f} \\ -\frac{1}{C_f} & -\frac{1}{C_f} & 0 \end{bmatrix}$$

$$B_1 = \begin{bmatrix} \frac{1}{L} \\ 0 \\ 0 \end{bmatrix}, B_2 = \begin{bmatrix} 0 \\ \frac{1}{L} \\ 0 \end{bmatrix}, B_3 = \begin{bmatrix} 0 \\ 0 \\ 0 \end{bmatrix}$$

From the state-space system, the definition for the steady-state values of the state variables is found as:

$$\begin{cases} I_L = \frac{V_1\, d_1}{R\, d_3^2} + \frac{V_2\, d_2}{R\, d_3^2} \\ I_f = -\frac{V_1\, d_1}{R\, d_3} - \frac{V_2\, d_2}{R\, d_3} \\ V_{C_f} = \frac{-V_1\, d_1}{d_3} - \frac{-V_2\, d_2}{d_3} \end{cases} \tag{5.45}$$

Average model and validation

To validate the system, the values of Table 5.8 are plugged into the state-space model. The results from the state-space model are then compared against the expected values. The peak value of the inductor current and the duty cycles are determined using the methodology previously developed in the *Neglected resonance* method. As described earlier, it is possible to calculate the duration of each charge or discharge period as given in (5.25).

Table 5.8: Three-port DC/DC/DC converter parameters with two sources one load

Parameter	**Value**	**Parameter**	**Value**
P_{max} [kW]	20	V_1 [V]	750
P_1 [kW]	7	V_2 [V]	500
P_2 [kW]	5	V_{C_f} [V]	375
Link Frequency [kHz]	5	Filter inductance [μH]	6.2
Link inductance [mH]	0.156	Filter capacitance [μF]	120

The average inductance current I_{Lavg} is calculated through the area of the waveform, as shown in Fig. 5.50. The formula shown in (5.46) represents the sum of the areas of two triangles and a trapezoid.

$$I_{Lavg} = \frac{1}{2T}(t_1\, I_1 + t_2\,(I_1 + I_{Lpeak}) + t_3\, I_{Lpeak}) \tag{5.46}$$

Where I_1 represents the peak current attained by the first port. As in the two-port case, the duty cycle of each port can be calculated using the period duration t_i and the total period T, as shown in (5.47).

$$d_1 = \frac{t_1}{T};\; d_2 = \frac{t_2}{T};\; d_3 = \frac{t_3}{T} \tag{5.47}$$

The parameters presented in Table 5.8 are used to compare the results of the equations to those of the state-space system. The following duty cycles are obtained with the previous equations: $d_1 = 0.2449$, $d_2 = 0.1136$, and $d_3 = 0.6414$. Table 5.9 shows the obtained results for both models for the inductor current I_L, output current I_{L_f}, and the output voltage V_{C_f}.

Table 5.9: Three-port converter state-space model output values comparison

Parameter	**Analytical equations**	**State-space model**
I_L [A]	51.333	49.890
I_{L_f} [A]	-32	-32
V_{C_f} [V]	-375	-375

It is seen that the result provided for I_L has a small deviation from the expected value. To further analyze the result, the output power P_{out} is calculated. The power given to the load can be obtained using the output current equation shown in (5.45) as follows:

$$P_{out} = V_{C_f} \, (\frac{V_1 \, d_1}{R \, d_3} + \frac{V_2 \, d_2}{R \, d_3}) \tag{5.48}$$

In (5.48), each fraction corresponds to the power of each port. If calculated using the previously shown parameters, the results obtained are: $P_1 = 9.165$ kW and $P_2 = 2.835$ kW, which do not correspond to the expected $P_1 = 7$ kW and $P_2 = 5$ kW. The source of this error can be attributed to the fact that the state-space model does not consider the value of I_1 nor the trapezoid in the middle of the waveform. Thus, in order to obtain the correct values, a new set of duty cycles d_s can be calculated. These are calculated by considering the average port current and average inductance current I_{Lavg} as follows:

$$d_{1s} = \frac{I_{P1avg}}{I_{Lavg}} \tag{5.49}$$

The new calculated duty cycles are shown in Table 5.10 along with the ones first calculated. If the calculations are performed again with the new duty cycles d_s, the proper power distribution is obtained with $P_1 = 7$ kW and $P_2 = 5$ kW. Furthermore, solving the state-space system provides the correct average inductor current while retaining the correct value for the other state variables, as shown in Table 5.11.

Table 5.10: Three-port DC/DC/DC converter calculated duty cycles.

Port	d	d_s
P_1	0.2449	0.1818
P_2	0.1136	0.1948
P_3	0.6414	0.6234

Table 5.11: Three-port DC/DC/DC converter state-space model output values comparison with new duty cycles

Parameter	**Analytical equations**	**State-space model**
I_L [A]	51.333	51.333
I_{L_f} [A]	-32	-32
V_{C_f} [V]	-375	-375

As with the two-port converter, the transfer function for this converter can also be derived. The output voltage step response of the developed model is depicted in Fig. 5.51. In this case, the output voltage step response is the sum of the response to two different steps. Indeed, one part of the response is linked to the step to the voltage V_1, while the other is linked to the input V_2. Fig. 5.51 displays the individual contributions of each input voltage to the output voltage response. The cumulative effect of these responses results in the output voltage reaching a steady-state value of -375 V, which is the desired output voltage.

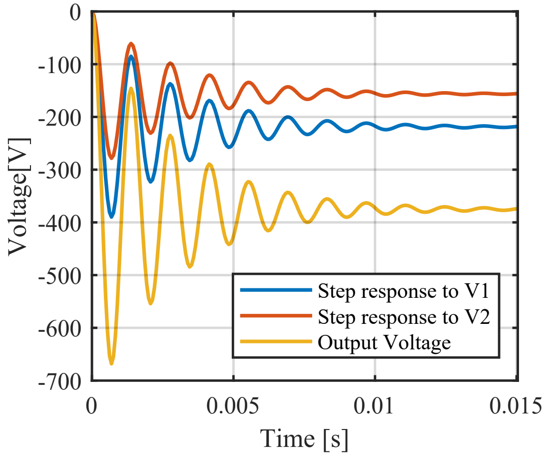

Figure 5.51: Three-port DC/DC/DC converter output voltage step response to inputs V_1 and V_2

Using the Variable-ratio transformer block, the three-port converter is implemented as shown in Fig. 5.52. The two inputs are connected in series via the transformers. The two voltages resulting from the transformers with turn ratios d_{1s} and d_{2s} make one equivalent voltage that is applied to the inductance and then transformed by a ratio d_{3s}. Notice that the case represented here corresponds to two sources feeding one load. For the case where one source feeds two loads, the circuit does not need to be modified. Applying a negative sign to the duty cycle of port 1 or 2 is all that is required to change their behavior into that of a load. The proposed circuit is implemented here with the parameters described in Table 5.8 and the new duty cycles ds of Table 5.10.

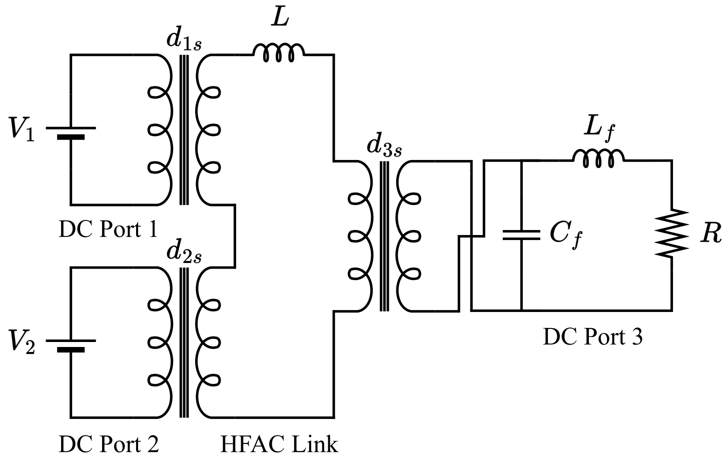

Figure 5.52: Average three-port DC/DC/DC converter implementation with two sources one load

As with the two-port case, three different signals of interest are shown. In Fig. 5.53a, the output voltage is shown. It can be observed that the signal stabilizes to the expected value of −375 V. Afterwards, in Figures 5.53b and 5.53c, the average link current I_L and the output current I_{Lf} are displayed, respectively. It is seen that both signals also achieve the expected values.

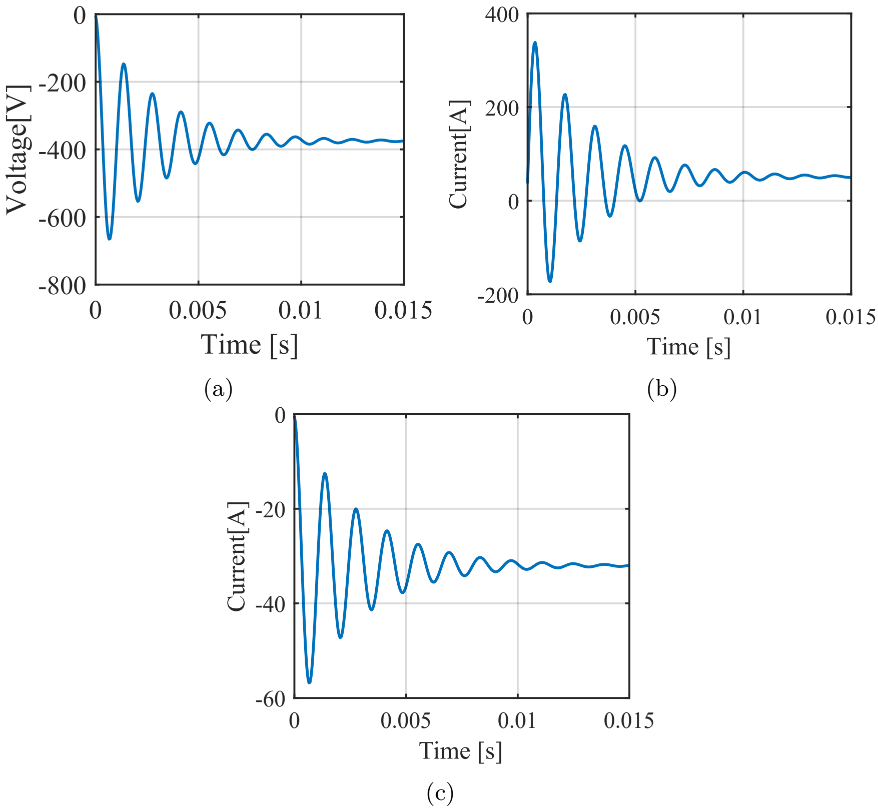

Figure 5.53: Three-port DC/DC/DC converter two sources one load Simulink implementation: (a) Output voltage V_{C_f} (b) Link current I_L (c) Output inductance current I_{Lf}

Finally, the response of the average model is compared to that of the transfer function. The response to a 5% drop in the input voltages will be tested. First, a voltage drop will be applied to V_1. After the system stabilizes, a second 5% voltage drop will be applied to V_2. Fig. 5.54 shows the described sequence where the first voltage drop is applied at $t = 0.5$ s. Compared to the two-port case of Fig. 5.44, it is seen that the voltage deviation is lower and the settling point is different in the three-port converter. This can be attributed to the fact that the load is being fed by two different sources. Thus, a part of the supply remains undisturbed. At $t = 0.52$ s, the voltage drop on V_2 is applied. It is shown that after this perturbation, the system stabilizes to a value close to -356.3 V, which is similar to the final value for the two-port converter.

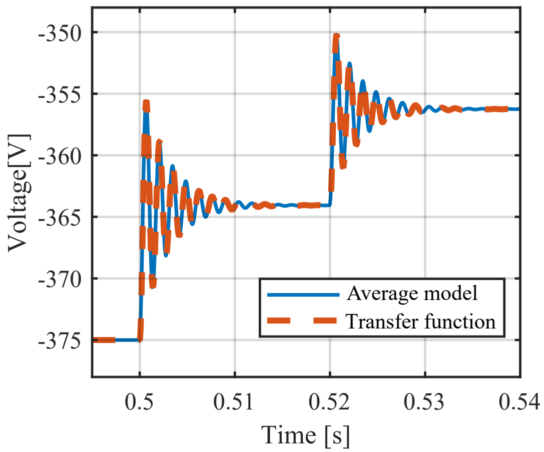

Figure 5.54: Three-port DC/DC/DC converter two sources one load output voltage response to a 5% input voltage drop on both sources

5.4.3 Modeling of three-port converters: One source two loads

State-space and model

The scenario in which a single source supplies two different loads is considered. The simplified circuit of the converter in this scenario is shown in Fig. 5.55. Here, the source is connected to Port 2 while the loads are connected to Port 1 and Port 3.

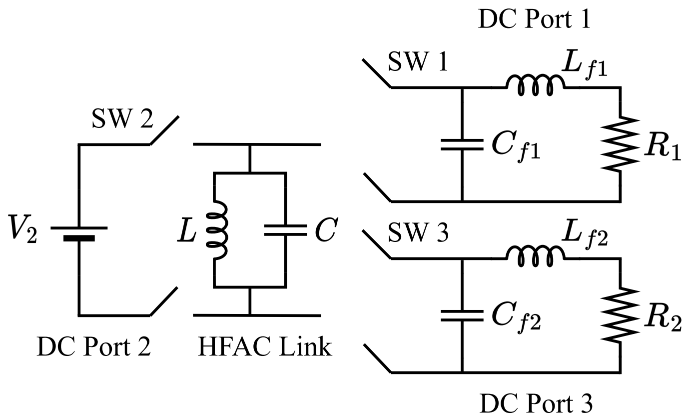

Figure 5.55: Simplified three-port DC/DC/DC converter circuit diagram: one source, two loads

The operation and switching behavior of the converter are illustrated in Fig. 5.56. Initially, The HFAC link is connected to Port 2, which has a source with voltage V_2. This source charges the link inductance, increasing the current in the HFAC link linearly. Once the link is charged to the desired value, the HFAC link is disconnected. This is followed by a resonance period, during which the voltage is adjusted to match the voltage of the next port. Once the voltage of Port 3 is reached, the HFAC link is connected with opposite polarity and partially discharges the inductance to the load. After the initial discharge, the HFAC link disconnects, entering another resonance period to adjust its voltage to that of Port 1. After connecting to the final port, the remaining link current is discharged to the second load. A final resonance occurs, swinging the voltage up to the maximum value V_{max} before returning to the input voltage, where the cycle recommences. Once again, a second energy transfer is performed with opposite voltage polarity to enhance the system's efficiency.

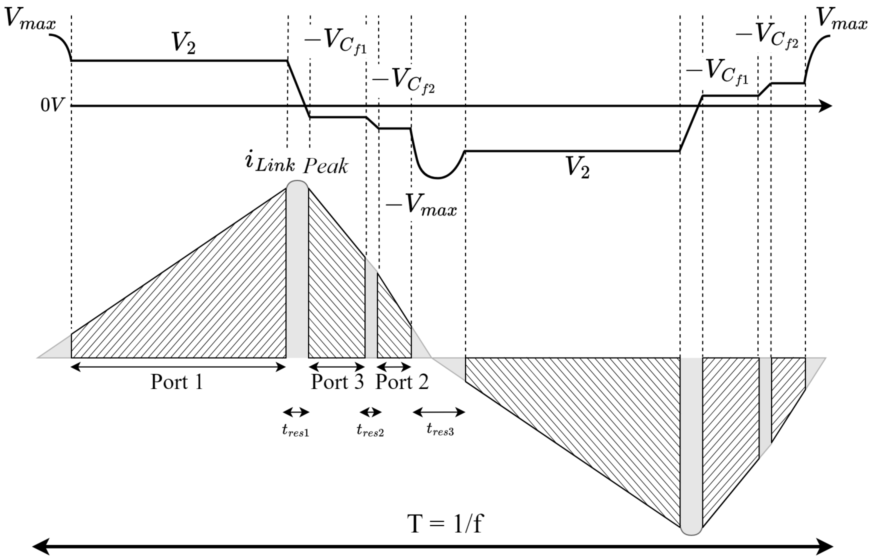

Figure 5.56: Three-port DC/DC/DC one sources two loads voltage and current waveform

The circuit is analyzed considering five state variables: link inductance current I_L, output filter inductance currents $I_{L_{f1}}$ and $I_{L_{f2}}$, and the output filter capacitor voltages $V_{C_{f1}}$ and $V_{C_{f2}}$. Three different switch cases are considered. First, when $SW2$ is closed and the inductance L is charged, the system is described by the equations shown in (5.50). The second case, when $SW1$ is closed and the first load R_1 is supplied, is described by (5.51). Finally, the equations for $SW3$ being closed, which corresponds to the discharge towards the second load R_2, are given in (5.52).

$$\begin{cases} L\frac{dI_L}{dt} = V_2 \\ L_{f1}\frac{dI_{L_{f1}}}{dt} = V_{C_{f1}} - I_{L_{f1}}R_1 \\ C_{f1}\frac{dV_{C_{f1}}}{dt} = -I_{L_{f1}} \\ L_{f2}\frac{dI_{L_{f2}}}{dt} = V_{C_{f2}} - I_{L_{f2}}R_2 \\ C_{f2}\frac{dV_{C_{f2}}}{dt} = -I_{L_{f2}} \end{cases} \tag{5.50}$$

$$\begin{cases} L\frac{dI_L}{dt} = -V_3 \\ L_{f1}\frac{dI_{L_{f1}}}{dt} = V_{C_{f1}} - I_{L_{f1}}R_1 \\ C_{f1}\frac{dV_{C_{f1}}}{dt} = -I_L - I_{L_{f1}} \\ L_{f2}\frac{dI_{L_{f2}}}{dt} = V_{C_{f2}} - I_{L_{f2}}R_2 \\ C_{f2}\frac{dV_{C_{f2}}}{dt} = -I_{L_{f2}} \end{cases} \tag{5.51}$$

$$\begin{cases} L\frac{dI_L}{dt} = -V_1 \\ L_{f1}\frac{dI_{L_{f1}}}{dt} = V_{C_{f1}} - I_{L_{f1}}R_1 \\ C_{f1}\frac{dV_{C_{f1}}}{dt} = -I_{L_{f1}} \\ L_{f2}\frac{dI_{L_{f2}}}{dt} = V_{C_{f2}} - I_{L_{f2}}R_2 \\ C_{f2}\frac{dV_{C_{f2}}}{dt} = -I_L - I_{L_{f2}} \end{cases} \tag{5.52}$$

With the previous equations in hand, the state-space model can be defined using a state matrix A, input matrix B, and the state vector x. The duration of the intervals during which $SW2$, $SW1$, or $SW3$ are closed is indicated by the duty cycles d_1, d_2, and d_3 respectively. Therefore, the state-space model is expressed again with (5.32) with:

$$A = d_1A_1 + d_2A_2 + d_3A_3$$
$$B = d_1B_1 + d_2B_2 + d_3B_3$$

$$A_1 = \begin{bmatrix} 0 & 0 & 0 & 0 & 0 \\ 0 & \frac{-R_1}{L_{f1}} & \frac{1}{L_{f1}} & 0 & 0 \\ 0 & -\frac{1}{C_{f1}} & 0 & 0 & 0 \\ 0 & 0 & 0 & \frac{-R_2}{L_{f2}} & \frac{1}{L_{f2}} \\ 0 & 0 & 0 & \frac{-1}{C_{f2}} & 0 \end{bmatrix}$$

$$A_2 = \begin{bmatrix} 0 & 0 & \frac{1}{L} & 0 & 0 \\ 0 & \frac{-R_1}{L_{f1}} & \frac{1}{L_{f1}} & 0 & 0 \\ \frac{-1}{C_{f1}} & -\frac{1}{C_{f1}} & 0 & 0 & 0 \\ 0 & 0 & 0 & \frac{-R_2}{L_{f2}} & \frac{1}{L_{f2}} \\ 0 & 0 & 0 & \frac{-1}{C_{f2}} & 0 \end{bmatrix}$$

$$A_3 = \begin{bmatrix} 0 & 0 & 0 & 0 & \frac{1}{L} \\ 0 & \frac{-R_1}{L_{f1}} & \frac{1}{L_{f1}} & 0 & 0 \\ 0 & -\frac{1}{C_{f1}} & 0 & 0 & 0 \\ 0 & 0 & 0 & \frac{-R_2}{L_{f2}} & \frac{1}{L_{f2}} \\ \frac{-1}{C_{f2}} & 0 & 0 & \frac{-1}{C_{f2}} & 0 \end{bmatrix}$$

$$B_1 = \begin{bmatrix} \frac{1}{L} \\ 0 \\ 0 \\ 0 \\ 0 \end{bmatrix}, B_2 = B_3 = \begin{bmatrix} 0 \\ 0 \\ 0 \\ 0 \\ 0 \end{bmatrix}$$

From the state-space system, the expression for the steady-state values of the state variables can be found, as shown in (5.53). Moreover, by utilizing the state-transition matrix $\Phi = (sI - A)^{-1}$, the transfer functions for the state variables can be acquired through the expression $H(s) = C\Phi B + D$. The average model for this case can be implemented, as shown in Fig. 5.57.

$$\begin{cases} I_L = \frac{V_2\, d_1}{R_1\, d_2^2 + R_2\, d_3^2} \\ I_{f1} = -\frac{V_2\, d_1\, d_2}{R_1\, d_2^2 + R_2\, d_3^2} \\ V_{C_{f1}} = -\frac{R_1\, V_2\, d_1\, d_2}{R_1\, d_2^2 + R_2\, d_3^2} \\ I_{f2} = -\frac{V_2\, d_1\, d_3}{R_1\, d_2^2 + R_2\, d_3^2} \\ V_{C_{f2}} = -\frac{R_2\, V_2\, d_1\, d_3}{R_1\, d_2^2 + R_2\, d_3^2} \end{cases} \tag{5.53}$$

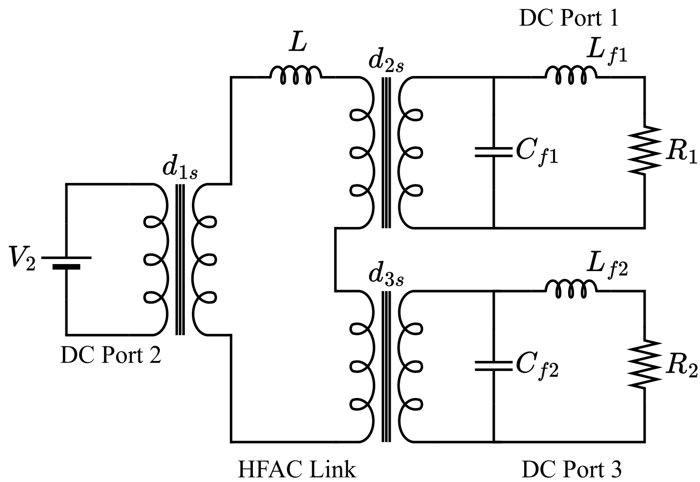

Figure 5.57: Average three-port DC/DC/DC converter implementation with one source two loads

Pole-zero analysis

A converter with the parameters shown in Table 5.12 is considered. The eigenvalues of the matrix A that describe the dynamics of the converter are shown in Table 5.13. It is shown that all the eigenvalues are located on the left-hand side of the plane, indicating that the system is stable. The first two poles have high magnitude values that are related to the filter inductances $I_{L_{f1}}$ and $I_{L_{f2}}$.

Table 5.12: Three-port DC/DC/DC 50 kW converter parameters with one source two loads

Parameter	**Value**	**Parameter**	**Value**
P_{max} [kW]	50	V_1 [V]	750
Link frequency [kHz]	5	V_2 [V]	500
Link inductance [μH]	62.5	V_3 [V]	375
L_{f1} [μH]	2.31	C_f [mF]	17.78
L_{f2} [μH]	16.65	C_{f2} [mF]	4.44
R_1 [Ω]	11.25	R_2 [Ω]	28.125

Table 5.13: Three-port DC/DC/DC 50 kW converter with one sources two loads eigenvalues

Real part	**imaginary part**
-4.8655E6	0
-1.6888E6	0
-5.8427	0
-3.5786	477.31
-3.5786	-477.31

The predominant dynamics of the systems are governed by the lowest three eigenvalues listed in Table 5.13. There exists however a pronounced coupling among distinct outputs. This coupling emerges due to the interplay between the loads, filters of individual ports, and the three duty cycles. This can be illustrated by studying the behavior of the dominant poles of the transfer function of $V_{C_{f1}}$. Fig. 5.58 depicts the pole displacement resulting from incremental increases of 5Ω in each of the load resistances. It is seen that changing the load resistance R_2 of the other output port induces a shift in the poles of $V_{C_{f1}}$. Notably, the poles remain on the left-hand side of the plane, indicating that the system remains stable.

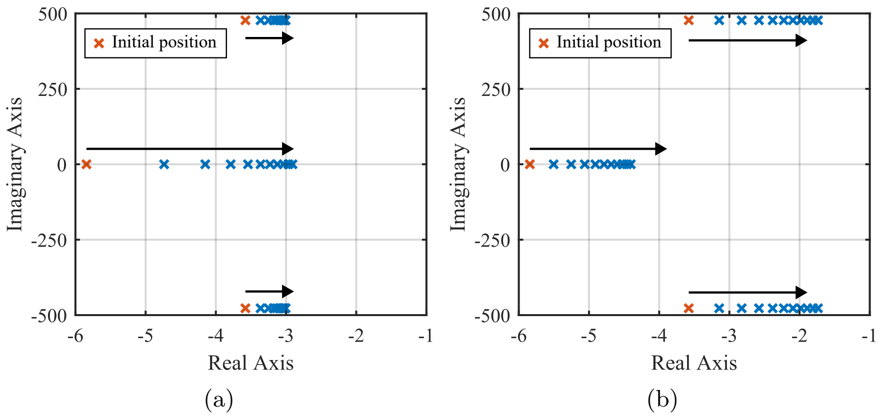

Figure 5.58: Impact of load resistors size on $V_{C_{f1}}$ response: (a) R_1 (b) R_2

A similar test is performed with the filter capacitors. Fig. 5.59 shows the displacements of the poles for the transfer function of $V_{C_{f1}}$ as the values of the filter capacitors are individually increased by 5 μF. Similar to the case of resistances, it is demonstrated that altering the filter capacitance of either port impacts the behavior of $V_{C_{f1}}$, highlighting the presence of coupling within the system. As in the previous case, the poles remain on the left-hand side of the plane, thus ensuring the stability of the system.

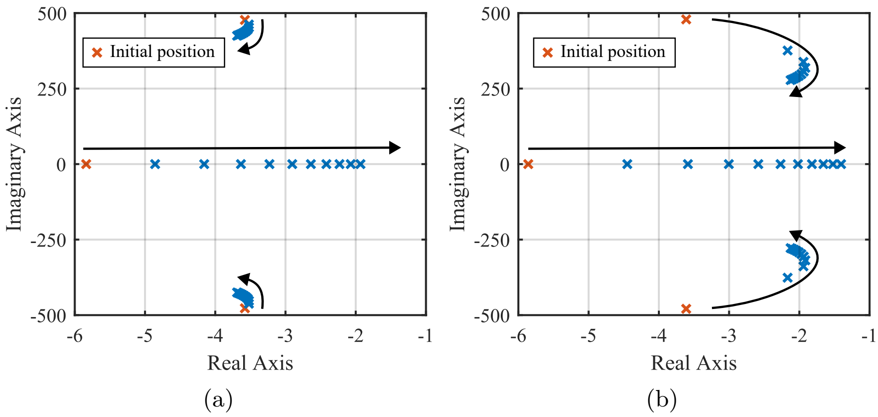

Figure 5.59: Impact of filter capacitors size on $V_{C_{f1}}$ response: (a) C_{f1} (b) C_{f2}

The previous two pole-zero analyses serve to illustrate one limitation of the three-port model, which is the coupling of the Ports. Changes in the parameters of the filter or the loads of one port can impact the behavior of another port. During simulation, only the load values will change. The change in load demand of one port can cause a perturbation in the other port.

5.5 Control of three-port DC/DC/DC HFAC link conveters

As shown through the state space model, the average model is controlled through the use of three duty cycles. In this section, the implemented control for each port through the use of these duty cycles is detailed. Different combinations of loads and sources are considered to this effect.

5.5.1 Control with batteries

The converters will be used within the context of a DC microgrid. It is considered that one port will manage the voltage of the DC distribution bus. Therefore, the ports are assumed to be connected to three distinct elements: a battery acting as a source, a resistive load, and the DC microgrid bus. The port connected to the DC microgrid bus is controlled through droop control. The port connected to the resistive load is controlled as a grid-forming port. In other words, it maintains its output voltage at the designated reference nominal voltage. Fig. 5.60 shows the implementation of these two controllers. In Fig. 5.60, V_1 and V_3 are the nominal voltage of the corresponding ports. I_1 is the measured output current of the respective port. The normalized error is input to a proportional-integral (PI) controller, which generates the duty cycle for each port. The error is normalized by diving it by the nominal voltage of the corresponding port. For example in Fig. 5.60, the difference between V^* and V_{1mes} is divided by the nominal port voltage V_1. Although the converter is controlled via three duty cycles, only two controllers are needed. Indeed, the third duty cycle is found through the relationship $1 = d_{Grid} + d_{Load} + d_{Battery}$.

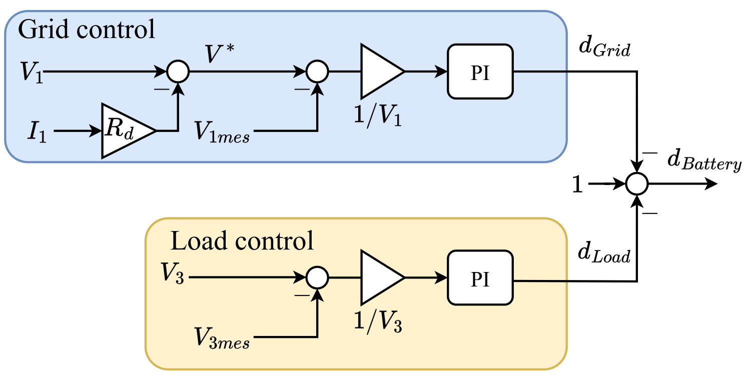

Figure 5.60: Control scheme for battery fed three-port DC/DC/DC converters connected to the DC microgrid and a load

5.5.2 Control with PVs

A similar controller is applied for converters that have PVs connected to them. The duty cycle for the PV panel port is determined directly by the maximum power tracking (MPPT) algorithm, which seeks to maximize the power produced by the PV according to the irradiance Irr and the temperature T. Fig. 5.61 shows the implemented controller for a converter connected to both PVs and a battery. Interaction with the grid is governed by the previously discussed droop control, while the PV port is managed using the MPPT algorithm. The battery maintains power balance between the other two ports by either absorbing or supplying the required power.

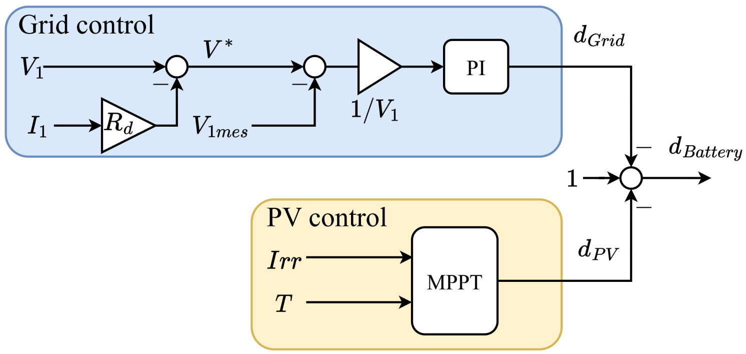

Figure 5.61: Control scheme for battery and PV-fed three-port DC/DC/DC converters connected to the DC microgrid

Fig. 5.62 illustrates the control strategy when a load is connected in place of a battery. The load port is controlled as a grid-forming port to ensure proper voltage regulation for the load. In this case, the DC microgrid is responsible for maintaining the power balance between the two other ports. Therefore, any surplus power will be injected into the DC microgrid, while any deficit in power will be supplied by the DC microgrid.

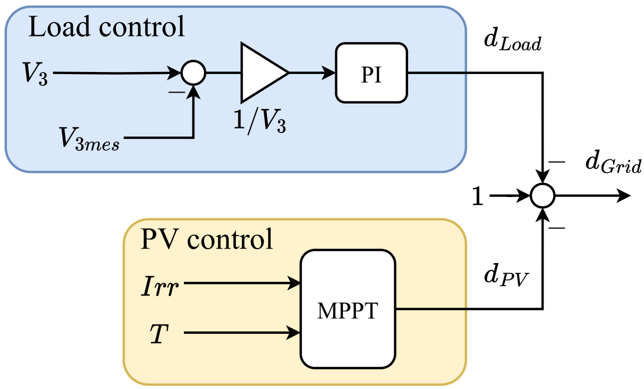

Figure 5.62: Control scheme for PV-fed three-port DC/DC/DC converters connected to the DC microgrid and a load

5.6 Three-port DC/DC/DC converter DC microgrid implementation

To assess the performance of the proposed model, the DC microgrid shown in Fig. 5.63 is studied through its model implementation in Matlab/Simulink. A unipolar DC microgrid is considered, this type of microgrid represents the kind of microgrid that one might encounter in an industrial project like the MIRACCLE project [63]. This DC microgrid comprises four parallel-operating three-port converters, connected by lines of varying lengths. The ports of the converters shown in Fig. 5.63 are equipped with PVs, batteries, loads, or a connection to the DC microgrid, as elaborated in Table 5.14. The averaged model of each converter is implemented as it was shown previously. The utilized PV and battery models are the pre-existing ones within Simscape in Matlab/Simulink. 50 kW DC/DC/DC converters are used, which have the same parameters that were shown in Table 5.12. Each DC microgrid connected port has a voltage $V_1 = 750V$ and a filter with parameters L_{f2} and C_{f2}. The load ports have a voltage $V_3 = 375V$ and a filter with parameters L_{f1} and C_{f1}. The conductor considered for this simulation is an aluminium line with a cross-section of 149 mm^2. The parameters were obtained from the lines database of panda power where the line is listed as 149-AL1/24-ST1A 10.0 [118]. Thus, the transmission lines used have a resistance of 0.194 Ω/km and an inductance of 1 mH/km.

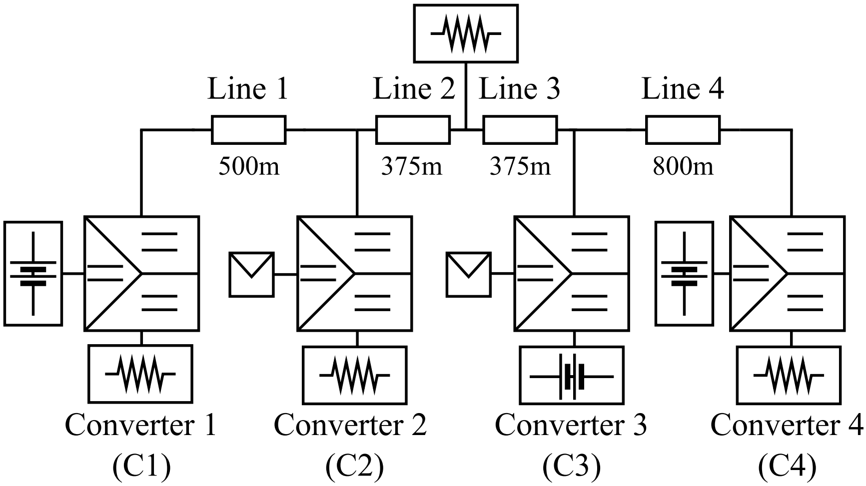

Figure 5.63: Implemented DC microgrid in Matlab/Simulink

Table 5.14: Three-port DC/DC/DC converter port configuration

Converter	**Microgrid**	**Battery**	**PVs**	**Load**
1	✓	✓		✓
2	✓		✓	✓
3	✓	✓	✓	
4	✓	✓		✓

Within the implemented DC microgrid, an initial load of 20 kW is positioned between line 2 and line 3. This load draws power from the DC microgrid ports of different converters. C1 and C4 both have a 12.5 kW load connected to their bottom ports. C3 has a batery connected to one port and a PV with a production close to 15 kW in the other. C2 has at its ports a PV production close to 19.5 kW and a load of 16 kW to be supplied. Two different events occur in the grid. At $t = 3$s, the load of C1 is increased to 18.75 kW, and at $t = 5$s a second load of 14 kW is connected in the DC microgrid between Line 1 and Line 2. Fig. 5.64a and Fig. 5.64b show, respectively, the evolution of the load voltages and the power supplied to each load during these events. It is seen that the nominal voltage value is reached. The events in the system cause perturbations in this voltage. As previously demonstrated, the converter ports are highly coupled, and adjustments in the duty cycle of one port will impact others correspondingly. This explains the origins of the perturbations seen. However, the perturbations are minimal as the voltage deviation stays below 0.01 p.u. It is seen that power is provided correctly to the loads, and the output power follows the expected reference.

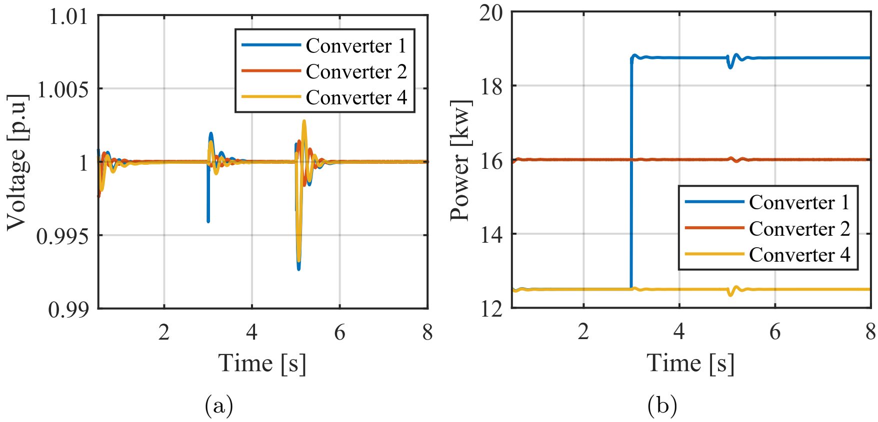

Figure 5.64: Three-port DC/DC/DC converters load port output regulation: (a) Voltage (b) Power supplied

The voltage of each port connected to the DC microgrid is shown in Fig. 5.65a. As described in the previous section, the voltage of the DC microgrid is regulated by C1, C3, and C4 using droop control. Thus, each converter will deviate from the nominal voltage proportionally to the power supplied. This is shown after $t = 5$s where the increase in power demand causes the voltage to deviate further from the nominal value. It is seen that the voltage is properly regulated, with the voltage deviations barely exceeding 0.95 p.u.

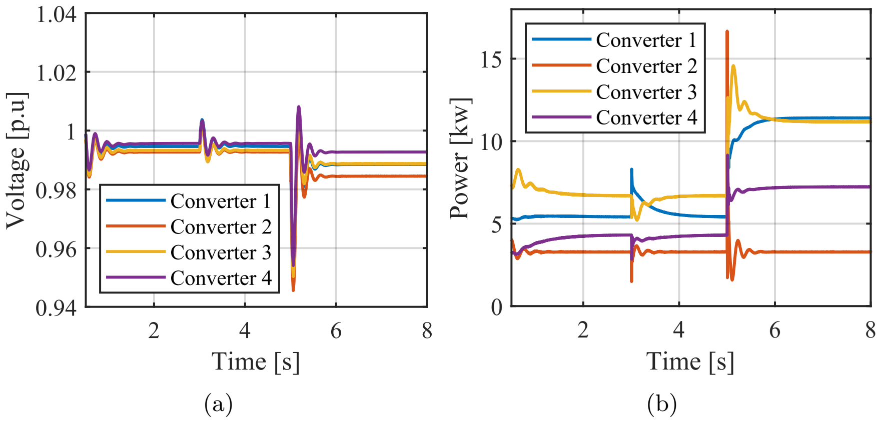

Figure 5.65: Three-port DC/DC/DC converters DC microgrid port output regulation: (a) Voltage (b) Power supplied

The power supplied to the DC microgrid by each converter is shown in Fig. 5.65b. Due to its control strategy, C2 does not directly regulate the DC voltage; rather, it injects any excess power generated by its PV panels. This explains the constant power injection exhibited by Converter 3 throughout the simulation. It is seen that C1, C3, and C4 adapt their power injection to maintain the grid voltage. Although the same droop resistance is used in all three converters, the power injected by each one differs. This is due to the line impedance, which affects power distribution. When only one load is connected to the DC microgrid bus, it is C3 that provides the most power, as it is the closest converter to the load. C4 has a distance of 1175 m to the load and thus provides a lower amount of power. Upon connecting the second load, C1 exhibits the most notable increase in its power output. This is due to the second load being the closest to C1.

The power of each port of C3 is shown in Fig. 5.66. It is seen that the power output of the PV panels is kept constant through the MPPT control. However, it is also due to the MPPT that a ripple can be observed in the power coming from the PV port. Indeed, the perturb and observe algorithm induces small variations in the duty cycle that produce the observed ripple. Although the PVs generate more than 15 kW, this power is not directly injected into the DC microgrid. Instead, a portion of this output is injected in line with the load sharing achieved via droop control. It is shown that the surplus power is absorbed by the battery. Should the PV production decrease, the battery would discharge to maintain grid voltage and sustain load sharing.

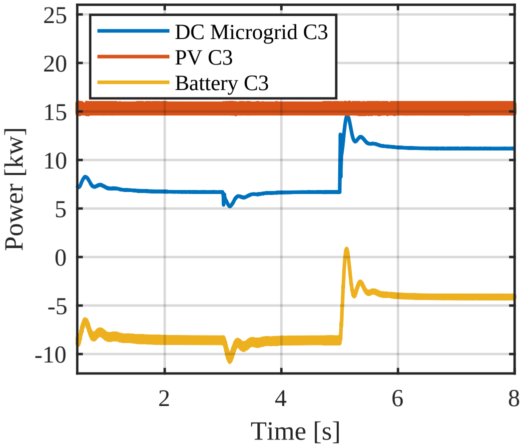

Figure 5.66: Power transfer in each port of Converter 3

5.7 Conclusion

In this chapter, the need for average models of power electronics converters was addressed. Switched models for converters require more complex computation. Average models allow retaining certain dynamics of the converters while alleviating the computational load. The concept of DC transformer was introduced, and the corresponding average models for DC/DC converters using DC transformers were shown. Similarly, approaches for average models of AC-DC converters were illustrated.

As the adoption of renewable energy sources continues to grow, there is an increasing need for converters in energy sources and storage systems. This demand is further driven by the rise in electric vehicles and other loads. Three-port converters utilizing a High-frequency AC link have emerged as a promising solution in this context. The advantages of High-frequency AC link converters and three-port converters were introduced. The operational principles of the converters were illustrated. A state-space model was formulated for the proposed converter, and an averaged model was formulated accordingly. From the state-space model, the corresponding average value equations were obtained. The influence of the converter parameters on the placement of the system's poles was also considered. The principles were initially demonstrated using two-port converters and subsequently extended to three-port converters. It was highlighted that due to the averaged nature of the model presented, the initially calculated duty cycles provide inaccurate power distribution. Thus, duty cycles taking into account the averaged model have to be used. The performance of the proposed model was validated through Simulink simulations, showcasing its ability to capture the essential characteristics of the system while significantly reducing computational complexity. Three control schemes were proposed for the converter according to the elements connected to each port. To validate the proposed model and control scheme, a DC microgrid with four three-port DC/DC/DC converters was simulated. The results showed proper voltage regulation for the loads and the DC microgrid bus. Furthermore, the results demonstrated that the different control loops successfully achieved their objectives.

In future work, certain improvements could be applied to the proposed three-port converter model. First, the control of the converter could be further improved through cascade PI controllers, incorporating a current control loop. Furthermore, the addition of decoupling and feedforward terms could be analyzed. Additionally, while the presented models focused on DC/DC and DC/DC/DC converters, this type of converter can also exist in a DC/DC/AC configuration. Future work could adapt one of the ports into an AC port. Finally, the HFAC link topology is not limited to three-port converters; the proposed models can be extended to include more ports. However, it's important to note that as the number of ports increases, the control of the converter will become more complex.

Chapter 6

DC Microgrid Dynamic Behaviour

Chapter contributions.

- A comparison of first level controls is performed
- A comparison of second level controls is performed
- An analysis of the comparisons is performed, and use cases for the different controllers are proposed

In this chapter, the different control methods presented in Chapter 3 are implemented and tested. The implementation consists of a dynamic simulation using the average models of converters introduced in Chapter 5. The objective here is to observe the performance of the various controllers at different load levels and to highlight the differences between them. The different controllers are tested in the unipolar DC microgrid shown in Fig. 6.1, where some loads are initially connected ($t = 0$ s) and others are added throughout the simulation. These loads are spread across the DC microgrid. In this test system, four sources are connected to the DC microgrid via boost converters, while all the different loads are interfaced by buck converters. Both the boost converters and the buck converters have cascaded control loops with Proportional Integral (PI) controllers. It is worth noting that the different sources are connected by lines of different lengths, which will affect the performance of the controllers. When using droop control or non-linear droop controls, all the converters use the same parameters and should thus share the loads equally. The general test bench parameters are provided in Table 6.1. The conductor considered for this simulation is an aluminium line with a cross-section of 149 mm^2. The parameters were obtained from the lines database of panda power where the line is listed as 149-AL1/24-ST1A 10.0 [118].

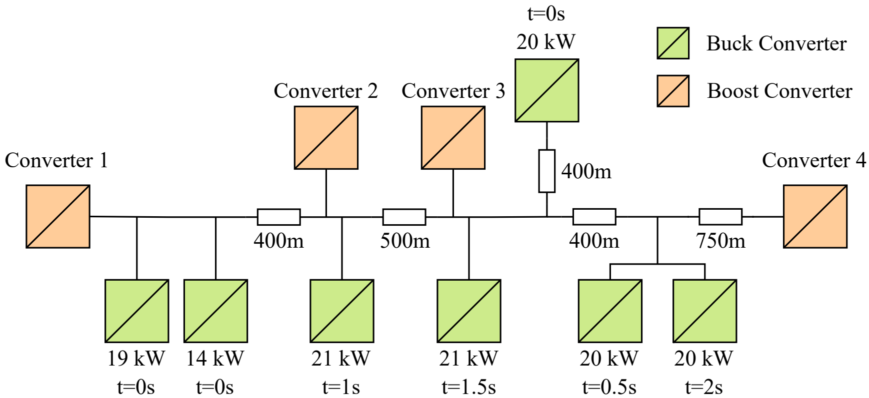

Figure 6.1: DC microgrid testbench

Table 6.1: DC microgrid testbench parameters

Parameter	**Value**	**Parameter**	**Value**
Microgrid nominal voltage [V]	700	Sources nominal voltage [V]	500
Loads nominal voltage [V]	350	Sources nominal power [kW]	40
Line resistance [Ω/km]	0.194	Line inductance [mH/km]	1

Simulations are conducted where the load is increased from 33% to 84% of the maximum load capacity (160 kW). Three moments are analyzed: 33% ($t = 0.4$ s), 58% ($t = 1.4$ s), and 84% ($t = 2.4$ s). The simulations use the same parameters, with only the control method being changed. These simulations allow for the study of signal evolution, as shown in Fig. 6.2. However, only the steady-state values are used for comparison.

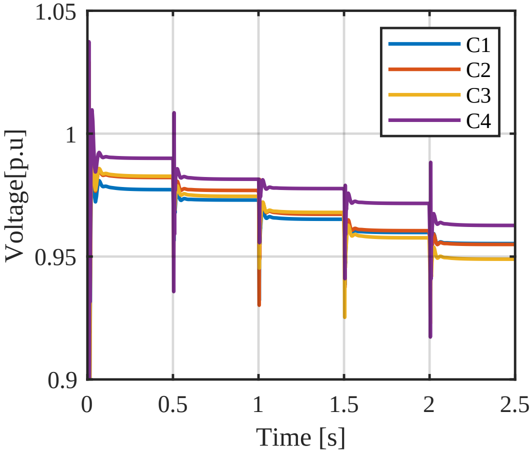

Figure 6.2: Voltage evolution of the simulated DC microgrid using linear droop control

Indeed, the transient behavior is imposed by the inner PI control loops and the value of the output capacitor, which remain constant across all simulations. Consequently, only the steady-state value is influenced by the control method, as illustrated in Fig. 6.3. A droop controlled converter is initially connected to a resistive load. A second load is connected, resulting in a transient response. The droop control serves as the reference case, against which two other cases are compared: one with the same droop control but with a smaller output capacitor, and another using the same converter but utilizing a different control method (Ellipse droop). Notice that the droop control with a smaller output capacitor exhibits the same steady-state values to the reference case. Indeed, a different behavior is shown only for the transient due to the second load connecting. Examining the third curve, corresponding to the same converter but with a different control method, it is seen that the steady-state value is changed, but the transient behavior remains consistent (albeit with an offset due to the higher steady-state value). Thus, the compared control methods only influence the steady-state values.

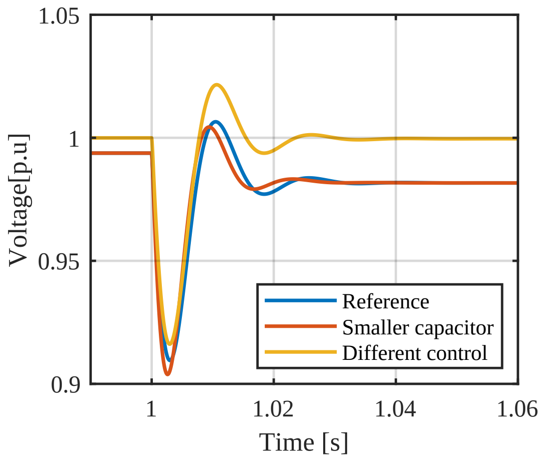

Figure 6.3: Influence of control method and output impedance on transients and steady-state values

The results for load capacities of 33%, 58%, and 84% are analyzed as they represent the most common scenarios: light, medium, and heavy loading of the microgrid. The comparison is conducted using two metrics: the percentage of voltage deviation, and the percentage of load contribution. The percentage of voltage deviation represents the deviation from the nominal voltage. For instance, a 2% voltage deviation corresponds to a voltage of 0.98 p.u. The percentage of load contribution indicates the proportion of power provided by each converter to supply the total load in the microgrid. For example, if one converter has a load contribution of 100%, it means that it alone provides all the loads, with the other converters contribute 0%. If perfect load sharing is achieved, each converter will have a load contribution of 25%.

Note that the power considered is the power measured at the converters' output. Thus, line losses are not taken into account. However, their impact on the results is minimal. For example, a worst-case scenario would be C4 supplying one load the farthest away possible, which would be the loads close to C1. Considering the highest expected voltage deviation, the maximum converter current would be $I_{o\,max} = P_{max}/V_{min} = 40kW/665V = 60.15A$. The distance from the converter to the loads would be 2.058 Km. The total line resistance would be $R_{max} = 2058 \times 0.194 = 0.3993\Omega$. The maximum amount of line losses, considering the return conductor resistance, would be $P_{l\,max} = (2 \times 0.3993) * (60.15^2) = 2.89kW$. Therefore, in a worst-case scenario, only 7.22% of the converter power would be lost in transmission. However, this worst-case scenario does not occur as the loads are supplied by multiple converters and primarily by those closest to them.

6.1 First level controls

6.1.1 General first level controls

33% load capacity

A first set of first level controls is compared. These include grid forming (GF), Master-slave control (M/S), linear droop control, and piecewise control. Implementing all converters as GF converters ensures that the voltage remains close to the nominal value, as seen in Fig. 6.4a. In the case of M/S, the choice of the master converter has to be made. One approach is to assess the power output of each converter when they are all operating as GF. In this case, load sharing is imposed by the resistances between the converters and the loads. It is observed that C3 delivers the highest power output while C4 delivers the lowest. Choosing C3 as the master will cause the other converters to tend to go progressively above the nominal value. In Fig. 6.4a it can be seen that this is the case already for C4. Conversely, choosing C4 as the master will cause the other converters to operate below nominal value. The remaining two control methods are linear droop control and piecewise droop control. The piecewise control consists of three segments, or slopes. The first slope imposes a 0.8% voltage deviation, while the second slope imposes a 2.3% voltage deviation. Finally, the last slope allows for a 5% voltage deviation. It changes between slopes at setpoint currents of 20 A and 41 A. During this light loading stage, the piecewise control follows the 0.8% slope, providing tighter voltage regulation than linear droop control. Notice that the location of active loads also influences voltage deviations. At this operating point, most of the load is located next to C1, hence its voltage deviation.

Fig. 6.4b shows how the load is distributed among the different converters at 33% of the maximum load capacity. When all converters function as grid-forming converters, load sharing is imposed by the line resistances, making proximity to the load significant. This explains why C1 and C3 provide most of the power at this power point. In contrast, master-slave control (Shown as M/S in the figures) results in an equal distribution of the loads in both cases. This results from the other converters following the current reference from the master. Among the last two control methods, it is seen that linear droop control provides better load sharing. This is expected because, at this load point, piecewise control follows a flatter droop slope, prioritizing better voltage regulation at the expense of less accurate load sharing.

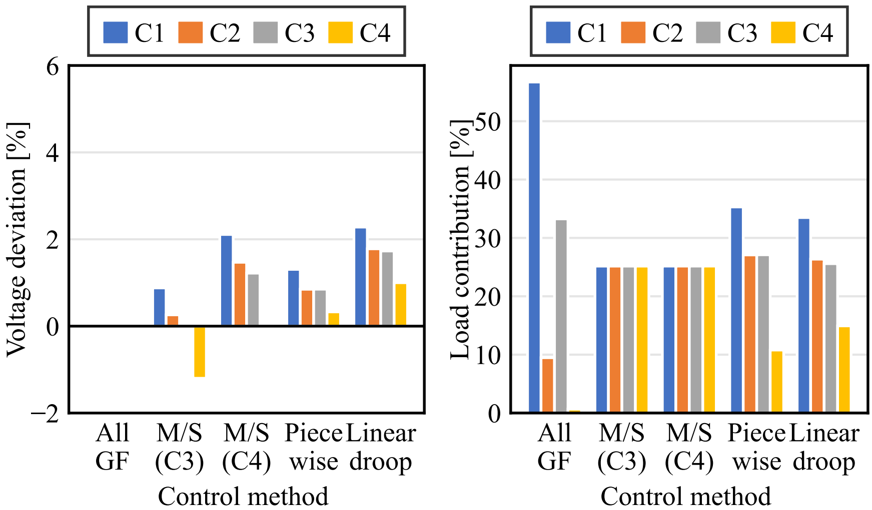

(a) (b)

Figure 6.4: First level controls performance at 33% load capacity: (a) Voltage deviation (b) Load distribution

58% load capacity

Fig. 6.5 shows the behavior of the controllers as the load increases to 58% of the max load capacity. The GF converters continue to operate effectively, maintaining minimal voltage deviation. Similarly, the master-slave controllers exhibit the same behavior observed at 33% load capacity. At this operating point, the piecewise controller has transitioned to the second segment, which allows an increased voltage deviation, although it remains lower than that of linear droop control. The load distribution at 58% load capacity is shown in Fig. 6.5b. The GF converters still show uneven load distribution, with most of the power is still provided by C1 and C3. The master-slave controllers continue to show an equal distribution of 25% on each converter. The load distribution of the linear droop control has been improved, with the converters' load contributions approaching 25%. However, C4 is still lags behind, as its load sharing is affected by the line resistance connecting it to the rest of the grid. Most of the piece wise controlled converters also approach 25%, as they now have a slope that allows them to improve their load sharing capabilities.

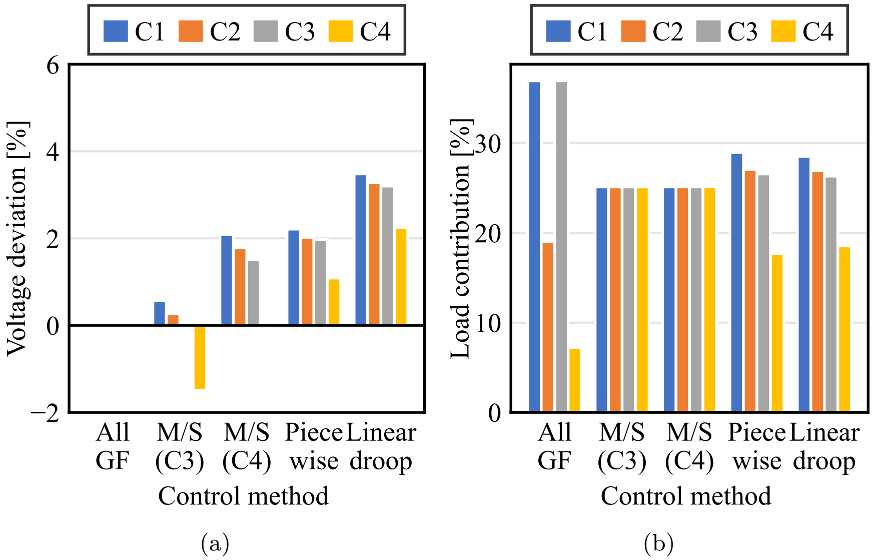

Figure 6.5: First level controls performance at 58% load capacity: (a) Voltage deviation (b) Load distribution

84% load capacity

Finally, a load demand of 84% is tested, and the resulting voltage deviations are shown in Fig. 6.6a. When all converters are operating as GF, the voltage deviations are almost nonexistent. Only a deviation of less than 1% is observed at C3. This deviation could be attributed to the converter reaching its nominal power limit and being unable to inject more power to mantain a perfect nominal voltage. In the case of the master-slave controllers, the impact of the choice of master converter becomes more apparent. If C3, which tends to provide the most power, is selected as the master, the other converters will need to exceed the nominal voltage level to inject power. Conversely, if C4, which provides the least amount of power, is chosen as the master, the other converters will provide power while operating below the nominal voltage level. At this operating point, the piecewise controller enters its final segment, allowing a 5% voltage droop. The voltage deviations for both the piecewise and linear control approaches the design limit of 5%. Notice that this limit is proportional to the output current. However, the voltage can indeed deviate more than 5%, as is the case for C3 with linear control.

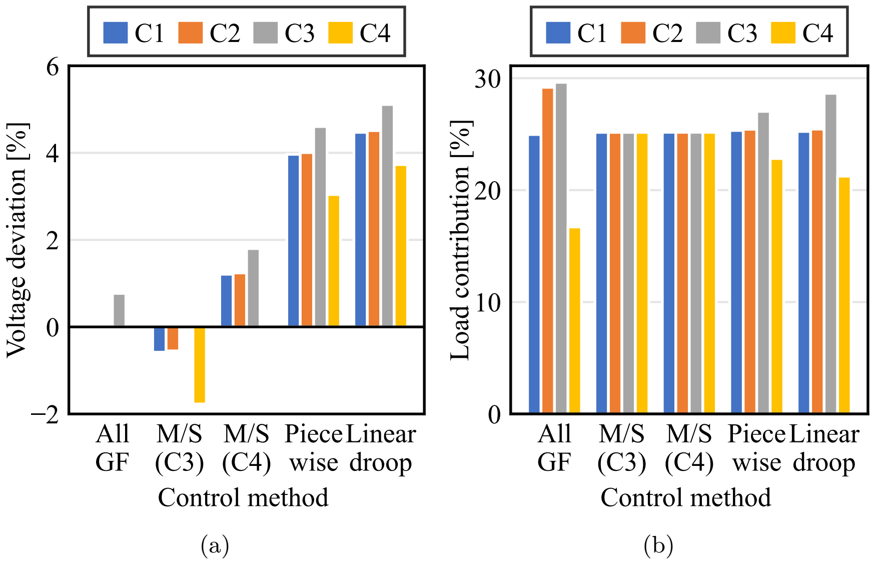

Figure 6.6: First level controls performance at 84% load capacity: (a) Voltage deviation (b) Load distribution

When the load capacity reaches 84%, as shown in Fig. 6.6b, it is shown that the load is shared better compared to the previous cases. In grid-forming mode, some converters reach their maximum output power, thus the other converters are forced to inject more power to maintain the grid voltage. This results in better load sharing compared to earlier load capacity points. In the case of the master-slave controllers, the load is shared equally, as observed in previous load points. Finally, both piecewise droop control and linear droop control show their respective best results. The droop curves approach their maximum deviation points. However, there is still an unequal load sharing in converters C3 and C4. This is attributed to the significant line resistance linking C4 to the rest of the DC microgrid. Notice that although the allowed voltage deviation for both controllers at this point is 5%, the obtained results differ. This is due to the differences in droop resistance. While the allowed deviation is the same, the current range for which it is valid is different. The droop resistance for each control at that point is calculated as $\Delta V/I_{max}$. In the piecewise controller, this 5% droop is valid for a smaller current range, and thus a smaller I_{max}, resulting in a greater droop resistance. This fact explains the improved load sharing shown by the piecewise controller.

Results Analysis

Based on the obtained results, the control methods are evaluated using the four parameters shown in Table 6.2. Load sharing refers to the capacity to distribute the load equally or proportionally among the converters in the microgrid. Voltage regulation, as implied by its name, is the ability to regulate voltage and remain close to the nominal voltage. The reliability criterion refers to the capacity of the control scheme to continue operating even if certain converters or the communication system fail. Finally, the communication criterion refers to whether communication is required between the converters or a central controller.

Table 6.2: Comparison of primary control methods

Control	**Load sharing**	**Voltage regulation**	**Reliability**	**Communication**
All GF	✗	✓	✓	✗
Master-Slave	✓	✓	✗	✓
Linear droop	✓	✓	✓	✗
Non-linear droop	✓	✓	✓	✗

The case where all the converters are functioning as GF is first analyzed. Being the most basic control scheme, it is indeed easy to implement and modular. It can be considered reliable, as the converters operate independently, so if one converter fails, the others will continue to regulate the voltage at their outputs. There is no communication required for this control method. However, as shown in the previous section, there is no load sharing with this type of control, and therefore, a single converter can supply most of the loads in certain occasions.

M/S control is the first control scheme to show a load sharing capacity. As shown in the previous results, when using master-slave control, the load is equally shared among the converters. Notice that it is shared equally, but not proportionally. Indeed, even if the slaves had different nominal current capacities, they would all receive the same reference current. Achieving proportional current sharing would require adjusting the reference current given by the master by multiplying or decreasing it by a certain factor. For example, one converter could receive 120 % of the reference current while another receives 80 %. This can improve the load sharing, but even then it would not be necessarily proportional to the nominal current of the converter. Furthermore, it would be necessary to verify that the factors sum up to a total of 100% of the current. Master-slave control provides good voltage regulation, but depending on the master converter, the slave converters may operate either above or below the nominal voltage. When a converter acts as a master and generates references for the other converters, it introduces a reliability issue. If the master converter encounters problems, the slave converters will not receive a reference current and will not know how to operate. While the master converter could be appointed dynamically, this increases the communication requirements. Furthermore, this type of control requires a certain level of communication between the master and slave converters. If communication issues arise, the slave converters may not receive the correct current reference, increasing reliability problems.

Linear droop control and piecewise control respond similarly to the evaluated parameters for the same reasons. As they correspond to decentralized controls, droop controls are reliable beacause each converter operates independently from the others. Therefore, even if multiple converters are disconnected from the microgrid, the remaining converters will naturally adjust their voltage and power injection. Due to this characteristic, no communication mechanisms are needed to implement this controller. Droop controllers are able to provide voltage regulation within a certain allowed voltage deviation. The key difference with droop controls is that they allow for load sharing not only equally, but also proportionally to the maximum output capacity of the converter. While this load sharing may not be perfect, it can be implemented easily by adjusting the droop resistance to an appropriate value.

Based on the previous discussion, a primary control method can be recommended depending on the application. If tight voltage regulation with no load sharing is required, using all converters as GF converters can be a viable control approach. If an EMS is available or if specific current injections are needed, utilizing both GF and GFL converters could be advantageous. Master-slave control has its origins in the context of uninterruptible power supplies. Therefore, it is better suited for similar applications, such as relatively small systems where the sources have similar rated currents. It is well suited for cases where the load needs to be evenly distributed among the converters. Finally, linear droop and non-linear droop controls are well suited for applications where a certain voltage deviation can be allowed and where load sharing needs to be proportional. Proportional load sharing based on the maximum output current is ideal for systems where different types of sources are connected.

6.1.2 Non-linear droop control

The same comparison is repeated with the non-linear controls presented in Chapter 3, comparing them against the traditional linear droop control. Indeed, non-linear controls were developed to address the shortcomings of linear control, making it reasonable to use linear control as the baseline performance. As a reminder to the reader and to ease the understanding of the results, the non-linear droop voltage curve and output resistance are reproduced in Fig. 6.7.

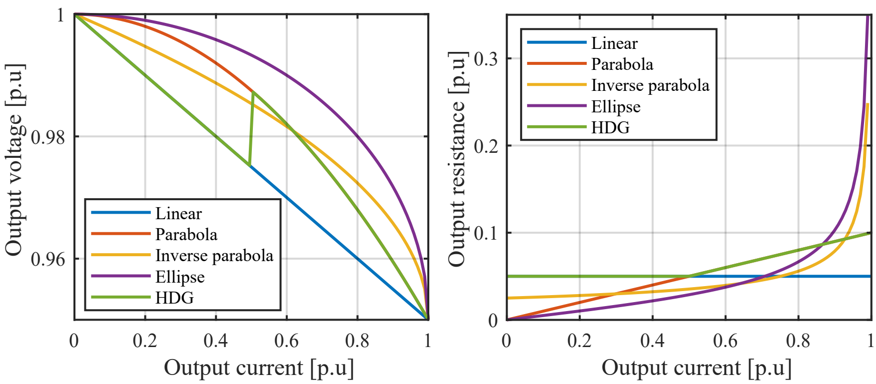

(a) (b)

Figure 6.7: Non-linear droop controls: (a) Voltage curves (b) Provided resistances

33% load capacity

Fig. 6.8a shows the voltage deviation of each control method at 33% load capacity, corresponding to a light load case. The linear droop control can be taken as a reference for the voltage deviation. It is observed that the non-linear droop methods provide better voltage regulation at this point, as the voltage deviation is smaller. In the case of HDG control, at this power level, it follows the linear droop slope and thus provides the same results.

Among the non-linear controls, parabola and ellipse droop provide better voltage regulation. Indeed, at low demand, non-linear controls provide a flatter voltage curve, as previously observed in Fig. 6.7a. Similarly, in Fig. 6.7b, it is observed that they provide a low resistance value at this operation point, resulting in smaller voltage deviation.

The contribution of each converter to the load at this power point is shown in Fig. 6.8b. At low power levels, both linear droop control and HDG provide the highest droop resistance. A higher droop resistance value allows better load sharing, as shown in the results (C1 and C4 are closer to 25%). In contrast, the load sharing of the non-linear control methods is less effective. At this operation point, they provide a low droop resistance and thus worse load sharing. Here, ellipse control exhibits the most uneven load sharing. Notice that Converter 4 provides significantly less power. This can be attributed to the longer line section connecting it to the rest of the DC microgrid. A longer line implies a greater line resistance, which reduces the accuracy of the droop control.

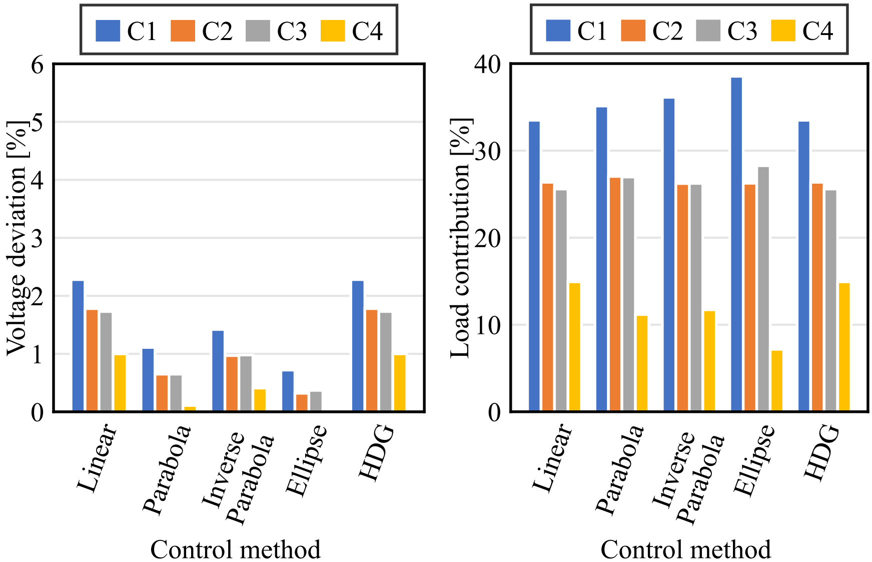

(a) (b)

Figure 6.8: Non-linear droop controls performance at 33% load capacity: (a) Voltage deviation (b) Load distribution

58% load capacity

As the load demand increases, the converters provide more power. The increase in output current causes them to deviate further from the nominal value, as shown in Fig. 6.9a. Ellipse droop control provides the best voltage regulation. This corresponds to the voltage curve of Fig. 6.7a, where it is seen that it maintains tight voltage regulation for a wider range compared to the other control methods. Notice that the voltage deviation for HDG control does not correspond to either linear droop or parabola droop. This is because C4 does not change the curve it is following until later. Thus, C1, C2, and C3 are utilizing parabola droop while C4 is still utilizing linear droop, resulting in different voltage regulation for C4. The load contribution can be seen in Fig. 6.9b. Compared to the light load case, it is shown that the non-linear controllers start providing better load sharing, resulting in a load contribution comparable to that of droop control. The two exceptions are the ellipse control and HDG control. As mentioned before, ellipse control still provides tight voltage regulation, and HDG control has one converter using a different curve.

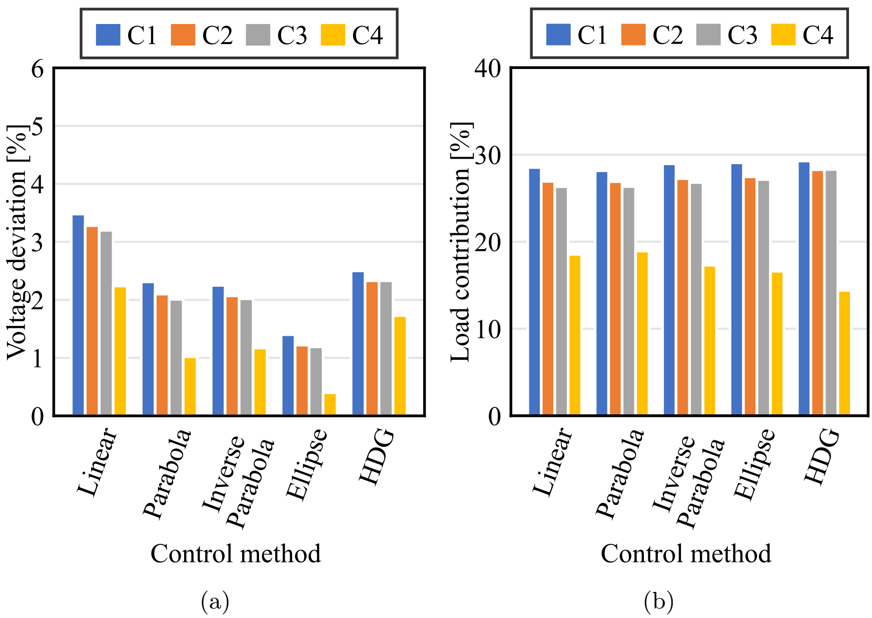

Figure 6.9: Non-linear droop controls performance at 58% load capacity: (a) Voltage deviation (b) Load distribution

84% load capacity

The performance of the controllers under high load conditions is evaluated, considering an 84% load capacity. The voltage deviation of the converters is shown in Fig. 6.10a. Linear droop control shows the highest amount of voltage deviation, while the non-linear methods result in better voltage regulation. This is explained by the voltage curves shown in Fig. 6.7a. HDG control shows the same voltage regulation as parabola control. Indeed, at this operating point, HDG control follows the curve of the parabola droop, which offers a higher droop resistance (see Fig. 6.7b). The load sharing at 84% load capacity is shown in Fig. 6.10b. Linear droop control shows the most uneven load distribution among converters 3 and 4. The non-linear control methods demonstrate better load sharing among converters 3 and 4. This improved load sharing can be attributed to the non-linear control methods providing a higher droop resistance. Similar to the voltage, HDG shows the same results as the parabola droop. The load sharing among the non-linear methods is very similar, with ellipse droop control showing the best load sharing between converters 3 and 4.

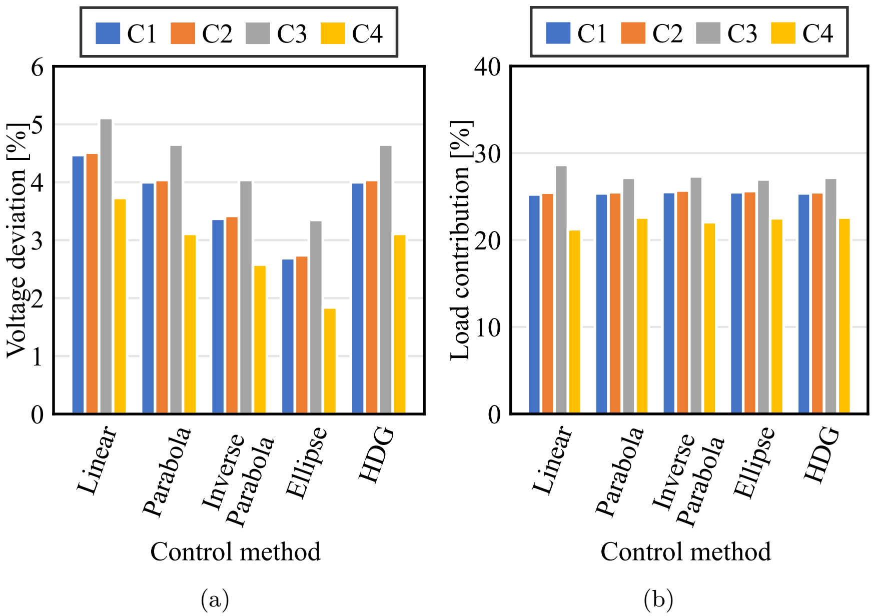

Figure 6.10: Non-linear droop controls performance at 84% load capacity: (a) Voltage deviation (b) Load distribution

Results Analysis

The obtained results show that at light load capacity, non-linear droops provide better voltage regulation but worse load sharing compared to linear droop. At high load capacity, the load sharing is better with non-linear droop controls. While voltage deviations increase at high load capacity, the voltage regulation of non-linear droop controls remains superior to its linear counterpart. Two criteria on which to base the choice of controller are the provided droop resistance and the operation point of the microgrid. Parabola and ellipse control provide minimal or negligible droop resistance under light load conditions. Thus, the load sharing will be defined by the resistances of the lines. If this tradeoff is not acceptable, then another droop control should be considered. The operation point of the microgrid has to be considered for the same reasons. If the output current of the converters remains on average below 0.5 p.u, linear droop control will provide greater droop resistance compared to the non-linear methods except for HDG. Similarly, if the output current of the converters will rarely go above 0.85 p.u, the increased output resistance of the inverse parabola and ellipse will not be utilized. However, the voltage regulation advantages will be retained. Finally, when using HDG, some converters may switch to the parabola curve while others remain in the linear curve. This inaccuracy, along with the possible instability at the switching point, should be considered.

6.2 Second level controls

In this section, the same test applied to second level controls. Thus, droop control is implemented as a first level control, and the second level controls try to compensate for its shortcomings. To assist the reader, the table comparing the differences between the second level controls is repeated here, as it can be used to better interpret the obtained results. Seven different controls are tested: Voltage resotration (VR), Average voltage restoration (AVR), Digital average current sharing (DACS), Average current and voltage (ACV) control, Adaptive droop (AD) control , Average current and average droop resistance droop (ACD) control, Average current and average voltage droop (ACVD) control. In the case of VR, C3 is chosen as the reference voltage node.

Table 6.3: Comparison of secondary control methods

Second level control	Improved load sharing	Improved voltage regulation	Voltage offset	Slope offset
Voltage restoration [67]	✗	✓	✓	✗
Average voltage restoration	✗	✓	✓	✗
DACS [81]	✗	✓	✓	✗
Average current and voltage control[82]	✓	✓	✓	✗
Adaptive droop control[83], [84]	✓	✓	✓	✓
Average current and average droop resistance droop control [85]	✓	✓	✓	✓
Average current and average voltage droop control [86], [87]	✓	✓	✓	✓

33% load capacity

First, the light loading case is analyzed. The voltage deviation percentage is shown in Fig. 6.11a. Compared to the results obtained for droop control, an improvement in voltage regulation is seen. In Fig. 6.8a linear droop control exhibits a maximum voltage deviation close to 2.3 %, whereas second-level controls keep the voltage deviations to a maximum of 1.2%. Notice that the first three controls methods (VR, AVR, DACS) show a different profile, while the last four (ACV, AD, ACD, ACVD) exhibit the same profile. This can be explained by the fact that the last four methods use the average grid voltage for improved voltage regulation. Additionally, as shown in Table 6.3, they also all provide improved load sharing via different methods. This can be observed easily in Fig. 6.11b, where it is shown that the load contribution of the converters is almost equal across these control methods. In contrast, the first three control methods (VR, AVR, DACS) do not provide improved load sharing and thus have unequal load contribution.

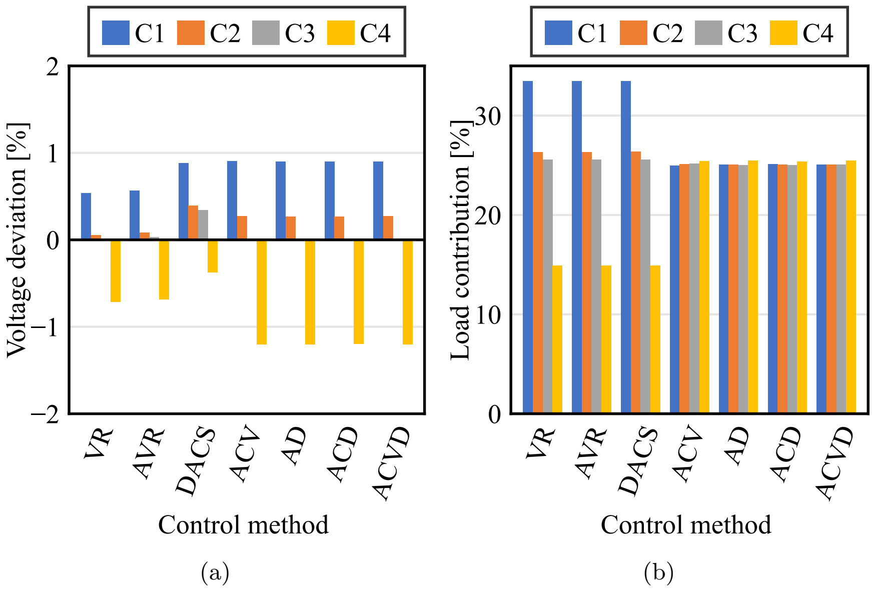

Figure 6.11: Second level controls performance at 33% load capacity: (a) Voltage deviation (b) Load distribution

58% load capacity

As with the previous case, at 58% load capacity, the last four methods show the same regulation in terms of voltage and load contribution. The first three methods show the same load sharing pattern as well. However, as shown in Fig. 6.12b, the load contribution is approaching 25%, which can be attributed to more loads being connected at this moment and thus having the loads more evenly distributed throughout the microgrid. In terms of voltage regulation, the choice of voltage reference node can be more clearly seen for VR control. Fig. 6.12a shows that the voltage is regulated so that C3 has no voltage deviation. DACS control provides an offset to the voltage proportional to the output current. In this case, since all converters have the same parameters, the offset is the same for all converters. Thus, the one providing the most power will have the highest voltage deviation, as shown in Fig. 6.12a. At 58% loading, this offset causes C4 to have a reference higher than the nominal voltage, which explains the negative voltage deviation. However, compared to the linear droop deviation at this operating point (Fig. 6.9), the voltage regulation is significantly improved.

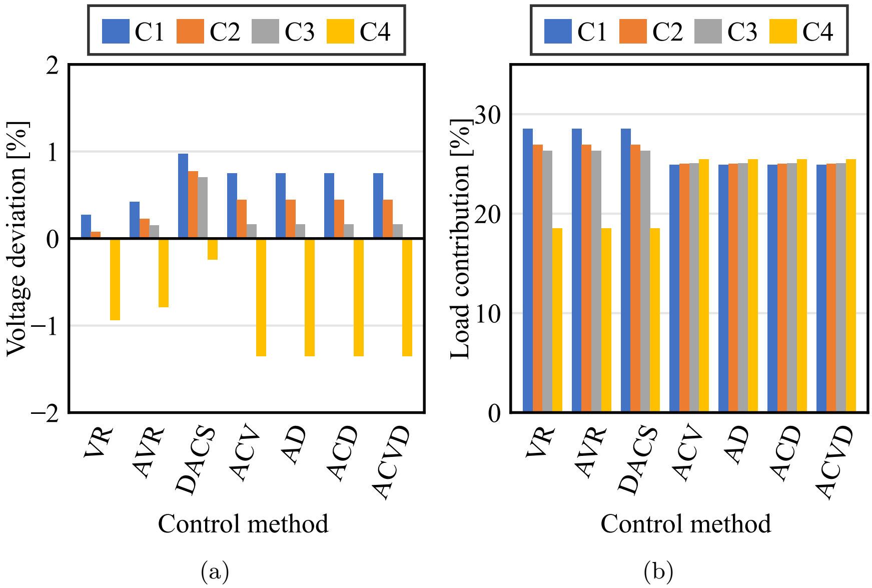

Figure 6.12: Second level controls performance at 58% load capacity: (a) Voltage deviation (b) Load distribution

84% load capacity

At 84% load capacity, the characteristics of each method are further highlighted. Fig. 6.13a shows how in VR control, the reference node has no voltage deviation. However, due to this choice, the other nodes experience an overvoltage (similar to what was seen in M/S control). AVR shows better voltage regulation compared to VR, with the tradeoff being the deviations seen in C3 and C4. DACS shows the highest voltage deviations, but these are lower than what would be experienced utilizing linear droop control. Concerning the last four methods (ACV, AD, ACD, ACVD), as shown in Fig. 6.13a and Fig. 6.13b, they exhibit the same voltage regulation and load contribution with minimal differences. These methods show good voltage regulation but have the best load sharing capabilities.

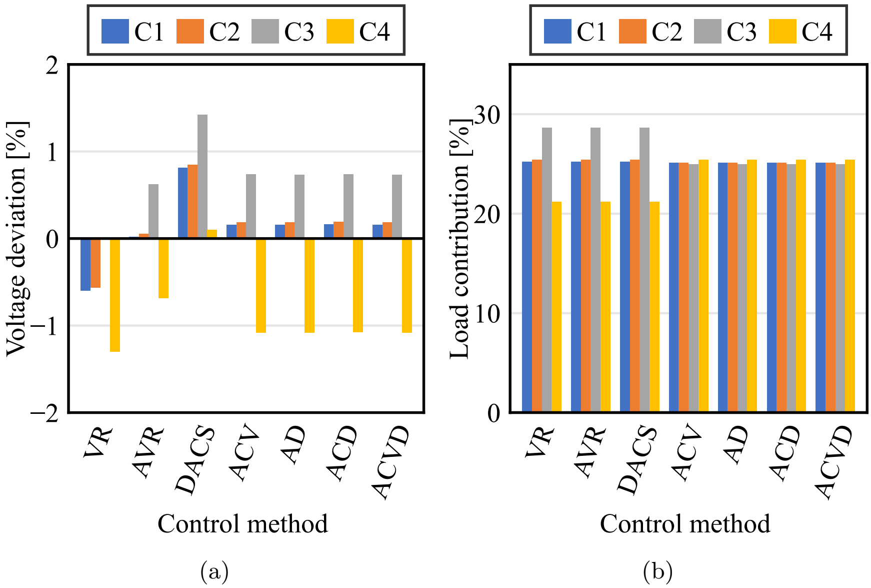

Figure 6.13: Second level controls performance at 84% load capacity: (a) Voltage deviation (b) Load distribution

With different capacity converters

To further test these second level controllers, the same test is repeated on the different second level controls. However, this time, the converters each have a different power capacity. A different rated power implies a different maximum output current and thus a different droop parameter. The new power ratings are as follows: C1 50 kW, C2 20 kW, C3 40 kW, and C4 80 kW. Thus, a total power of 190 kW is available in the system. C4 provides about 42% of this new capacity, while C2 provides about 10%. The loads remain the same. To maintain brevity, only two cases are shown: 33% loading and 84% loading in Fig. 6.14 and Fig. 6.15 respectively.

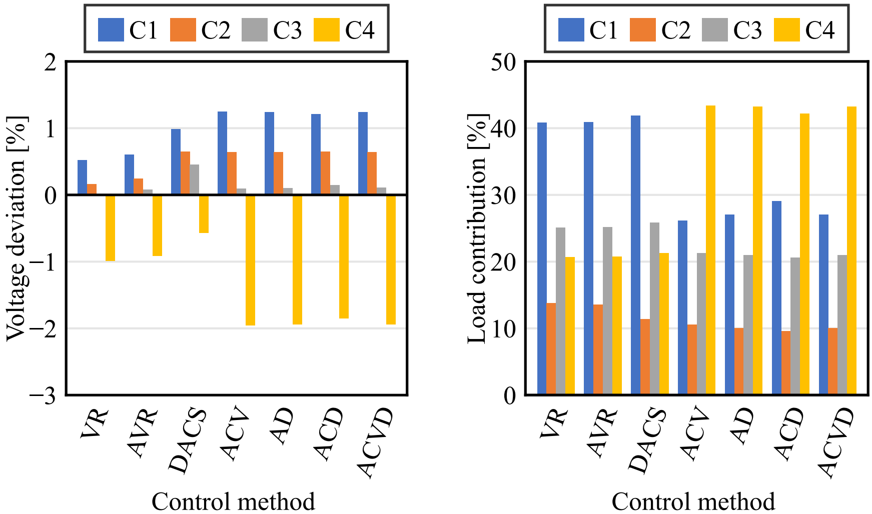

(a) (b)

Figure 6.14: Second level controls performance at 33% load capacity with varying converter power ratings: (a) Voltage deviation (b) Load distribution

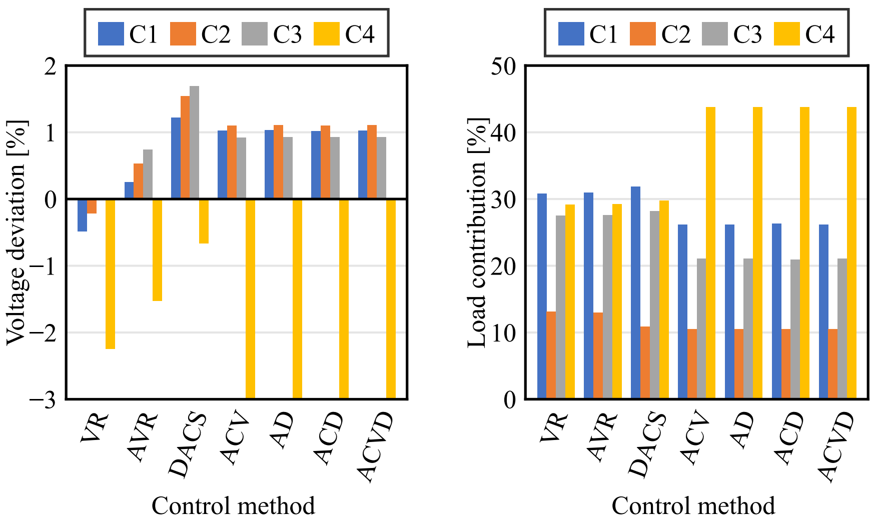

(a) (b)

Figure 6.15: Second level controls performance at 84% load capacity with varying converter power ratings: (a) Voltage deviation (b) Load distribution

The first three control methods (VR, AVR, and DACS) are analyzed together. It is seen that with respect to the previous case study, there are no significant differences. The voltage deviations are reduced, resulting in improved voltage regulation. The load sharing is mainly imposed by the droop resistance and the line resistances. Because C4 has a higher power rating, its droop parameter is smaller, causing it to provide more power. However, it still provides less than C1, which is rated for 30 kW less.

The other four control methods (ACV, AD, ACD, and ACVD) exhibit good voltage regulation. Notice though, that because the load sharing is improved with these control methods, in order for C4 to provide the most power, it requires C4 to experience a non-negligible overvoltage. This is why at 33% and 84% loading, C4 shows a high voltage deviation. In terms of load contribution, it is seen that the four methods achieve a load contribution proportional to their nominal power. As mentioned before, C4 represents about 42% of the total available power. It is seen that the load contribution of C4 is close to this number. The same applies to C2 with its 10% load contribution. Finally, C1 provides more than C3, which corresponds to their rated capacity of 50 kW and 40 kW.

Results Analysis

The previous results show that second level controls provide effective improvements to linear droop control. They achieve this by improving voltage regulation in all cases and improving load sharing in others. Let us first analyze the first three control methods which provide only improved voltage regulation: VR, AVR, and DACS. VR improves voltage regulation overall but utilizes one node as a reference node. Similar to master-slave control, the chosen reference node will affect which nodes experience overvoltage or undervoltage. However, because it can maintain one node close to the nominal voltage, it can have valuable applications in DC microgrids where critical loads are present and require stable voltage. AVR shows a better voltage regulation on average. However, because the average voltage is utilized, it allows certain nodes to experience overvoltages and undervoltages. DACS employs a different method to achieve the same result, which is an upward shift in the droop slope. The gain related to this shift can be chosen by the user, allowing for minimized voltage deviations if desired. One final advantage of DACS is that it does not require an additional PI controller. All three controllers have straightforward implementations and provide good results.

The last four second level controllers provide improved voltage regulation and load sharing. As the results have shown, in steady-state, the differences between these four controllers are relatively small. Furthermore, they also provide enhanced proportional load sharing, as demonstrated in the results using converters of different nominal power. Notice that to achieve equal or proportional load contribution, the voltage regulation is impacted. Particularly, in the proposed testbench, C4 has a higher line resistance, causing it to provide less power. Second level controls cause an overvoltage in C4 to ensure the appropriate load contribution percentage. Although the voltage deviations remain within an acceptable range (reaching a maximum of 3%), this constraint must be kept in mind.

ACV, AD, and ACVD provide the same results and require the implementation of only two additional PI controllers compared to linear droop control. In contrast, ACD requires three PI controllers. While all of them provide similar steady-state results, ACD is less appealing as it requieres determining more parameters. In the author's opinion, certain elements of these controllers could be further investigated. It is known that second level controls should have a slower dynamic than first level control, but it is not mentioned what the dynamic relationship should be between control loops in second-level controls. For example, the relationship between the voltage control loop and the load sharing loop is not specified. Similarly, the same question remains for ACD, where the relationship between the current control and the droop resistance control is not stated. Furthermore, these control loops have conflicting objectives to some extent. Therefore, understanding which loop should be faster or slower is important.

The usage of saturation to limit the output of the PI controls is recommended; however, no guideline is given as to what value it should be limited. The general idea is to limit it to avoid significant voltage deviations. Another point related to this question is the limits of the proposed controls: Are there voltage deviations too significant to be regulated, or are there load sharing proportions that cannot be imposed due to the relationship between the converters and the lines interfacing them? Further analysis is required to find these answers and valuable differences between the controls. This could include a small signal analysis to evaluate how the different controllers impact converter stability.

Chapter 7

Conclusions

The contents presented in this work are summarized hereafter. The contributions of the work are equally highlighted. Finally, an analysis of the work done and possible future work is provided.

Content Overview

This thesis aims to provide a comprehensive guide to DC microgrids and their modeling. This modeling encompasses long-term simulations via steady-state simulations and shorter-term simulations via dynamic simulations.

The concept of DC microgrids was introduced in Chapter 2. Their advantages, topology, and architectures were discussed. The existing challenges in terms of power quality, fault protection, and standardization were presented. Finally, existing implementations were highlighted.

Chapter 3 provided an overview of control methods in DC microgrids. The controls were presented following the hierarchical control structure. Different types of first level controls were introduced, including four types of non-linear controls. The advantages and limitations of droop control were discussed. Furthermore, the way in which non-linear droop controls aim to address the shortcomings of linear droop control was detailed. Similarly, second level controls were presented, encompassing seven different controls and their structures.

Chapter 4 details the methodology to implement a linear power flow. This methodology is explained for unipolar and bipolar DC microgrids. Chapter 4 demonstrates how this method can be used sequentially to simulate the behavior of a DC microgrid over long periods of time. Possible applications of this approach were discussed by analyzing microgrid voltage, current amplitude, and self-sufficiency and self-consumption indexes. Finally, a comparison of the performance of unipolar and bipolar microgrids was performed.

The modeling of power electronics was addressed in Chapter 5. First, the importance of developing average models was highlighted. Average DC/DC converters based on the DC transformer model were proposed and demonstrated. Afterwards, potential average models for AC/DC converters were presented. The latter part of the chapter focused on modeling three-port HFAC link converters. The operation and switching of this type of converter were detailed for both two-port and three-port versions. A state machine model was developed to study the HFAC link, followed by an analysis of HFAC link frequency calculation. After gaining a better understanding of the converter, average modeling based on the DC transformer concept was introduced. To this end, state-space models for both two-port and three-port converters were initially developed. Utilizing the developed average model, a set of basic control structures for three-port converters was proposed. Finally, a small DC microgrid utilizing three-port converters was simulated.

Chapter 6 presented a comparison of the control methods detailed in Chapter 3. The performance of the different controls was assessed based on their capabilities for voltage regulation and equal or proportional load sharing. The results were analyzed, and possible utilization cases for the controls were proposed.

Perspectives

Concerning the linear power flow, the author believes that there is still room for possible improvements and applications. First, only radial networks have been considered in this study. The first paper concerning the linear power flow has already demonstrated that this method can be utilized to treat complex networks. Therefore, the author believes that it could be interesting to test radial DC microgrids with branches, that is to say radial netwroks were the main bus splits into subnetworks that are themselves radial systems. It can also be of interest to explore different topologies such as ring DC microgrids, and investigate the possibility of implementing meshed DC microgrids using linear power flow. Another area of study could involve analyzing new loads such as electrolyzers and electric vehicles in DC microgrids using linear power flow. This analysis could help identify the impact these loads could have in terms of voltage regulation and line currents. Furthermore, the implementation of other first and second level controllers could be of interest. This would enable the assessment of the power quality and energy benefits of each control method over an extended period of time. Finally, another possibility could be the inclusion of an EMS or optimization algorithm that could coordinate the different converters in the DC microgrid.

In terms of control methods, it has been shown that most controls can achieve their goals effectively. There is a great variety with sometimes minor differences. Therefore, assessing their advantages or strengths is not a straightforward process. As suggested by the author in Chapter 6, a small signal study of the control methods could be useful. This would allow to further identify differences in controls, mainly in terms of provided stability. As mentioned in Chapter 6, second level controls merit further investigation concerning the speed of the different control loops and their interactions. Finally, the list of controls studied here is nonexhaustive. Other types of controls could still be investigated and analyzed. For example fuzzy logic based first level controllers, adaptive droop controls that consider the State of charge of the battery, or control methods that use DC bus signaling.

The presented average converters have useful applications, but their validity depends on the type of phenomena to be studied, which is something that must be kept in mind. Regarding the average three-port converter model, the proposed control scheme could be further improved. Exploring the possibility of implementing cascaded PI controllers to enhance performance could be beneficial. Furthermore, it has been shown that there is a degree of coupling between the converter ports. It could be interesting to implement feedforward terms to mitigate this coupling, thus increasing the independence of the ports from each other.

The presented work has primarily focused on modeling DC microgrids; however, two main areas were not studied to limit the scope of the work. These are fault behavior and the interactions of DC microgrids with the main AC grid. Both subjects merit their own dedicated studies and are of interest in the current state of technology. Further development on both subjects could provide valuable insights for standardization and the implementation of DC microgrids.

Bibliography

[1] E. V. Mayen and E. De Jaeger, “Linearised bipolar power flow for droop-controlled dc microgrids,” in *2021 International Conference on Engineering and Emerging Technologies (ICEET)*, 2021, pp. 1–6. DOI: 10.1109/ICEET53442.2021.9659746.

[2] E. V. Mayen and E. De Jaeger, “Industrial dc microgrid analysis through linear power flow,” in *2022 IEEE International Conference on Environment and Electrical Engineering and 2022 IEEE Industrial and Commercial Power Systems Europe (EEEIC / I&CPS Europe)*, 2022, pp. 1–6. DOI: 10.1109/EEEIC/ICPSEurope54979.2022.9854709.

[3] J. Allard, E. V. Mayen, and E. De Jaeger, “Resonance model comparison for high-frequency ac link three-port converter,” in *2023 IEEE International Conference on Environment and Electrical Engineering and 2023 IEEE Industrial and Commercial Power Systems Europe (EEEIC / I&CPS Europe)*, 2023, pp. 1–6. DOI: 10.1109/EEEIC/ICPSEurope57605.2023.10194661.

[4] E. Vasquez Mayen and E. De Jaeger, “Comparative study of unipolar and bipolar industrial dc microgrids through linear power flow,” in *27th International Conference on Electricity Distribution (CIRED 2023)*, vol. 2023, 2023, pp. 194–198. DOI: 10.1049/icp.2023.0273.

[5] E. Vasquez Mayen and E. De Jaeger, “Average modeling of high frequency ac link three-port dc/dc/dc converters,” *Electricity*, vol. 5, no. 2, pp. 397–425, 2024, ISSN: 2673-4826. DOI: https://doi.org/nbqb. [Online]. Available: https://www.mdpi.com/2673-4826/5/2/21.

[6] E. V. Mayen, E. De Jaeger, G. W. Ndiwulu, and A. K. Lusala, “Voltage unbalance compensation for islanded microgrids with hybrid control approach,” in *2021 International Conference on Engi-*

neering and Emerging Technologies (ICEET), 2021, pp. 1–6. DOI: 10.1109/ICEET53442.2021.9659678.

[7] G. Wanlongo Ndiwulu, E. Vasquez Mayen, and E. De Jaeger, "Effect of a large proton exchange membrane electrolyser on power system small-signal angular stability," *Electricity*, vol. 4, no. 4, pp. 381–409, 2023, ISSN: 2673-4826. DOI: 10.3390/electricity4040021. [Online]. Available: https://www.mdpi.com/2673-4826/4/4/21.

[8] E. V. Mayen, G. W. Ndiwulu, V. Kluyskens, and E. De Jaeger, "Non-linear control of pem electrolyzers in dc microgrids," in *2024 IEEE International Conference on Environment and Electrical Engineering and 2021 IEEE Industrial and Commercial Power Systems Europe (EEEIC / I&CPS Europe)*, 2024, pp. 1–6.

[9] G. W. Ndiwulu, E. V. Mayen, and E. a. De Jaeger, "Dynamic interactions of a high-current thyristor-rectifier interfaced pem electrolyzer with the angular dynamics of synchronous machines," in *2024 IEEE International Conference on Environment and Electrical Engineering and 2021 IEEE Industrial and Commercial Power Systems Europe (EEEIC / I&CPS Europe)*, 2024, pp. 1–6.

[10] International Energy Agency, "Energy technology perspectives 2023," IEA, Paris, Tech. Rep., 2023, License: CC BY 4.0. [Online]. Available: https://www.iea.org/reports/energy-technology-perspectives-2023.

[11] REN21, *Renewables 2023 Global Status Report Collection, Global Overview.* Paris: REN21 Secretariat, 2023, ISBN: 978-3-948393-11-3. [Online]. Available: https://www.ren21.net/gsr-2023/.

[12] REN21, *Renewables 2023 Global Status Report Collection, Energy Systems & Infrastructure.* Paris: REN21 Secretariat, 2023, ISBN: 978-3-948393-09-0. [Online]. Available: https://www.ren21.net/gsr-2023/.

[13] International Renewable Energy Agency, "Renewable power generation costs in 2022," International Renewable Energy Agency, Abu Dhabi, Tech. Rep., 2023. [Online]. Available: https://www.irena.org/Publications/2023/Aug/Renewable-Power-Generation-Costs-in-2022.

[14] A. Ipakchi and F. Albuyeh, "Grid of the future," *IEEE Power and Energy Magazine*, vol. 7, no. 2, pp. 52–62, Mar. 2009, ISSN: 1558-4216. DOI: 10.1109/MPE.2008.931384.

[15] B. Kroposki, R. Lasseter, T. Ise, S. Morozumi, S. Papathanassiou, and N. Hatziargyriou, "Making microgrids work," en, *IEEE Power and Energy Magazine*, vol. 6, no. 3, pp. 40–53, May 2008, ISSN: 1540-7977, 1558-4216. DOI: 10.1109/MPE.2008.918718. [Online]. Available: https://ieeexplore.ieee.org/document/4505826/.

[16] W. Jing, C. Hung Lai, S. H. W. Wong, and M. L. D. Wong, "Battery-supercapacitor hybrid energy storage system in standalone dc microgrids: Areview," *IET Renewable Power Generation*, vol. 11, no. 4, pp. 461–469, 2017. DOI: https://doi.org/10.1049/iet-rpg.2016.0500. eprint: https://ietresearch.onlinelibrary.wiley.com/doi/pdf/10.1049/iet-rpg.2016.0500. [Online]. Available: https://ietresearch.onlinelibrary.wiley.com/doi/abs/10.1049/iet-rpg.2016.0500.

[17] The Pew Charitable Trusts, *Why (and how) microgrid technology is a good power source*, Issue Brief, Clean Energy Initiative, Feb. 2016. [Online]. Available: https://www.pewtrusts.org/-/media/assets/2016/02/why_and_how_microgrid_technology_is_a_good_power_source.pdf.

[18] R. Lasseter, "MicroGrids," en, in *2002 IEEE Power Engineering Society Winter Meeting. Conference Proceedings (Cat. No.02CH37309)*, vol. 1, New York, NY, USA: IEEE, 2002, pp. 305–308, ISBN: 978-0-7803-7322-8. DOI: 10.1109/PESW.2002.985003. [Online]. Available: http://ieeexplore.ieee.org/document/985003/.

[19] G. Venkataramanan and S. Bala, "Resource Aggregation Using Microgrids," en, in *Power Electronics for Renewable and Distributed Energy Systems: A Sourcebook of Topologies, Control and Integration*, ser. Green Energy and Technology, S. Chakraborty, M. G. Simões, and W. E. Kramer, Eds., London: Springer London, 2013, pp. 469–491, ISBN: 978-1-4471-5104-3. DOI: 10.1007/978-1-4471-5104-3_12. [Online]. Available: https://doi.org/10.1007/978-1-4471-5104-3_12.

[20] J. J. Justo, F. Mwasilu, J. Lee, and J.-W. Jung, "AC-microgrids versus DC-microgrids with distributed energy resources: A review," en, *Renewable and Sustainable Energy Reviews*, vol. 24, pp. 387–405, Aug. 2013, ISSN: 13640321. DOI: 10.1016/j.rser.2013.03.067. [Online]. Available: https://linkinghub.elsevier.com/retrieve/pii/S1364032113002268.

[21] I. E. Agency, *Energy Access Outlook 2017*. 2017, p. 140. DOI: https://doi.org/https://doi.org/10.1787/9789264285569-en. [Online]. Available: https://www.oecd-ilibrary.org/content/publication/9789264285569-en.

[22] M. Uddin, H. Mo, D. Dong, S. Elsawah, J. Zhu, and J. M. Guerrero, "Microgrids: A review, outstanding issues and future trends," en, *Energy Strategy Reviews*, vol. 49, p. 101 127, Sep. 2023, ISSN: 2211467X. DOI: 10.1016/j.esr.2023.101127. [Online]. Available: https://linkinghub.elsevier.com/retrieve/pii/S2211467X23000779.

[23] J. Paserba and J. J. Cunningham, "DC Survival: Myth of the War of the Currents [History]," en, *IEEE Power and Energy Magazine*, vol. 22, no. 3, pp. 104–109, May 2024, ISSN: 1540-7977, 1558-4216. DOI: 10.1109/MPE.2024.3379454. [Online]. Available: https://ieeexplore.ieee.org/document/10521906/.

[24] Elia. "Two years of outstanding performance for nemo link: The uk-belgium interconnector." Accessed: February 10, 2024, Elia. (2021), [Online]. Available: https://www.elia.be/en/news/press-releases/2021/02/20210203_two-years-of-outstanding-performance-for-nemo-link-the-uk-belgium-interconnector.

[25] Elia. "Triton link." Accessed: February 10, 2024, Elia. (2024), [Online]. Available: https://www.elia.be/en/infrastructure-and-projects/infrastructure-projects/tritonlink.

[26] Elia. "Princess elisabeth island." Accessed: February 10, 2024, Elia. (2024), [Online]. Available: www.elia.be/en/infrastructure-and-projects/infrastructure-projects/princess-elisabeth-island.

[27] D. Kumar, F. Zare, and A. Ghosh, "DC Microgrid Technology: System Architectures, AC Grid Interfaces, Grounding Schemes, Power Quality, Communication Networks, Applications, and Standardizations Aspects," *IEEE Access*, vol. 5, pp. 12 230–12 256, 2017, ISSN: 2169-3536. DOI: 10.1109/ACCESS.2017.2705914.

[28] C. Papadimitriou, E. Zountouridou, and N. Hatziargyriou, "Review of hierarchical control in DC microgrids," en, *Electric Power Systems Research*, vol. 122, pp. 159–167, May 2015, ISSN: 03787796. DOI: 10.1016/j.epsr.2015.01.006. [Online]. Available: https://linkinghub.elsevier.com/retrieve/pii/S0378779615000073.

[29] G. Van den Broeck, "Voltage control of bipolar DC distribution systems," en, Ph.D. dissertation, KU Leuven, Nov. 2019, p. 262. [Online]. Available: https://lirias.kuleuven.be/2855166&lang=en.

[30] L. N. da Silva, G. S. Djambolakdjian, B. A. d. Andrade, *et al.*, "Line Losses and Power Capacity in Low Voltage AC and DC Distribution Systems: A Numerical Comparative Study," en, in *2021 IEEE International Conference on Environment and Electrical Engineering and 2021 IEEE Industrial and Commercial Power Systems Europe*

(EEEIC / I&CPS Europe), Bari, Italy: IEEE, Sep. 2021, pp. 1–6, ISBN: 978-1-66543-613-7. DOI: 10.1109/EEEIC/ICPSEurope51590.2021.9584638. [Online]. Available: https://ieeexplore.ieee.org/document/9584638/.

[31] "CIRED DC distribution networks - wg 2019-1," Tech. Rep. [Online]. Available: http://www.cired.net/cired-working-groups/dc-distribution-networks-wg-2019-1.

[32] Royal Dutch Standardization Institute (NEN), "NPR 9090:2018 NL: DC Installations for Low Voltage," Royal Dutch Standardization Institute (NEN), Tech. Rep., Sep. 2018, pp. 1–50.

[33] S. Rivera, R. Lizana F., S. Kouro, T. Dragicevic, and B. Wu, "Bipolar DC Power Conversion: State-of-the-Art and Emerging Technologies," en, *IEEE Journal of Emerging and Selected Topics in Power Electronics*, vol. 9, no. 2, pp. 1192–1204, Apr. 2021, ISSN: 2168-6777, 2168-6785. DOI: 10.1109/JESTPE.2020.2980994. [Online]. Available: https://ieeexplore.ieee.org/document/9036877/.

[34] R. Adam, C. Hildmann, M. Hemken, K. Backhaus, and S. Rupp, "Research of components for an increase of transmission capacity in distribution grids by changing existing AC links into DC Links," en, in *27th International Conference on Electricity Distribution (CIRED 2023)*, Rome, Italy: Institution of Engineering and Technology, 2023, pp. 3459–3463, ISBN: 978-1-83953-855-1. DOI: 10.1049/icp.2023.0823. [Online]. Available: https://digital-library.theiet.org/content/conferences/10.1049/icp.2023.0823.

[35] Y. Cho, J. Lee, S. Kim, and J. Kim, "Development of underground cable for lvdc of 1mw class," in *27th International Conference on Electricity Distribution (CIRED 2023)*, vol. 2023, 2023, pp. 1545–1548. DOI: 10.1049/icp.2023.0929.

[36] J. Barros, M. de Apráiz, and R. Diego, "Power Quality in DC Distribution Networks," en, *Energies*, vol. 12, no. 5, p. 848, Mar. 2019, ISSN: 1996-1073. DOI: 10.3390/en12050848. [Online]. Available: https://www.mdpi.com/1996-1073/12/5/848.

[37] J. Liao, Y. Liu, C. Guo, *et al.*, "Power quality of DC microgrid: Index classification, definition, correlation analysis and cases study," en, *International Journal of Electrical Power & Energy Systems*, vol. 156, p. 109 782, Feb. 2024, ISSN: 01420615. DOI: 10.1016/j.ijepes.2024.109782. [Online]. Available: https://linkinghub.elsevier.com/retrieve/pii/S0142061524000036.

[38] G. Van den Broeck, J. Stuyts, and J. Driesen, “A critical review of power quality standards and definitions applied to DC microgrids,” en, *Applied Energy*, vol. 229, pp. 281–288, Nov. 2018, ISSN: 03062619. DOI: 10.1016/j.apenergy.2018.07.058. [Online]. Available: https://linkinghub.elsevier.com/retrieve/pii/S0306261918310869.

[39] “LVDC Systems—Assessment of Standard Voltages and Power Quality Requirements,” IEC, Genève, Switzerland, Tech. Rep. IEC TR 63282, 2020.

[40] P. Prabhakaran and V. Agarwal, “Mitigation of voltage unbalance in a low voltage bipolar DC microgrid using a boost-SEPIC type interleaved dc-dc compensator,” in *2016 IEEE 2nd Annual Southern Power Electronics Conference (SPEC)*, Dec. 2016, pp. 1–6. DOI: 10.1109/SPEC.2016.7846222.

[41] A. Knockaert, “Bipolar dc microgrids: State of the art and solutions to voltage unbalance problem,” Master’s Thesis, Ecole polytechnique de Louvain, Université catholique de Louvain, 2023. [Online]. Available: http://hdl.handle.net/2078.1/thesis:40498.

[42] Z. Ali, Y. Terriche, L. Q. N. Hoang, *et al.*, “Fault Management in DC Microgrids: A Review of Challenges, Countermeasures, and Future Research Trends,” en, *IEEE Access*, vol. 9, pp. 128 032–128 054, 2021, ISSN: 2169-3536. DOI: 10.1109/ACCESS.2021.3112383. [Online]. Available: https://ieeexplore.ieee.org/document/9536721/.

[43] A. Hooshyar and R. Iravani, “Microgrid Protection,” en, *Proceedings of the IEEE*, vol. 105, no. 7, pp. 1332–1353, Jul. 2017, ISSN: 0018-9219, 1558-2256. DOI: 10.1109/JPROC.2017.2669342. [Online]. Available: http://ieeexplore.ieee.org/document/7885003/.

[44] S. Beheshtaein, R. M. Cuzner, M. Forouzesh, M. Savaghebi, and J. M. Guerrero, “DC Microgrid Protection: A Comprehensive Review,” *IEEE Journal of Emerging and Selected Topics in Power Electronics*, pp. 1–1, 2019, ISSN: 2168-6785. DOI: 10.1109/JESTPE.2019.2904588.

[45] R. Rodrigues, Y. Du, A. Antoniazzi, and P. Cairoli, “A Review of Solid-State Circuit Breakers,” en, *IEEE Transactions on Power Electronics*, vol. 36, no. 1, pp. 364–377, Jan. 2021, ISSN: 0885-8993, 1941-0107. DOI: 10.1109/TPEL.2020.3003358. [Online]. Available: https://ieeexplore.ieee.org/document/9120203/.

[46] Y. Xu, H. Yang, and J. Liu, "Calculation method of short-circuit current and voltage considering the interaction of different ports in DC system," en, *J. eng.*, vol. 2019, no. 16, pp. 711–714, Mar. 2019, ISSN: 2051-3305, 2051-3305. DOI: 10.1049/joe.2018.8384. [Online]. Available: https://onlinelibrary.wiley.com/doi/10.1049/joe.2018.8384.

[47] J. Yang, J. E. Fletcher, and J. O'Reilly, "Short-Circuit and Ground Fault Analyses and Location in VSC-Based DC Network Cables," en, *IEEE Trans. Ind. Electron.*, vol. 59, no. 10, pp. 3827–3837, Oct. 2012, ISSN: 0278-0046, 1557-9948. DOI: 10.1109/TIE.2011.2162712. [Online]. Available: http://ieeexplore.ieee.org/document/5959977/.

[48] P. Zhao, Q. Chen, and L. Xing, "DC fault analysis of VSC-HVDC and DC cable protection principle," en, in *2015 IEEE PES Asia-Pacific Power and Energy Engineering Conference (APPEEC)*, Brisbane, Australia: IEEE, Nov. 2015, pp. 1–5, ISBN: 978-1-4673-8132-1. DOI: 10.1109/APPEEC.2015.7380928. [Online]. Available: http://ieeexplore.ieee.org/document/7380928/.

[49] Y. Zhang, W. Zhang, Q. Peng, *et al.*, "Impact of Grid Topology on Pole-to-ground Fault Current in Bipolar DC Grids: Mechanism and Evaluation," en, *Journal of Modern Power Systems and Clean Energy*, vol. 11, no. 2, pp. 434–445, 2023, ISSN: 2196-5625. DOI: 10.35833/MPCE.2021.000399. [Online]. Available: https://ieeexplore.ieee.org/document/9673696.

[50] A. Meghwani, S. Chakrabarti, S. C. Srivastava, and S. Anand, "Analysis of fault characteristics in DC microgrids for various converter topologies," en, in *2017 IEEE Innovative Smart Grid Technologies - Asia (ISGT-Asia)*, Auckland: IEEE, Dec. 2017, pp. 1–6, ISBN: 978-1-5386-4950-3. DOI: 10.1109/ISGT-Asia.2017.8378426. [Online]. Available: https://ieeexplore.ieee.org/document/8378426/.

[51] L. Hallemans, G. Govaerts, G. Van Den Broeck, *et al.*, "Modelling and Experimental Validation of a Pole-To-Ground Protection Device in Low Voltage DC Microgrids," en, in *2020 22nd European Conference on Power Electronics and Applications (EPE'20 ECCE Europe)*, Lyon, France: IEEE, Sep. 2020, pp. 1–10, ISBN: 978-90-75815-36-8. DOI: 10.23919/EPE20ECCEEurope43536.2020.9215792. [Online]. Available: https://ieeexplore.ieee.org/document/9215792/.

[52] L. Hallemans, "A methodological approach to short circuit protection for low voltage dc grids," en, Ph.D. dissertation, KU Leuven, 2023-

06-12. [Online]. Available: https://lirias.kuleuven.be/4082448&lang=en.

[53] S. S. Khan and H. Wen, "A Comprehensive Review of Fault Diagnosis and Tolerant Control in DC-DC Converters for DC Microgrids," en, *IEEE Access*, vol. 9, pp. 80 100–80 127, 2021, ISSN: 2169-3536. DOI: 10.1109/ACCESS.2021.3083721. [Online]. Available: https://ieeexplore.ieee.org/document/9440977/ (visited on 01/20/2023).

[54] S. Singh, A. R. Gautam, and D. Fulwani, "Constant power loads and their effects in DC distributed power systems: A review," en, *Renewable and Sustainable Energy Reviews*, vol. 72, pp. 407–421, May 2017, ISSN: 13640321. DOI: 10.1016/j.rser.2017.01.027. [Online]. Available: https://linkinghub.elsevier.com/retrieve/pii/S1364032117300412 (visited on 09/28/2020).

[55] T. Dragičević, X. Lu, J. C. Vasquez, and J. M. Guerrero, "DC Microgrids—Part I: A Review of Control Strategies and Stabilization Techniques," *IEEE Transactions on Power Electronics*, vol. 31, no. 7, pp. 4876–4891, Jul. 2016, ISSN: 1941-0107. DOI: 10.1109/TPEL.2015.2478859.

[56] R. D. Middlebrook, "Input filter considerations in design and application of switching regulators," in *PESC'76, IEEE Power Electronics Specialists, Conference*, 1976.

[57] A. Riccobono and E. Santi, "Comprehensive Review of Stability Criteria for DC Power Distribution Systems," en, *IEEE Transactions on Industry Applications*, vol. 50, no. 5, pp. 3525–3535, Sep. 2014, ISSN: 0093-9994, 1939-9367. DOI: 10.1109/TIA.2014.2309800. [Online]. Available: http://ieeexplore.ieee.org/document/6757016/ (visited on 12/08/2022).

[58] J. Kim, H. Kim, Y. Cho, H. Kim, and J. Cho, "Application of a DC Distribution System in Korea: A Case Study of the LVDC Project," en, *Applied Sciences*, vol. 9, no. 6, p. 1074, Mar. 2019, ISSN: 2076-3417. DOI: 10.3390/app9061074. [Online]. Available: https://www.mdpi.com/2076-3417/9/6/1074.

[59] A. Lana, A. Pinomaa, P. Nuutinen, T. Kaipia, and J. Partanen, "Control and monitoring solution for the LVDC power distribution network research site," en, in *2015 IEEE First International Conference on DC Microgrids (ICDCM)*, Atlanta, GA, USA: IEEE, Jun. 2015, pp. 7–12, ISBN: 978-1-4799-9880-7. DOI: 10.1109/ICDCM.2015.7152001. [Online]. Available: http://ieeexplore.ieee.org/document/7152001/.

[60] P. Nuutinen, T. Kaipia, P. Peltoniemi, *et al.*, "Research Site for Low-Voltage Direct Current Distribution in a Utility Network—Structure, Functions, and Operation," en, *IEEE Transactions on Smart Grid*, vol. 5, no. 5, pp. 2574–2582, Sep. 2014, ISSN: 1949-3053, 1949-3061. DOI: 10.1109/TSG.2014.2308365. [Online]. Available: http://ieeexplore.ieee.org/document/6777363/.

[61] DC Systems. "Highway n470 project." (2023), [Online]. Available: https://www.dc.systems/projects/highway-n470.

[62] D. S. Lee, J. H. Lee, S. Y. Lee, and J. H. Kim, "A study on the protection scheme for lvdc distribution system in commercial buildings," in *27th International Conference on Electricity Distribution (CIRED 2023)*, vol. 2023, 2023, pp. 1378–1381. DOI: 10.1049/icp.2023.0733.

[63] Pôle MecaTech. "Projet MIRACCLE." (2024), [Online]. Available: https://www.polemecatech.be/fr/projets/miraccle/.

[64] K. Jithin, P. P. Haridev, N. Mayadevi, R. P. Harikumar, and V. P. Mini, "A review on challenges in dc microgrid planning and implementation," *Journal of Modern Power Systems and Clean Energy*, vol. 11, no. 5, pp. 1375–1395, 2023. DOI: 10.35833/MPCE.2022.000053.

[65] G. Vandenbroeck. "Overview of LVDC grid projects worldwide." Accessed on: Jan 25, 2024. (2024), [Online]. Available: https://www.google.com/maps/d/viewer?mid=1Wo_4jR2VH3E7e78zP-NOmGq_DC0&hl=nl&femb=1&ll=-3.81666561775622e-14%2C0&z=1.

[66] P. Singh, P. Paliwal, and A. Arya, "A Review on Challenges and Techniques for Secondary Control of Microgrid," en, *IOP Conference Series: Materials Science and Engineering*, vol. 561, no. 1, p. 012 075, Oct. 2019, ISSN: 1757-8981, 1757-899X. DOI: 10.1088/1757-899X/561/1/012075. [Online]. Available: https://iopscience.iop.org/article/10.1088/1757-899X/561/1/012075.

[67] J. M. Guerrero, J. C. Vasquez, J. Matas, L. G. de Vicuna, and M. Castilla, "Hierarchical control of droop-controlled ac and dc microgrids—a general approach toward standardization," *IEEE Transactions on Industrial Electronics*, vol. 58, no. 1, pp. 158–172, 2011. DOI: 10.1109/TIE.2010.2066534.

[68] F. GAO, R. KANG, J. CAO, and T. YANG, "Primary and secondary control in DC microgrids: A review," *Journal of Modern Power Systems and Clean Energy*, vol. 7, no. 2, pp. 227–242, Mar. 2019, ISSN: 2196-5420. DOI: 10.1007/s40565-018-0466-5. [Online]. Available: https://doi.org/10.1007/s40565-018-0466-5.

[69] Y. Zahraoui, I. Alhamrouni, S. Mekhilef, *et al.*, "Energy Management System in Microgrids: A Comprehensive Review," en, *Sustainability*, vol. 13, no. 19, p. 10 492, Sep. 2021, ISSN: 2071-1050. DOI: 10.3390/su131910492. [Online]. Available: https://www.mdpi.com/2071-1050/13/19/10492.

[70] L. Meng, Q. Shafiee, G. F. Trecate, *et al.*, "Review on Control of DC Microgrids and Multiple Microgrid Clusters," *IEEE Journal of Emerging and Selected Topics in Power Electronics*, vol. 5, no. 3, pp. 928–948, Sep. 2017, ISSN: 2168-6785. DOI: 10.1109/JESTPE.2017.2690219.

[71] R. Maurya, D. Nishad, A. K. Singh, and S. Prakash, "A Comprehensive Review on DC Microgrid Controlling Techniques," en, in *2023 IEEE 3rd International Conference on Sustainable Energy and Future Electric Transportation (SEFET)*, Bhubaneswar, India: IEEE, Aug. 2023, pp. 1–8, ISBN: 9798350319972. DOI: 10.1109/SeFeT57834.2023.10244927. [Online]. Available: ieeexplore.ieee.org/document/10244927/.

[72] F. Chen, R. Burgos, D. Boroyevich, J. C. Vasquez, and J. M. Guerrero, "Investigation of Nonlinear Droop Control in DC Power Distribution Systems: Load Sharing, Voltage Regulation, Efficiency, and Stability," en, *IEEE Transactions on Power Electronics*, vol. 34, no. 10, pp. 9404–9421, Oct. 2019, ISSN: 0885-8993, 1941-0107. DOI: 10.1109/TPEL.2019.2893686. [Online]. Available: ieeexplore.ieee.org/document/8616804/.

[73] F. Chen, R. Burgos, D. Boroyevich, and W. Zhang, "A nonlinear droop method to improve voltage regulation and load sharing in DC systems," en, in *2015 IEEE First International Conference on DC Microgrids (ICDCM)*, Atlanta, GA, USA: IEEE, Jun. 2015, pp. 45–50, ISBN: 978-1-4799-9880-7. DOI: 10.1109/ICDCM.2015.7152008. [Online]. Available: http://ieeexplore.ieee.org/document/7152008/.

[74] P. Prabhakaran, Y. Goyal, and V. Agarwal, "Novel Nonlinear Droop Control Techniques to Overcome the Load Sharing and Voltage Regulation Issues in DC Microgrid," en, *IEEE Transactions on Power Electronics*, vol. 33, no. 5, pp. 4477–4487, May 2018, ISSN: 0885-8993, 1941-0107. DOI: 10.1109/TPEL.2017.2723045. [Online]. Available: http://ieeexplore.ieee.org/document/7967860/.

[75] P. J. dos Santos Neto, J. P. C. Silveira, T. A. d. S. Barros, E. R. Filho, J. C. Vasquez, and J. M. Guerrero, "Enhanced Power Management System for Droop Control in a Grid Connected DC Microgrid," in *2019 IEEE 15th Brazilian Power Electronics Conference and 5th*

IEEE Southern Power Electronics Conference (COBEP/SPEC), Dec. 2019, pp. 1–6. DOI: 10.1109/COBEP/SPEC44138.2019.9065864.

[76] T. Hailu and J. A. Ferreira, "Piece-wise linear droop control for load sharing in low voltage DC distribution grid," en, in *2017 IEEE Southern Power Electronics Conference (SPEC)*, Puerto Varas, Chile: IEEE, Dec. 2017, pp. 1–6, ISBN: 978-1-5090-6425-0. DOI: 10.1109/SPEC.2017.8333598. [Online]. Available: http://ieeexplore.ieee.org/document/8333598/.

[77] S. Liu, J. Zheng, Z. Li, R. Li, W. Fang, and X. Liu, "Distributed Piecewise Droop Control of DC Microgrid with Improved Load Sharing and Voltage Compensation," in *2019 IEEE Third International Conference on DC Microgrids (ICDCM)*, Matsue, Japan: IEEE, May 2019, pp. 1–6, ISBN: 978-1-72813-491-8. DOI: 10.1109/ICDCM45535.2019.9232724. [Online]. Available: https://ieeexplore.ieee.org/document/9232724/.

[78] S. Sharma, V. M. Iyer, and S. Bhattacharya, "A Load Profile Based Optimized Piecewise Droop Control for DC Microgrids," en, in *2021 IEEE Fourth International Conference on DC Microgrids (ICDCM)*, Arlington, VA, USA: IEEE, Jul. 2021, pp. 1–7, ISBN: 978-1-72818-641-2. DOI: 10.1109/ICDCM50975.2021.9504628. [Online]. Available: https://ieeexplore.ieee.org/document/9504628/.

[79] T. R. Lanjewar, M. Mounica, and B. A. Rajpathak, "Application of Piecewise-smooth Droop Control in Solar PV Based Electric Vehicle charging Station," en, in *2023 IEEE Renewable Energy and Sustainable E-Mobility Conference (RESEM)*, Bhopal, India: IEEE, May 2023, pp. 1–6, ISBN: 9798350311327. DOI: 10.1109/RESEM57584.2023.10236380. [Online]. Available: https://ieeexplore.ieee.org/document/10236380/.

[80] J. M. Guerrero, L. Hang, and J. Uceda, "Control of Distributed Uninterruptible Power Supply Systems," en, *IEEE Transactions on Industrial Electronics*, vol. 55, no. 8, pp. 2845–2859, Aug. 2008, ISSN: 0278-0046. DOI: 10.1109/TIE.2008.924173. [Online]. Available: http://ieeexplore.ieee.org/document/4582449/.

[81] P.-C. Liu, P.-H. Huang, W. Xiao, H. H. Zeineldin, and M. Elmoursi, "Improved digital average current sharing control strategy for DC microgrids," en, in *IECON 2014 - 40th Annual Conference of the IEEE Industrial Electronics Society*, Dallas, TX, USA: IEEE, Oct. 2014, pp. 4300–4305, ISBN: 978-1-4799-4032-5. DOI: 10.1109/IECON.2014.7049149. [Online]. Available: http://ieeexplore.ieee.org/document/7049149/.

[82] X. Lu, J. M. Guerrero, K. Sun, and J. C. Vasquez, "An Improved Droop Control Method for DC Microgrids Based on Low Bandwidth Communication With DC Bus Voltage Restoration and Enhanced Current Sharing Accuracy," *IEEE Transactions on Power Electronics*, vol. 29, no. 4, pp. 1800–1812, Apr. 2014, ISSN: 1941-0107. DOI: 10.1109/TPEL.2013.2266419.

[83] V. Nasirian, A. Davoudi, F. L. Lewis, and J. M. Guerrero, "Distributed Adaptive Droop Control for DC Distribution Systems," en, *IEEE Transactions on Energy Conversion*, vol. 29, no. 4, pp. 944–956, Dec. 2014, ISSN: 0885-8969, 1558-0059. DOI: 10.1109/TEC.2014.2350458. [Online]. Available: http://ieeexplore.ieee.org/document/6894594/.

[84] V. Nasirian, S. Moayedi, A. Davoudi, and F. L. Lewis, "Distributed Cooperative Control of DC Microgrids," en, *IEEE Transactions on Power Electronics*, vol. 30, no. 4, pp. 2288–2303, Apr. 2015, ISSN: 0885-8993, 1941-0107. DOI: 10.1109/TPEL.2014.2324579. [Online]. Available: http://ieeexplore.ieee.org/document/6816073/.

[85] P. Wang, X. Lu, X. Yang, W. Wang, and D. Xu, "An Improved Distributed Secondary Control Method for DC Microgrids With Enhanced Dynamic Current Sharing Performance," en, *IEEE Transactions on Power Electronics*, vol. 31, no. 9, pp. 6658–6673, Sep. 2016, ISSN: 0885-8993, 1941-0107. DOI: 10.1109/TPEL.2015.2499310. [Online]. Available: https://ieeexplore.ieee.org/document/7323851/.

[86] R. Kumar and M. K. Pathak, "Distributed droop control of dc microgrid for improved voltage regulation and current sharing," en, *IET Renewable Power Generation*, vol. 14, no. 13, pp. 2499–2506, Oct. 2020, ISSN: 1752-1416, 1752-1424. DOI: 10.1049/iet-rpg.2019.0983. [Online]. Available: https://onlinelibrary.wiley.com/doi/10.1049/iet-rpg.2019.0983.

[87] R. Kumar and M. K. Pathak, "Control of DC Microgrid for Improved Current Sharing and Voltage Regulation," en, in *2020 3rd International Conference on Energy, Power and Environment: Towards Clean Energy Technologies*, Shillong, Meghalaya, India: IEEE, Mar. 2021, pp. 1–4, ISBN: 978-1-66542-536-0. DOI: 10.1109/ICEPE50861.2021.9404421. [Online]. Available: https://ieeexplore.ieee.org/document/9404421/.

[88] S. Anand, B. G. Fernandes, and J. Guerrero, "Distributed Control to Ensure Proportional Load Sharing and Improve Voltage Regulation in Low-Voltage DC Microgrids," *IEEE Transactions on Power Elec-*

tronics, vol. 28, no. 4, pp. 1900–1913, Apr. 2013, ISSN: 1941-0107. DOI: 10.1109/TPEL.2012.2215055.

[89] C. Li, S. K. Chaudhary, M. Savaghebi, J. C. Vasquez, and J. M. Guerrero, "Power Flow Analysis for Low-Voltage AC and DC Microgrids Considering Droop Control and Virtual Impedance," en, *IEEE Transactions on Smart Grid*, vol. 8, no. 6, pp. 2754–2764, Nov. 2017, ISSN: 1949-3053, 1949-3061. DOI: 10.1109/TSG.2016.2537402. [Online]. Available: http://ieeexplore.ieee.org/document/7442160/.

[90] A. Maulik and D. Das, "Application of linearised load flow method for droop-controlled DCMGs," en, *IET Generation, Transmission & Distribution*, vol. 14, no. 6, pp. 1114–1126, Mar. 2020, ISSN: 1751-8687, 1751-8695. DOI: 10.1049/iet-gtd.2018.7113. [Online]. Available: https://digital-library.theiet.org/content/journals/10.1049/iet-gtd.2018.7113.

[91] Chendan Li, S. K. Chaudhary, T. Dragicevic, J. C. Vasquez, and J. M. Guerrero, "Power flow analysis for DC voltage droop controlled DC microgrids," en, in *2014 IEEE 11th International Multi-Conference on Systems, Signals & Devices (SSD14)*, Castelldefels-Barcelona, Spain: IEEE, Feb. 2014, pp. 1–5, ISBN: 978-1-4799-3866-7. DOI: 10.1109/SSD.2014.6808896. [Online]. Available: http://ieeexplore.ieee.org/document/6808896/.

[92] B. S. H. Chew, Y. Xu, and Q. Wu, "Voltage Balancing for Bipolar DC Distribution Grids: A Power Flow Based Binary Integer Multi-Objective Optimization Approach," *IEEE Transactions on Power Systems*, vol. 34, no. 1, pp. 28–39, Jan. 2019, ISSN: 1558-0679. DOI: 10.1109/TPWRS.2018.2866817.

[93] J.-O. Lee, Y.-S. Kim, and S.-I. Moon, "Current injection power flow analysis and optimal generation dispatch for bipolar dc microgrids," *IEEE Transactions on Smart Grid*, vol. 12, no. 3, pp. 1918–1928, 2021. DOI: 10.1109/TSG.2020.3046733.

[94] *IEC 60228: Conductors of insulated cables*, Edition 4.0, 2023. [Online]. Available: https://webstore.iec.ch/publication/71891.

[95] P. Ferreira Torres, J. de Arimatéia Alves Vieira Filho, V. Chaar Junior, *et al.*, "Load flow simulation of a low-voltage pv-battery based dc micro-grid to supply small isolated communities," English, in *Proceedings of the 35th European Photovoltaic Solar Energy Conference and Exhibition*, ser. European Photovoltaic Solar Energy Conference and Exhibition (EU PVSEC), Sep. 2018, pp. 1636–1640, ISBN: 3936338507. DOI: 10.4229/35thEUPVSEC20182018-6CO.3.6.

[96] A. Ciocia, A. Amato, P. Di Leo, *et al.*, "Self-Consumption and Self-Sufficiency in Photovoltaic Systems: Effect of Grid Limitation and Storage Installation," en, *Energies*, vol. 14, no. 6, p. 1591, Mar. 2021, ISSN: 1996-1073. DOI: 10.3390/en14061591. [Online]. Available: https://www.mdpi.com/1996-1073/14/6/1591.

[97] M. Schreiber and P. Hochloff, "Capacity-dependent tariffs and residential energy management for photovoltaic storage systems," en, in *2013 IEEE Power & Energy Society General Meeting*, Vancouver, BC, Canada: IEEE, 2013, pp. 1–5, ISBN: 978-1-4799-1303-9. DOI: 10.1109/PESMG.2013.6672200. [Online]. Available: https://ieeexplore.ieee.org/document/6672200/.

[98] R. Luthander, J. Widén, D. Nilsson, and J. Palm, "Photovoltaic self-consumption in buildings: A review," en, *Applied Energy*, vol. 142, pp. 80–94, Mar. 2015, ISSN: 03062619. DOI: 10.1016/j.apenergy.2014.12.028. [Online]. Available: https://linkinghub.elsevier.com/retrieve/pii/S0306261914012859.

[99] H. Azaioud, R. Claeys, J. Knockaert, L. Vandevelde, and J. Desmet, "A Low-Voltage DC Backbone with Aggregated RES and BESS: Benefits Compared to a Traditional Low-Voltage AC System," en, *Energies*, vol. 14, no. 5, p. 1420, Mar. 2021, ISSN: 1996-1073. DOI: 10.3390/en14051420. [Online]. Available: https://www.mdpi.com/1996-1073/14/5/1420.

[100] S. Cuk, "Modeling, analysis, and design of switching converters," Jan. 1977.

[101] R. W. Erickson and D. Maksimovic, *Fundamentals of Power Electronics*. Springer, 2020.

[102] V. Vorperian, "Quasi-square-wave converters: Topologies and analysis," en, *IEEE Transactions on Power Electronics*, vol. 3, no. 2, pp. 183–191, Apr. 1988, ISSN: 0885-8993, 1941-0107. DOI: 10.1109/63.4348. [Online]. Available: https://ieeexplore.ieee.org/document/4348/.

[103] P. Sood, T. Lipo, and I. Hansen, "A versatile power converter for high frequency link systems," en, in *1987 IEEE Applied Power Electronics conference and Exposition*, San Diego, CA USA: IEEE, Mar. 1987, pp. 249–256. DOI: 10.1109/APEC.1987.7067159. [Online]. Available: http://ieeexplore.ieee.org/document/7067159/.

[104] P. Sood and T. Lipo, "Power conversion distribution system using a high-frequency AC link," en, *IEEE Transactions on Industry Applications*, vol. 24, no. 2, pp. 288–300, Apr. 1988, ISSN: 00939994. DOI:

10.1109/28.2869. [Online]. Available: http://ieeexplore.ieee.org/document/2869/.

[105] W. Alexander, "Universal power converter," 7,778,045 B2, U.S. Patent, Aug. 17, 2010.

[106] A. Balakrishnan, H. A. Toliyat, and W. C. Alexander, "Soft switched ac link buck boost converter," en, in *2008 Twenty-Third Annual IEEE Applied Power Electronics Conference and Exposition*, Austin, TX, USA: IEEE, Feb. 2008, pp. 1334–1339, ISBN: 978-1-4244-1873-2 978-1-4244-1874-9. DOI: 10.1109/APEC.2008.4522896. [Online]. Available: http://ieeexplore.ieee.org/document/4522896/.

[107] H. A. Toliyat, A. Balakrishnan, M. Amirabadi, and W. Alexander, "Soft switched ac-link AC/AC and AC/DC buck-boost converter," en, in *2008 IEEE Power Electronics Specialists Conference*, Rhodes, Greece: IEEE, Jun. 2008, pp. 4168–4176, ISBN: 978-1-4244-1667-7. DOI: 10.1109/PESC.2008.4592609. [Online]. Available: http://ieeexplore.ieee.org/document/4592609/.

[108] M. Amirabadi, A. Balakrishnan, H. A. Toliyat, and W. Alexander, "Soft switched ac-link direct-connect photovoltaic inverter," en, in *2008 IEEE International Conference on Sustainable Energy Technologies*, Singapore, Singapore: IEEE, Nov. 2008, pp. 116–120, ISBN: 978-1-4244-1887-9. DOI: 10.1109/ICSET.2008.4746983. [Online]. Available: http://ieeexplore.ieee.org/document/4746983/.

[109] M. Amirabadi, A. Balakrishnan, H. A. Toliyat, and W. C. Alexander, "High-Frequency AC-Link PV Inverter," en, *IEEE Transactions on Industrial Electronics*, vol. 61, no. 1, pp. 281–291, Jan. 2014, ISSN: 0278-0046, 1557-9948. DOI: 10.1109/TIE.2013.2245616.

[110] J. Sadeghi, E. F. Choolabi, and M. H. Zare, "A new topology of unidirectional multistring PV inverter with high frequency AC-Link," en, in *2016 24th Iranian Conference on Electrical Engineering (ICEE)*, Shiraz, Iran: IEEE, May 2016, pp. 1254–1259, ISBN: 978-1-4673-8789-7. DOI: 10.1109/IranianCEE.2016.7585714. [Online]. Available: http://ieeexplore.ieee.org/document/7585714/.

[111] M. Amirabadi, H. A. Toliyat, and W. C. Alexander, "A Multiport AC Link PV Inverter With Reduced Size and Weight for Stand-Alone Application," en, *IEEE Transactions on Industry Applications*, vol. 49, no. 5, pp. 2217–2228, Sep. 2013, ISSN: 0093-9994, 1939-9367. DOI: 10.1109/TIA.2013.2262093.

[112] A. Alfares, S. A. K. H. Mozaffari Niapour, and M. Amirabadi, “High frequency AC microgrid based on a highly reliable single-stage converter,” en, in *2015 IEEE Energy Conversion Congress and Exposition (ECCE)*, Montreal, QC: IEEE, Sep. 2015, pp. 2361–2367, ISBN: 978-1-4673-7151-3. DOI: 10.1109/ECCE.2015.7309992.

[113] R. Dosquet, D. Rixhon, and P. Bleus, “Future local intelligent transactional energy node for ev charging and mobility hub,” in *CIRED Porto Workshop 2022: E-mobility and power distribution systems*, vol. 2022, 2022, pp. 965–969. DOI: 10.1049/icp.2022.0857.

[114] J. Allard, E. V. Mayen, and E. De Jaeger, “Resonance model comparison for high-frequency ac link three-port converter,” in *2023 IEEE International Conference on Environment and Electrical Engineering and 2023 IEEE Industrial and Commercial Power Systems Europe (EEEIC / I&CPS Europe)*, 2023, pp. 1–6. DOI: 10.1109/EEEIC/ICPSEurope57605.2023.10194661.

[115] M. Amirabadi, J. Baek, H. A. Toliyat, and W. C. Alexander, “Soft-Switching AC-Link Three-Phase AC–AC Buck–Boost Converter,” en, *IEEE Transactions on Industrial Electronics*, vol. 62, no. 1, pp. 3–14, Jan. 2015, ISSN: 0278-0046, 1557-9948. DOI: 10.1109/TIE.2014.2331011.

[116] H. Young, R. Freedman, A. Ford, and M. Zemansky, *University Physics* (Sears and Zemansky’s University Physics). Addison Wesley, 2012, ISBN: 9780321733382. [Online]. Available: https://books.google.be/books?id=6K93wgEACAAJ.

[117] T. M. Inc., *Discrete variable-ratio two-winding ideal transformer*, Natick, Massachusetts, United States, 2024. [Online]. Available: https://www..mathworks.com/help/sps/powersys/ref/variableratiotransformer.html (visited on 06/13/2024).

[118] P. Documentation. “Pandapower documentation: Standard types.” (2024), [Online]. Available: https://pandapower.readthedocs.io/en/v2.13.1/std_types/basic.html.